Topological Quantum Optics in Two-dimensional Atomic Lattices

by

János Perczel

B.Sc., University of St Andrews (2011)
M.A.St., University of Cambridge (2012)

Submitted to the Department of Physics
in partial fulfillment of the requirements for the degree of

Doctor of Philosophy

at the

MASSACHUSETTS INSTITUTE OF TECHNOLOGY

February 2019

Author .....
Department of Physics
October 31, 2018

Certified by .....
Mikhail D. Lukin
Professor of Physics, Harvard University
Thesis Supervisor

Certified by .....
Vladan Vuletić
Professor of Physics
Thesis Co-supervisor

Accepted by .....
Nergis Mavalvala
Professor of Astrophysics, Associate Department Head

Topological Quantum Optics in Two-dimensional Atomic Lattices

by

János Perczel

Submitted to the Department of Physics
on October 31, 2018, in partial fulfillment of the
requirements for the degree of
Doctor of Philosophy

Abstract

A key goal in quantum science is to build quantum systems that are robust to disorder and experimental imperfections. The application of topology to quantum physics is one of the most promising avenues towards achieving this goal, since topological systems are generally insensitive to moderate, local perturbations. This thesis is dedicated to the introduction and analysis of novel platforms for engineering topological states in the optical domain.

First, we analyze the interaction of atoms in Maxwell's fish eye lens, which is an optical medium mimicking light propagation on the surface a sphere. Due to the underlying (trivial) spherical topology of the system, light follows circular trajectories in the lens, giving rise to special focusing properties. We investigate the long-range atomic interactions mediated by the lens and the efficiency of entangling operations.

We then turn our attention to two-dimensional atomic arrays in free space, where interactions are mediated by photons. We show that in the presence of a uniform magnetic field, the system exhibits a photonic band structure with non-trivial Chern numbers and a topological gap. We explore the topological edge states that arise on the system boundaries, identify the conditions under which edge states are long-lived and show that they are robust to imperfections in the lattice.

Finally, we study two-dimensional atomic emitter arrays embedded in photonic crystals. We engineer a quasi-two-dimensional photonic crystal slab that mediates long-range dipolar interactions between emitters and gives rise to topological behavior. We analyze the topological edge states of the system and show that they are robust to the inhomogeneous broadening of the emitters and to missing lattice sites.

Thesis Supervisor: Mikhail D. Lukin
Title: Professor of Physics, Harvard University

Thesis Co-supervisor: Vladan Vuletić
Title: Professor of Physics

Dedicated to my family, Kinga, István,
Juli, Jakab, Léna
and Dorci.

Acknowledgments

First and foremost, I would like to thank my supervisor, Prof. Mikhail Lukin, for guiding me throughout my PhD with patience, trust and unwavering interest in our research projects. His extraordinary physical intuition and insights have been a constant source of inspiration throughout these years. Working with someone, who is both an exceptional scientist and an excellent supervisor, was a real privilege.

I would also like to thank the other members of my thesis committee, Prof. Wolfgang Ketterle, Prof. Vladan Vuletić and Prof. Max Metlitski. I became interested in atomic physics after taking Wolfgang's class on Atomic and Optical Physics during the first year of my PhD, which naturally lead me to Misha's research group at Harvard due to my interest in doing theoretical work. I would also like to thank Vladan for all of his help with the administrative aspects of pursuing research off-campus at Harvard. I am also grateful to Max for agreeing to serve on my committee.

I am also indebted to Prof. Peter Zoller in Innsbruck for his mentorship over the years. Our intermittent, but extensive discussions during his visits greatly helped to crystalize the ideas behind my work on topological quantum optics and never failed to illuminate the problem at hand from a completely novel perspective. I am also grateful to Prof. Darrick Chang at ICFO for the numerous times his explanations clarified obscure aspects of quantum optics and his insights pushed my projects forward. I also want to thank Prof. Susanne Yelin at Harvard for illuminating discussions.

A manifest privilege of being part of the Lukin group is working alongside its brilliant, motivated and unusually productive members. During the first few years of my PhD, I benefited greatly from my collaboration with Péter Kómár, who taught me how to think about open quantum systems and who seemed to have already thought through all questions that came to my mind about quantum optics. Despite its brevity, the time I spent working with Hannes Pichler was transformative, as he introduced me to the power of running simple MatLab scripts to quickly explore and visualize problems that are too difficult to handle analytically. This is a skill that served me well throughout my PhD. I also learned a great deal from our

frequent discussions with Dominik Wild, whose technical skill and clarity of thought contributed to my own development. Working with Johannes Borregaard was both a terrific boost to my productivity as well as a calming force during a time in my PhD, when none of my projects seemed to go anywhere. I was also fortunate to share an office and spend countless hours of discussion with Emma Rosenfeld, Alexander Keesling, Sylvain Schwartz, Thibault Peyronel, Tobias Tiecke and David Levonian.

It was also a great pleasure to interact and work with other current and past members of the Lukin group, including Arthur Safira, Ruffin Evans, Efi Shahmoon, Soonwon Choi, Joonhee Choi, Jeff Thompson, Nathalie de Leon, Alp Sipahigil, Alexei Bylinskii, Kristiaan de Greve, Polnop Samutraphoot, Leo Zhou, Trond Andersen, Mihir Bhaskar, Harry Levine, Shimon Kolkowitz, Georg Kucsko, Manuel Endres, Denis Sukachev, Shengtao Wang and Florentin Reiter.

Outside the Lukin group, I have very much enjoyed collaborating with Alex High and Rob Devlin from the research group of Prof. Hongkun Park in the Department of Chemistry at Harvard. Working with Qian Lin from Prof. Shanhui Fan's group at Stanford has also been a great pleasure. In addition, I have also benefitted significantly from discussions with Márk Mezei and Maksym Serbyn at MIT; Daniel Greif, Márton Kanasz-Nagy and Fabian Grusdt at Harvard; and Johannes Motruk and Norman Yao at Berkeley.

Our PhD cohort at MIT developed into a tightly-knit group and was an invaluable source of support over the years. I am particularly grateful for the friendship of Boris Shteynas. He has been a selfless and dependable friend and flatmate ever since we got to know each other at the very first orientation event six years ago. I am also thankful for the friendship of Junru Li, Jenny Schloss and Tom Mahony, Ian Counts, Alex Ji, William Cody Burton, Matt Nichols, Alex Leder, Murphy Yuezhen Niu, Nancy Aggarwal and Mukund Varma.

Being a teaching assistant was also an important part of my PhD experience. Teaching a TEAL electromagnetism class with Prof. Jesse Thaler was one of my most enjoyable experiences at MIT, not the least because of Jesse's infectious energy and enthusiasm for explaining physics to students. I have also learned a great deal

from teaching alongside Prof. Krishna Rajagopal, whose articulate explanations and unique organizational skills I much admire. It was also very instructive to observe the teaching skills of Prof. Scott Hughes from up-close.

I am also thankful to my friends in Boston. From my first day in the US, when I crashed at their couch, the endless help and kindness of Nadia Shalaby and her daughters Tali Shalaby and Dina Voevodsky has been invaluable. I am also grateful for the friendship of Márk Mezei and Anna Pósfai, Márton Kanasz-Nagy, Bence Béky, Laszló Lovász, Temple He and Monica Kang, Fruzsina Veress and Peter Gács, Rumen Dangovski, Sam Rodriquez and Albert López.

I also want to thank my physicist friends Aaron Levy, Dániel Tóth and Levente Krizsan for being great friends and peers over the years.

I am particularly grateful for the early support of my St Andrews undergraduate supervisor, Prof. Ulf Leonhardt, without whose help I would have never got the chance to attend MIT. Doing research with Ulf was a transformational experience that turned my attention to 'practical theoretical physics', which remained my focus throughout my PhD. I am also thankful to Dr. Natalia Korolkova and Dr. Chris Hooley, who supported and guided me during my St Andrews years.

I also want to thank Mr. Botond Molnar, my high school physics teacher, who made me interested in physics in the first place. Without his early influence, I would not have dedicated the past 10 years to studying and doing research in physics.

I am especially grateful to my parents, Kinga Korényi and István Perczel, and my siblings, Júlia, Jakab and Léna for their unconditional support during my whole PhD. Finally, I owe the greatest thanks to my wife, Dorottya Demszky, for being such a loving and supportive companion throughout these years. You have been the light of my life.

Contents

Citations to Previously Published Work

Most of the chapters of this thesis have appeared in print elsewhere. By chapter number, they are:

- Chapter 2:

  J. Perczel, P. Kómár, and M. D. Lukin, "Quantum Optics in Maxwell's Fish Eye Lens with Single Atoms and Photons", Physical Review A **98**, 033803 (2018).

- Chapter 3:

  J. Perczel, J. Borregaard, D. E. Chang, H. Pichler, S. F. Yelin, P. Zoller, and M. D. Lukin, "Photonic Band Structure of Two-dimensional Atomic Lattices", Physical Review A **96**, 063801 (2017).

- Chapter 4:

  J. Perczel, J. Borregaard, D. E. Chang, H. Pichler, S. F. Yelin, P. Zoller, and M. D. Lukin, "Topological Quantum Optics in Two-dimensional Atomic Arrays", Physical Review Letters **119**, 023603 (2017).

- Chapter 5:

  J. Perczel, and M. D. Lukin, "Theory of Dipole Radiation Near a Dirac Photonic Crystal", arXiv preprint (2018), arXiv:1810.12815.

- Chapter 6:

  J. Perczel, J. Borregaard, Darrick E. Chang, Susanne F. Yelin, and M. D. Lukin, "Topological Quantum Optics in Two-dimensional Photonic Crystals", arXiv preprint (2018), arXiv:1810.12299.

Other publications I worked on during my PhD, but not discussed in this thesis:

- A. High, R. Devlin, A. Dibos, M. Polking, D. Wild, J. Perczel, N. de Leon, M. D. Lukin, and H. Park, "Visible Frequency Hyperbolic Metasurface", Nature **522**, 192 (2015).

- Q. Lin, J. Perczel, M. D. Lukin, and S. Fan, "Topological Edge States in a Three-dimensional Atomic Lattice with a Screw Dislocation", in preparation.

Chapter 1

Introduction

An outstanding challenge in quantum science is to build quantum systems, which are robust to imperfections and disorder. For small quantum systems, composed of just a few qubits, imperfections can be controlled by improving the experimental apparatus and applying well-established techniques for coherent control. However, as a quantum system is scaled up to hundreds or thousands of qubits, the probability of errors increases exponentially, making it difficult to maintain coherence. Given that quantum devices with a large number of qubits are expected to find various important technological applications – such as secure communications [1], factoring large numbers [2] and simulating complicated physical systems [3] – finding ways to improve the robustness of large quantum systems is a fundamental goal in quantum science.

The application of topology to quantum physics is one of the most promising paths towards designing large quantum systems that would be robust to imperfections and disorder [4]. Topological physical systems are typically insensitive to small, local perturbations. Therefore, such systems have the potential to maintain their useful quantum properties even when the system size is scaled up. Over the past decades, topological quantum physics and its potential applications to quantum information processing have been the subject of intense research efforts [4, 5].

This thesis is focused on topological quantum optics – a novel branch of topological quantum physics –, which involves the study of light-matter interactions at *optical*

frequencies in the presence of topology. Quantum systems that operate at optical frequencies are particularly well-suited for building large-scale quantum networks [6], as optical photons are excellent carriers of information between distant quantum nodes (as opposed to e.g. microwave photons). In the quantum systems studied here, all atomic interactions are mediated by optical photons. Through these interactions, atoms and photons become intricately interwoven, forming a hybrid system composed of polaritons that have both atomic and photonic character.

Such a hybrid system has several advantages. Due to its atomic character, time-reversal symmetry can be broken simply by applying a magnetic field. In addition, atoms are inherently non-linear, providing a pathway towards introducing interactions, which are crucial for studying interesting many-body states. This contrast sharply with traditional topological photonics, where breaking time-reversal symmetry at optical frequencies remains a significant challenge [7] and non-linearities are typically weak [8]. At the same time, the photonic character of the hybrid system also ensures that the system evolves at a fast (typically tens of MHz) time scale, thereby avoiding some of the technical issues associated with very low energy scales, such as the ubiquitous problem of unwanted heating in systems of ultracold atoms.

The main trade-off in the case of quantum optics is that, in general, atoms also couple to far-field photons carrying the excitation away from the system, leading to irreversible decay. Thus, photon-mediated atom-atom interactions are always in competition with photon decay from the system. There exist various techniques to mitigate this problem. The most widely employed strategy is to use cavities to confine the photon and prevent it from flying away [9]. This is a technique that we repeatedly adopt in this thesis, including in Chapters 2, 5 and 6.

The other technique, that we utilize in Chapters 3 and 4, is more subtle. It exploits the conservation of momentum, which demands that, when an excitation is transformed from being a hybrid polariton to a free-space photon, momentum has to be preserved. The range of possible momenta for free-space photons is capped at $k = \omega/c$, where ω is the photon frequency and c is the speed of light. Thus, if the momentum of a given mode is larger than ω/c, it simply cannot couple to

free-space photons, as this would violate conservation of momentum. Consequently, we can effectively decouple our quantum optical system from free-space photons by increasing the momenta of our hybrid polaritonic modes beyond ω/c. As we shall see, this can be conveniently achieved by using subwavelength interatomic spacing.

All systems discussed in this thesis are quasi-two-dimensional. The implicit motivation for this is that two-dimensional topological physics is expected to be the most interesting from the perspective of quantum information processing. The underlying reasoning is that *anyons*, which are theorized to be useful for quantum computing [10], only exist in two dimensions. Anyons are special types of quasi-particles, with unusual quantum statistics [11]. In particular, the exchange of two identical anyons can give rise to a global phase shift to their wavefunction. Anyons with Abelian statistics are excitations that arise in the context of the Fractional Quantum Hall effect [12] and have been experimentally observed before [4]. Anyons with non-Abelian statistics are also theorized to arise among the states of the Fractional Quantum Hall effect (e.g. the states with filling fractions $\nu = 5/2$ and $\nu = 12/5$) [4, 13]. Non-Abelian anyons are strong candidates for the realization of topological quantum computing.

1.1 Topology and geometry

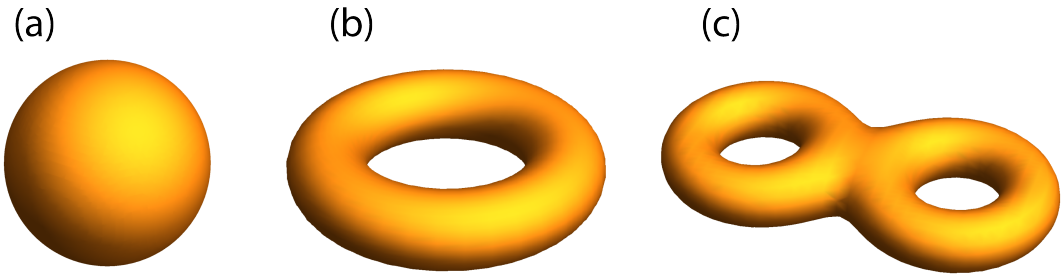

Figure 1-1: (a) Sphere with genus 0. (b) Torus with genus 1. (c) Double torus with genus 2.

A recurring theme in this thesis is the role of geometry and topology in guiding light and mediating interactions between atoms.

Topology is a branch of mathematics that studies geometric properties that are

unaffected by continuous deformations [7]. Fig. 1-1 shows three different geometric objects, which are topologically distinct entities. From the perspective of topology, an important concept for the classification of these shapes is the *genus*, or the number of holes. Clearly, the sphere, the torus and the double torus have genus 0, 1 and 2, respectively. The only way to change the number of holes of these objects is to cut them and re-glue the resulting open boundaries (e.g. poke a hole into the sphere). Simply squashing them or putting dents into the surface does not change the genus. The genus of these objects is a *topological invariant* that does not change under smooth deformations. The genus of these objects can be calculated using the formula

$$g = 1 - \frac{1}{4\pi} \int K dS, \tag{1.1}$$

where g stands for the genus, K is the *Gaussian curvature* and the integral is performed over the closed surface of each object [7].

In Chapter 2, we study the influence of the simplest possible topology on photons and atoms – a sphere with genus 0. In particular, we study the photon-mediated interactions between atoms in Maxwell's fish eye lens. The fish eye is an optical instrument that closely mimics the surface of a sphere and, therefore, light rays in the lens trace out perfectly circular trajectories. The special spherical topology associated with the fish eye lens leads to unique focusing properties for light, which in turn can be used to mediate long-range interactions and entanglement between photons.

In physics we also often use a special topological invariant, called the *Chern number*, to classify physical systems [14]. This is a slightly more abstract, but analogous concept to genus. Instead of studying shapes in real space, we analyze periodic physical systems in momentum space. In analogy to counting the number of real holes, we count the number of monopoles of *Berry flux* in such systems. The Berry flux is an abstract, quantized quantity that captures how the phase of the wavefunction of our system changes across the Brillouin zone. It can be calculated via

$$C = \frac{1}{2\pi} \int \mathbf{F} \cdot d\mathbf{S}, \tag{1.2}$$

where C is the Chern number, $\mathbf{F}$ is the *Berry curvature* and the integral is performed over the entire Brillouin zone for a given energy band [7, 14]. If the Chern number of each band is zero, the system is topologically trivial from a physics perspective. Non-zero Chern numbers indicate that the system could exhibit interesting topological phenomena.

In each of Chapters 3, 4 and 6, we study periodic atomic lattices that feature energy bands with non-zero Chern numbers. The non-trivial topology gives rise to interesting topological phenomena, such as topological edges states that are robust to imperfections and disorder.

1.2 Topology and dipolar interactions

Topology in physical systems was first discovered in the context of electronic systems, in particular, the Quantum Hall Effect [15]. The Quantum Hall Effect is intricately tied to the fact that electrons are charged particles, which experience the Lorentz force and follow Landau orbits in the presence of a uniform magnetic field [16]. In 1988, Haldane realized that topological behavior can be generalized to electronic systems, where the net magnetic field is zero [17]. This was followed by the gradual realization that topological phenomena are, in fact, not confined to electronic systems, but are much more general and can be found in a plethora physical systems, including those with chargeless excitations. Over the past three decades, topological phenomena have been studied in the context of cold neutral atoms [18–21], microwave [22–27] and optical photonics [28–31], acoustic waves [32–34] and mechanical systems [35–37].

In general, in a system of chargeless particles, the key objective is to ensure that the excitations experience an effective magnetic field. For example, in optical lattices with cold neutral atoms, this is typically achieved by engineering an artificial gauge field via control of the hopping parameters between sites [18]. As a result, the matter wave excitations behave like electrons hopping on an atomic lattice in the presence of a real magnetic field. In photonic systems, a common strategy is the use of gyromagnetic materials, which change their electromagnetic response as a function of an

external magnetic field [22–27]. As a result, chargeless photons propagating through a gyromagnetic medium indirectly experience the effects of the external magnetic field and behave analogously to charged particles.

In Chapters 3-6 of this thesis, we focus on engineering effective magnetic fields for chargeless photons hopping on an atomic lattice. However, instead of adjusting the hoppings or using gyromagnetic materials, we utilize the intrinsic geometric phases associated with *dipolar interactions* to obtain topological behavior and simply use the *Zeeman effect* to imprint the presence of an external magnetic field on the constituent atoms.

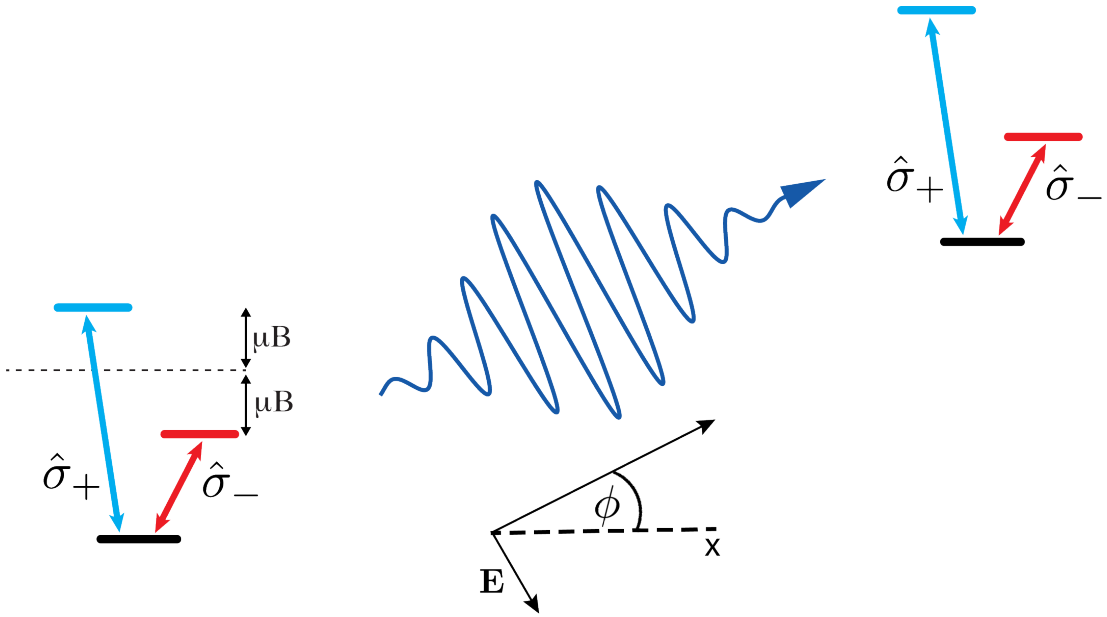

Figure 1-2: Schematic depiction of photon-mediated dipolar atomic interactions between two atoms with $\hat{\sigma}_+ = (\hat{x} + i\hat{y})/\sqrt{2}$ and $\hat{\sigma}_- = (\hat{x} - i\hat{y})/\sqrt{2}$ transitions that are Zeeman-shifted by an external magnetic field. The two atoms are generally positioned at an angle ϕ relative to the x axis and the electric field of the photon is parameterized as $\mathbf{E} \sim \sin\phi\, \hat{x} - \cos\phi\, \hat{y}$.

The emergence of topological phases in a system of atoms with dipolar interactions can be understood from the following simple argument. Let's consider dipolar atoms with a ground state and two excited states with $\hat{\sigma}_+ = (\hat{x} + i\hat{y})/\sqrt{2}$ and a $\hat{\sigma}_- = (\hat{x} - i\hat{y})/\sqrt{2}$ transitions (see Fig. 1-2). In the presence of an external magnetic field, the two transitions are Zeeman-split. Thus, it is meaningful to consider the dipolar exchange of a photon between one atom in its $|\sigma_+\rangle$ state and another atom, some

distance away, in its $|\sigma_-\rangle$ state. Each atom ($i = 1, 2$) couples to the electromagnetic field via the term

$$V_i = -\mathbf{d}_i \cdot \mathbf{E}, \tag{1.3}$$

where $\mathbf{d}_i$ stands for the transition dipole moment of the i^{th} atom and $\mathbf{E}$ denotes the electric field. The transition dipole moments of the two atoms are proportional to

$$\mathbf{d}_1 \sim (\hat{x} + i\hat{y}) \qquad \text{and} \qquad \mathbf{d}_2 \sim (\hat{x} - i\hat{y}). \tag{1.4}$$

In general, the two atoms are located at an angle ϕ with respect to the x axis (see Fig. 1-2) and, therefore, the electric field of the photon propagating between them is parameterized as

$$\mathbf{E} \sim \sin\phi\, \hat{x} - \cos\phi\, \hat{y}, \tag{1.5}$$

where we assume that the polarization of the photon is perpendicular to the direction of its propagation. After adiabatically eliminating the photonic degrees of freedom [38], we find that the dipolar interaction between the two atoms is given by

$$V_{12} \sim V_1 V_2^* \sim (\sin\phi - i\cos\phi)(\sin\phi + i\cos\phi)^* \sim e^{2i\phi}. \tag{1.6}$$

The above phase in the dipolar interaction between the two atoms is a *winding phase*, as it winds around as a function of the angular position of atoms. These phases become ill-defined for $\mathbf{r} = 0$, which constitutes a phase defect. Such winding phases provide a straightforward recipe for engineering topology in a dipolar system [39]. In particular, the phase defects associated with such winding lead to monopoles of Berry flux in momentum space and, thus, to non-trivial Chern numbers.

As this simple argument indicates, dipolar interactions in the presence of a magnetic field naturally give rise to non-trivial topology. The exploration of the topological phenomena that arise in dipolar systems in free space forms the backbone of Chapters 3 and 4. Besides finding photonic bands with non-trivial Chern numbers, we also study the edge states that arise on the system boundaries of finite atomic lattices. Depending on the geometry of the edge termination, we find edge states

that are short- or long-lived. We also explore the robustness of these edge states to imperfections and defects of the atomic lattice.

1.3 Topology and photonic crystals

The argument for the existence of a winding phase in the dipolar interaction of atoms is very general and holds not only in free space, but also in other electromagnetic environments [40]. The only requirement is that the polarization of the interaction-mediating photon be tied to the direction of propagation, as in Eq. (1.5). For example, a standing wave would not satisfy this requirement, but most propagating waves do – even in structured photonic environments. This is a powerful generalization, as it opens up the rich and varied toolbox of nanophotonics [41] for the purposes of engineering topological atomic systems.

In Chapters 5 and 6, we consider dipolar interactions mediated by quasi-two-dimensional photonic crystal slabs. In particular, in Chapter 5 we engineer photonic crystals slabs, where the direction-dependent polarization of the guided photons has a simple and explicit form, enabling precise, analytic calculations of the slab-mediated dipolar interactions. Then, in Chapter 6 we consider a two-dimensional lattice of atomic emitters embedded in such a photonic crystal slab and explicitly show that the system has a topological band structure. We also study the edge states that arise in a finite lattice and show that the edge states are robust to defects expected in realistic systems, such as emitters missing from sites and inhomogeneous broadening.

Chapter 2

Quantum Optics in Maxwell's Fish Eye Lens with Single Atoms and Photons

2.1 Introduction

Maxwell's two-dimensional fish eye is an optical lens with remarkable imaging properties. Light emitted from *any* point inside the lens refocuses at the antipodal point on the opposite side of the lens. Since J. C. Maxwell's original work that studied ray optics inside the lens [42], the properties of the fish eye have been analyzed in a variety contexts, including electromagnetic waves [43, 44], scalar waves [45], quantum mechanics [46] and supersymmetry [47].

More recently, it was proposed that Maxwell's fish eye lens may have the ability to perfectly refocus electromagnetic waves emerging from a point source [48–50], thereby overcoming the diffraction limit [51]. The idea of perfect imaging with Maxwell's fish eye has generated vigorous debate [52–79]. It has focused on how the presence of a point-like detector, placed at the focus point, changes the image formed and whether perfect imaging is an artifact of the detector. On the one hand, it has been argued that the presence of the detector, which can absorb the incoming radiation, is necessary to

form a perfect image [48–50, 52–55]. On the other hand, concerns have been raised that the detector itself would contribute electromagnetic waves to the image formed, giving rise to the apparent subwavelength focus point [55–58]. Subsequently, the discussion about perfect imaging has shifted to finding a simple and realistic model for such detectors [59–64, 71]. More recently, it was suggested that perfect imaging may be possible when operating very close to the resonances of the fish eye lens [76–79].

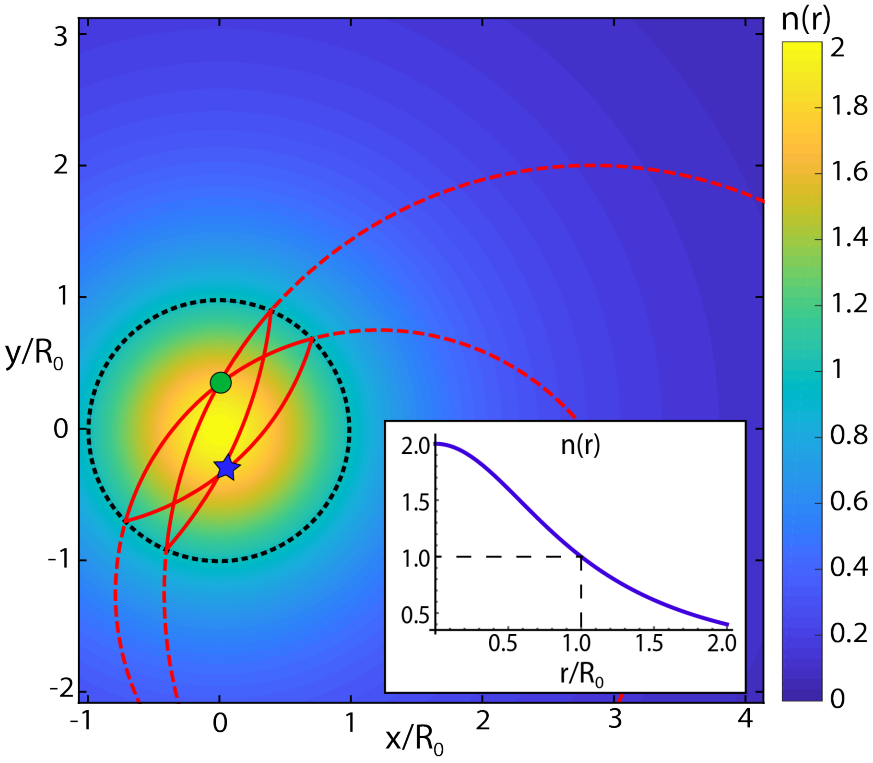

Figure 2-1: Light rays propagating within the infinite 2D fish eye lens trace out perfect circles (dashed red lines). If a mirror of radius R_0 is introduced (black dotted circle), the trajectories remain closed (solid red lines). All light rays emerging from an arbitrary point within the lens (green dot) refocus at the antipodal point (blue star). The color code and the inset show the spatial variation of the refractive index as a function of the radius, where we assume that $n_0 = 1$ in Eq. (2.1). For $r > R_0$ the refractive index of the fish eye dips below 1.

In this Chapter, we study the imaging properties of Maxwell's two-dimensional (2D) fish eye lens at the single-photon level using single atoms. In particular, we assume that both the source and the detector of the photon are individual atoms and

thus no ambiguity arises regarding their fundamental properties. One atom, initially in its excited state, emits the photon and the second atom, initially in its ground state, absorbs the photon, storing it in a metastable state for fluorescent readout. This is conceptually the simplest model for a source and a detector [78].

We model the 2D lens as an effective photonic cavity filled with an inhomogeneous dielectric material and solve for the atom-photon dynamics inside the lens. Since the rate of photon exchange between the atoms is set by the local electric field strength, the atomic dynamics is a sensitive indicator of the electric field distribution of the photon during absorption. In particular, we find the the photon exchange rate between the two atoms, which are detuned from the cavity resonances, is well described by a simple model, which assumes that the photon is focused to a diffraction-limited area during absorption.

We also analyze the capabilities of the fish eye to enhance the interaction between distant atoms. In particular, we show that the dipole-dipole interaction mediated by the fish eye lens is effectively infinite in range. This infinite-range interaction is a consequence of the unique focusing properties of the fish eye lens and is analogous to the infinite-range interactions mediated by quasi-1D waveguides, which have been the subject of extensive research in recent years in the context of hollow [80, 81], plasmonic [82–84], microwave [85–87] and dielectric [88–93] waveguides. Within this model, we quantitatively evaluate entangling operations and discuss a realistic experimental realization.

This Chapter is organized as follows. In Section 2.2 we discuss the general formalism behind our work and derive the dipole-dipole interaction mediated by the lens between atoms. In Section 2.3 we discuss the entanglement of atoms within the lens. In Section 2.4 we analyze the validity of the Born-Markov approximation. In Section 2.5 we discuss a possible physical realization of the 2D fish eye using transformational plasmon optics. Key insights of our work are summarized in Section 2.6.

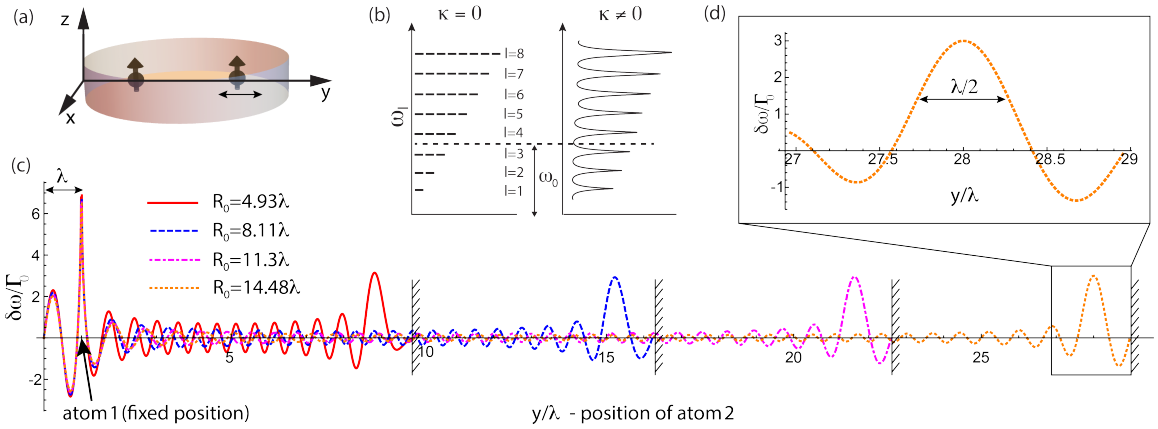

Figure 2-2: (a) Schematic depiction of the two dipoles embedded in the fish eye cavity, which is surrounded by mirrors on all sides. (b) Spectrum of the cavity ($\omega_l = \sqrt{l(l+1)}c/(R_0 n_0)$, $l = 1, 2, 3\ldots$) in the absence ($\kappa = 0$) and the presence ($\kappa \neq 0$) of losses. The atomic resonant frequency ω_0 is tuned between two resonances of the cavity. (c) Strength of the dipole-dipole interaction $\delta\omega(\mathbf{r}_1, \mathbf{r}_2)/\Gamma_0$ between two atoms for four different lens radii: (i) $R_0 = 4.93\lambda$, (ii) $R_0 = 8.11\lambda$, (iii) $R_0 = 11.3\lambda$ and (iv) $R_0 = 14.48\lambda$, assuming lens thickness $b = \lambda/10$ and $\Gamma_0 = d_z^2\omega_0^3/(3\pi\varepsilon_0\hbar c^3)$. The lens radii are chosen such that the transition frequency of the atoms $\omega_0 = 2\pi c/\lambda$ lies halfway between the resonances of the lens ($l = 1, 2, 3\ldots$). In particular, we chose the order parameters (i) $\nu = 30.5$, (ii) $\nu = 50.5$, (iii) $\nu = 70.5$ and (iv) $\nu = 90.5$, where $\nu = \frac{1}{2}(\sqrt{16\pi^2(R_0 n_0/\lambda)^2 + 1} + 1)$ and $n_0 = 1$. The atom on the left is positioned exactly λ away from the mirror, whereas the position of the second atom is sweeped. The strength of the interaction peaks λ away from the opposite mirror surface with a height that is independent of the radius of the lens and the interatomic distance. (d) Enlarged view of the dipole-dipole interaction near the antipodal point, showing that the width of the peak is approximately $\lambda/2$.

2.2 General Formalism

In this section we describe the general formalism behind our calculations for exploring the quantum optical properties of the system and calculate the dipole-dipole interaction between atoms placed inside the lens.

2.2.1 Maxwell's Fish Eye Lens

The two-dimensional fish eye lens is a dielectric medium of infinite size with refractive index [49]

$$n(\mathbf{r}) = \frac{2n_0}{1 + (r/R_0)^2}, \tag{2.1}$$

where $r = \sqrt{x^2 + y^2}$, R_0 is the natural length scale of the problem and $n_0 \geq 1$ can be chosen arbitrarily. We assume $n_0 = 1$ for all numerical calculations in this Chapter. In the limit of geometric optics, light rays propagate in perfect circles (Fig. 2-1, dashed circles). All rays emitted from a single point inside the lens ultimately meet at the antipodal point. For $|\mathbf{r}| > R_0$ the refractive index varies between n_0 and 0, which is difficult to achieve in practice. Thus the lens is modified by placing a mirror around the circle of radius $|\mathbf{r}| = R_0$ (black circle in Fig. 2-1). In the presence of the mirror the trajectories still remain closed (solid red lines in Fig. 2-1) [48].

The 2D fish eye can be realized for *electromagnetic waves* in a thin disk of radius R_0 with a dielectric material of radially varying refractive index given in Eq. (2.1), which is constant along the $\hat{z}$ direction. When the top and bottom surfaces of the disk are covered with two parallel mirrors, the lowest-frequency transverse electromagnetic (TEM) mode is invariant along the $\hat{z}$ direction and realizes the ideal dynamics of the 2D fisheye [50, 70]. While other modes with higher frequencies will also be present, when the operating frequency is below a certain cut-off, only the lowest TEM mode is excited. Specifically, this is achieved when the frequency of the radiating source ω_0 is much smaller than the cut-off frequency $\pi c/b$, where c is the speed of light in vacuum and b is the thickness of the disk [70, 94]. Later, we consider a realistic realization of the two-dimensional fish eye with surface plasmons, where the transverse confinement

arises naturally from the confinement of the plasmons to the metal-dielectric interface [95, 96].

2.2.2 Hamiltonian

We model the atoms as two-level systems with ground and excited states denoted by $|g\rangle$ and $|e\rangle$, respectively. The Hamitonian describing the evolution of the system composed of the two atoms and the fish eye modes is given by

$$H = H_{\text{atom}} + H_{\text{field}} + V, \tag{2.2}$$

where the atoms evolve according to $H_{\text{atom}} = \hbar\omega_0 \sum_{i=1,2} |e_i\rangle \langle e_i|$ and the evolution of the electromagnetic field is described by $H_{\text{field}} = \sum_{l,m} \hbar\omega_l a^\dagger_{l,m} a_{l,m}$, where $a_{l,m}$ is the annihilation operator of an eigenmode of the lens labelled by (l, m). The interaction of the two atoms with the electromagnetic field is given by $V = -\sum_{i=1,2} \mathbf{d}_i \cdot \mathbf{E}(\mathbf{r}_i)$, where $\mathbf{d}_i = d_z(\sigma_i^\dagger + \sigma_i)\hat{z}$ with $\sigma_i = |g_i\rangle \langle e_i|$ and d_z is the z-component of the dipole moment of the $e \to g$ transition of the atom, $\mathbf{E}(\mathbf{r}_i)$ is the electric field operator at position $\mathbf{r}_i$ within the lens, and we neglect variations of the field over the size of the atoms. The two atoms are positioned at $\mathbf{r}_1$ and $\mathbf{r}_2$ (see Fig. 2-2(a)). Note that Eq. (2.2) describes a closed lossless system composed of the lens and the two atoms with no coupling to free-space modes. Later we will consider how photon loss from the fish eye modes affects our results.

2.2.3 Quantization in the Fish Eye Lens

We follow the quantization scheme of Glauber and Lewenstein [97] to write down the expression for the quantized electromagnetic field $\mathbf{E}(\mathbf{r}_i)$ of the lens

$$\mathbf{E}(\mathbf{r}_i) = i \sum_{l,m} \left(\frac{\hbar\omega_l}{2\varepsilon_0} \right)^{1/2} [a_{l,m}\mathbf{f}_{l,m}(\mathbf{r}_i) - a^\dagger_{l,m}\mathbf{f}^*_{l,m}(\mathbf{r}_i)], \tag{2.3}$$

where $\mathbf{f}_{l,m}$ are the classical eigenmodes of the cavity that are solutions of the wave equation

$$n(\mathbf{r})^2 \frac{\omega_{l,m}^2}{c^2}\mathbf{f}_{l,m}(\mathbf{r}) - \nabla \times [\nabla \times \mathbf{f}_{m,l}(\mathbf{r})] = 0, \tag{2.4}$$

subject to the transversality condition

$$\nabla \cdot \left[n(\mathbf{r})^2\, \mathbf{f}_{l,m}(\mathbf{r})\right] = 0, \tag{2.5}$$

together with the boundary condition that $\mathbf{f}_{l,m} \cdot \hat{z} = \mathbf{f}_{l,m} \cdot \hat{\phi} = 0$ at $|\mathbf{r}| = R_0$ due to the presence of the mirror. The position-dependent refractive index $n(\mathbf{r})$ is given by Eq. (2.1). The solutions of Eq. (2.4) and Eq. (2.5) can be chosen to form an orthonormal set satisfying

$$\int_{\mathcal{V}} d^3r\; n(\mathbf{r})^2\, \mathbf{f}_{l,m}(\mathbf{r}) \cdot \mathbf{f}^*_{l',m'}(\mathbf{r}) = \delta_{ll'}\delta_{mm'}, \tag{2.6}$$

where the integral is performed over the quantization volume $\mathcal{V}$.

Solving these equations, the lowest TEM modes of the fish eye take the following form

$$\mathbf{f}_{l,m}(r,\phi) = \sqrt{\frac{2}{bR_0^2 n_0^2}} Y_l^m\left(\arccos\left(\frac{|\mathbf{r}|^2 - R_0^2}{|\mathbf{r}|^2 + R_0^2}\right), \phi\right)\hat{z}, \tag{2.7}$$

where $Y_l^m(\theta,\phi)$ are the spherical harmonic functions, $\phi = \arccos(x/|\mathbf{r}|)$ is the azimuthal angle associated with position $\mathbf{r}$ and the eigenfrequencies are

$$\omega_l = c\sqrt{l(l+1)}/(R_0 n_0). \tag{2.8}$$

The modes $\mathbf{f}_{l,m}$ are labelled with the rescaled wavenumber $l = 1, 2, 3\ldots$ and the angular momentum index m, where $m(l) = -(l-1), -(l-3), \ldots, (l-1)$ is enforced by the boundary condition $\mathbf{f}_{l,m}(R_0,\phi) = 0$. The discrete spectrum of the fish eye is schematically shown in Fig. 2-2(b). The number of degenerate states increases linearly with l, since $\sum_{m(l)} 1 = l$.

2.2.4 Photon transfer between two atoms via dipole-dipole interaction

In this section, we investigate the resonant transfer of a photon between two atoms via the dipole-dipole interaction, the strength of which we denote by $\delta\omega$.

In quantum optics, the most fundamental model for photon emission and detection assumes that one atom is initially in its excited state $|e_1\rangle$, while the second atom is in its ground state $|g_2\rangle$. When the system evolves coherently in time, the excited atom (virtually) emits the photon and after time $t_{\text{int}} \sim \pi/(2\delta\omega)$ the second atom fully absorbs the photon as its atomic population is transferred to the excited state $|e_2\rangle$ [84, 98].

Furthermore, by making use of additional metastable states $|s_i\rangle$ with $i = 1, 2$ (see Fig. 2-3) that only couple to $|e_i\rangle$ via the time-dependent classical control pulse $\Omega_i(t)$ (such that $\Omega_i \gg \delta\omega$), the photon transfer can be performed in a controlled, realistic scheme [99–101]. In particular, by adjusting $\Omega_1(t)$ and $\Omega_2(t)$, the photon transfer can be initiated via the excitation of $|e_1\rangle$ and, as the photon is reabsorbed, the atomic population of the second atom can be transferred to the metastable state $|s_2\rangle$. Then, by switching off $\Omega_2(t)$, reemission into the cavity can be prevented. From the metastable state the photon can be read out using standard fluorescence techniques [102, 103]. This completes the detection of the photon.

In a standard quantum optical setting, the dipole-dipole interaction between two atoms with level spacing ω_0 between ground $|g_i\rangle$ and excited states $|e_i\rangle$ in any environment can be expressed in terms of the classical Green's function components $G_{\alpha\beta}(\mathbf{r}_1, \mathbf{r}_2, \omega_0)$ (with $\alpha, \beta = x, y, z$) through the following expression [104–107]

$$\delta\omega(\mathbf{r}_1, \mathbf{r}_2) = \frac{d_z^2\omega_0^2}{\hbar\varepsilon_0 c^2}\text{Re}\{G_{zz}(\mathbf{r}_1, \mathbf{r}_2, \omega_0)\}, \tag{2.9}$$

where we assume that the two atoms are located at $\mathbf{r}_1$ and $\mathbf{r}_2$ and their dipole moments d_z are oriented along the z-axis. Note that the real (imaginary) part of the Green's function $G_{zz}(\mathbf{r}_1, \mathbf{r}_2, \omega_0)$ has the simple interpretation of being the z-component of the in-phase (out-of-phase) component of the electric field generated at position $\mathbf{r}_2$ within

the lens due to the presence of a z-oriented point-like dipole at position $\mathbf{r}_1$ radiating at frequency ω_0.

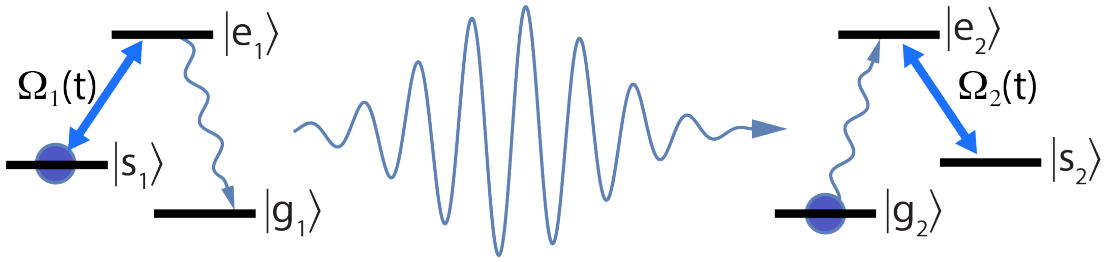

Figure 2-3: Schematic depiction of a realistic scheme for the photon transfer between the two atoms. The first atom emits the photon, while the second atom fully absorbs it. By applying classical time-dependent control pulses $\Omega_1(t)$ and $\Omega_2(t)$, the transfer can be initiated and the photon can be captured in the metastable state of the second atom, from which the photon can be read out using fluorescence techniques.

We note that, when the classical Green's function of a problem is analytically known, it is typically a simple matter to evaluate Eq. (2.9) and find the dipole-dipole interaction between atoms. However, for the fish eye there is debate about what Green's function correctly describes the imaging process. The subtlety of the issue arises from the fact that the fish eye, which models the closed surface of the sphere, is inherently a closed system from which radiation cannot escape in the absence of losses and detectors [48–50]. As mentioned previously, the accurate mathematical modeling of detectors has been a key focus of the discussion regarding perfect imaging [52, 53, 55–75, 78, 79].

Here, since we model both the 'source' of the radiation and the 'detector' as atoms, the exact expression for the dipole-dipole interaction can be obtained from the standard quantum optical master equation [38], where no ambiguity arises in the derivation of the results. Furthermore, as we show below, the expression obtained for the dipole-dipole interaction from the master equation exactly matches one of the two Green's functions discussed extensively in the fish eye literature, allowing us to directly use Eq. (2.9), which substantially simplifies numerical calculations.

The quantum optical master equation in the Born-Markov approximation, which

governs the evolution of the atoms inside the lens, takes the following form in the interaction picture [38]

$$\frac{d\tilde{\rho}}{dt} = -\frac{1}{\hbar^2}\int_0^\infty d\tau \,\mathrm{Tr}\left[\tilde{V}(t),\left[\tilde{V}(t-\tau),\tilde{\rho}(t)\otimes|0\rangle\langle 0|\right]\right], \tag{2.10}$$

where $|0\rangle\langle 0|$ is a projector onto the vacuum state of the lens (i.e. no photons in the lens) and the trace is implied over all photonic Fock states of the lens, $\sum_n \langle n|...|n\rangle$, and

$$\tilde{\rho}(t) = e^{iH_{\mathrm{atom}}t/\hbar}\rho(t)e^{-iH_{\mathrm{atom}}t/\hbar}, \tag{2.11}$$

and

$$\tilde{V}(t) = e^{i[H_{\mathrm{atom}}+H_{\mathrm{field}}]t/\hbar}V(t)e^{-i[H_{\mathrm{atom}}+H_{\mathrm{field}}]t/\hbar}. \tag{2.12}$$

In Eq. (2.10), the Born approximation was performed by writing the density matrix for the system in the form $\tilde{\rho}(t-\tau)\otimes|0\rangle\langle 0|$, which amounts to neglecting correlations between the atoms and the electromagnetic modes of the lens [38]. The Markov approximation was made by replacing $\tilde{\rho}(t-\tau)$ by $\tilde{\rho}(t)$, which is based on the assumption that the atom-field correlation time is negligibly short compared to the time scale on which the system evolves [38]. The Markov approximation allowed us to self-consistently extend to infinity the upper limit of the integration with respect to $d\tau$. We confirm the validity of the Born-Markov approximation in Section 2.4.

After performing the trace over the modes of the fish eye lens, we need to evaluate the following standard integral

$$\int_0^\infty d\tau e^{-i(\omega_l \mp \omega_0)\tau} = \pi\delta(\omega_0 \mp \omega_l) \pm iP\frac{1}{\omega_0 \mp \omega_l}, \tag{2.13}$$

where $\delta(x)$ stands for the Dirac delta and $Pf(x)$ denotes the principal value component of the function $f(x)$. Since the spectrum of the fish eye modes (which act as the reservoir for the atoms) is discreet, the Dirac delta and the principal value do not contribute away from resonances and we may simply replace the right-hand side of Eq. (2.13) with $\pm i/(\omega_0 \mp \omega_l)$. More specifically, in the absence of any mechanism for photon loss that would broaden the energy levels, the atoms experience no sponta-

neous decay or cooperative emission when their transition frequency does not coincide with the resonant frequencies of the lens. The master equation then describes the fully coherent, lossless evolution of the atoms and takes the form

$$\frac{d\rho}{dt} = \frac{1}{i\hbar}[H_{\rm at}, \rho] - i\sum_{\substack{i,j=1,2 \\ i\neq j}} \delta\omega(\mathbf{r}_i, \mathbf{r}_j)\,[\sigma_i^\dagger \sigma_j, \rho], \tag{2.14}$$

where the dipole-dipole interaction between the atoms is given by

$$\delta\omega(\mathbf{r}_i, \mathbf{r}_j) = \frac{d_z^2}{\hbar\varepsilon_0} \sum_{l,m} \frac{\omega_l^2}{\omega_l^2 - \omega_0^2}\, f_{l,m}^*(\mathbf{r}_i) f_{l,m}(\mathbf{r}_j), \tag{2.15}$$

where the fish eye modes $f_{l,m}(\mathbf{r})$ are given by Eq. (2.7) and the summation runs over all eigenmodes of the fish eye. Given the summation over an infinite number of modes, it is difficult to work directly with the expression given in Eq. (2.15) and it is desirable to replace it with a simple, closed-form expression.

As shown in Appendix A.1, the right-hand side of Eq. (2.15) can indeed be replaced by an expression of the same form as Eq. (2.9) using a Green's function, where the Green's function is given by the following expression

$$G_{zz}(\mathbf{r}_1, \mathbf{r}_2, \omega) = -\frac{P_\nu(\xi(\alpha_1, \alpha_2)) - P_\nu(\xi(\alpha_1, 1/\alpha_2^*))}{4b\sin(\pi\nu)}, \tag{2.16}$$

where P_ν is the Legendre function of (non-integer) order

$$\nu = \frac{1}{2}(\sqrt{16\pi^2\,(R_0 n_0/\lambda)^2 + 1} - 1). \tag{2.17}$$

Note that the order parameter ν depends on the atom frequency ω_0 through the free-space wavelength $\lambda = 2\pi c/\omega_0$ and the order parameters with integer values ($\nu = 1, 2, 3\ldots$) correspond to the resonances of the lens. We have also defined $\xi(\alpha_1, \alpha_2) = (|\zeta(\alpha_1, \alpha_2)|^2 - 1)/(|\zeta(\alpha_1, \alpha_2)|^2 + 1)$ and $\zeta(\alpha_1, \alpha_2) = (\alpha_1 - \alpha_2)/(\alpha_1\alpha_2^* + 1)$, with $\alpha_j = \frac{r_j}{R_0} e^{i\phi_j}$, where (r_j, ϕ_j) are the cylindrical coordinates of the positions of the two atoms ($j = 1, 2$) within the lens. In Eq. (2.16) the second term on the right hand

side accounts for the presence of the mirror at $|\mathbf{r}| = R_0$, ensuring that the electric field goes to zero [48]. This Green's function was first derived in Ref. [54], and is obtained from the canonical equation of the dyadic Green's function in the presence of a single source term [48, 50, 53]. This Green's function has been used previously to describe the static electric field distribution inside the lens for the case when a diffraction-limited image forms at the antipodal point in the presence of a classical source and in the absence of a 'drain' [53, 56].

Using Eq. (2.9) and Eq. (2.16), the dipole-dipole interaction can be calculated in a straightforward manner within the lens. In Fig. 2-2(c) we plot the strength of the dipole-dipole interaction between two atoms. The position of the first atom is fixed exactly one wavelength away from the mirror and the position of the second atom is varied across the lens. We plot the interaction strength for four different radii of the fish eye. As Fig. 2-2(c) shows, the strength of the dipole-dipole interaction peaks at the antipodal point, exactly one wavelength away from the mirror.

As noted at the start of this section, in quantum optics the strength of the dipole-dipole interaction sets the rate at which a photon can be resonantly transferred from one atom to the other. Physically, this exchange rate depends on the strength of the photon field at the location of the second atom that absorbs the photon. In general, the smaller the volume the photon is focused to, the larger the field strength gets. Thus, the dipole-dipole exchange rate depends sensitively on the area the photon is focused to. Fig. 2-2(d) provides an enlarged view that shows the dipole-dipole interaction rate – and thus the electric field strength – experienced by the second atom near the antipodal point[1]. The width of the peak is approximately $\lambda/2$, suggesting that the photon is focused to a diffraction-limited area at the location of the second atom. These results for the rate of photon transfer are numerically confirmed in Section 2.4.

Fig. 2-2(c) also shows that the height of the peak remains constant as the radius of the fish eye and, therefore, the distance between the two atoms is increased. The

[1]Note that since the Green's function in Eq. (2.16) is purely real, the dipole-dipole interaction is simply proportional to the electric field strength.

photon emitted by an atom anywhere within the cavity gets refocused at the antipodal point regardless of the size of the lens. Such infinite range dipole-dipole interaction is a well-known feature of quasi-1D waveguides [80–93]. Intuitively, the 2D fish eye lens acts as quasi-1D system due to the fact that the lens mimics the propagation of light on the surface of a sphere [49]. Just as in 1D light is confined to propagate along a single axis without dispersion, the same way light emitted from a point on the 2D surface of a sphere is constrained to propagate along the geodesics of the sphere and refocuses at the antipodal point without any dispersion.

The functional form of the dipole-dipole interaction can also be understood analytically by considering the asymptotic behavior of the Green's function near the source and image points. In particular, note that the source and image points in the lens correspond to $\xi(\alpha_1, \alpha_2) = -1$ and $\xi(\alpha_1, 1/\alpha_2^*) = +1$ respectively [48]. As $\xi \to -1$ we obtain the asymptotic expansion [48, 108]

$$P_\nu(\xi) \to \frac{\sin(\nu\pi)}{\pi}\left[\quad \log\left(\frac{1+\xi}{2}\right) + F(\nu)\right], \tag{2.18}$$

where we have defined the function

$$F(\nu) = \gamma + 2\psi(\nu+1) + \pi\cot(\nu\pi). \tag{2.19}$$

Here γ is Euler's constant and ψ is the digamma function. In addition, when $\xi \to 1$ we obtain the asymptotics $P_\nu(\xi) \to 1$ [48, 108]. Thus, near the source point the first term dominates in Eq. (2.16) and a logarithmic divergence is formed. In contrast, near the image point, the second term dominates and we can analytically approximate the Green's function as

$$G_{zz} \approx -\frac{1}{4b\sin(\pi\nu)}. \tag{2.20}$$

This shows that the absolute value of the Green's function is maximized when the frequency falls half-way between two resonances such that $\nu = m + 0.5$, where $m \in \mathbb{N}$. Furthermore, this expression also shows that the height of the peak at a given frequency only depends on the transverse confinement of the modes b and is independent

of the lens radius R_0. Finally, we note that Eq. (2.20) also shows that the dipole-dipole interaction is independent of where we place the atoms within the lens as long as they are situated at antipodal points.

2.2.5 Spontaneous and cooperative decay of atoms

In all calculations so far, we assumed that the fish eye lens is completely isolated from its surrounding environment and the photon cannot leak out of the cavity. Here, we next consider the situation when the lifetime of the eigenmodes of the fish eye are finite e.g. due to the imperfection of the mirrors and dissipation in the dielectrics. We account for the gradual loss of photons from the fish eye modes by modifying the Hamiltonian in Eq. (2.2) with a non-Hermitian term [109–114] of the following form

$$H_{\text{field}} = \sum_{l,m} \hbar(\omega_l - i\kappa) a^\dagger_{l,m} a_{l,m}, \tag{2.21}$$

where 2κ sets the rate of decay from the modes, which is assumed to be frequency-independent in the range of interest. The decay of the cavity modes broadens the discrete energy levels of the fish eye, creating a continuous spectrum, as shown schematically in Fig. 2-2(b).

With this modification, we can re-derive the master equation from Eq. (2.11). We evaluate the following integral

$$\int_0^\infty d\tau e^{-i(\omega_l \mp \omega_0)\tau} e^{-\kappa\tau} = \frac{1}{i(\omega_l \mp \omega_0) + \kappa}, \tag{2.22}$$

and after neglecting the off-resonant decay terms [38] we obtain the master equation in the following form

$$\begin{aligned} \frac{d\rho}{dt} = \frac{1}{i\hbar}[H_{\text{at}}, \rho] - i \sum_{\substack{i,j=1,2 \\ i\neq j}} \delta\omega(\mathbf{r}_i, \mathbf{r}_j) \left[\sigma_i^\dagger \sigma_j, \rho\right] \\ - \sum_{\substack{i,j=1,2 \\ i\neq j}} \Gamma(\mathbf{r}_i, \mathbf{r}_j) \left(\sigma_i \rho \sigma_j^\dagger - \frac{1}{2} \left\{ \sigma_i^\dagger \sigma_j, \rho \right\} \right), \end{aligned} \tag{2.23}$$

where the rate of decay is given by

$$\Gamma(\mathbf{r}_i, \mathbf{r}_j) = \frac{d_z^2}{\hbar\varepsilon_0} \sum_{l,m} \kappa \, f_{l,m}^*(\mathbf{r}_i) f_{l,m}(\mathbf{r}_j)(L_l^+ + L_l^-), \tag{2.24}$$

and the modified dipole-dipole interaction is given by

$$\delta\omega(\mathbf{r}_1, \mathbf{r}_2) = \frac{d_z^2}{2\hbar\varepsilon_0} \sum_{l,m} \omega_l \, f_{l,m}^*(\mathbf{r}_1) f_{l,m}(\mathbf{r}_2)\big(D_l^+ + D_l^-\big), \tag{2.25}$$

where we have defined

$$L_l^\pm = \frac{\mp\omega_l}{\kappa^2 + (\omega_l \pm \omega_0)^2} \;\text{ and }\; D_l^\pm = \frac{\omega_l \pm \omega_0}{\kappa^2 + (\omega_l \pm \omega_0)^2}. \tag{2.26}$$

Since we are now including losses in the system, the excited states of the two atoms can irreversibly decay into the eigenmodes of the lens and leave the cavity, leading to non-zero single atom decay $\gamma(\mathbf{r}_i) = \Gamma(\mathbf{r}_i, \mathbf{r}_i)$ (with $i = 1, 2$) and cooperative decay $\gamma_{\text{coop}}(\mathbf{r}_1, \mathbf{r}_2) = \Gamma(\mathbf{r}_1, \mathbf{r}_2)$. The single atom decay γ describes how quickly an excitation decays from state $|e\rangle$ of an individual atom to the fish eye modes, whereas the cooperative decay γ_{coop} governs the coherent joint emission of the two atoms into the modes leading to super $(\gamma + \gamma_{\text{coop}})$ and subradiant decay $(\gamma - \gamma_{\text{coop}})$ of the symmetric and anti-symmetric superpositions of the two atoms, respectively [38].

As for the lossless case, it is desirable to find closed-form expressions to replace the expressions that involve infinite summations on the right-hand side of Eq. (2.24) and Eq. (2.25). As shown in Appendix A.1, the decay rates and the dipole-dipole interaction can be expressed using the Green's function of Eq. (2.16) in the following form

$$\Gamma(\mathbf{r}_i, \mathbf{r}_j) = \frac{2d_z^2}{\hbar\varepsilon_0 c^2} \text{Im}\{(\omega_0 + i\kappa)^2 G_{zz}(\mathbf{r}_i, \mathbf{r}_j, \omega_0 + i\kappa)\}, \tag{2.27}$$

and

$$\delta\omega(\mathbf{r}_i, \mathbf{r}_j) = \frac{d_z^2}{\hbar\varepsilon_0 c^2} \text{Re}\{(\omega_0 + i\kappa)^2 G_{zz}(\mathbf{r}_i, \mathbf{r}_j, \omega_0 + i\kappa)\}. \tag{2.28}$$

These simple, analytic expressions provide a convenient way to calculate the quantum optical properties of atoms inside the lossy fish eye lens and to study the atomic dynamics.

We also note that when $\kappa \ll \omega_0$, Eq. (2.27) and Eq. (2.28) can be approximated as

$$\Gamma(\mathbf{r}_i, \mathbf{r}_j) \approx \frac{2d_z^2\omega_0^2}{\hbar\varepsilon_0 c^2}\mathrm{Im}\{G_{zz}(\mathbf{r}_i, \mathbf{r}_j, \omega_0 + i\kappa)\}, \tag{2.29}$$

and

$$\delta\omega(\mathbf{r}_i, \mathbf{r}_j) \approx \frac{d_z^2\omega_0^2}{\hbar\varepsilon_0 c^2}\mathrm{Re}\{G_{zz}(\mathbf{r}_i, \mathbf{r}_j, \omega_0 + i\kappa)\}. \tag{2.30}$$

Eq. (2.29) and Eq. (2.30) suggest an alternative way of accounting for the loss of photons from the modes of the fish eye. In particular, it can be shown (see Appendix A.1) that $G_{zz}(\mathbf{r}_i, \mathbf{r}_j, \omega_0 + i\kappa)$ is the Green's function of the fish eye lens with the following complex refractive index

$$\tilde{n}(\mathbf{r}) = n(\mathbf{r})(1 + i\alpha), \tag{2.31}$$

where

$$\alpha = \kappa/\omega_0, \tag{2.32}$$

and $n(\mathbf{r})$ is given by Eq. (2.1). Therefore, the loss of photons from the modes of the fish eye can also be thought to arise from material absorption in the dielectric [48]. This is a key observation, which allows us to associate a κ value with material absorption and, therefore, treat all losses that contribute to photon decay from the fish eye modes in a unified manner. In particular, even if different loss processes are present, e.g. material absorption and leakage through the mirror, we can still associate a κ value with each of these processes and calculate the total decay rate via

$$\kappa_{\mathrm{total}} = \kappa_{\mathrm{abs}} + \kappa_{\mathrm{mirror}}, \tag{2.33}$$

which can be substituted into Eq. (2.29) and Eq. (2.30) to calculate the relevant atomic properties in the lossy lens. This will be particularly useful when we consider a possible physical realizations of the fish eye lens with plasmons (see Section 2.5).

Furthermore, we can also find how ν, Γ and $\delta\omega$ scale with α for system parameters of interest. First, we note that $16\pi^2(R_0/\lambda)^2 \gg 1$, whenever $\lambda \lesssim R_0$. Assuming $\alpha \ll 1$, to first order in α we find that

$$\nu \approx \frac{2\pi R_0}{\lambda}(1 + i\alpha). \tag{2.34}$$

Assuming that $\mathrm{Re}[\nu] = m + 0.5$ with $m \in \mathbb{N}$ (which corresponds to tuning the atomic frequency between two resonances), from Eq. (2.20) we obtain that, to lowest order in α, the following approximation holds at the image point ($\mathbf{r}_1 = -\mathbf{r}_2$)

$$\begin{aligned} G_{zz}(\mathbf{r}, -\mathbf{r}, \omega_0 + i\kappa) &\approx -\frac{1}{4b\sin(\pi\nu)} \\ &\approx \mp\frac{1}{4b(1 + (2\pi^2 R_0\alpha/\lambda)^2)}, \end{aligned} \tag{2.35}$$

where the choice of sign $\mp$ depends on whether m is even or odd. This is a purely real quantity and, therefore, from Eq. (2.29) and Eq. (2.30) we find that the cooperative decay is given by

$$\gamma_{\mathrm{coop}} = \Gamma(\mathbf{r}, -\mathbf{r}) \approx 0, \tag{2.36}$$

and the dipole-dipole interaction takes the form

$$\delta\omega(\mathbf{r}, -\mathbf{r}) \approx \mp\frac{d_z^2\omega_0^2}{\hbar\varepsilon_0 c^2}\frac{1}{4b(1 + (2\pi^2 R_0\alpha/\lambda)^2)}. \tag{2.37}$$

Finally, we can find the single atom decay rate γ by substituting $\mathbf{r}_i = \mathbf{r}_j$ into Eq. (2.29) and substituting Eq. (2.18) and Eq. (2.34) into Eq. (2.16). We find that to leading order in α the following approximation holds

$$\gamma = \Gamma(\mathbf{r}, \mathbf{r}) \approx \frac{d_z^2\omega_0^2}{\hbar\varepsilon_0 c^2}\frac{\pi^2 R_0\alpha}{b\lambda}. \tag{2.38}$$

2.3 Entanglement of atoms

Structures that mediate long-range dipole-dipole interactions are of significant interest in quantum information processing, as such interactions make it possible to entangle [81] and perform deterministic phase gates between distant atoms [84]. In this section, we characterize the potential of the fish eye to entangle distant atomic quits. We focus on the simple case of a single excitation being exchanged between two atoms due to the dipole-dipole interaction. In what follows, for simplicity we assume that the two atoms are located at antipodal points (i.e. $|\mathbf{r}_1| = |\mathbf{r}_2|$ and $\phi_1 = \phi_2 + \pi$) and, therefore, $\gamma = \Gamma(\mathbf{r}_1, \mathbf{r}_1) = \Gamma(\mathbf{r}_2, \mathbf{r}_2)$.

In the absence of a driving field, the no-jump evolution of the system can be described by a non-Hermitian effective Hamiltonian of the form [115]

$$\begin{aligned} H_0 &= (\hbar\omega_0 - i\gamma)|e_1, e_2\rangle\langle e_1, e_2| \\ &+ (\delta\omega - i(\gamma + \gamma_{\text{coop}})/2)\,|+\rangle\langle +| \\ &+ (-\delta\omega - i(\gamma - \gamma_{\text{coop}})/2)\,|-\rangle\langle -|, \end{aligned} \tag{2.39}$$

where we have defined $|\pm\rangle = (|e_1, g_2\rangle \pm |g_1, e_2\rangle)/\sqrt{2}$, and recall from the previous section that $\gamma_{\text{coop}} = \Gamma(\mathbf{r}_1, \mathbf{r}_2)$ and $\delta\omega(\mathbf{r}_1, \mathbf{r}_2)$ stand for the cooperative decay and dipole-dipole interaction of the atoms, respectively. Note that the overall decrease of population in Eq. (2.39) due to the non-Hermitian terms reflects the gradual loss of the photonic excitation from the cavity.

Assuming that at $t = 0$ the two atoms are in the state

$$|\psi(0)\rangle = \big|e_1, g_2\big\rangle = (|+\rangle + |-\rangle)/\sqrt{2}, \tag{2.40}$$

the time evolution of the atomic wavefunction is governed by

$$|\psi(t)\rangle = \frac{1}{\sqrt{2}}\Big(e^{-i[\delta\omega - \frac{i}{2}(\gamma+\gamma_{\text{coop}})]t}|+\rangle + e^{-i[-\delta\omega - \frac{i}{2}(\gamma-\gamma_{\text{coop}})]t}|-\rangle\Big), \tag{2.41}$$

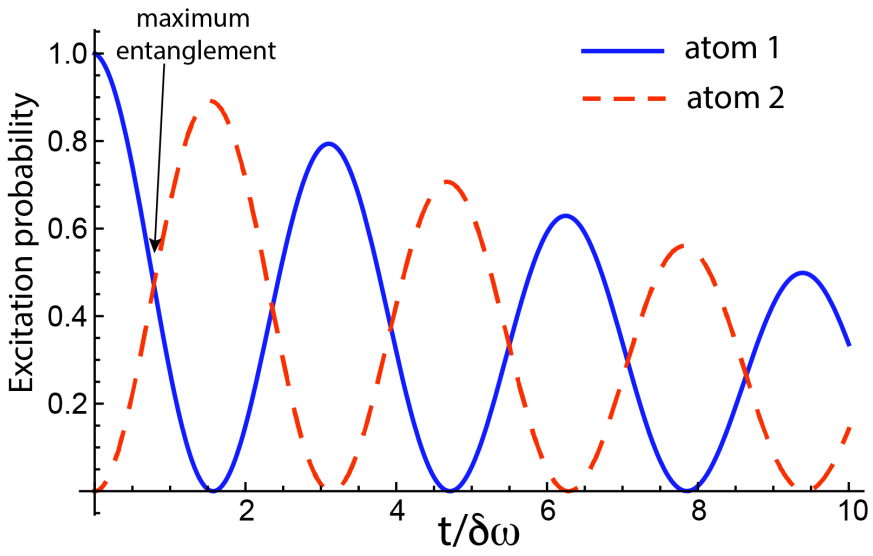

Figure 2-4: Excitation probability of two atoms within the cavity as a function of time. Initially, atom 1 is excited and atom 2 is in its ground state. As the system evolves, the two atoms repeatedly exchange a photon via the dipole-dipole interaction. The photon gradually decays from the cavity modes, leaving the atoms in their ground states. A fully entangled state with maximal fidelity is formed at $t = \pi/(4\delta\omega)$ (see arrow). The plot was obtained for $R_0 = 3.34\lambda$ with a cavity loss rate of $\alpha = \kappa/\omega_0 = 5\times10^{-4}$, assuming that the two atoms are located at two antipodal points within the lens such that $|\mathbf{r}_1| = |\mathbf{r}_2| = 0.27R_0$ and $\phi_1 = \phi_2 + \pi$.

which, upon substitution, yields

$$|\psi(t)\rangle = C_+(t)|e_1, g_2\rangle + C_-(t)|g_1, e_2\rangle, \tag{2.42}$$

where

$$|C_\pm(t)|^2 = \frac{e^{-\gamma t}}{2}\left[\cosh(\gamma_{\text{coop}}t) \pm \cos(2\delta\omega t)\right]. \tag{2.43}$$

The expressions $|C_+|^2$ and $|C_-|^2$ give the excitation probability of atom 1 and atom 2, respectively, as a function of time. In Fig. 2-4 we plot the excitation probability of the two atoms as a function of time. As the plots shows, the photon is coherently exchanged a number of times between the two atoms before it gradually decays from the cavity modes.

During time evolution, the state $|\psi(t)\rangle$ will have maximal overlap with the maximally entangled state $|\xi\rangle = \left(|e_1, g_1\rangle - i|g_1, e_1\rangle\right)/\sqrt{2}$ when $|C_+(t)| = |C_-(t)|$, which

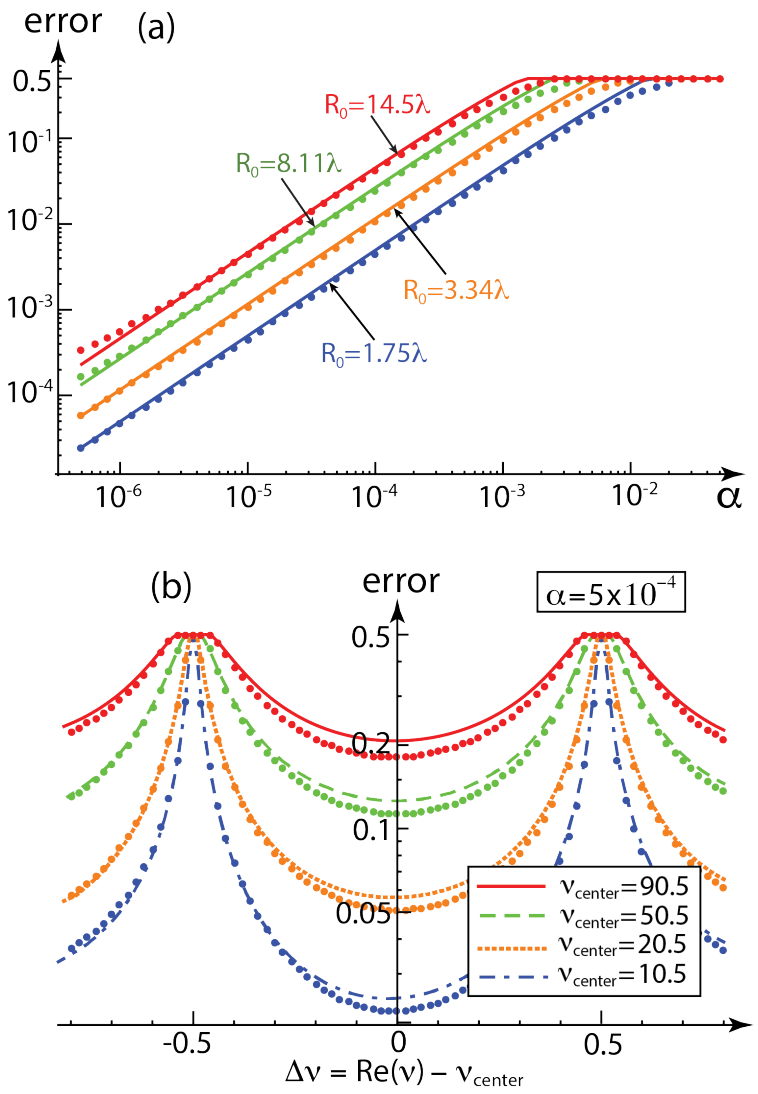

Figure 2-5: Error $(1-F)$ of the entangling operation between two qubits located at two antipodal points within the lens ($|\mathbf{r}_1| = |\mathbf{r}_2| = 0.27R_0$ and $\phi_1 = \phi_2 + \pi$). (a) Error of the entangling operation as a function of the cavity loss rate $\alpha = \kappa/\omega_0$ for four different lens sizes $R_0 \in \{1.75, 3.34, 8.11, 14.5\}\lambda$, where the R_0/λ ratio was chosen such that $\mathrm{Re}(\nu) = \frac{1}{2}(\sqrt{16\pi^2(R_0/\lambda)^2+1}+1) \in \{10.5, 20.5, 50.5, 90.5\}$. The error increases as the losses and lens radii increase. (b) Error of the entangling operation for a fixed loss rate $\alpha = 5\times10^{-4}$ as a function of the detuning $\Delta\nu = \mathrm{Re}(\nu) - \nu_{\mathrm{center}}$, where $\nu_{\mathrm{center}} \in \{10.5, 20.5, 50.5, 90.5\}$. Error is plotted for the same four lens radii as in (a). The error increases with radius and as the frequency approaches one of the resonances. Numerical results are shown with large dots. Good agreement is obtained between analytic and numerical data, confirming the validity of the Born-Markov analysis.

happens when $2\delta\omega t \approx \frac{\pi}{2} + m\pi$, where $m \in \mathbb{Z}$. Since in the presence of losses the fidelity decreases over time, we choose $m = 0$. Thus, the time needed to reach the maximal overlap with the entangled state is $t_0 = \pi/(4\delta\omega)$ (see arrow in Fig. 2-4) and the maximum fidelity of the entanglement operation will be

$$F = \left|\langle\xi|\psi(t_0)\rangle\right|^2 = \exp\left(-\frac{\pi}{4}\left|\frac{\gamma}{\delta\omega}\right|\right)\cosh\left(\frac{\pi}{4}\left|\frac{\gamma_{\text{coop}}}{\delta\omega}\right|\right). \tag{2.44}$$

Eq. (2.44) gives a simple, analytic expression for the fidelity of the entangling operation in terms of $\gamma = \Gamma(\mathbf{r}_i, \mathbf{r}_i)$, $\gamma_{\text{coop}} = \Gamma_{\text{coop}}(\mathbf{r}_i, \mathbf{r}_j)$ and $\delta\omega(\mathbf{r}_i, \mathbf{r}_j)$, which can be evaluated analytically through Eq. (2.27) and Eq. (2.28). Here, the key figure of merit is the ratio $\beta = \delta\omega/(\gamma + \gamma_{\text{coop}})$. If the frequency of the atoms is chosen to lie half-way between two resonances of the fish eye (see Fig. 2-2(b)), the single atom decay γ and the cooperative decay γ_{coop} are small and the dipole-dipole interaction dominates [115]. Intuitively, in the absence of losses ($\gamma = \gamma_{\text{coop}} = 0$), the fidelity of the entangling operation is 1.

In Fig. 2-5(a) we plot the error in the entangling operation $(1 - F)$ for four different lens radii as a function of α, where $\alpha = \kappa/\omega_0 = 1/Q$ is the inverse of the cavity Q-factor, characterizing the ratio of the lifetime of the eigenmodes of the lens to the frequency of the excitation. For all lens sizes, the position of the two atoms is fixed at two antipodal points such that $|\mathbf{r}_1| = |\mathbf{r}_2| = 0.27R_0$ and $\phi_1 = \phi_2 + \pi$. The ratio of the lens radius to the transition wavelength (R_0/λ) was chosen such that the real part of the order parameter $\nu = \frac{1}{2}(\sqrt{16\pi^2(R_0/\lambda)^2 + 1} + 1)$ associated with the atomic frequency falls half-way between two resonances of the fish eye for all four lens radii (i.e. $\text{Re}(\nu) = q + 0.5$ with $q \in \{10, 20, 50, 90\}$, where note that for $\text{Re}(\nu) = 1, 2, 3\ldots$ the transition frequency ω_0 is resonant with one of the eigenenergies ω_l of the lens). Clearly, the error increases with increasing α and increasing R_0 (i.e. increasing interatomic distance). The maximal value of the error is 0.5, which is reached when β becomes so small that the initial state has the highest fidelity $(F = |\langle\xi|\psi(0)\rangle|^2 = 0.5)$.

Fig. 2-5(b) shows the error for a fixed value of $\alpha = 5 \times 10^{-4}$ for the same four lens

radii as in (a) and the same antipodal atomic positions. The error is now plotted as a function of the detuning $\Delta\nu = (\mathrm{Re}(\nu) - \nu_{\mathrm{center}})$, where $\nu_{\mathrm{center}} = q + 0.5$ with $q \in \{10, 20, 50, 90\}$. Clearly, the error is minimal half-way between the resonances and increases as the frequency approaches the resonances.

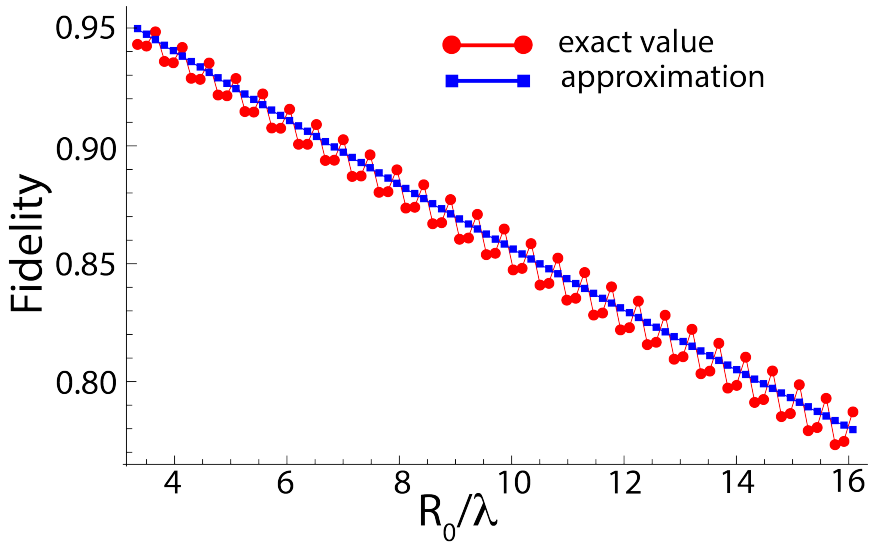

Figure 2-6: Maximum fidelity of the entanglement operation as a function of the lens radius. The fidelity was evaluated at discrete values of R_0/λ that correspond to tuning the atomic frequency half-way between two resonances, i.e. $\mathrm{Re}[\nu] = m + 0.5$, where m is an integer. The red line marked with circles was obtained from the exact analytical expression in Eq. (2.44), whereas the blue line marked with squares was obtained from the approximate expression in Eq. (2.45). Good agreement is obtained between the two curves. The loss rate was assumed to be $\alpha = \kappa/\omega_0 = 5 \times 10^{-4}$.

To gain further insight, we assume that the atomic frequencies lie between two resonances of the lens and obtain the scaling of the fidelity with system parameters by substituting Eq. (2.36), Eq. (2.37) and Eq. (2.38) into Eq. (2.44). We obtain the following simple expression

$$F = e^{-\pi^3 R_0 \alpha/\lambda}. \tag{2.45}$$

In Fig. 2-6 we plot the fidelity of the entangling operation as a function of the lens radius using both the exact expression in Eq. (2.44) and the analytic approximation in Eq. (2.45). Very good agreement is observed between the two curves.

Finally, we note that the fish eye lens could be used for entangling many pairs

of atoms simultaneously. As the radius of the fish eye is increased, the dipole-dipole interaction at all points further than $\lambda/2$ away from the antipodal point monotonically decreases. For lens radii with $R_0 > 5\lambda$, the dipole-dipole interaction at the antipodal point is an order of magnitude larger than anywhere else in the cavity (see Fig. 2-2(c)). Thus, by placing numerous pairs of atoms into the cavity simultaneously, they can be entangled pairwise, without substantial interaction between the different pairs.

2.4 Validity of the Born-Markov approximation

In our derivation of Eq. (2.15), Eq. (2.24) and Eq. (2.25) we made use of the Born-Markov approximation, which presupposes that the environment is large and the correlation time of the environment is very short compared to the evolution of the atomic states [38]. Since in our formalism the role of the 'environment' is played by the modes of the finite cavity, the validity of these assumptions needs to be evaluated carefully.

In order to verify the validity of the above results, we numerically solve the Schödinger equation, where the Hamiltonian is given by Eq. (2.2) together with the non-Hermitian term introduced in Eq. (2.21). The form of V is considerably simplified when the two atoms are placed at two antipodal points within the lens such that $|\mathbf{r}_1| = |\mathbf{r}_2|$ and $\phi_1 = \phi_2 + \pi$. In this case the in-phase combination of the atomic dipole moments $(d_z(\sigma_1 + \sigma_2)/\sqrt{2} + \text{h.c.})$ only couples to the odd modes $(l = 1, 3, 5 \ldots)$ and the out-of-phase combination of the dipole moments $(d_z(\sigma_1 - \sigma_2)/\sqrt{2} + \text{h.c.})$ only couples to the even modes $(l = 2, 4, 6 \ldots)$ of the fish eye (see Appendix A.2). This reduces the size of the Hilbert space, making it possible to efficiently simulate the system while including a large number of the eigenmodes of the lens with frequencies close to ω_0. We further restrict the Hilbert space to have at most a single excitation in the system.

We numerically determine the time-evolution, starting from the state $|\psi(0)\rangle = |e_1, g_2\rangle$ via the operator $U(t) = \exp[-iHt/\hbar]$. To obtain the maximum fidelity of the entangling operation, the overlap of the time-evolved atomic state is calculated with

the maximally entangled state $(|e,g\rangle - i|g,e\rangle)/\sqrt{2}$. In Figs. 2-5(a) and 2-5(b) we plot the numerically obtained values for the error $(1-F)$ (dotted lines) for different lens radii as a function of losses and atom frequencies, respectively. Even though the analytical results were derived using the Born-Markov approximation and neglecting retardation [98], good agreement is obtained between the analytic results and numerical data. This confirms the validity of the analytical formalism described in previous sections.

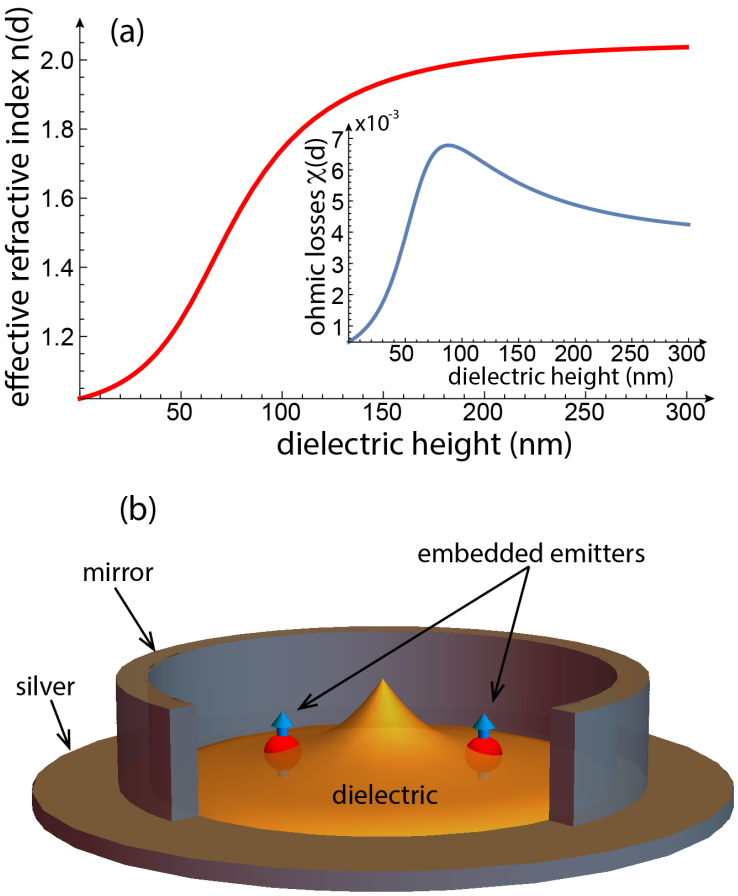

Figure 2-7: Physical realization of the fish eye lens using transformation plasmon optics. (a) Effective refractive index $n(d) = \mathrm{Re}\{\tilde{n}(d)\}$ created as a function of the height of the dielectric d deposited on the silver surface. The inset shows the material losses $\chi(d) = \mathrm{Im}\{\tilde{n}(d)\}$ as a function of the dielectric height d. (b) Schematic depiction of the plasmonic fish eye lens. The two emitters are embedded in the dielectric. The height of the dielectric varies across the lens, which creates the effective refractive index distribution of the fish eye lens. The lens is surrounded by mirrors from all sides (the front part of the mirror has been removed to show the interior).

2.5 Possible experimental realization

A promising way to realize the fish eye lens is via transformational plasmon optics [95, 96]. The idea behind this approach is to engineer an effective refractive index distribution for surface plasmon polaritons by depositing a layer of high-index dielectric on top a 2D silver surface (see Fig. 2-7). By varying the height of the dielectric layer on the surface, the effective refractive index seen by the plasmons can be changed. In particular, when there is no dielectric on top of the silver, the effective refractive index seen by the plasmons is close to 1, whereas in the presence of a thick dielectric layer, the effective plasmonic refractive index will be close to the refractive index of the dielectric itself. Through this experimental technique, complex spatially-varying refractive index profiles can be engineered [95]. Crucially, the behavior of plasmons in a plasmonic lens with a particular refractive index profile closely mimics the predicted behavior of classical light rays in the corresponding 2D lens. This correspondence between 2D classical lenses and quasi-2D plasmonic lenses was theoretically established in Ref. [95] and experimentally confirmed for the nanoscale Luneburg and Eaton lenses [96].

We expect that the plasmonic version of the nanoscale fish eye lens could be experimentally realized analogously to the Luneburg and Eaton lenses. A dielectric layer of varying height could be deposited on a flat silver surface while the lens is surrounded by a circular mirror (see Fig. 2-7(b)). To explore the quantum optical properties of the fish eye, atom-like color defects in diamond could be used as quantum emitters. Subwavelength positioning and coherent manipulation of such color defects has been experimentally demonstrated previously [116–119]. Recently, the entanglement of two silicon-vacancy (SiV) color defects inside a nanoscale waveguide was also demonstrated [120].

For illustration, we provide here an estimate of the entanglement fidelity of two atoms inside a particular example of a plasmonic fish eye lens. We assume that the lens operates at 406.706THz, which is the zero-phonon resonance of SiVs corresponding to a vacuum wavelength of $\lambda_{\mathrm{SiV}} = 737\mathrm{nm}$. Furthermore, we assume that the lens has

a radius of $R_0 = 1.749\,\lambda_{\mathrm{SiV}}$, which ensures that the SiV resonance falls between two resonant modes of cavity ($\mathrm{Re}(\nu) = 10.5$). We also assume that the flat silver substrate is made of single-crystal silver [121], which at the SiV resonance frequency has a permittivity of $\epsilon_m = -25.23 + 0.589i$ and gives rise to plasmonic propagation distances on the order of $\sim 160\,\lambda_{\mathrm{Siv}}$. It is also assumed that there is a thin ($\sim 10 - 15$nm) diamond layer on top of the metal that has two SiVs implanted at two antipodal points such that $|\mathbf{r}_1| = |\mathbf{r}_2| = 0.27R_0$ and $\phi_1 = \phi_2 + \pi$, as schematically shown in Fig. 2-7(b). Due to their proximity to the silver surface, the two $\hat{z}$-polarized emitters will couple strongly to the surface plasmons, which are tightly confined to the metal-dielectric interface.

The spatially varying refractive index $n(\mathbf{r})$ of the fish (Eq. (2.1) with $n_0 = 1$) could be experimentally realized by depositing a dielectric of permittivity $\epsilon_d = 3.6$ on top of thin diamond layer. By varying the height of the dielectric between 0 and 200nm, the effective refractive index seen by the plasmons can be varied between 1 and 2. The refractive index of the dielectric ($n_d = \sqrt{\epsilon_d} = 1.9$) was chosen such that the effective index can reach 2, but a dielectric with even higher index (such as diamond with $\epsilon_{\mathrm{diamond}} = 5.76$) was avoided to ensure that the plasmons are not confined unnecessarily tightly to the silver surface, which would give rise to significantly higher ohmic losses.

The direct relationship between the height of the dielectric layer d and the resulting (complex) refractive index $\tilde{n}(d) = n(d) + i\chi(d)$ can be obtained from the following implicit equation [95]

$$\tanh(k_d \epsilon_d d) = -\frac{k_{\mathrm{air}} k_d + k_d k_m}{k_d^2 + k_{\mathrm{air}} k_m}, \tag{2.46}$$

where

$$k_{\mathrm{air}} = \sqrt{(\tilde{n}k_0)^2 - k_0^2}, \tag{2.47}$$

$$k_d = \frac{\sqrt{(\tilde{n}k_0)^2 - \varepsilon_d k_0^2}}{\varepsilon_d}, \tag{2.48}$$

and

$$k_m = \frac{\sqrt{(\tilde{n}k_0)^2 - \varepsilon_m k_0^2}}{\varepsilon_m}, \tag{2.49}$$

where $k_0 = 2\pi/\lambda_{\mathrm{SiV}}$ and in our calculation we ignored, for simplicity, the presence of the diamond layer, as it does not significantly modify the effective index seen by the plasmons as long as the diamond layer is much thiner than the transverse confinement of the plasmons, which is on the order of a wavelength.

Fig. 2-7(a) shows the real part $n(d)$ and imaginary part $\chi(d)$ (inset) of the complex refractive index $\tilde{n}(d)$ seen by the plasmons as the thickness of the dielectric d is varied. The effective refractive index increases monotonically with the thickness of the dielectric layer. Since the refractive index of the fish eye increases radially inward (see Eq. (2.1)), the dielectric layer in the fish eye lens takes a conical shape as shown in Fig. 2-7(b).

From the imaginary part of the effective refractive index $\chi(d)$, we can estimate the average photon loss rate due to ohmic losses via the relation $\kappa_{\mathrm{abs}}(\mathbf{r})/\omega_0 = \chi(\mathbf{r})/n(\mathbf{r})$ (see Section 2.2.5). Since this loss rate varies significantly across the lens, we numerically average $\chi(\mathbf{r})/n(\mathbf{r})$ over the radius of the lens and obtain the averaged quantity $\overline{\kappa_{\mathrm{abs}}(\mathbf{r})}/\omega_0 \approx 3 \times 10^{-3}$. This is the leading order contribution to the photon loss.

Photons can also be lost from the lens by leaking out through the mirror. Assuming that the reflectivity of the mirror is r^2, we can estimate the loss rate $\kappa_{\mathrm{mirror}}/\omega_0$. In the absence of other loss mechanisms, the photon would bounce off the mirror $\sim 1/t^2$ times before being lost, where $t^2 = 1 - r^2$. The time interval between two bounces is approximately $(2R_0)/(c/\bar{n})$, where R_0 is the radius of the lens, c is the speed of light in vacuum and $\bar{n}$ is the average index of refraction in the lens. Thus the lifetime of the photon due to the finite mirror reflectivity is

$$\tau_{\mathrm{mirror}} \sim \frac{1}{\kappa_{\mathrm{mirror}}} \sim \frac{2R_0}{c/\bar{n}} \frac{1}{t^2}. \tag{2.50}$$

Making the conservative estimate that $r^2 = 0.95$, we obtain the following loss rate

$$\frac{\kappa_{\mathrm{mirror}}}{\omega_0} \sim \frac{1}{4\pi} \frac{1}{\bar{n}} \frac{\lambda_0 t^2}{R_0} \sim 4 \times 10^{-4}, \tag{2.51}$$

where we have used $\overline{n(\mathbf{r})} = 1.57$, which is obtained by numerically averaging the refractive index over the radius of the lens. Note that this shows that the losses due

to the finite reflectivity of the mirror are an order of magnitude smaller than the ohmic losses.

Next, we consider emission into free space γ_0. In the close proximity of a metal surface, the rate of decay of the emitter into plasmonic modes γ can significantly exceed the rate of emission into free-space modes $\gamma_0 = d_z^2\omega_0^3/(3\pi\varepsilon_0\hbar c^3)$ [82, 122]. Here, we take the Purcell factor to be $\eta = \gamma/\gamma_0 \approx 3$, which is the approximate value for a z-oriented dipole 10-15 nm away from a flat silver surface emitting radiation at 737nm [2]. Furthermore, we also make the conservative estimate that the emission to free space is reduced by a factor of two due to the presence of the silver surface [124]. In order to account for the presence of this additional decay channel, we need to make the replacement $\gamma \to \gamma + \gamma_0/2$ in Eq. (2.39), and thus Eq. (2.45) becomes

$$F = e^{-\pi^3\left(1+\frac{1}{2\eta}\right)\frac{R_0}{\lambda}\alpha} . \tag{2.52}$$

Note that this equation holds only if the atomic frequencies fall half-way between two resonances and the atoms are placed at two antipodal points anywhere in the lens. Substituting $R_0/\lambda_{\mathrm{SiV}} = 1.749$, $\alpha = (\overline{\kappa_{\mathrm{abs}}} + \kappa_{\mathrm{mirror}})/\omega_0 = 3.4 \times 10^{-3}$ and $\eta = 3$ into Eq. (2.52), we obtain that the fidelity of the entangling operation would be approximately $F = 80\%$. We note that this fidelity could be further improved by utilizing the adiabatic passage of a dark state in a Raman scheme [99].

2.6 Conclusion

In conclusion, we have investigated the single-photon dynamics of atoms inside the fish eye lens. We demonstrated that the lens mediates long-range interactions between distant emitters. The dipole-dipole interaction has an infinite range, limited only by the decay rate of the cavity modes. Furthermore, our results show that the fish eye focuses a single photon to a diffraction-limited area during the exchange of a photon

[2] We calculate the Purcell factor exactly near a flat metal surface by evaluating $\gamma_{\mathrm{pl}} = 2d_z^2\omega_0^2/(\hbar\varepsilon_0 c^2)\mathrm{Im}\{G_{zz}\}$, where G_{zz} is the exact Green's function of a z-oriented dipole near the surface [123]

between two antipodal atoms, whose frequency is tuned between two resonances of the cavity. We derived closed-form expressions for the decay rates and dipole-dipole interaction of atoms in the presence of losses and studied the fidelity of entangling operations. We confirmed the validity of our analysis, which relied on the Born-Markov approximation, by numerically solving the Schrödinger equation. Finally, we proposed a possible realization for the fish eye lens using tranformational plasmon optics and silicon-vacancy centers that could open up the fish eye for practical applications.

We note that while this work has focused on atoms whose frequencies were tuned in-between two resonances, we expect that our analysis can be adapted near resonant frequencies as well, where the Born-Markov approximation may not be accurate. In particular, our method for numerically solving the Schrödinger equation for single photons could shed further light on whether perfect imaging is possible very close to the resonant frequencies of the fish eye lens [76–79].

Chapter 3

Photonic Band Structure of Two-dimensional Atomic Lattices

3.1 Introduction

Quantum optical properties of lattices of atoms and atom-like emitters are being actively explored both theoretically and experimentally [109–113, 125–134]. In such lattices, atoms are assumed to be confined such that tunneling between sites is negligible and they interact via photon-mediated dipole-dipole interactions giving rise to hybridized atom-photon bands. The photonic band structure of three-dimensional (3D) atomic lattices has been investigated in a number of studies [109, 126–129]. Recently, there has been significant interest in the photonic properties of two-dimensional (2D) atomic lattices, which have been shown to exhibit a variety of remarkable phenomena, including subradiance [134, 135], near perfect reflection of radiation [110, 132] and long-lived topological excitations [113, 131].

In such lattices, a key distinction arises between the radiative interatomic coupling that gives rise to collective behavior and the radiative coupling to free-space modes that leads to unwanted losses. In order to fully account for the radiative loss of atoms, the atomic coupling to all free-space modes, including propagating long-range photons, has to be considered. Determining the eigenmodes of the lattice in the presence of such long-range interactions between atoms is a non-trivial task, requiring

careful treatment in order to obtain accurate results and to understand the photonic properties of the lattice.

In this Chapter, we describe a general approach for the calculation of photonic band structures in two-dimensional atomic lattices with arbitrary lattice geometries. Previously, general methods have been put forward [109, 126–129] to accurately calculate photonic band structures for 3D infinite atomic lattices. Here, we make use of the general approach described in Refs. [109, 129] and focus on 2D lattices, where the axial symmetry is broken along the third dimension. Previous photonic calculations involving infinite 2D atomic lattices were either restricted to two-level atoms in a square lattice [134], required summations in real-space where convergence is slow [110, 131], or relied on the method that we will now describe in detail [113]. As an application of our method, we study the topological properties of both Bravais and non-Bravais lattices in free space.

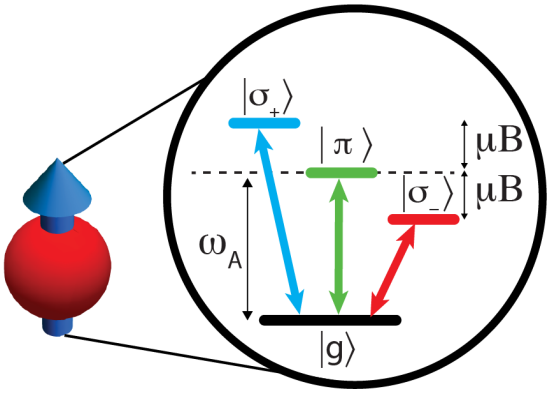

Figure 3-1: Constituent atoms in the 2D atomic lattice. Each atom is assumed to have one ground $|g\rangle$ and three excited states $|\sigma_+\rangle$, $|\sigma_-\rangle$ and $|\pi\rangle$ that can be Zeeman split by a magnetic field.

Furthermore, our formalism can also be used to describe two-dimensional lattices of emitters near planar surfaces. As a novel application, we study atomic lattices close to plasmonic surfaces and describe their emerging topological character. We note that studying the emission pattern of dipoles near metallic surfaces has been an active research area for over a century [136] and has been at the forefront of plasmonics research over the past few years [82, 121, 137–142]. Our work provides a new and simple framework to study the collective decay rates into both free-space modes and

plasmonic channels of a periodic lattice of dipole-like emitters near a metal surface, while also taking into account realistic metallic dispersion.

This Chapter is organized as follows. In Section 3.2 we describe a general analytical approach to finding the Bloch modes of an infinite two-dimensional atomic lattice. In Section 3.3 we apply our formalism to analyze a non-Bravais square lattice and a triangular lattice of atoms in free space and discuss their topological properties. In Section 3.4 we discuss a square lattice and a triangular lattice of atoms in the vicinity of a silver surface and discuss the topological properties of the latter. Key results and conclusions are summarized in Section 3.5.

3.2 General formalism

We consider a 2D lattice of atoms in the x-y plane with interatomic spacing a. The quantization axis $\hat{z}$ is perpendicular to the plane of the atoms. Each atom is assumed, for simplicity, to have transitions from the ground state $|g\rangle$ to the excited states $|\sigma_\pm\rangle = \mp(|x\rangle \pm i|y\rangle)/\sqrt{2}$ and $|\pi\rangle = |z\rangle$, which are excited by $\hat{\sigma}_\pm$ and $\hat{z}$ polarized light respectively (Fig. 3-1). Note that our formalism can be extended in a straightforward way to describe atoms with different internal level structures as long as only a single ground state is considered.

3.2.1 Hamiltonian

We use the dipole approximation to write down the Hamiltonian describing the interaction of the atoms with the quantized radiation field [109, 129, 143]

$$\begin{aligned} H = \hbar \sum_{n=1}^{N} \omega_A \Big(|\sigma_{+,n}\rangle\langle\sigma_{+,n}| + |\sigma_{-,n}\rangle\langle\sigma_{-,n}| + |\pi_n\rangle\langle\pi_n| \Big) \\ + \int d^3k \sum_{\epsilon} \hbar c k a^\dagger_{\mathbf{k}\epsilon} a_{\mathbf{k}\epsilon} - \sum_{n=1}^{N} \mathbf{d}_n \cdot \mathbf{E}(\mathbf{r}_n) + H_{\text{Zeeman}}, \end{aligned} \tag{3.1}$$

where N is the number of atoms, $\omega_A = 2\pi c/\lambda$ is the atomic transition frequency with wavelength λ and c is the speed of light in vacuum. Here $|\sigma_{\pm,n}\rangle\langle\sigma_{\pm,n}|$ and $|\pi_n\rangle\langle\pi_n|$

represent operators that only act on the subspace of the n-th atom. The creation and annihilation operators of the electromagnetic field satisfy $[a_{\mathbf{k}\epsilon}, a^\dagger_{\mathbf{k}',\epsilon'}] = \delta_{\epsilon,\epsilon'}\delta(\mathbf{k}-\mathbf{k}')$, where $\mathbf{k}$ is the wave vector with magnitude $k = |\mathbf{k}|$ and ϵ labels the two photon polarizations $\hat{\epsilon}_\mathbf{k}$ perpendicular to $\mathbf{k}$. The atomic transition dipole operator is given by $\mathbf{d} = d(|\sigma_+\rangle\langle g|\hat{\sigma}_+ + |\sigma_-\rangle\langle g|\hat{\sigma}_- + |\pi\rangle\langle g|\hat{z}) + \text{h.c.}$, where we assume, for simplicity, that all three transition dipole moments are equal. The dipole operator couples to the quantized transverse electromagnetic field modes $\mathbf{E}(\mathbf{r}) = \int d^3k \sum_\epsilon [\mathcal{E}_k \hat{\epsilon}_\mathbf{k} a_{\mathbf{k}\epsilon} e^{i\mathbf{k}\cdot\mathbf{r}} + \text{h.c.}]$, where $\mathcal{E}_k = i(2\pi)^{-3/2}[\hbar k c/(2\epsilon_0)]^{1/2}$ and $\mathbf{r}_n$ denotes the position vector of individual atoms. The Hamiltonian accounting for the Zeeman splitting of the atoms is given by

$$H_{\text{Zeeman}} = \hbar \sum_{n=1}^{N} \mu B \big(|\sigma_{+,n}\rangle\langle\sigma_{+,n}| - |\sigma_{-,n}\rangle\langle\sigma_{-,n}|\big), \tag{3.2}$$

where μB is the Zeeman shift of the atomic levels with magnetic moment μ due to an out-of-plane magnetic field $\mathbf{B} = B\hat{z}$.

Following the adiabatic elimination of the reservoir degrees of freedom via the Born-Markov approximation [109, 126–129, 134, 143, 144], we obtain a master equation for the evolution of the system density operator $\rho(t)$, which in the single excitation sector is given by

$$\begin{aligned} \dot{\rho} &= -\frac{i}{\hbar}\left(H_{\text{eff}}\rho - \rho H^\dagger_{\text{eff}}\right) \\ &+ \frac{6\pi\hbar\Gamma_0 c}{\omega_A} \sum_{i,j=1}^{N} \sum_{\alpha,\beta=\sigma_+,\sigma_-,\pi} \text{Im}\, G_{\alpha\beta}(\mathbf{r}_i - \mathbf{r}_j)|g_i\rangle\langle\alpha_i|\rho|\beta_j\rangle\langle g_j|, \end{aligned} \tag{3.3}$$

where the non-Hermitian, effective spin Hamiltonian reads

$$\begin{aligned} H_{\text{eff}} &= \hbar \sum_{i=1}^{N} \sum_{\alpha=\sigma_+,\sigma_-,\pi} \left(\omega_A - \text{i}\frac{\Gamma_0}{2}\right)|\alpha_i\rangle\langle\alpha_i| + H_{\text{Zeeman}} \\ &+ \frac{3\pi\hbar\Gamma_0 c}{\omega_A} \sum_{i\neq j} \sum_{\alpha,\beta=\sigma_+,\sigma_-,\pi} G_{\alpha\beta}(\mathbf{r}_i - \mathbf{r}_j)|\alpha_i\rangle\langle\beta_j|, \end{aligned} \tag{3.4}$$

and $\Gamma_0 = d^2\omega_A^3/(3\pi\epsilon_0\hbar c^3)$ is the radiative linewidth of a single atom in free space and

$G_{\alpha\beta}(\mathbf{r})$ is the dyadic Green's function describing the dipolar spin-spin interactions (see Section 3.2.4). Note that as part of the Markov approximation, the only frequency-dependence is through the atomic frequency ω_A [134].

The first term on the right-hand side of Eq. (3.3) describes the deterministic evolution of the atomic wavefunction and includes dipole-dipole interactions mediated via photon exchange, whereas the second term accounts for stochastic quantum jumps [134, 145–147]. In the absence of a driving field, the dynamics in the single excitation sector is completely characterized by the non-Hermitian Hamiltonian in Eq. (3.4), since a quantum jump prepares the system in a trivial state where all atoms are in their ground states and the system does not evolve. Therefore, it is not necessary to keep track of these quantum jumps and the system dynamics can be studied without including the second term on the right-hand side of Eq. (3.3). The time evolution of the system is then described by the non-Hermitian Hamiltonian in Eq. (3.4) via the equation

$$H_{\text{eff}}|\psi(t)\rangle = i\hbar\partial_t|\psi(t)\rangle, \tag{3.5}$$

where the overall decrease in amplitude reflects the dissipative transfer of population to the ground state.

3.2.2 Bravais lattices

For an infinite periodic Bravais lattice, which has a single atom per unit cell, the single excitation eigenmodes of Eq. (3.4) are Bloch modes of the form

$$|\psi_{\mathbf{k}_B}\rangle = \sum_n e^{i\mathbf{k}_B\cdot\mathbf{R}_n}\Big(c_+|\sigma_{+,n}\rangle + c_-|\sigma_{-,n}\rangle + c_z|z_n\rangle\Big), \tag{3.6}$$

where the summation runs over all lattice vectors $\{\mathbf{R}_n\}$, $\mathbf{k}_B$ is the Bloch wavevector, and c_+, c_- and c_z are constants that depend, in general, on $\mathbf{k}_B$.

It is convenient to solve for and manipulate the dyadic Green's function in the Cartesian basis. Therefore, we transform Eq. (3.4) and Eq. (3.6) using the relation $|\sigma_\pm\rangle = \mp(|x\rangle \pm i|y\rangle)/\sqrt{2}$ and perform all calculations in the Cartesian basis in the

rest of this Chapter.

Using the Bloch ansatz for the wavefunction, finding the eigenvalues $E_{\mathbf{k}_B}$ of the effective Hamiltonian H_{eff} reduces to diagonalizing the following 3×3 matrix $\mathbf{M}$, whose components are given by

$$\mathbf{M}_{\alpha\beta} = (\omega_A - i\Gamma_0/2)\,\delta_{\alpha\beta} + \xi_{\alpha\beta} + \chi_{\alpha\beta}, \tag{3.7}$$

where $\alpha, \beta = x, y, z$ label the polarization components, and $\delta_{\alpha\beta}$ is the Kronecker delta. Here $\xi_{\alpha\beta}$ and $\chi_{\alpha\beta}$ stand for the components of the complex matrices accounting for the magnetic field and the atom-atom interactions, respectively, and take the form

$$\xi_{\alpha\beta} = -i\mu B(\delta_{\alpha x}\delta_{\beta y} - \delta_{\alpha y}\delta_{\beta x}), \tag{3.8}$$

and

$$\chi_{\alpha\beta} = \frac{3\pi\Gamma_0 c}{\omega_A} \sum_{\mathbf{R}\neq 0} e^{i\mathbf{k}_B\cdot\mathbf{R}} G_{\alpha\beta}(\mathbf{R}). \tag{3.9}$$

The matrix $\mathbf{M}$ captures how the energy levels, decay rates, and internal level couplings of a single atom are affected by the magnetic field and the presence of all the other atoms in the periodic lattice for a given Bloch vector $\mathbf{k}_B$. For example, the matrix element χ_{xy} captures how the $|x\rangle$ state of an individual atom is affected by the couplings to the $|y\rangle$ states of all the other atoms in the lattice. The diagonalization of $\mathbf{M}$ yields three complex eigenvalues for each value of the Bloch vector $\mathbf{k}_B$ of the form $E_{\mathbf{k}_B} = \omega_{\mathbf{k}_B} - i\gamma_{\mathbf{k}_B}$, where the real part $\omega_{\mathbf{k}_B}$ corresponds to the energy of the Bloch eigenmode and the imaginary part $\gamma_{\mathbf{k}_B}$ characterizes the overall decay rate of the mode.

3.2.3 Non-Bravais lattices

For an infinite periodic non-Bravais lattice, with m sites per unit cell, the single excitation eigenmodes of Eq. (3.4) are Bloch modes of the form [148]

$$|\psi\rangle = \sum_{n} \sum_{b=1}^{m} e^{i\mathbf{k}_B \cdot \mathbf{R}_n} \Big(c_+^b |\sigma_{+,n}^b\rangle + c_-^b |\sigma_{-,n}^b\rangle + c_z^b |z_n^b\rangle \Big), \tag{3.10}$$

where b labels the different atoms within the unit cell. In this case, the eigenmodes of the system are obtained by diagonalizing a $3m \times 3m$ matrix.

For simplicity, we focus on non-Bravais lattices with two sites per cell, but the formalism can be extended in a straightforward way to include more sites per cell. For $m = 2$, the non-Bravais lattice can be thought of as a lattice arising from the union of two sublattices $\{R_1\}$ and $\{R_2\}$, which are shifted with respect to each other by the basis vector $\mathbf{b}$ that points from one site to the other within the periodic unit cell. With this notation, the matrix components of the relevant 6×6 complex matrix $\mathbf{M}$ are given by

$$\begin{aligned} \mathbf{M}_{\alpha\mu,\beta\nu} &= \Big(\omega_A^{(1)} - i\Gamma_0/2 \Big) \delta_{\alpha\beta} \delta_{1\mu} \delta_{1\nu} + \xi_{\alpha\mu,\beta\nu} \\ &+ \Big(\omega_A^{(2)} - i\Gamma_0/2 \Big) \delta_{\alpha\beta} \delta_{2\mu} \delta_{2\nu} + \chi_{\alpha\mu,\beta\nu}, \end{aligned} \tag{3.11}$$

where $\omega_A^{(1)}$ and $\omega_A^{(2)}$ are the transition frequencies of the atoms located on the two sublattices, while μ and ν are sublattice labels than run over $\mu, \nu = 1, 2$. The terms accounting for the magnetic field interaction are given by

$$\xi_{\alpha\mu,\beta\nu} = -i\mu B (\delta_{\alpha x}\delta_{\beta y} - \delta_{\alpha y}\delta_{\beta x})(\delta_{1\mu}\delta_{1\nu} + \delta_{2\mu}\delta_{2\nu}), \tag{3.12}$$

and the terms describing the atom-atom interactions take the form

$$\chi_{\alpha\mu,\beta\nu} = \frac{3\pi\Gamma_0 c}{\omega_A^{(1)}} \Bigg[\sum_{\mathbf{R}_1 \neq 0} e^{i\mathbf{k}_B\cdot\mathbf{R}_1} G_{\alpha\beta}(\mathbf{R}_1)\delta_{1\mu}\delta_{1\nu} + \sum_{\mathbf{R}_1} e^{i\mathbf{k}_B\cdot\mathbf{R}_1} G_{\alpha\beta}(\mathbf{R}_1+\mathbf{b})\delta_{1\mu}\delta_{2\nu} + \sum_{\mathbf{R}_2 \neq 0} e^{i\mathbf{k}_B\cdot\mathbf{R}_2} G_{\alpha\beta}(\mathbf{R}_2)\delta_{2\mu}\delta_{2\nu} + \sum_{\mathbf{R}_2} e^{i\mathbf{k}_B\cdot\mathbf{R}_2} G_{\alpha\beta}(\mathbf{R}_2-\mathbf{b})\delta_{2\mu}\delta_{1\nu} \Bigg], \tag{3.13}$$

where we have used the fact that $|\omega_A^{(1)} - \omega_A^{(2)}|/\omega_A^{(1)} \ll 1$ to replace all occurrences of $\omega_A^{(2)}$ with $\omega_A^{(1)}$ in $\chi_{\alpha\mu,\beta\nu}$ and factor out a common prefactor. In Eq. (3.13) the first term on the right-hand side describes how atoms in sublattice $\{R_1\}$ affect each other, whereas the second term describes how atoms in sublattice $\{R_1\}$ are affected by atoms in sublattice $\{R_2\}$. The third and fourth terms can be interpreted similarly.

In principle, the eigenmodes of the lattice can be directly calculated from Eqs. (3.7) and (3.9) for Bravais lattices, and Eqs. (3.11) and (3.13) for non-Bravais lattices for arbitrary lattice geometries using the expression for the Green's function in real space and summing over all lattice sites. However, in the presence of long range interactions, as for example in free space, the summation over the lattice sites converges very slowly, making accurate numerical computations difficult. Furthermore, in certain geometries, e.g. near planar surfaces (see Section 3.4), no closed form expression exists for the Green's function in real space. Below we describe a method to perform the relevant summations in momentum space, where convergence is fast and the expression for the Green's function in momentum-space can be used for the calculation, which is typically easier to obtain than the equivalent expression in real space.

3.2.4 Dyadic Green's function

The dyadic Green's function $G_{\alpha\beta}$ that appears in Eqs. (3.3), (3.4), (3.9) and (3.13) is the solution of the dyadic equation [104]

$$\varepsilon(\omega,\mathbf{r})\frac{\omega^2}{c^2}G_{\alpha\beta}(\mathbf{r},\mathbf{r}') - (\partial_\alpha\partial_\nu - \delta_{\alpha\nu}\partial_\eta\partial_\eta)\,G_{\nu\beta}(\mathbf{r},\mathbf{r}') = \delta_{\alpha\beta}\delta(\mathbf{r}-\mathbf{r}'), \tag{3.14}$$

where $\mathbf{r} = x\hat{x} + y\hat{y} + z\hat{z}$ and $r = |\mathbf{r}|$. Summation is implied over repeated indices. The dielectric permittivity $\varepsilon(\omega,\mathbf{r})$ is potentially spatially inhomogeneous and frequency-dependent and we assume a non-magnetic medium with magnetic permeability $\mu(\omega,\mathbf{r}) = 1$. Physically, the Green's function describes the electromagnetic radiation at position $\mathbf{r}$ emitted by a point-like dipole oscillating at frequency ω at position $\mathbf{r}'$.

In free space, the permittivity is $\varepsilon = 1$ and Eq. (3.14) has a closed-form solution for the free-space dyadic Green's function $G_{0,\alpha\beta}$ (see Appendix B.1). The components of the Green's function with radiating boundary conditions are given by [104, 149]

$$\begin{aligned} G_{0,\alpha\beta}(\mathbf{r}) = -\frac{e^{ikr}}{4\pi r}\Bigg[&\left(1+\frac{i}{kr}-\frac{1}{(kr)^2}\right)\delta_{\alpha\beta} \\ &+\left(-1-\frac{3i}{kr}+\frac{3}{(kr)^2}\right)\frac{x_\alpha x_\beta}{r^2}\Bigg] + \frac{\delta_{\alpha\beta}\delta^{(3)}(\mathbf{r})}{3k^2}, \end{aligned} \tag{3.15}$$

where $k = \omega/c$ and we have used the fact that the Green's function only depends on $\mathbf{r}-\mathbf{r}'$ to write it with a single argument. This is the well-known expression describing dipole-dipole interactions in free space, which can also be derived using conventional quantum optical techniques [38, 98].

In the presence of planar interfaces, the expression for the dyadic Green's function gets more complicated and the components can be evaluated in a closed form only in momentum space. The explicit expressions for the momentum-space components of the Green's function near planar surfaces are described in detail in Appendix B.4.

3.2.5 Summation in momentum space

From Eq. (3.15) it is clear that the Green's function decays as $\sim 1/r$ in the far-field limit. In the presence of such long-range interactions between atoms it is desirable to perform the summations in Eq. (3.9) and Eq. (3.13) in momentum space, where all sums converge rapidly as previously noted. The summation in position space is transformed to a summation in momentum space using the following form of Poisson's identity

$$\sum_{\mathbf{R}} e^{i(\mathbf{p}_{x\text{-}y}+\mathbf{k}_B)\cdot\mathbf{R}} = \frac{1}{\mathcal{A}}\sum_{\mathbf{G}}(2\pi)^2\delta^{(2)}(\mathbf{p}_{x\text{-}y}+\mathbf{k}_B-\mathbf{G}), \tag{3.16}$$

where $\mathbf{p}_{x\text{-}y} = p_x\hat{x} + p_y\hat{y}$, $\mathcal{A}$ is the area of the unit cell and the reciprocal lattice vectors $\{\mathbf{G}\}$ are related to the lattice vectors $\{\mathbf{R}\}$ by $\mathbf{G}\cdot\mathbf{R} = 2\pi m$ for integer m [150]. Making use of Eq. (3.16), we obtain

$$\begin{aligned}\sum_{\mathbf{R}\neq 0} e^{i\mathbf{k}_B\cdot\mathbf{R}}G_{\alpha\beta}(\mathbf{R}) &= \sum_{\mathbf{R}} e^{i\mathbf{k}_B\cdot\mathbf{R}}G_{\alpha\beta}(\mathbf{R}) - G_{\alpha\beta}(\mathbf{0}) \\ &= \frac{1}{\mathcal{A}}\sum_{\mathbf{G}} g_{\alpha\beta}(\mathbf{G}-\mathbf{k}_B;0) - G_{\alpha\beta}(\mathbf{0}),\end{aligned} \tag{3.17}$$

where we have used the *Weyl decomposition* of the Green's function in terms of 2D plane waves [151], which is defined via

$$G_{\alpha\beta}(\mathbf{r}) = \int \frac{dp_x dp_y}{(2\pi)^2} g_{\alpha\beta}(\mathbf{p}_{x\text{-}y};z)e^{i(p_x x+p_y y)}. \tag{3.18}$$

In free space the Weyl decomposition is given by (see Appendix B.1)

$$g_{\alpha\beta}(\mathbf{p}_{x\text{-}y};z) = \int \frac{dp_z}{2\pi} e^{ip_z z}\frac{1}{k^2}\frac{k^2\delta_{\alpha\beta}-p_\alpha p_\beta}{k^2-p^2}, \tag{3.19}$$

where $p = p_x^2 + p_y^2 + p_z^2$. Following similar reasoning, we also obtain

$$\sum_{\mathbf{R}} e^{i\mathbf{k}_B\cdot\mathbf{R}} G_{\alpha\beta}(\mathbf{R}\pm\mathbf{b}) = \frac{1}{\mathcal{A}}\sum_{\mathbf{G}} g_{\alpha\beta}(\mathbf{G}-\mathbf{k}_B;0)e^{\pm i\mathbf{b}\cdot(\mathbf{G}-\mathbf{k}_B)}. \tag{3.20}$$

3.2.6 Green's function regularization and quantum fluctuations

In order to evaluate the right-hand side of Eq. (3.17), special care has to be taken. While the left-hand side of Eq. (3.17) is finite and physically meaningful, the two terms on the right-hand side diverge individually — only their difference is finite. An established technique to avoid such divergences is to take into account the quantum fluctuations of the particles [109, 129]. These fluctuations 'smear out' the divergent part of the Green's function at $\mathbf{r} = 0$ over a finite volume, making it finite. In practice, this can be achieved by averaging the free-space Green's function with respect to the ground state wavefunction of a harmonically trapped atom [109, 129]

$$G^*_{\alpha\beta}(\mathbf{r}) = \int d^3\mathbf{q}\, G_{0,\alpha\beta}(\mathbf{r}-\mathbf{q})|\psi_0(\mathbf{q})|^2, \tag{3.21}$$

where $\psi_0(\mathbf{q})$ is the ground state wavefunction of a quantum harmonic oscillator of frequency $\omega_{\rm ho} = \hbar/(2ma_{\rm ho}^2)$ given by

$$|\psi_0(\mathbf{q})|^2 = \frac{1}{(\sqrt{2\pi}a_{\rm ho})^3} e^{-q^2/2a_{\rm ho}^2}. \tag{3.22}$$

Performing this integral with $\mathbf{r} = \mathbf{0}$ yields the following non-divergent, closed-form expression for the fluctuation-averaged Green's function at the source [109]

$$G^*_{\alpha\beta}(\mathbf{0}) = \frac{k}{6\pi}\left[\left(\frac{\mathrm{erfi}(ka_{\rm ho}/\sqrt{2}) - i}{e^{(ka_{\rm ho})^2/2}}\right) - \frac{(-1/2) + (ka_{\rm ho})^2}{(\pi/2)^{1/2}(ka_{\rm ho})^3}\right]\delta_{\alpha\beta}, \tag{3.23}$$

where $\mathrm{erfi}(b) = 2/\sqrt{\pi}\int_0^b dy \exp(y^2)$ is the imaginary error function.

The regularization techniques of Refs. [109, 129] can be specialized to the two-

dimensional lattice to derive the fluctuation-averaged Weyl decomposition of the Green's function $g^*_{\alpha\beta}(\mathbf{p}_{x\text{-}y};0)$ in the $z=0$ plane (see Appendix B.2 for details of the derivation). The components of the resulting expression are given by

$$\begin{aligned}
g^*_{xx}(\mathbf{p}_{x\text{-}y};0) &= (k^2-p_x^2)\mathcal{I}_0,\\
g^*_{yy}(\mathbf{p}_{x\text{-}y};0) &= (k^2-p_y^2)\mathcal{I}_0,\\
g^*_{zz}(\mathbf{p}_{x\text{-}y};0) &= (k^2\mathcal{I}_0-\mathcal{I}_2),\\
g^*_{xy}(\mathbf{p}_{x\text{-}y};0) &= g^*_{yx}(\mathbf{p}_{x\text{-}y};0)=-p_xp_y\mathcal{I}_0\\
g^*_{xz}(\mathbf{p}_{x\text{-}y};0) &= g^*_{zx}(\mathbf{p}_{x\text{-}y};0)=0,\\
g^*_{yz}(\mathbf{p}_{x\text{-}y};0) &= g^*_{zy}(\mathbf{p}_{x\text{-}y};0)=0.
\end{aligned} \tag{3.24}$$

where

$$\mathcal{I}_0(p_x,p_y)=\mathcal{C}\,\frac{\pi e^{-a_{\rm ho}^2\Lambda^2/2}}{\Lambda}\left[-i+\mathrm{erfi}\left(\frac{a_{\rm ho}\Lambda}{\sqrt{2}}\right)\right], \tag{3.25}$$

and

$$\mathcal{I}_2(p_x,p_y)=\mathcal{C}\left(-\frac{\sqrt{2\pi}}{a_{\rm ho}}+e^{-a_{\rm ho}^2\Lambda^2/2}\pi\Lambda\left[-i+\mathrm{erfi}\left(\frac{a_{\rm ho}\Lambda}{\sqrt{2}}\right)\right]\right). \tag{3.26}$$

The functions $\mathcal{C}$ and Λ depend on p_x and p_y and their explicit form is given by

$$\mathcal{C}(p_x,p_y)=\frac{1}{2\pi k^2}e^{-a_{\rm ho}^2(p_x^2+p_y^2)/2}. \tag{3.27}$$

and

$$\Lambda(p_x,p_y) = (k^2-p_x^2-p_y^2)^{1/2}\geq 0. \tag{3.28}$$

We note that the last two lines in Eq. (3.24) are identically zero, since the polarization of the radiation emitted by a dipole is always parallel to the dipole orientation in the plane perpendicular to the dipole.

After substituting the regularized expressions from Eq. (3.23) and Eq. (3.24) into Eq. (3.17) and Eq. (3.20), we may use Eq. (3.7) and Eq. (3.9) (or Eq. (3.11) and Eq. (3.13)) to obtain the eigenmodes of any Bravais (or non-Bravais) 2D lattice in the presence of atomic fluctuations.

Furthermore, the eigenmodes for point-like atoms (that are pinned to their lattice sites) can also be obtained through the simple modification of the fluctuation-averaged expressions for the Green's function. In particular, it can be shown (see Ref. [109] and Appendix B.3) that the expression

$$e^{k^2 a_{\mathrm{ho}}^2/2} \frac{1}{\mathcal{A}} \sum_{\mathbf{G}} g^*_{\alpha\beta}(\mathbf{G} - \mathbf{k}_B; 0) - G^*_{\alpha\beta}(\mathbf{0}) \tag{3.29}$$

approaches an a_{ho}-independent value as the limit $a_{\mathrm{ho}} \to 0$ is taken. Therefore, when $a_{\mathrm{ho}} \ll 1/k$, the following approximation holds

$$\sum_{\mathbf{R}\neq 0} e^{i\mathbf{k}_B \cdot \mathbf{R}} G_{\alpha\beta}(\mathbf{R}) \approx \frac{e^{k^2 a_{\mathrm{ho}}^2/2}}{\mathcal{A}} \sum_{\mathbf{G}} g^*_{\alpha\beta}(\mathbf{G} - \mathbf{k}_B; 0) - G^*_{\alpha\beta}(\mathbf{0}). \tag{3.30}$$

Using this approximation in Eq. (3.9) or Eq. (3.13), we obtain the eigenmodes for arbitrary 2D lattice geometries made up of point-like atoms.

The regularized expressions given above provide a straightforward, efficient and accurate way of calculating the eigenmodes of any 2D lattice composed of point-like or fluctuating atoms. Since we perform the summations in momentum space, only a few dozens of reciprocal lattice sites have to be included for full convergence. This contrasts sharply with performing summations in real space, where convergence often remains an issue even after tens of thousands of lattice sites have been included. To illustrate our formalism, we analyze below particular examples of 2D atomic lattices in free space and near planar metallic surfaces.

3.3 Atomic lattices in free space

As an application of our formalism, we study 2D atomic lattices in free space. We focus on two examples – a non-Bravais square lattice of three-level atoms and a triangular lattice of three-level atoms – and discuss their topological properties.

3.3.1 Non-Bravais Square lattice of three-level atoms

As our first example, we consider a non-Bravais square lattice of closely spaced ($a \approx \lambda/20$) atoms in free space as shown schematically in Fig. 3-2(a). The properties of a non-Bravais honeycomb lattice in free space was studied previously in Ref. [113], where long-lived topological edge states were shown to exist on the system boundaries. Here, we show that a non-Bravais square lattice also supports long-lived topological edge excitations. These results demonstrate that these topological phenomena are not confined to any particular non-Bravais lattice geometry. Later, we will also see that these results stand in contrast with those obtained in Bravais lattices, where edge excitations are short-lived.

The atomic non-Bravais square lattice lies in the x-y plane with the quantization axis set along the z-axis and the interatomic spacing is a. Each atom is assumed to have two excited states $|\sigma_+\rangle$ and $|\sigma_-\rangle$, which can be excited by $\hat{\sigma}_+$ and $\hat{\sigma}_-$ polarized light, respectively. Note that the atoms could also have a transition to the $|z\rangle$ state, but from Eq. (3.15) (see also Eq. (3.24)) it follows that $G_{xz} = G_{zx} = G_{yz} = G_{zy} = 0$ in the x-y plane and, therefore, the $\sigma_\pm$ transitions are decoupled from the transition to the $|z\rangle$ state and we can ignore the latter. The lattice is assumed to consist of atoms of two different resonant transition frequencies $\omega_A^{(1)}$ (red atoms in Fig. 3-2(a)) and $\omega_A^{(2)} = \omega_A^{(1)} + \delta\omega$ (green atoms), where $\delta\omega$ is a non-zero energy shift that may originate from having two different atomic species or a position-dependent Stark-shift. Here we assume that the atoms are point-like and their position is fixed.

First, we consider the atomic lattice in the absence of a magnetic field. After substituting Eq. (3.20) and Eq. (3.30) into Eq. (3.13), we diagonalize the matrix in Eq. (3.11) to obtain the complex eigenvalues $E_{\mathbf{k}_B} = \omega_{\mathbf{k}_B} - i\gamma_{\mathbf{k}_B}$ for each Bloch vector

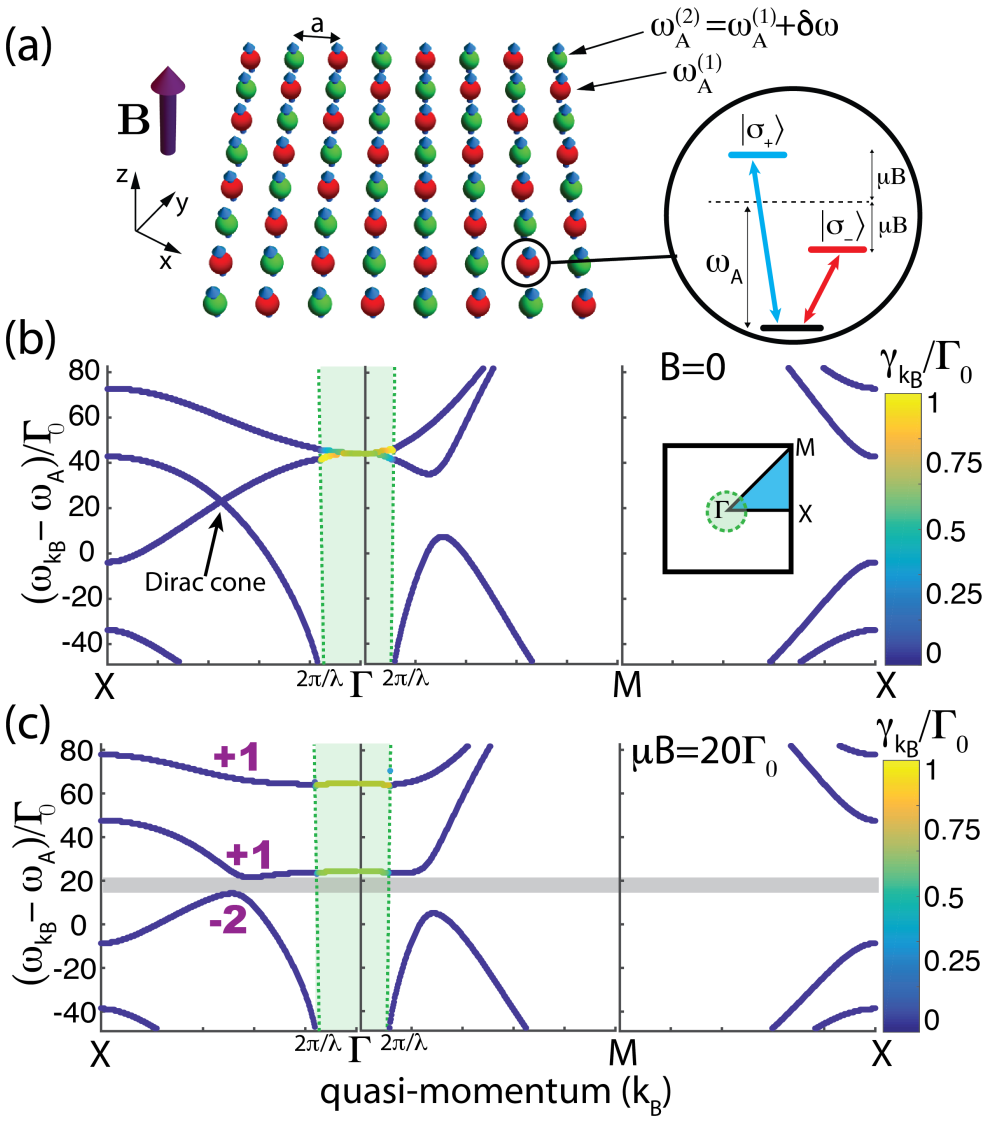

Figure 3-2: (a) Non-Bravais square lattice of atoms in free space. Atoms marked in red (green) have resonant frequency $\omega_A^{(1)}$ ($\omega_A^{(2)} = \omega_A^{(1)} + \delta\omega$). Each atom has two excited states $|\sigma_+\rangle$ and $|\sigma_-\rangle$ that are Zeeman shifted by $\pm\mu B$ in the presence of an out-of-plane magnetic field B. (b) Part of the photonic band structure of the lattice for $B = 0$. Green dashed lines mark the edges of the light cone. Modes that have quasi-momentum $k_B < \omega_{\mathbf{k}_B}$ (green shaded region) can couple to free-space modes of the same momentum, making them short-lived. Modes that have quasi-momentum $k_B > \omega_{\mathbf{k}_B}$ cannot couple to free-space modes and are long-lived. Decay rates of the modes are color coded. Bands are degenerate near the mid-point of the line joining the $\mathbf{X}$ and $\mathbf{\Gamma}$ points. (c) An out-of-plane magnetic field ($\mu B = 20\Gamma_0$) opens a gap ($\Delta = 7\Gamma_0$) between the bands (grey shaded region). The bands acquire non-trivial Chern numbers (purple numbers). Relevant parameters are $\lambda = 790$nm, $\delta\omega = 30\Gamma_0$, $\Gamma_0 = 2\pi \times 6$MHz and $a = 0.054\lambda$.

$\mathbf{k}_B$ inside the Brillouin zone. Fig. 3-2(b) shows the resulting band structure along the lines joining the high symmetry points $\mathbf{\Gamma}$, $\mathbf{M}$ and $\mathbf{X}$ inside the irreducible Brillouin zone (see inset of Fig. 3-2(b)).

The decay rates of the modes ($\gamma_{\mathbf{k}_B}$) are shown using a color code. The edges of the light cone are marked by green dashed lines at $k_B = 2\pi/\lambda$. These lines correspond to free space modes propagating in the x-y plane with maximal in-plane momentum $k_B = \omega_{\mathbf{k}_B}/c$. All other free-space modes have an in-plane momentum component that satisfies $k_B < \omega_{\mathbf{k}_B}/c$ (green shaded region in Fig. 3-2(b)). The hybridized atom-photon modes of the atomic lattice with quasi-momentum $k_B < \omega_{\mathbf{k}_B}/c$ can couple to free-space modes with matching momentum and energy, making these lattice modes short-lived. In contrast, lattice modes with quasi-momentum $k_B > \omega_{\mathbf{k}_B}/c$ cannot couple to any of the free-space modes due to the momentum mismatch (since $\langle k|k'\rangle = \delta_{kk'}$ in the momentum eigenbasis) [113, 134]. Therefore, lattice modes with $k_B > \omega_{\mathbf{k}_B}/c$ are decoupled from free-space modes and do not decay when the lattice is infinite.

This distinction between short-lived modes inside the light cone and long-lived modes outside the light cone is well-known in the literature of photonic crystal slabs, where periodic subwavelength dielectric structures are used to confine light in quasi-2D structures [41]. We also note that even though the edges of the light cone indeed trace out a conical shape in k-space, the dashed green lines in Fig. 3-2(b) appear vertical as we are only looking at a small energy range of a few linewidths around the atomic transition frequency and $\Gamma_0 \ll \omega_A$ at optical frequencies.

Due to the underlying symmetries of the lattice, the bands in Fig. 3-2(b) form Dirac cones along the paths joining the $\mathbf{\Gamma}$ point with the four $\mathbf{X}$ points and there is a quadratic degeneracy at the $\mathbf{\Gamma}$ point. These degeneracies arise due to the degeneracy of the $|\sigma_+\rangle$ and $|\sigma_-\rangle$ transitions in the absence of a magnetic field. When a magnetic field $\mathbf{B} = B\hat{z}$ is switched on, the energy levels of the $|\sigma_\pm\rangle$ transitions are shifted by $\pm\mu B$ due to Zeeman splitting. Breaking the degeneracy of the $|\sigma_+\rangle$ and $|\sigma_-\rangle$ transitions lifts the degeneracy of the bands and a complete band gap forms across the Brillouin zone (grey shaded band in Fig. 3-2(c)).

We investigate the topological character of the bands by calculating their Chern

numbers [14], which are defined via the integral

$$C = \frac{1}{2\pi} \int \nabla_{\mathbf{k}_B} \times \mathcal{A}(\mathbf{k}_B) \cdot \mathrm{d}\mathbf{k}_B. \tag{3.31}$$

The integral is performed over each band inside the irriducible Brillouin zone and the integrand is curl of the 'Berry curvature', which is defined via

$$\mathcal{A}(\mathbf{k}_B) = \langle \psi_{\mathbf{k}_B} | \, i\nabla_{\mathbf{k}_B} \, | \psi_{\mathbf{k}_B} \rangle \,, \tag{3.32}$$

where $\psi_{\mathbf{k}_B}$ is the wavefunction of the Bloch mode with Bloch momentum $\mathbf{k}_B$. We use the discretization method in Ref. [152] to numerically obtain the Chern numbers for the bands. The resulting non-zero Chern numbers for the bands above and below the gap are shown in Fig. 3-2(c). The four Dirac points between the two middle bands contribute +2 and -2 to the Chern numbers of the upper and lower bands respectively. At the same time, the quadratic degeneracy between the top two bands contributes +1 and -1 to the upper and lower bands respectively. Thus the three bands, from top to bottom, acquire Chern numbers +1, (+2-1)=+1 and -2.

Band gaps between topological bands are associated with edge states [14]. We investigate the spectrum of edge states by finding the eigenmodes of a periodic strip of the atomic lattice (see Fig. 3-3(a)). The calculation proceeds by defining an MxN lattice of atoms in real space, where the lattice has periodic boundary conditions along the first direction (Fig. 3-3(a)). The interactions between atoms is calculated using Eq. (3.4) and the range of the interactions is truncated after M/2 sites[1]. The wavefunctions of the resulting eigenmodes are then Fourier-analyzed to find k_x, the component of the Bloch quasi-momentum along the x-axis, associated with each mode.

Fig. 3-3(b) shows the spectrum of H_{eff} for such a configuration, where the eigenergies are plotted versus k_x. Edge modes on the lower and upper boundaries of the

[1]Since the interactions are long range ($\sim 1/r$), assuming periodic boundary conditions along one direction requires the truncation of the range of interaction. This leads to small deviations in the decay rates, potentially making them negative. This is an artifact of our numerical method with no physical significance. When the edge modes are obtained for a lattice of atoms that is finite in all directions (see Fig. 3-4), no such truncation is necessary and all decay rates are non-negative.

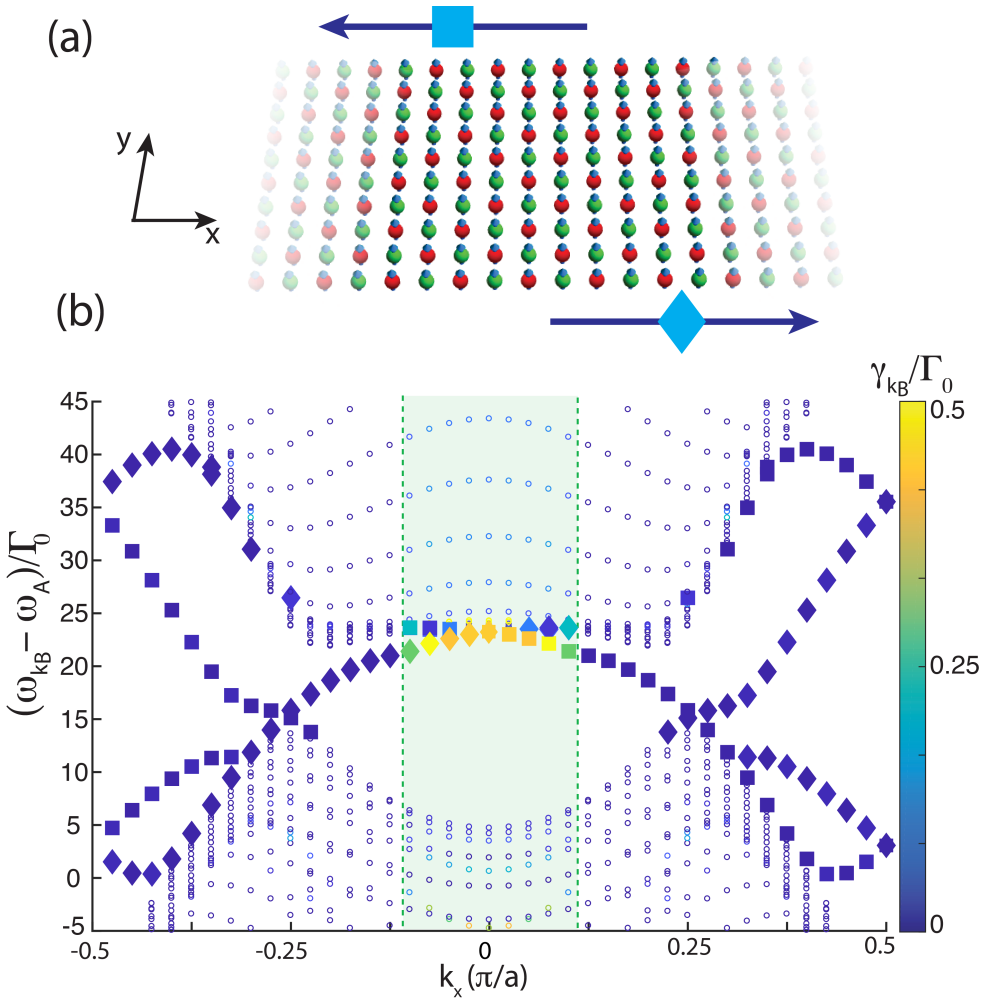

Figure 3-3: (a) Periodic strip of atoms in a non-Bravais square lattice. Each edge has edge modes propagating only in a single direction. (b) Modes that propagate on the upper (lower) edge are marked by squares (diamonds) in the band structure diagram. Extended bulk modes are marked with dots. There are two sets of edge modes on each boundary. Decay rates of modes are color coded. The edge modes cross the gap with quasi-momentum $k_B > \omega_{\mathbf{k}_B}$ and thus are long-lived. Parameters are the same as in Fig. 3-2(c). The spectrum was obtained for a 80x40 lattice of atoms with periodic boundary conditions along one direction. A state is classified as an edge state on the (upper) lower boundary if the excitation probability on the top (bottom) four rows is at least 15 times the excitation probability on the bottom (top) four rows.

strip are marked by diamonds and squares respectively. The edge states cross the gap connecting the two bulk bands. Since the sum of the Chern numbers above and below the band gap is +2 and -2 respectively, there are two sets of edge modes on each boundary. Note that both sets of edge modes on the lower boundary carry energy to the right, whereas both sets of modes on the top boundary carry energy to the left. Since energy flow is unidirectional on each boundary, these edge states carry energy forward without backscattering. Crucially, we find that the edge modes cross the gap outside the light cone with quasi-momenta $k_B > \omega_{\mathbf{k}_B}/c$. Therefore, these edge states do not couple to free-space modes due to the momentum mismatch, making them long-lived with decay rates much smaller than $\Gamma_0/2$. This suppression of losses is the key result, which leads to long-lived edge excitations. Such edge excitations can carry energy around the boundaries of the lattice with minimal losses.

Fig. 3-4 shows a snapshot of the excitation probabilities during the no-jump time evolution of the system when a single atom is continuously excited by a laser on the boundaries of the lattice. If the driving field is weak, the dynamics are essentially captured by the single excitation description introduced above. We add to Eq. (3.10) the ground state component $+c_g|g_*\rangle$ of the driven atom and $|g_*\rangle$ is coupled to the excited states $|\sigma_{+,*}\rangle$ and $|\sigma_{-,*}\rangle$ of the atom by adding the driving terms $\Omega(t)\left(|\sigma_{+,*}\rangle\langle g_*| + |\sigma_{-,*}\rangle\langle g_*| + \text{h.c.}\right)$ to the effective Hamiltonian H_{eff}. We obtain the time-evolved wavefunction at time t by numerically finding

$$|\psi(t)\rangle = \exp\left(-iH_{\text{eff}}/\hbar t\right)|\psi(0)\rangle, \tag{3.33}$$

where the excitation is initially in the ground state of the driven atom ($|\langle g_*|\psi(0)\rangle|^2 = 1$). The laser is resonant with the edge states inside the band gap and is switched on adiabatically to avoid exciting non-resonant modes. We find that approximately 96% of the excitation emitted by the atom is coupled into the edge modes carrying energy in the clockwise direction, while coupling into modes circulating anti-clockwise and into the bulk modes is strongly suppressed due to the gap and topology. Given the absence of channels for backscattering and highly suppressed coupling to free space

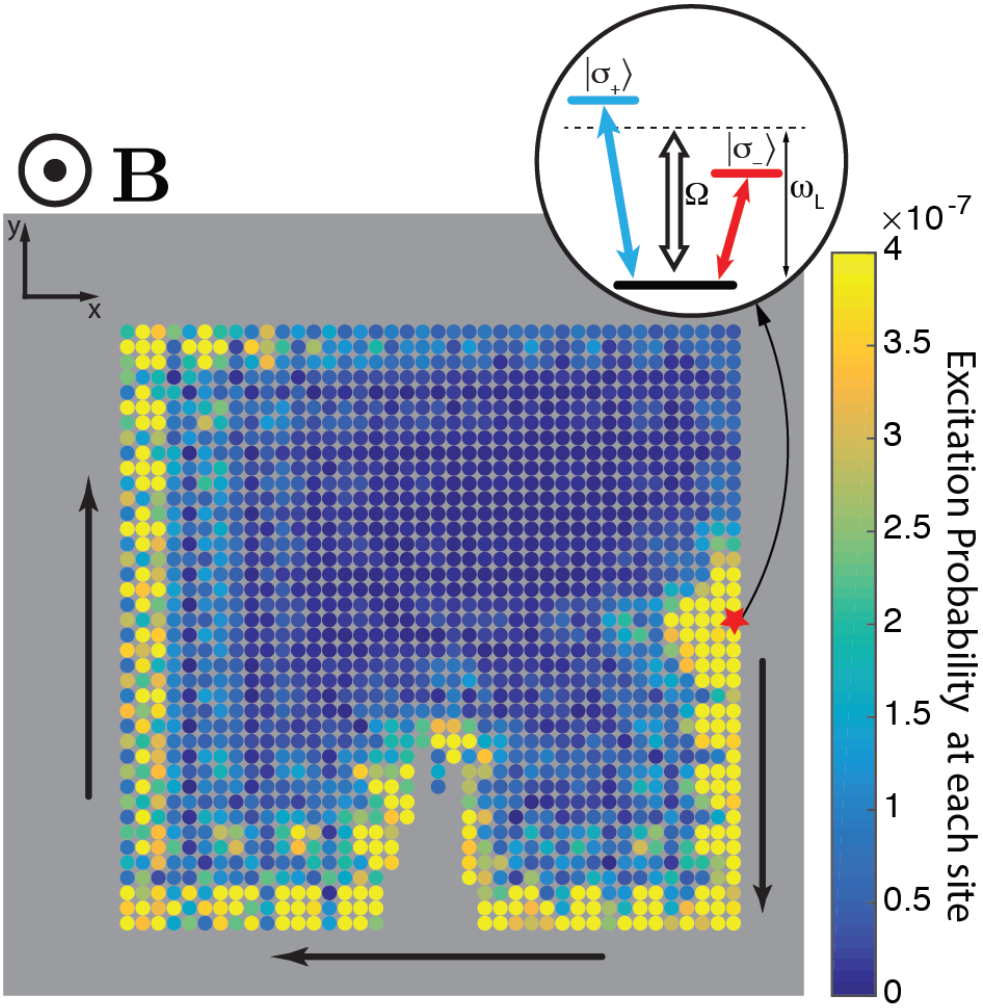

Figure 3-4: Snapshot of the time evolution (at $t = 11.1\Gamma_0^{-1}$) of a finite non-Bravais square lattice in free space with an irregular defect. An atom on the edge (marked by the red star) is driven by a laser (see inset). The color code depicts the excitation probability $|\langle\psi(t)|\sigma_+^i\rangle|^2 + |\langle\psi(t)|\sigma_-^i\rangle|^2$ at each site. Approximately 96% of the emitted excitation is coupled into the forward direction. Emission into bulk modes and the backward edge modes is suppressed. The excitation goes around the corners and routes around the large, irregular defect, which demonstrates the robustness of the topological excitation to disorder. Relevant parameters are $N = 1576$, $\lambda = 790$nm, $\delta\omega = 30\Gamma_0$, $\Gamma_0 = 2\pi \times 6$MHz, $a = 0.054\lambda$ and $\mu B = 20\Gamma_0$. The strength of the drive is $\Omega = 0.1\Gamma_0$ and the driving frequency is $\omega_L = \omega_A + 18\Gamma_0$. The driving laser is adiabatically switched on with a Gaussian profile $\Omega(t) = \Omega \exp(-[t - 4.5\Gamma_0^{-1}]^2/[1.35\Gamma_0^{-2}])$ for $t < 4.5\Gamma_0^{-1}$.

modes, the excitation routes around corners with approximately 97% efficiency as well as around the irregular defect with approximately 86% efficiency. We emphasize that these results illustrate the key point that topological quantum optical systems are protected against both losses into free space and large defects in the lattice. We also note that qualitatively similar results were obtained in the non-Bravais honeycomb lattice in Ref. [113].

3.3.2 Triangular lattice of three-level atoms

Topological photonic bands in atomic lattices can also be obtained when $a \approx \lambda/2$ — a trapping regime that is routinely explored in cold atom laboratories worldwide [153]. Fig. 3-5(a) shows a triangular Bravais lattice of atoms in the x-y plane in free space with $a = \lambda/2$ and quantization axis along the z-axis. As in the case of the non-Bravais square lattice, each atom is assumed to have two excited states $|\sigma_+\rangle$ and $|\sigma_-\rangle$.

Initially, we assume point-like atoms in zero magnetic field. After substituting Eq. (3.30) into Eq. (3.9), we diagonalize the matrix in Eq. (3.7) to obtain the complex eigenvalues. Fig. 3-5(b) shows the band structure along lines joining the high symmetry points $\mathbf{\Gamma}$, $\mathbf{K}$ and $\mathbf{M}$ of the Brillouin zone (see inset of Fig. 3-5(b)).

The decay rates of the modes $\gamma_{\mathbf{k}_B}$ are encoded using a color code and the light cone edges are marked by green dashed lines. Given the $a = \lambda/2$ spacing of the atoms, the boundaries of the irreducible Brillouin zone are close to the light cone edges. Therefore, the modes are decoupled from free-space modes only in a small region near the perimeter of the irreducible Brillouin zone.

The bands in Fig. 3-5(b) form a Dirac cone at the $\mathbf{K}$ point and a quadratic degeneracy at the $\mathbf{\Gamma}$ point. When a magnetic field $\mathbf{B} = B\hat{z}$ is switched on, the degeneracies are lifted and a small gap forms across the Brillouin zone (shaded band in Fig. 3-5(c)). The bands acquire non-zero Chern numbers (purple numbers) indicating the topological nature of the bands.

Fig. 3-5(d) shows the band structure in the presence of a magnetic field when the fluctuations of the atoms are taken into account. The plot is obtained by substituting

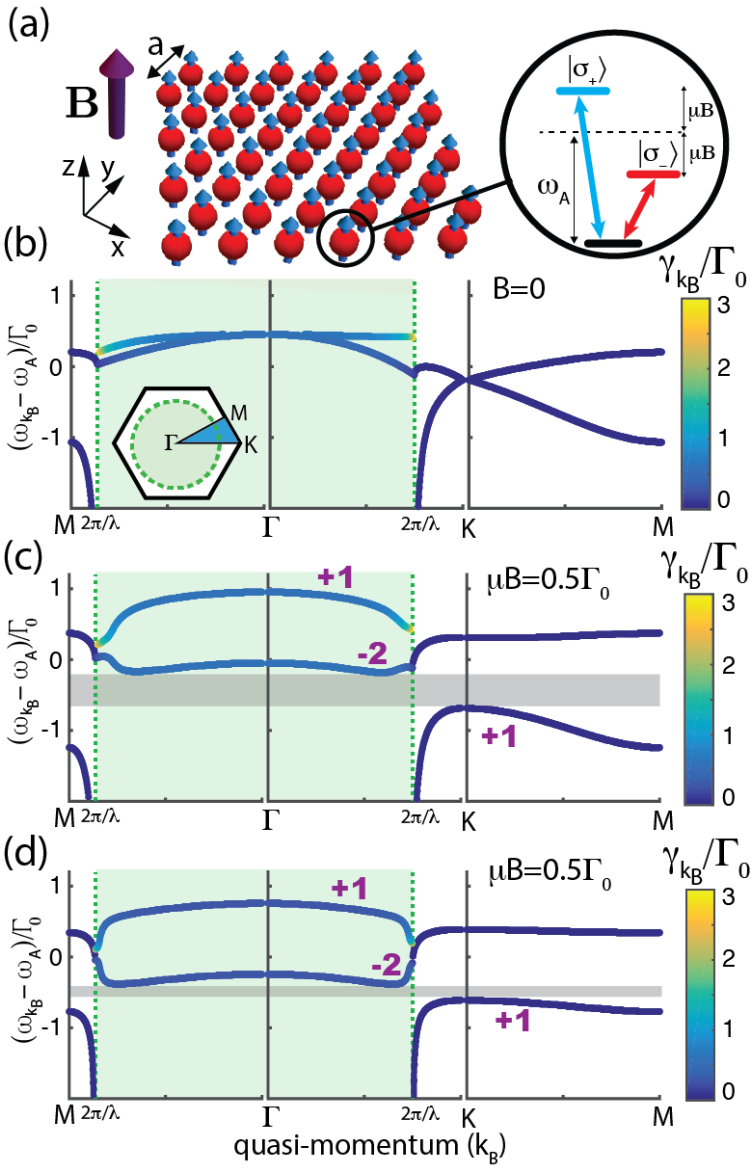

Figure 3-5: (a) Triangular lattice of atoms with interatomic spacing a in free space. Each atom has two excited states $|\sigma_+\rangle$ and $|\sigma_-\rangle$ with Zeeman-splitting $\pm\mu B$ due to an out-of-plane magnetic field B. (b) Photonic band structure for $B = 0$ and point-like atoms pinned to their lattice sites. Green dashed lines mark the light cone edges. Modes with quasi-momentum $k_B < \omega_{\mathbf{k}_B}$ (green shaded region) couple to free-space, making them short-lived. Modes with quasi-momentum $k_B > \omega_{\mathbf{k}_B}$ are long-lived. Decay rates of the modes are color coded. Bands are degenerate at the $\mathbf{\Gamma}$ and $\mathbf{K}$ points. (c) A transverse magnetic field ($\mu B = 0.5\Gamma_0$) opens a small gap ($\Delta = 0.5\Gamma_0$) between the bands (grey shaded region). The bands acquire non-trivial Chern numbers (purple numbers). (d) When the atoms fluctuate around the lattice sites, the size of the gap is reduced. Here the amplitude of fluctuations is $a_{\text{ho}} = 0.4a$. Relevant parameters for all three plots are $\lambda = 790$nm, $\Gamma_0 = 2\pi \times 6$MHz and $a = \lambda/2$.

the regularized expressions from Eq. (3.23) and Eq. (3.24) into Eq. (3.17) and diagonalizing Eq. (3.7) with $a = \lambda/2$ and $a_{\text{ho}} = 0.4a$. Since fluctuations smear out the relative phases between sites, the band gap becomes smaller relative to the case when atoms were assumed to be point-like. For even larger fluctuations the gap closes. We note that the band structure is not significantly affected by fluctuations as long as $a_{\text{ho}} \lesssim 0.15a$.

The presence of the gap between the topologically non-trivial bands implies that for a finite lattice, edge states appear on the system boundaries. However, since the boundaries of the light cone are very close to the boundaries of the irreducible Brillouin zone, all edge states will fall within the light cone. Therefore, all edge states couple to the free-space modes, making them short-lived. This makes energy transfer with these edge states impractical. The spacing of the atoms can be reduced slightly to increase the size of the Brillouin zone and establish larger areas that are outside the light cone. However, as the spacing between atoms is reduced, the gap size gradually decreases and closes before the edge states cross the edges of the light cone. This stands in contrast with the case of a honeycomb lattice of atoms, where the gap size increases as $\sim 1/a^3$ with decreasing interatomic distance [113].

Qualitatively similar results can be obtained in a square Bravais lattice of atoms with $a \approx \lambda/2$ and identical atomic level structure. In this case, quadratic degeneracies form both at the $\mathbf{\Gamma}$ and $\mathbf{M}$ points. A magnetic field lifts the degeneracies, opening a gap. The size of the gap varies with interatomic spacing and is non-negligible ($\Delta \sim 0.5\Gamma_0$) only when $a \approx \lambda/2$. The maximum gap size is generally smaller in the square lattice than for a triangular lattice with similar parameters, as the Brillouin zone of the square lattice is less circular than that of the triangular lattice [40].

3.4 Atomic lattices near a metalic planar surface

The study of dipole-like atomic emitters near metallic surfaces has received significant attention lately as part of recent research efforts into plasmonics [82, 121, 137–142]. The technique developed so far can be extended in a straightforward way to describe

atomic lattices in the vicinity of planar metal surfaces as long as the plane of the atomic lattice is parallel to all surfaces, thus ensuring that translational invariance is preserved in the x-y plane. Here, we analyze atoms placed near a single metal-dielectric interface. In Appendix B.4, we also discuss how our method generalizes to describe atomic lattices in the presence of arbitrarily layered planar media.

We assume that the plane of the atomic lattice lies at $z = 0$ and the metal-dielectric interface is located at a distance h below the dipoles at $z = -h$. The eigenmodes of the atomic lattice are then obtained form Eq. (3.7) and Eq. (3.11) by substituting $G_{\alpha\beta}$ into Eq. (3.9) and Eq. (3.13), where $G_{\alpha\beta}$ is the solution of Eq. (3.14) with the following spatially inhomogeneous and frequency-dependent permittivity

$$\varepsilon(\omega, \mathbf{r}) = \begin{cases} \varepsilon_d, & \text{if } z > -h \\ \varepsilon_m(\omega) < 0, & \text{if } z < -h \end{cases}, \tag{3.34}$$

where ε_d is the permittivity of the dielectric and $\varepsilon_m(\omega)$ is the frequency-dependent permittivity of the metal. In the presence of a planar interface, there is no known closed-form solution for $G_{\alpha\beta}$ in position space. In contrast, it is possible to exactly solve for the Weyl decompositon $g_{\alpha\beta}(\mathbf{p}_{x\text{-}y}; z)$ in momentum space in the presence of arbitrarily layered planar media (see Appendix B.4 for more details), which allows us to efficiently perform the band structure calculations using the expressions Eq. (3.17) and Eq. (3.20)[2].

For illustration, below we analyze two examples of atomic lattices near plasmonic surfaces – a square lattice of four-level atoms featuring a non-topological gap and a triangular lattice of three-level atoms giving rise to topological gaps.

[2]We note that using the exact Green's function in momentum space has the other advantage of allowing us to account for the interaction of the atoms not only with surface plasmons, but also with other types of surface waves, which are collectively known as "creeping waves" or "quasi-cylindrical waves" [139, 154–156]

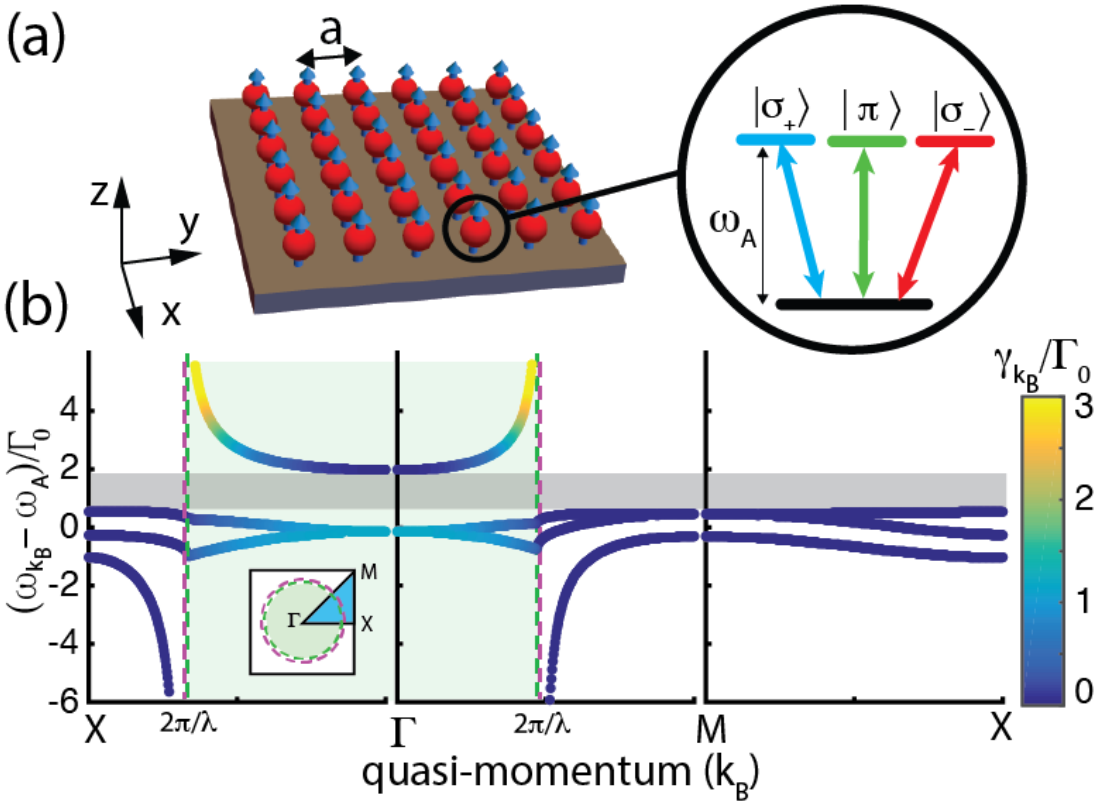

Figure 3-6: (a) Square lattice of atoms with interatomic spacing a and distance h from a silver surface. Each atom has three transitions to the $|\sigma_+\rangle$, $|\pi\rangle$ and $|\sigma_-\rangle$ states. (b) Band structure of the lattice. Green dashed lines mark the edges of the free-space light cone (green shaded region), purple dashed lines show the plasmonic dispersion of the metal surface. Decay rate of the modes is color coded. Due to the strong coupling of the $|\pi\rangle$ state to the plasmons, a non-topological gap opens in the spectrum (grey shaded region). Relevant parameters are $\lambda = 737$nm, $\Gamma_0 = 2\pi \times 0.95$MHz, $a = \lambda/3$ and $h = \lambda/10$.

3.4.1 Square lattice of four-level atoms

As our first example, we consider a square lattice of atoms in free space ($\varepsilon_d = 1$) near a silver surface as shown in Fig. 3-6(a). Each atom is assumed to have three excited states $|\sigma_+\rangle$, $|\sigma_-\rangle$ and $|\pi\rangle$, which are excited by $\hat{\sigma}_+$, $\hat{\sigma}_-$ and $\hat{z}$ polarized light. The atoms are assumed to be very close to the surface $h \ll \lambda$, such that coupling to plasmons is strong at optical frequencies. For the frequency-dependent dielectric permittivity of metal we use the material properties reported for single-crystal silver in Ref. [121], which were experimentally shown to give rise to propagation distances on the order of 150-200λ for plasmons at optical frequencies. Therefore, we disregard the imaginary part of the permittivity with the understanding that the propagation distance of the hybrid atom-plasmon modes of the lattice is eventually limited by ohmic losses. For a discussion of the notion of band gaps in the presence of losses see Ref. [125].

Fig. 3-6(b) shows the band structure of the atomic lattice near the metal surface with $a = \lambda/3$ and $h = \lambda/10$. Due to the proximity of the metal surface, the in-plane components of the electromagnetic field are small. Therefore, the bare resonant energy ω_A of the $|\sigma_+\rangle$ and $|\sigma_-\rangle$ transitions of the individual atoms is not strongly affected by the presence of the other atoms, resulting in the two nearly flat bands near ω_A. In contrast, the $|\pi\rangle$ transition couples strongly to plasmons, which are predominantly polarized along $\hat{z}$. The strong interaction splits the $\hat{z}$ polarized band into two bands (top and bottom band in Fig. 3-6(b)), resulting in a (non-topological) band gap. At energies inside the band gap no plasmonic modes can propagate.

The edges of the light cone are marked by green dashed lines in Fig. 3-6(b). For frequencies far away from the plasma frequency, the plasmonic modes fall just outside the edges of the light cone. These plasmonic modes are marked by magenta dashed lines in Fig. 3-6(b). Modes within the light cone couple strongly to free space modes, whereas modes outside the light cone do not decay.

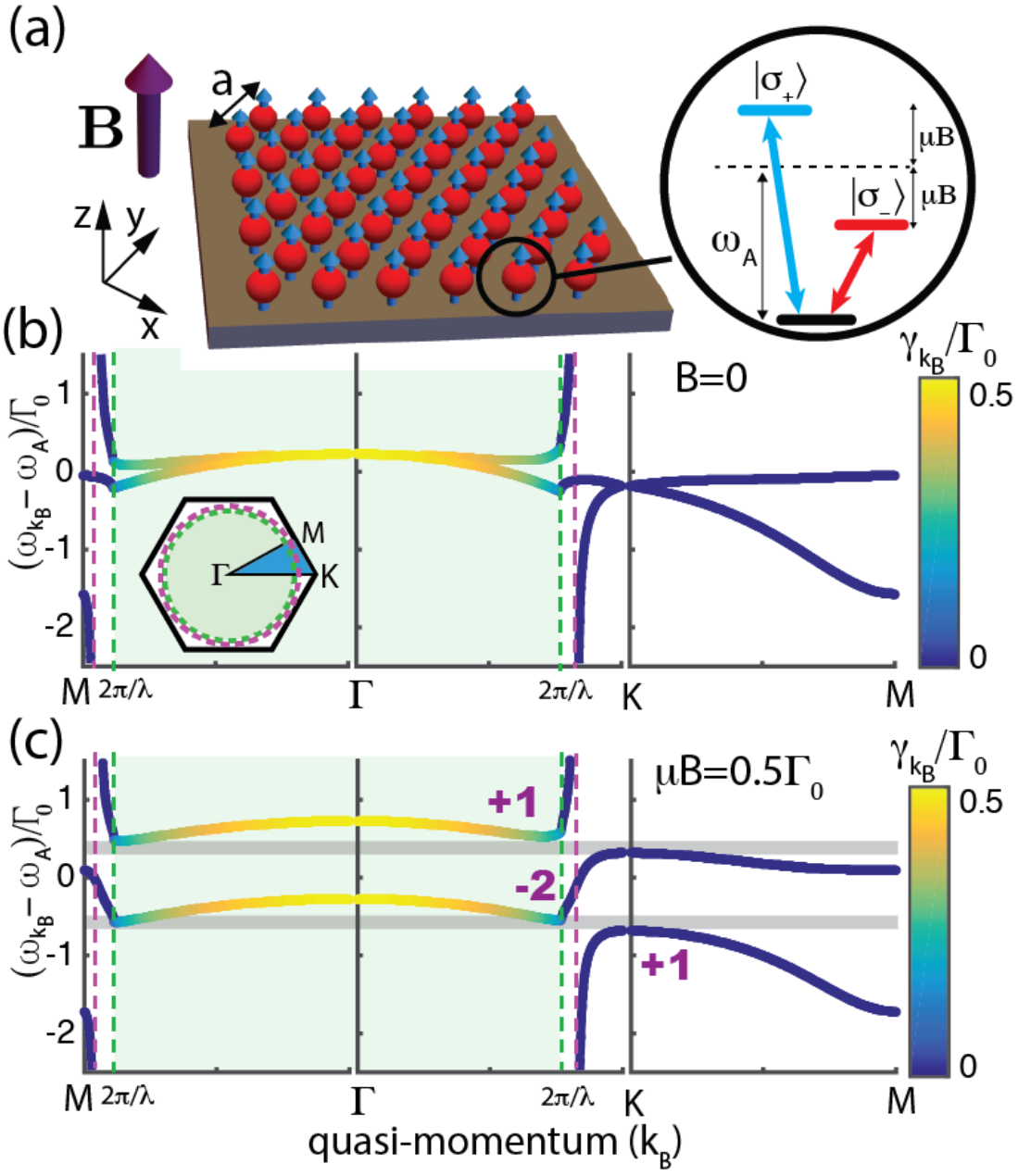

Figure 3-7: (a) Triangular lattice of atoms with transitions to the $|\sigma_+\rangle$ and $|\sigma_-\rangle$ states near a metal surface. (b) Band structure of the lattice for $B = 0$. Green dashed lines mark the edges of the free-space light cone (green shaded region), purple dashed lines show the plasmonic dispersion of the metal surface. Decay rate of the modes is color coded. Bands are degenerate at the $\mathbf{\Gamma}$ and $\mathbf{K}$ points. (c) A transverse magnetic field ($\mu B = 0.5\Gamma_0$) opens two small gaps between bands that have non-trivial Chern numbers. The relevant parameters are $\lambda = 437$nm, $\Gamma_0 = 2\pi \times 0.95$MHz, $a = \lambda/1.95$ and $h = \lambda/15$.

3.4.2 Triangular lattice of three-level atoms

Hybridized atom-plasmon-photon bands may also have topological character in the proximity of the metal surface. Fig. 3-7 shows a triangular lattice of three-level atoms with V-level structure near a metal surface, where the transition to the $|\pi\rangle$ state is not included since it decouples completely from the transition to the $|\sigma_+\rangle$ and $|\sigma_-\rangle$ states (see discussion in Section 3.3.1). The $|\sigma_+\rangle$ and $|\sigma_-\rangle$ transitions are assumed to be near-UV ($\lambda = 437$nm). Such transitions are favorable, since at higher frequencies the plasmons get more tightly confined to the metal surface and the in-plane components of the plasmonic fields increase, making interactions with the $|\sigma_\pm\rangle$ transitions stronger. Fig. 3-7(b) shows the band structure in the absence of a magnetic field. A quadratic degeneracy forms at the $\mathbf{\Gamma}$ point and a Dirac point is found at the $\mathbf{K}$ point, just as in free space. Applying a magnetic field lifts the degeneracies and opens up two small gaps in the spectrum (grey shaded bands in Fig. 3-7(c)) and the bands acquire non-trivial Chern numbers (purple numbers). The bands remain topological even if atoms with longer transition wavelength are used. However, in this case the interactions will be weaker, making the 'avoided crossings' of bands smaller and the gap disappears. Note that the band structures in Fig. 3-7(b) and (c) are qualitatively similar to the band structures obtained for a triangular lattice of atoms in free space (Fig. 3-5(b) and (c)). The key difference is that in Fig. 3-7 the uppermost band asymptotically approaches the unperturbed plasmonic modes of the metal surface (purple dashed lines) for $\omega_{\mathbf{k}_B} \gg \omega_A$, whereas in Fig. 3-5 the decay rate of the uppermost band diverges as the edges of the light cone are approached, effectively dissolving the band [113].

3.5 Conclusions

We have described a general method for calculating the photonic band structure for infinite two-dimensional atomic lattices in free space and near planar surfaces with arbitrary Bravais and non-Bravais geometries. This method takes into account the full radiation pattern emitted by individual atoms, which gives rise to long-range in-

teractions that scale as $\sim 1/r$. By performing the required summations in momentum space rather than in real space, calculation of collective energy shifts and decay rates can be performed efficiently. This method makes it possible to account for atomic position fluctuations and can be extended to describe atomic lattices near metallic surfaces.

As applications of our method, we studied non-Bravais square lattices and triangular Bravais lattices in free space and investigated their topological properties, including topological edge states in the band gap. We also obtained the band structure of an atomic square lattice near metallic surfaces and studied the topological bands that arise when a triangular lattice of atoms is placed near the metal surface. Given the generality of our method, we expect that it will pave the way for further studies of two-dimensional atomic lattices both in free space and near planar surfaces and will facilitate finding experimentally accessible parameter regimes for the realization of topological quantum optics and other intriguing phenomena.

Chapter 4

Topological Quantum Optics in Two-Dimensional Atomic Arrays

4.1 Introduction

Charged particles in two-dimensional systems exhibit exotic macroscopic behavior in the presence of magnetic fields and interactions. These include the integer [15], fractional [12] and spin [157] quantum Hall effects. Such systems support topologically protected edge states [158, 159] that are robust against defects and disorder. There is a significant interest in realizing topologically protected photonic systems. Photonic analogues of quantum Hall behavior have been studied in gyromagnetic photonic crystals [22–27], helical waveguides [28], two-dimensional lattices of optical resonators [29–31] and in polaritons coupled to optical cavities [40]. An outstanding challenge is to realize optical systems which are robust not only to some specific backscattering processes but to *all* loss processes, including scattering into unconfined modes and spontaneous emission. Another challenge is to extend these effects into a nonlinear quantum domain with strong interactions between individual excitations. These considerations motivate the search for new approaches to topological photonics.

In this Chapter, we introduce and analyze a novel platform for engineering topological states in the optical domain. It is based on atomic or atom-like quantum optical systems [110], where time-reversal symmetry can be broken by applying mag-

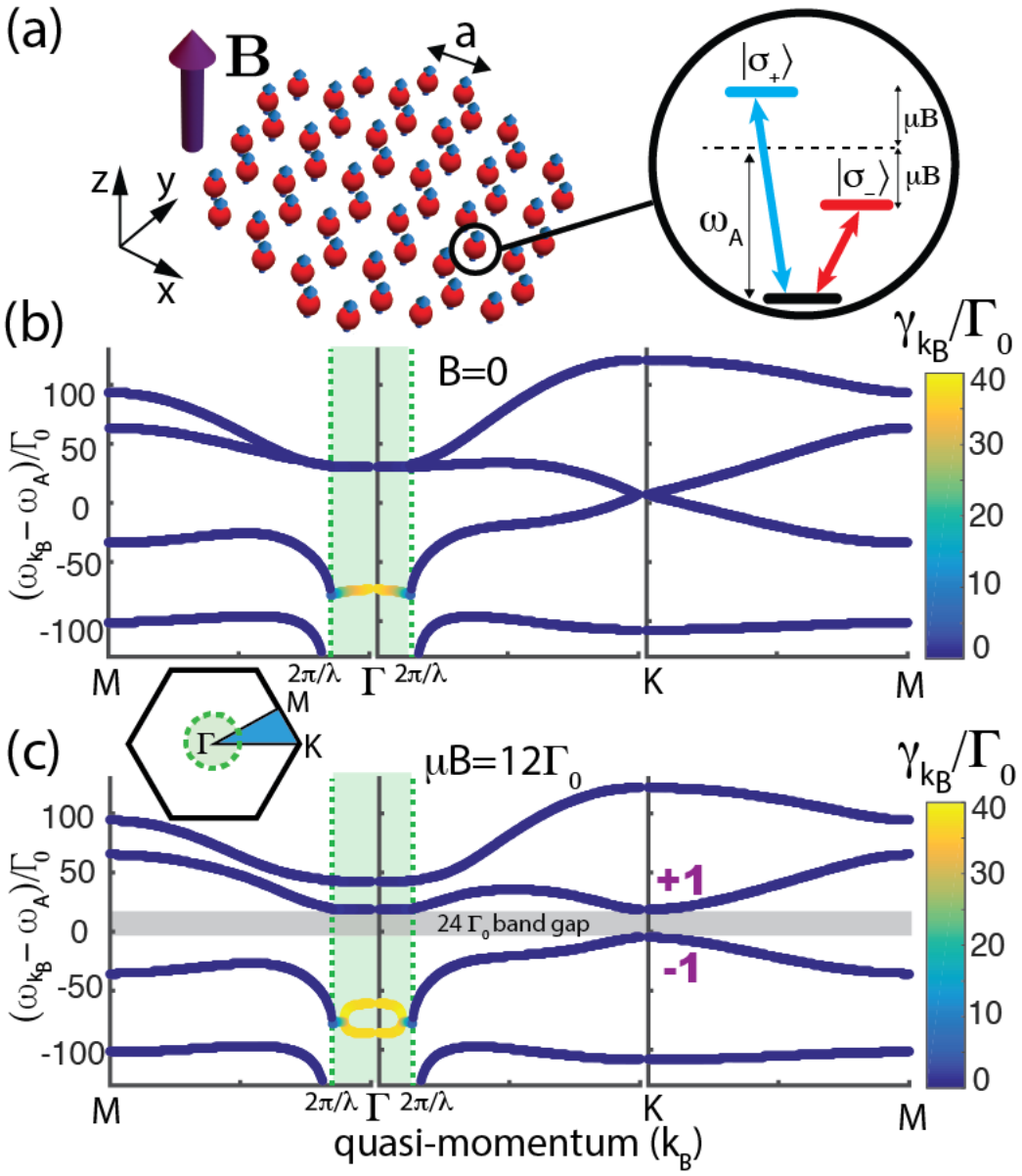

Figure 4-1: (a) Honeycomb lattice of atomic emitters with interatomic spacing a. Each atom has a V-type level structure with optical transitions to the $|\sigma_+\rangle$ and $|\sigma_-\rangle$ states. A B-field breaks the degeneracy via the Zeeman splitting. (b) Band structure of the lattice with $B = 0$. Green dashed lines indicate the edges of the free-space light cone. Modes with quasi-momentum $k_{\mathrm{B}} < \omega_{\mathbf{k}_B}/c$ couple to free-space modes and are short lived (green shaded region). Decay rates of the modes are color-coded. Bands are degenerate at the symmetry points **K** and **Γ**. (c) A transverse magnetic field ($\mu B = 12\Gamma_0$) opens a gap (grey-shaded region) between topological bands with non-trivial Chern numbers. Relevant parameters are $\lambda = 790$nm, $\Gamma_0 = 2\pi \times 6$MHz and $a = 0.05\lambda$.

netic fields and the constituent emitters are inherently nonlinear. Specifically, we focus on optical excitations in a two-dimensional honeycomb array of closely spaced emitters. We show that such systems maintain topologically protected confined optical modes that are immune to large imperfections as well as to the most common loss processes such as scattering into free-space modes. Such modes can be used to control individual atom emission, and to create quantum nonlinearity at a single photon level.

4.2 Physical system

The key idea is illustrated in Fig. 4-1(a). We envision an array with interatomic spacing a and quantization axis $\hat{z}$ perpendicular to the plane of the atoms. Each emitter has a V-type level structure with transitions from the ground state to the excited states $|\sigma_+\rangle$ and $|\sigma_-\rangle$, excited by the corresponding polarization of light[1]. The hybridized atomic and photonic states result in confined Bloch modes with large characteristic quasi-momenta that for dense atomic arrays significantly exceed the momentum of free-space photons. These confined modes are outside of the so-called "light cone" and are decoupled from free space resulting in long-lived, sub-radiant states[2]. Atomic Zeeman-shifts induced by a magnetic field, create a bandgap in the optical excitation spectrum, and the Bloch bands acquire non-trivial Chern numbers. The resulting system displays all essential features associated with topological robustness. Before proceeding, we note that polar molecules coupled via near-field interactions [39, 160] and excitons in Moiré heterojunctions [161] have been shown to give rise to chiral excitations in 2D. In contrast, the present analysis includes both near- and far-field effects as well as scattering to free space. We also note that the emergence of Weyl excitations has been recently predicted [133] in 3D lattices of polar

[1]For simplicity we assume that the $|z\rangle$ state is far detuned from resonance, e.g. due to Stark shift. However, one can include the $|z\rangle$ state without detuning as long as there are no polarization-mixing perturbations in the system, as radiation from the $|\sigma_+\rangle$ and $|\sigma_-\rangle$ states is completely decoupled from the $|z\rangle$ transition

[2]Subradiance in periodic atomic lattices was also discussed recently, in the absence of topology, in Ref. [134].

particles.

In the single excitation case, following the adiabatic elimination of the photonic modes, the dynamics of the system (no-jump evolution in the master equation [144]) can be described by the following non-Hermitian spin Hamiltonian [109–112, 114]

$$H = \hbar \sum_{i=1}^{N} \sum_{\alpha=\sigma_+,\sigma_-} \left(\omega_A + \mathrm{sgn}(\alpha_i)\mu B - \mathrm{i}\frac{\Gamma_0}{2} \right) |\alpha_i\rangle\langle\alpha_i| + \frac{3\pi\hbar\Gamma_0 c}{\omega_A} \sum_{i\neq j} \sum_{\alpha,\beta=\sigma_+,\sigma_-} G_{\alpha\beta}(\mathbf{r}_i - \mathbf{r}_j)|\alpha_i\rangle\langle\beta_j|, \tag{4.1}$$

where N is the number of atoms, $\omega_A = 2\pi c/\lambda$ is the atomic transition frequency with wavelength λ, μB is the Zeeman-shift of the atoms with magnetic moment μ due to an out-of-plane magnetic field $\mathbf{B} = B\hat{z}$ with $\mathrm{sgn}(\sigma_\pm) = \pm$. Here, $\Gamma_0 = d^2\omega_A^3/(3\pi\epsilon_0\hbar c^3)$ is the radiative linewidth of an individual atom in free space, c is the speed of light, d is the transition dipole moment, $G_{\alpha\beta}(\mathbf{r})$ is the dyadic Green's function in free space describing the dipolar spin-spin interaction (see Appendix C.1) and $\mathbf{r}_i$ denotes the position of the atoms. Note that the Hamiltonian in Eq. (4.1) assumes the atoms are pinned to the lattice. The effect of fluctuating atomic positions is discussed in Appendix C.8.

4.3 Photonic band structure

For an infinite periodic honeycomb lattice, the single excitation eigenmodes of Eq. (4.1) are Bloch modes [148] given by

$$|\psi_{\mathbf{k}_B}\rangle = \sum_n \sum_{b=1,2} e^{\mathrm{i}\mathbf{k}_B\cdot\mathbf{R}_n} \left[c^b_{+,\mathbf{k}_B} |\sigma^b_{+,n}\rangle + c^b_{-,\mathbf{k}_B} |\sigma^b_{-,n}\rangle \right], \tag{4.2}$$

where the summation runs over all lattice vectors $\{\mathbf{R}_n\}$, $b = 1, 2$ labels the two atoms within the unit cell and $\mathbf{k}_B$ is the Bloch wavevector. For each $\mathbf{k}_B$ there are four eigenvalues of the form $E_{\mathbf{k}_B} = \omega_{\mathbf{k}_B} - \mathrm{i}\gamma_{\mathbf{k}_B}$, where the imaginary part corresponds to the overall decay rate of the modes (see Appendix C.2).

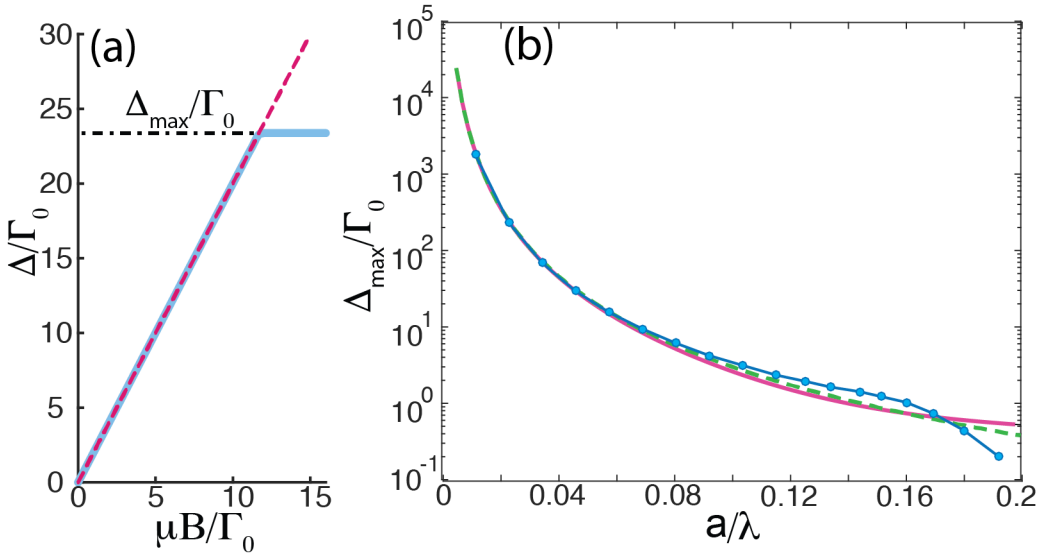

Figure 4-2: (a) Size of the gap between topological bands (blue line) as a function of magnetic field for $a = \lambda/20$. (b) The maximum gap size $\Delta_{\max}$ (blue dotted line) as a function of the interatomic spacing a. The solid magenta line shows the dipolar interaction strength J between two atoms with parallel dipole moments. The dashed green line is a phenomenological $J \sim 1/r^3$ fit. For $a \ll \lambda$, $\Delta_{\max}$ scales as $1/a^3$.

Fig. 4-1(b) shows the band structure in the absence of a magnetic field along the lines joining the symmetry points **M**, **Γ** and **K** of the irreducible Brillouin zone (see inset of Fig. 4-1(c)). The decay rates of the modes ($\gamma_{\mathbf{k}_B}$) are shown using a color code. Crucially, we find that the decay rate of some modes can be significantly smaller than $\Gamma_0/2$ due to collective interference effects. Green dashed lines at $k_B = 2\pi/\lambda$ mark the edges of the light cone corresponding to free space modes with dispersion $\omega_{\mathbf{k}_B} = k_B c$. The modes close to the center of the Brillouin zone (**Γ**) have quasi-momenta k_{B} less than the maximum momentum of free space photons at the same energy ($k_{\mathrm{B}} < \omega_{\mathbf{k}_B}/c$). These modes couple strongly to free-space modes with matching energy and momentum and decay rapidly (Appendix C.3). In contrast, modes with quasi-momenta greater than the momentum of free space photons ($k_{\mathrm{B}} > \omega_{\mathbf{k}_B}/c$), are completely decoupled and do not decay into free space due to the momentum mismatch.

Fig. 4-1(b) also shows that the photonic bands are degenerate at the symmetry points **Γ** and **K** in the absence of a magnetic field. These degeneracies originate from

the degeneracy of the $|\sigma_+\rangle$ and $|\sigma_-\rangle$ states at zero magnetic field. Due to the lattice symmetries, the degeneracy at the $\mathbf{\Gamma}$ point is quadratic [162], while a linear Dirac cone is formed at the $\mathbf{K}$ point [23]. Applying an out-of-plane magnetic field lifts this degeneracy and an energy gap forms across the Brillouin zone.

4.4 Topological properties of the system

We explore the topological nature of these bands, by calculating the Chern numbers using the method described in Ref. [152]. The sum of the Chern numbers above and below the band gap is $+1$ and -1, respectively. The origin of these topological bands can be understood intuitively by noting that at the $\mathbf{K}$ point the modes separated in energy due to Zeeman splitting have, respectively, $\hat{\sigma}_+$ and $\hat{\sigma}_-$ circular polarizations. The opposite chirality of the bands reflects the time-dependent circular rotation of the electric fields associated with the $\hat{\sigma}_+$ and $\hat{\sigma}_-$ polarizations in the x-y plane.

The size of the topological gap at the $\mathbf{K}$ point scales linearly with the magnetic field due to the Zeeman splitting ($2\mu B$) of the $|\sigma_+\rangle$ and $|\sigma_-\rangle$ states (Fig. 4-2(a)), but the gap size is eventually limited to a maximum value $\Delta_{\max}$ due to the level repulsion between the two upper bands at the $\mathbf{\Gamma}$ point. Fig. 4-2(b) shows the maximum gap size as a function of the interatomic spacing a (blue dotted line). The strength of the dipolar coupling $J = 3\pi\Gamma_0 c/\omega_A\, G_{xx}(a)$ between two parallel dipoles at a distance a is also shown. The close agreement between the two curves shows that the maximum gap size is determined by the dipolar interaction strength between the atoms. For $a \ll \lambda$ the maximum gap size has the simple scaling $\Delta_{\max} \sim 1/a^3$.

Gaps between topological bands are typically associated with the presence of one-way reflection-free edge modes at the boundaries of a finite system. To explore the spectrum of edge modes in the gap, we calculated the band structure for periodic stripes of atoms in a honeycomb lattice. The stripes may have bearded, armchair or zig-zag edges [14, 163]. Fig. 4-3 shows the edge geometries and the corresponding band structures of stripes with bearded and armchair edges. Zig-zag edges are discussed in Appendix C.4. Edge modes on the lower (upper) edge of the stripe traversing the

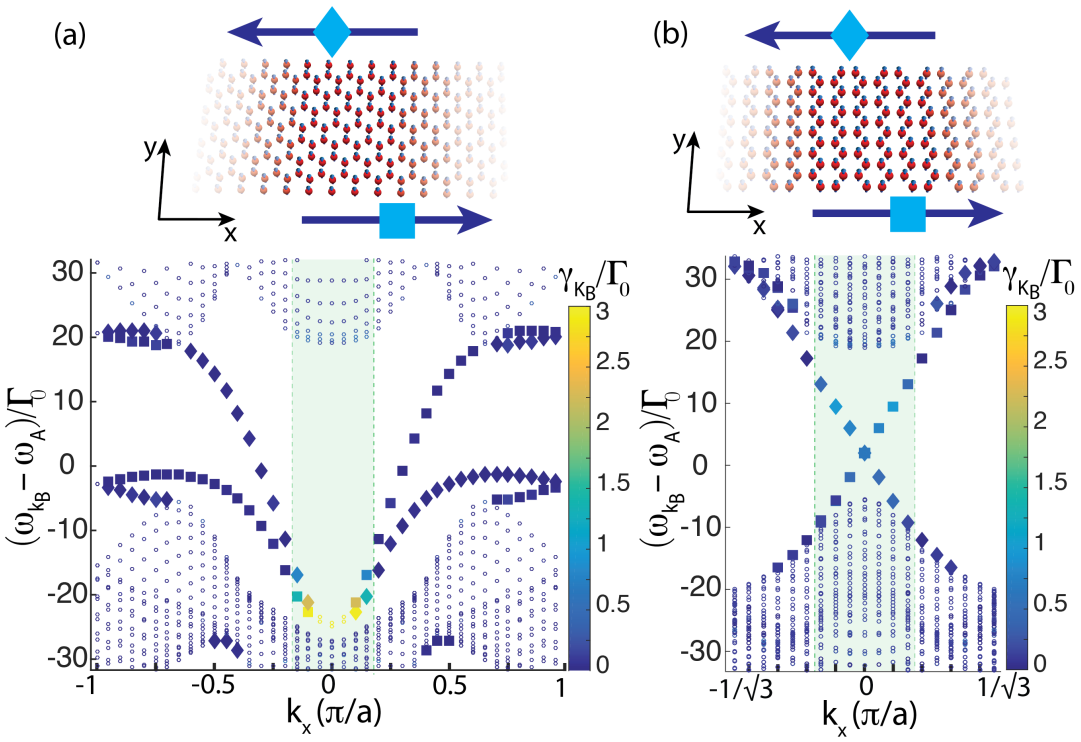

Figure 4-3: Topological edge states on the (a) bearded and (b) armchair edges of periodic stripes of atoms. Each edge supports only one unidirectional mode. Modes propagating on the upper (lower) edges of the stripes are marked by diamonds (squares) in the band diagrams. Bulk modes are marked with dots. Decay rates of the modes are color-coded. Modes of the bearded (armchair) edges cross the gap with quasi-momentum $k_{\mathrm{B}} > \omega_{\mathbf{k}_B}/c$ ($k_{\mathrm{B}} < \omega_{\mathbf{k}_B}/c$) making them long (short) lived. Parameters are the same as in Fig. 4-1(c). The spectrum was obtained for the bearded (armchair) edges from an 40x42 (40x41) lattice of atoms with periodic boundary conditions along the first dimension. States for which the ratio of the total amplitude on the top (bottom) four atom rows to the bottom (top) four rows is greater than 15 are classified as edge states.

gap have positive (negative) group velocity and carry energy to the right (left). Thus, energy transport by edge modes is unidirectional as a consequence of the broken time-reversal symmetry of the system. If the direction of the magnetic field is flipped, the direction of the energy flow on any given edge is reversed. Edge modes on bearded boundaries have quasi-momenta $k_{\mathrm{B}} > \omega_{\mathbf{k}_B}/c$ while crossing the gap and therefore couple weakly to free-space modes making them long-lived. In contrast, modes on the armchair edges cross the gap with quasi-momenta $k_{\mathrm{B}} < \omega_{\mathbf{k}_B}/c$ and the relatively strong coupling to free-space modes makes them short-lived. The lifetimes of edge modes are also influenced by the lattice size. Increasing the number of atoms N in a finite lattice, decreases the losses from finite-size effects and increases the lifetimes of long-lived edge modes (Appendix C.5).

Fig. 4-4 illustrates the unidirectional energy transport. It shows a honeycomb lattice of atoms with an overall hexagonal shape and a large defect on one edge. The geometry was chosen such that in the absence of defects, all boundaries are bearded edges supporting long-lived edge modes. An out-of-plane magnetic field $\mathbf{B}$ induces a band gap of size Δ in the energy spectrum. An atom on the boundary is adiabatically addressed by a laser at a frequency ω_{L} resonant with the long-lived edge modes in the topmost part of the band gap. The laser drives the σ_+ and σ_- transitions of the atom off-resonantly with equal coupling strengths Ω, where $\Omega \ll \Delta$. Fig. 4-4 shows a snapshot of the excitation probability of each atom in the lattice. Approximately 96% of the excitation emitted by the driven atom is coupled into the edge modes carrying energy in the forward direction. Coupling into the backward direction or into the bulk modes is suppressed due to topology and the large band gap. These results are qualitatively independent of the relative driving strengths of the σ_- and σ_+ transitions (Appendix C.6). The excitation routes around lattice corners with $\sim 97\%$ efficiency and goes around defects of arbitrary shape and size by forming new edge modes at the defect boundaries as shown in Fig. 4-4, where $\sim 83\%$ of the excitation survives. Atomic emission in the bulk is discussed in Appendix C.7.

The distance the photon propagates on an edge is set by the ratio of the group velocity and the intrinsic lifetime of the edge modes. The group velocity of the edge

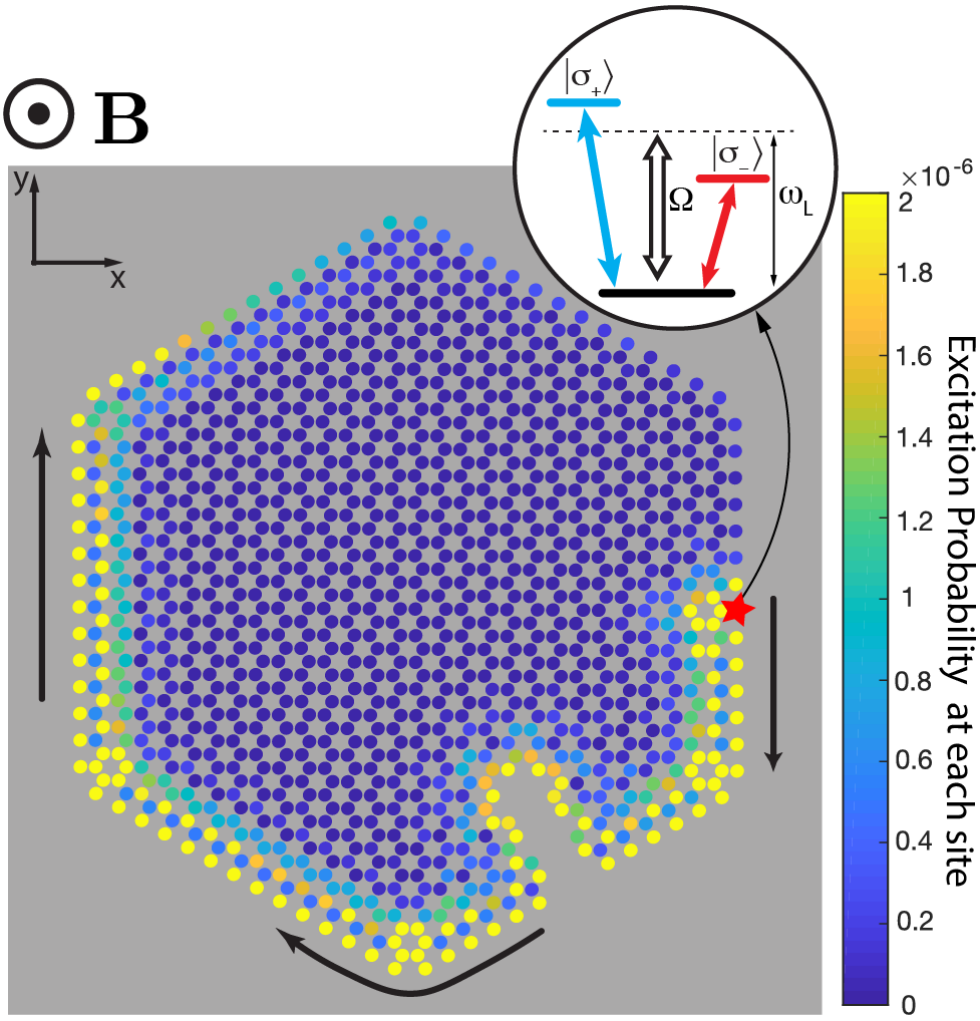

Figure 4-4: Snapshot of the time evolution (at $t = 5.7\Gamma_0^{-1}$) of the system as an atom on the edge (red star) is driven by a laser (inset). The color code shows the excitation probability $|\langle\psi(t)|\sigma_+^i\rangle|^2 + |\langle\psi(t)|\sigma_-^i\rangle|^2$ at each atomic site $i = 1, \ldots, N$. Approximately 96% of the emitted excitation is coupled into the forward direction and scattering into bulk and backward edge modes is strongly suppressed. The excitation goes around corners and routes around the large lattice defect. Relevant parameters are $N = 1243$, $\lambda = 790$nm, $\Gamma_0 = 2\pi \times 6$MHz, $a = 0.05\lambda$ and $\mu B = 12\Gamma_0$. The strength of the drive is $\Omega = 1/5\Gamma_0$ and the driving frequency is $\omega_L = \omega_A + 15\Gamma_0$. The driving laser is adiabatically switched on with a Gaussian profile $\Omega(t) = \Omega \exp(-[t - 1.5\Gamma_0^{-1}]^2/[0.15\Gamma_0^{-2}])$ for $t < 1.5\Gamma_0^{-1}$.

modes traversing the gap is $v_g \approx \delta\omega/\delta k_{\mathrm{B}} \sim \Delta/(\pi/a)$, where Δ is the size of the energy gap and a is the interatomic spacing. Thus for $a \ll \lambda$, the maximum group velocity of the edge modes scales as $v_g \sim \Delta_{\max}/(\pi/a) \sim a^{-2}$. While bearded edges support long-lived modes, any departure from the ideal hexagonal shape of Fig. 4-4 creates a combination of armchair and zig-zag modes that couple more strongly to free-space modes and thus have limited lifetimes. To ensure that only a small fraction of the excitation is lost while the photon is routed around a defect, large group velocities and, therefore, small interatomic spacing is required.

We note that efficient coupling of individual quantum emitters to a confined unidirectional channel (Fig. 4-4) immediately implies the feasibility of quantum nonlinear interactions between individual photons. This can be understood by considering a 'defect atom' placed along the path of the edge excitation. Such an atom can be used to capture and store an incident photon in a long-lived atomic state, following e.g. Ref. [101] (see also Refs. [164–167]). After photon storage, the defect atom will form a lattice defect for subsequent incoming photons, which will be routed around this defect and, as a result, will acquire a nonlinear phase shift.

4.5 Possible experimental realization

Atomic arrays with much smaller interatomic spacing than the transition wavelength ($a \ll \lambda$) could be experimentally realized using state-of-the-art experiments with bosonic Stronium atoms [133, 168]. Mott insulators in the $^1S_0$ ground state of ^{84}Sr atoms using a 532nm trapping laser have been realized experimentally [169] and the atoms can be further transferred to the metastable $^3P_0$ state [170]. Using the long-wavelength $^3P_0$–$^3D_1$ transition with $\lambda_{\mathrm{Sr}} = 2.6\mu$m for atom-atom interactions would give $a = 2\lambda_{\mathrm{laser}}/(3\sqrt{3}) = \lambda_{\mathrm{Sr}}/12.7$ in an optical honeycomb lattice. The interatomic spacing could be further reduced to $a = \lambda_{\mathrm{Sr}}/16.3$ using a 412.8nm 'magic wavelength' trapping laser providing equal confinement for the $^3P_0$ and $^3D_1$ states [168]. Typical trapping frequencies in Mott insulators are $\sim 5E_{\mathrm{recoil}}/h$ [153], where $E_{\mathrm{recoil}}/h \approx 13$kHz for Stronium. Since the linewidth is $\Gamma_{\mathrm{Sr}} = 290$kHz for the $^3P_0$–$^3D_1$ transition, the

motional states of individual atoms are not well resolved and we expect heating due to photon scattering to be small. The main experimental challenge is to ensure near-unity lattice filling [171] and near-uniform excitation of atoms to the $^3P_0$ state. Other approaches to deep subwavelength atomic lattices include utilizing vacuum forces in the proximity of dielectrics [172], using adiabatic potentials [173], dynamic modulation of optical lattices [174] or sub-wavelength positioning of atom-like color defects in diamond nanophotonic devices [116, 118–120][3].

Subwavelength emitter lattices could also be created using monolayer semiconductors, such as transition metal dichalcogenides (TMDCs) [175–180]. Large splitting of the σ_+, σ_- valley polarizations due to interaction-induced paramagnetic responses was recently demonstrated in TMDCs [181]. Moiré patterns [182] could provide deep subwavelength ($a < 36$nm) periodic potentials for TMDC excitons and give rise to topological bands and chiral excitonic edge states [161]. In such Moiré heterojunctions the band gaps – and thus the group velocities of edge states– are predicted to be small ($\Delta < 1\Gamma_0$). However, as our current analysis shows, edge states outside the light cone would be long-lived and thus could still propagate a significant distance along the edges of TMDCs prior to decay into far field modes.

4.6 Conclusion

In summary, we have shown that two-dimensional atomic lattices can be used to create robust quantum optical systems featuring band gaps between photonic bands with non-trivial Chern numbers. For a finite lattice, unidirectional reflection-free edges states form on the system boundaries at energies inside the band gap. These edge modes are robust against imperfections in the lattice as well as scattering and emission into free space. These can be used, e.g. to control emission of individual atoms. We emphasize that, in contrast to linear topological photonic systems, a distinguishing feature of the present approach is the intrinsic, built-in nonlinearity

[3]Given the robustness of topological lattices, inhomogeneous broadening present in solid-state systems will not significantly change the results as long as the broadening is small compared to the topological energy gap.

associated with quantum emitters in the lattice, which leads to strong interactions between individual excitations. Harnessing such interactions could open up exciting possibilities for studying topological phenomena with strongly interacting photons, including quantum optical analogues of fractional Quantum Hall states. These include exotic states, such as those with filling fractions $\nu = 5/2$ and $\nu = 12/5$, which may feature non-Abelian excitations [4]. In addition, the inherent protection against losses may also be used for the realization of robust quantum nonlinear optical devices for potential applications in quantum information processing and quantum state transfer[4].

[4]Following the completion of this work, we became aware of the related study by R. J. Bettles, J. Minář, I. Lesanovsky, C. S. Adams, B. Olmos, Physical Review A **96**, 041603(R) (2017).

Chapter 5

Theory of Dipole Radiation Near a Dirac Photonic Crystal

5.1 Introduction

Since the experimental discovery of single-atom graphene sheets [183], the Dirac-like energy spectrum of graphene has been studied extensively [184]. This has inspired research into finding photonic analogues of graphene with Dirac-like dispersion for photons, which have been shown to give rise to a number of remarkable phenomena, including topological waveguides at microwave and optical frequencies [22, 23, 185, 186], pseudo-diffusive transport of light [187, 188], Klein tunneling [189] and photonic Zwitterbewegung [190]. Photonic Dirac cones have also been studied in the context of quantum optics and were found to give rise to single-mode behavior over large areas [191] and two-dimensional localization without a band gap [192]. More recently, quantum emitters coupling to photonic Dirac cones were found to exhibit exotic quantum dynamics and purely long-range coherent interactions without exponential attenuation [193].

A key challenge for making such devices useful for quantum optical applications is to find realistic structures, in which the Dirac cone is energetically detuned from all other bands [185] and which support quasi-two-dimensional propagation of light [191]. An additional challenge is the inherent complexity of the electromagnetic spectrum

of such devices, which usually makes full-scale numerical analysis onerous [185, 191, 193]. Consequently, previous studies of the photonic Dirac cone relied on simplified analytic models that neglected key aspects of the electromagnetic properties of the devices, such as the polarization structure of the modes. Therefore, it is of significant interest to investigate whether there exist realistic quasi-two-dimensional structures with photonic Dirac cones, whose electromagnetic spectrum – including polarization effects – can be understood analytically.

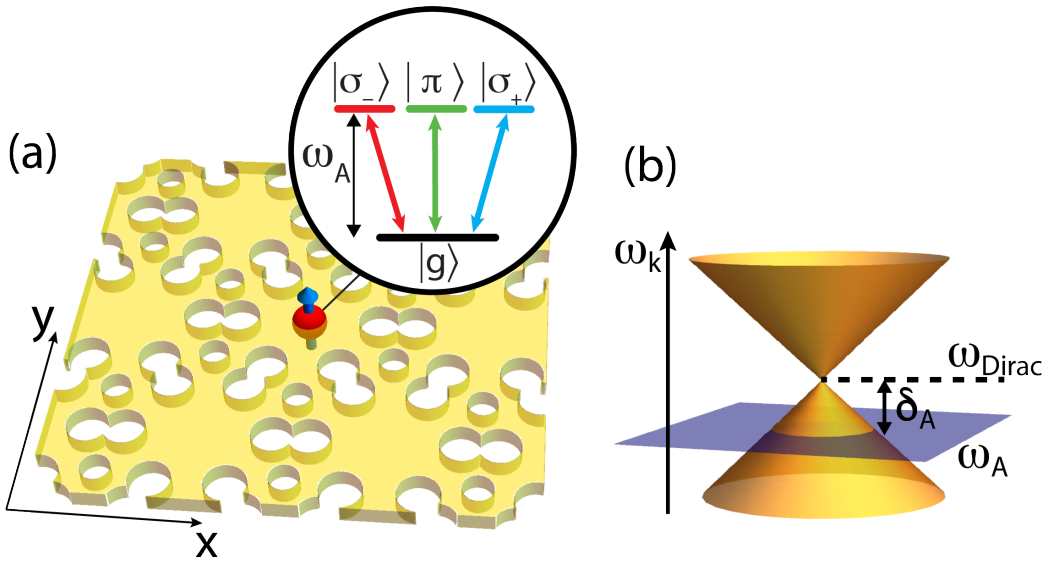

Figure 5-1: (a) Quantum emitter embedded in a quasi-two-dimensional photonic crystal slab with a cavity-like unit cell. The emitter is assumed to have three degenerate transitions of energy ω_A from the ground $|g\rangle$ to the excited states $|\sigma_\pm\rangle$ and $|\pi\rangle$. (b) The photonic bands of the slab feature a Dirac-like dispersion cone. The emitter transition frequency ω_A is detuned by δ_A from the vertex of the Dirac cone ω_{Dirac}.

In this Chapter, we develop an analytic formalism to describe dipole radiation near a realistic photonic crystal slab with a Dirac cone (Fig. 5-1(a)). The Dirac cone is energetically detuned from all the other bands, allowing us to tune the transition frequency of quantum emitters close to the Dirac point (i.e. the Dirac cone vertex) without interacting with any other bands, as shown in Fig. 5-1(b). Consequently, all dipolar interactions are mediated by the modes comprising the photonic Dirac cone, simplifying the form of the interaction. Crucially, we find that the polarization structure of the modes of the Dirac cone can be captured by an analytic model,

which allows us to incorporate polarization effects into our quantum optical treatment. Using our analytic model, we obtain a Green's function in a closed form, which captures all cooperative atomic effects relevant for the quantum dynamics of two or more emitters. In addition, we also find that the dipolar coupling between emitters exhibits winding phases, which are the key ingredients for engineering topological atomic arrays (see Chapter 6). Finally, as an application of our formalism, we study the coherent atomic interactions mediated by the photonic Dirac cone, which were recently shown to be unusually long-range with no exponential attenuation [193].

This Chapter is organized as follows. In Sec. 5.2 we describe how to engineer a two-dimensional photonic crystal slab with a Dirac-like dispersion that is energetically fully separated from the rest of the bands. In Sec. 5.3 we develop an analytic model for the photonic modes that constitute the Dirac cone. In Sec. 5.4 we calculate the Green's function that describes the dipolar coupling between emitters. In Sec. 5.5 we analyze the interactions mediated by the Dirac cone. Key results and conclusions are presented in Sec. 5.6.

5.2 Photonic crystal slab with a Dirac dispersion

In this section, we discuss how to engineer a quasi-two-dimensional photonic crystal slab that features bands with Dirac-like conical dispersion, such that the Dirac cone is energetically detuned from all other bands.

The key idea is illustrated in Fig. 5-2. We consider a gallium phosphate (GaP) photonic crystal of finite thickness h with air holes. The hole pattern of the slab has an underlying triangular lattice symmetry with lattice constant a and lattice vectors

$$\mathbf{a}_{\pm} = a(\pm\sqrt{3}\hat{x} + \hat{y})/2. \tag{5.1}$$

The hexagonal unit cell of the triangular lattice is comprised of 6 holes with radius r_l near the center of the cell and an additional set of holes with radius r_s on the boundaries, which fall only partially inside the unit cell. Fig. 5-2(a)-(c) shows the

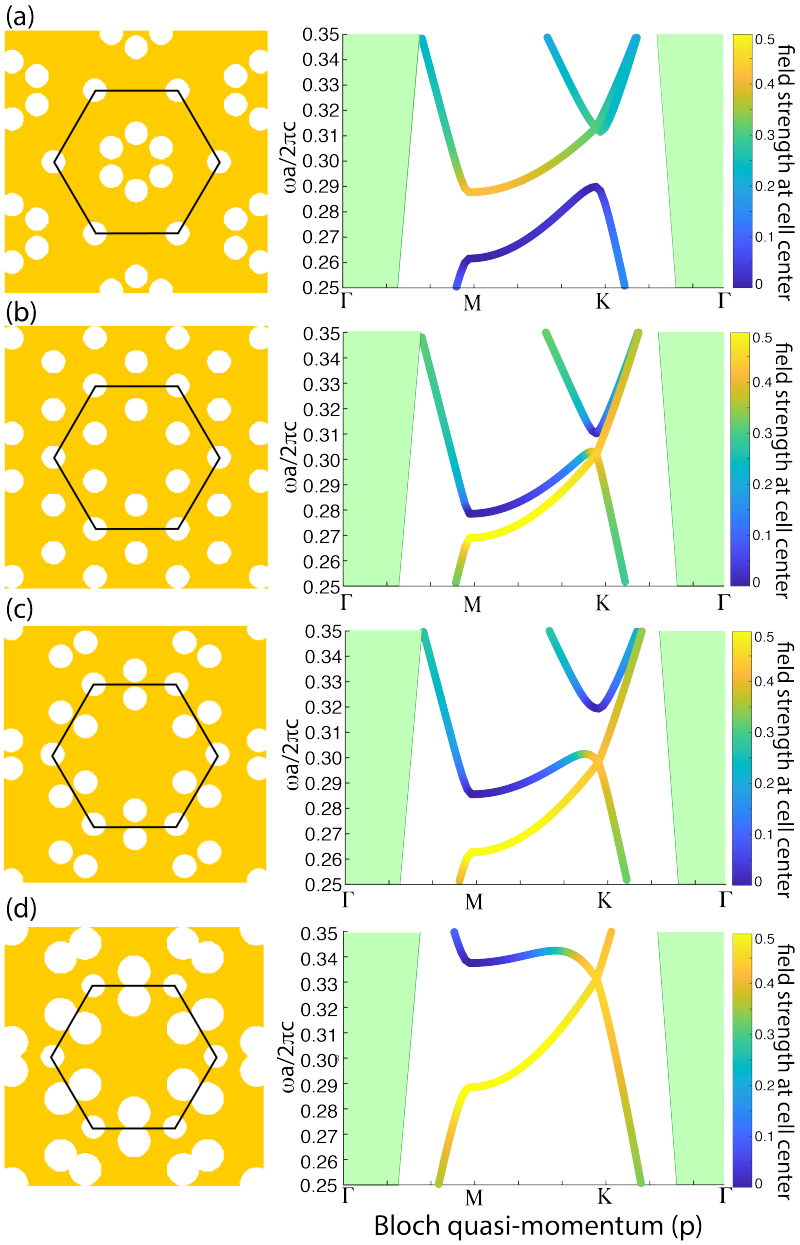

Figure 5-2: Photonic crystal slab unit cell and the corresponding TE-like band structure for 4 different geometries. The thickness of the slab is $h = 0.5a$, the radius of the holes is $r_s = 0.0833a$ and the dielectric permittivity is $\varepsilon_{\mathrm{GaP}} = 10.5625$. (a) When 6 holes are placed $l = 0.2a$ from the center, the modes in the upper band have a higher field intensity than in the lower band. Color code shows the electric field strength $|\mathbf{E_p}(\mathbf{0})|^2 a^3$ at the center of the cell for each mode. (b) For $l = 0.333a$ the modes in the lower band have a higher field intensity than in the upper band. (c) Pushing the holes to the edge of the cell ($l = 0.4a$) increases the energy gap between the bands at the **M** point. (d) Increasing the radius of the 6 holes to $r_l = 0.116a$ makes the Dirac cone energetically separated from all other bands.

holes for three different values of l, where l is the radial distance of the 6 holes from the center of the cell. We use the plane-wave expansion method to numerically solve Maxwell's equations [194] and obtain the lowest-lying transverse electric (TE-like) bands for the unit cells shown. Here, we only consider TE-like modes, since in what follows, we will assume that the quantum emitters sit at the center of the unit cell at $\mathbf{r} = \mathbf{0}$, where tranverse magnetic (TM-like) modes have zero field strength due to the inversion symmetry of the structure [41]. This symmetry ensures that the z-component of the TE-like modes is also zero at $\mathbf{r} = \mathbf{0}$. The color code for the bands shows the normalized electric field strength $|\mathbf{E}_{\mathbf{p}}(\mathbf{0})|^2 a^3$ of each mode, sampled at the center of the cell ($\mathbf{r} = \mathbf{0}$).

From the colors of the bands in Fig. 5-2(a), we see that when the 6 holes are close to each other, the modes in the lowest band have a low field concentration in the dielectric at the cell center, whereas the upper band has a high field concentration. As the holes are pushed radially outward, the two bands approach each other, and eventually cross, and thus the lower band has higher field concentration (Fig. 5-2(b)). When the holes are pushed radially further out, the two lowest bands energetically separate at the **M** point, while maintaining their degeneracy at the **K** point, forming a Dirac cone as shown in Fig. 5-2(c). Once the holes reach the edge of the irreducible Brillouin zone, the band separation at the **M** point can still be increased by expanding the radii of the 6 holes as shown in Fig. 5-2(d). For sufficiently large radii, the modes of the air band are no longer degenerate with the modes of the Dirac cone. Thus, the Dirac cone becomes energetically well-separated from all other bands, making it possible to tune emitters close to the Dirac point without coupling to any modes other than those constituting the Dirac cone. Note that similar techniques have been used previously to control the gap at the photonic Dirac cone for topological waveguiding with a single quantum emitter [185, 186].

In what follows, we will assume that the transition frequency of the emitters ω_A is tuned sufficiently close to the frequency of the Dirac point ω_{Dirac} (i.e. $\omega_{\text{Dirac}} - \omega_A \ll \omega_A$) that coupling to all modes away from the Dirac cone is small and can be neglected.

5.3 Analytic model for the Dirac cone

In this section, we develop an analytic approximation to the electromagnetic modes that constitute the photonic Dirac cone. This will enable us to derive a closed-form expression for the dyadic Green's function of the geometry (see Sec. 5.4), which describes the atomic properties inside the photonic crystal.

We start by parameterizing the linear dispersion of the Dirac cone as a function of the quasi-momentum $\mathbf{p}$ as

$$\omega_{\mathbf{p}}^{(\mathbf{K},\pm)} = \omega_{\text{Dirac}} \pm v_{\text{s}}|\mathbf{p} - \mathbf{p}_{\mathbf{K}}|, \tag{5.2}$$

where $(+)$ and $(-)$ correspond to the top and bottom bands respectively, ω_{Dirac} is the energy associated with the vertex of the cone, $\mathbf{p}_{\mathbf{K}} = 2\pi/a(1/\sqrt{3}, 1/3)$ is the momentum vector of the Dirac cone inside the irreducible Brillouin zone and v_{s} gives the group velocity of the guided modes in units of c. Mathematically, v_{s} corresponds to the slope of the Dirac cone. Both ω_{Dirac} and v_{s} can be obtained from numerical calculations.

While the dispersion is linear in the immediate vicinity of the Dirac cone, the slope v_{s} is found to vary slightly along different directions. Fig. 5-3(a) shows the cross section of the cone taken above the Dirac point. The black dashed line shows the results predicted by Eq. (5.2), while the solid blue line gives the numerically obtained results showing slight deviations from perfect circularity due to the underlying three-fold symmetry of the lattice. We average the numerical values of v_{s} along the different directions to obtain an effective value for v_{s}, which we can use in Eq. (5.2).

Next, we explore the polarization structure of the electromagnetic modes at the center of the unit cell. Fig. 5-3(b) shows the overall field intensity $|\mathbf{E}_{\mathbf{p}}(\mathbf{0})|^2 a^3$ of each mode in the top band at $\mathbf{r} = \mathbf{0}$. The intensity varies only weakly as a function of momentum and falls within a small interval. Similar results are obtained in the lower band. Therefore, we average the field intensity of all the modes to obtain an effective constant value $|E_0|^2 a^3$ that we use to parameterize the field intensity of all modes in the vicinity of the Dirac cone.

To understand the contributions of the different polarization components to the overall intensity, in Fig. 5-3(c) we color each of the modes of the Dirac cone according to the normalized intensity of the x-component of the field $|E_{\mathbf{p},x}(\mathbf{0})|^2/|\mathbf{E}_{\mathbf{p}}(\mathbf{0})|^2$. Fig. 5-3(d) shows the colored modes in the top band from above. The simple functional dependence of the resulting intensity pattern can be approximated by $\sin^2(\Phi_{\mathbf{K}}/2-\pi/4)$ for the top band and $\sin^2(\Phi_{\mathbf{K}}/2+\pi/4)$ for the bottom band, where the polarization is expressed as a function of the angle $\Phi_{\mathbf{K}}$ measured from the p_x axis. Figs. 5-3(e) and (f) show the corresponding results obtained from this simple analytic model and using Eq. (5.2). Good agreement is obtained between the numerical and analytic results. Similarly, for the y-component of the electric field $|E_{\mathbf{p},y}(\mathbf{0})|^2$ we find that the change in polarization as a function of $\Phi_{\mathbf{K}}$ is captured by $\sin^2(\Phi_{\mathbf{K}}/2+\pi/4)$ for the top band and $\sin^2(\Phi_{\mathbf{K}}/2-\pi/4)$ for the bottom band.

In general, we can model the electric field of the Dirac cone modes at $\mathbf{r}=\mathbf{0}$ as

$$\mathbf{E}_{\mathbf{p}}^{(\mathbf{K},\pm)} = E_0\left[\sin\left(\frac{\Phi_{\mathbf{K}}}{2}\mp\frac{\pi}{4}\right)\hat{x}\pm\sin\left(\frac{\Phi_{\mathbf{K}}}{2}\pm\frac{\pi}{4}\right)\hat{y}\right], \tag{5.3}$$

where

$$\Phi_{\mathbf{K}}(p_x,p_y) = \arctan\left(\frac{p_y-p_{\mathbf{K},y}}{p_x-p_{\mathbf{K},x}}\right). \tag{5.4}$$

Note that there are two inequivalent Dirac cones inside the irreducible Brillouin zone, and the dispersion at the second Dirac cone can be expressed as

$$\omega_{\mathbf{p}}^{(\mathbf{K}',\pm)} = \omega_{\text{Dirac}} \pm v_{\text{s}}|\mathbf{p}-\mathbf{p}_{\mathbf{K}'}|, \tag{5.5}$$

where $\mathbf{p}_{K'} = 2\pi/a(1/\sqrt{3},-1/3)$ is the momentum vector associated with the second Dirac cone. As in the case of the other Dirac cone, we find that the electric field of the modes of the second Dirac cone at $\mathbf{r}=\mathbf{0}$ can be expressed as

$$\mathbf{E}_{\mathbf{p}}^{(\mathbf{K}',\pm)} = E_0\left[\sin\left(\frac{\Phi_{\mathbf{K}'}}{2}\pm\frac{\pi}{4}\right)\hat{x}\mp\sin\left(\frac{\Phi_{\mathbf{K}'}}{2}\mp\frac{\pi}{4}\right)\hat{y}\right], \tag{5.6}$$

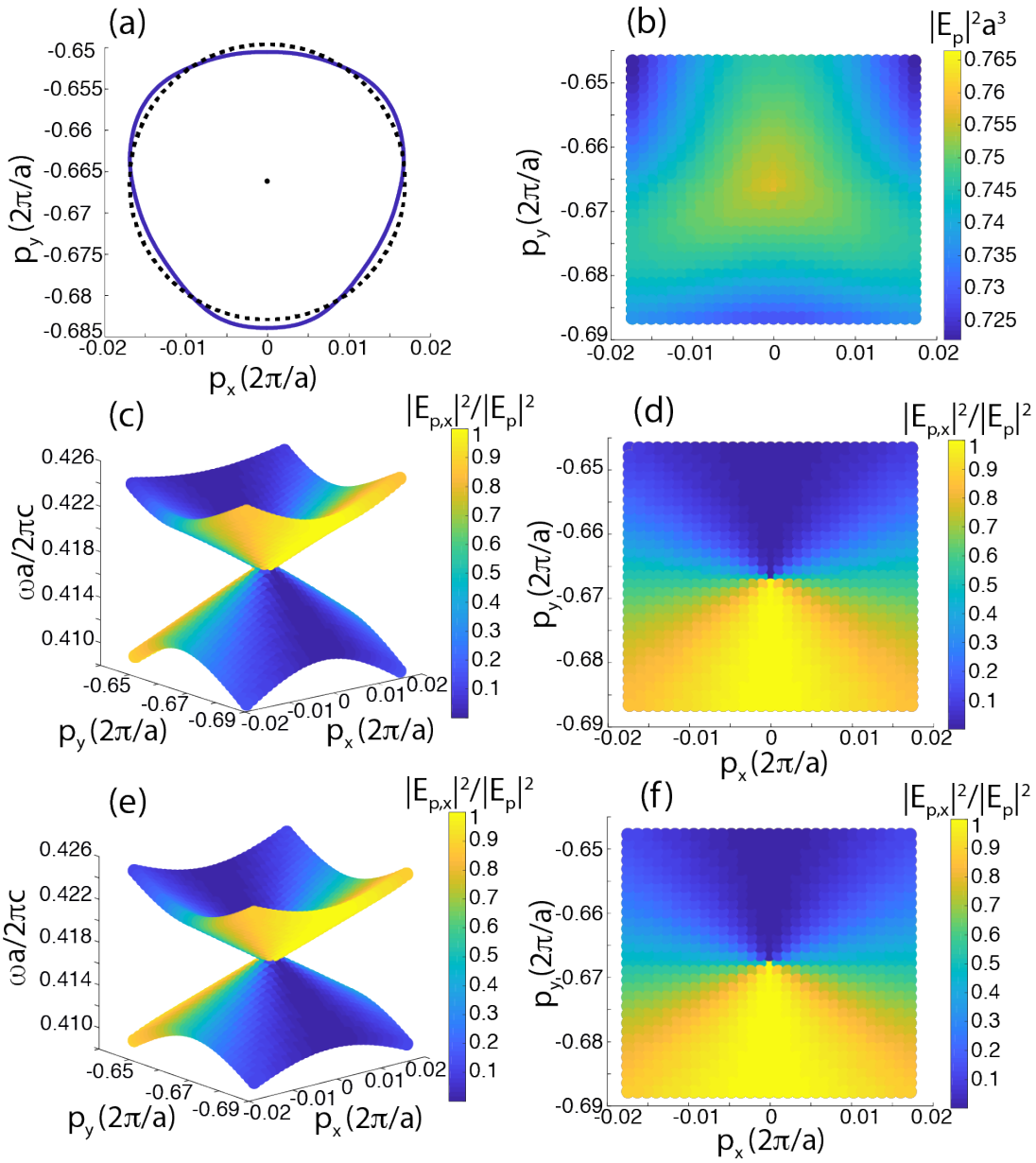

Figure 5-3: (a) Cross section of the Dirac cone for $\omega a/2\pi c = 0.422$. Numerical results are shown in solid blue, analytic prediction is shown in dashed black. (b) Field intensity $|\mathbf{E_p}(\mathbf{0})|^2 a^3$ in the top band near the Dirac cone. All values fall in a small interval of $[0.725, 0.765]$. (c) Numerically obtained results for the Dirac bands. Color code shows the x-component of the field $|E_{\mathbf{p},x}(\mathbf{0})|^2/|\mathbf{E_p}(\mathbf{0})|^2$. (d) Same as (c), showing the top band from above. (e) & (f) Analytic approximation to the band dispersion and the polarization of the modes. Numerical results were obtained for a GaP structure with geometric parameters $h = 0.25a$, $r_s = 0.0833a$, $r_l = 0.15a$ and $l = 0.4a$, for which we obtain the values $\omega_{\text{Dirac}} a/2\pi c = 0.4172$ and $v_s = 0.3c$.

where

$$\Phi_{\mathbf{K}'}(p_x, p_y) = \arctan\left(\frac{p_y - p_{\mathbf{K}',y}}{p_x - p_{\mathbf{K}',x}}\right). \tag{5.7}$$

The simple analytic model descibed by Eqs. (5.2)-(5.7) shows that the electromagnetic environment of an emitter tuned close to the vertex of the Dirac cone is completely described by the parameters ω_{Dirac}, v_{s} and E_0, as long as the second band near the **M** symmetry point is energetically separated from the Dirac point (see Fig. 5-2), i.e. $\omega_{\mathbf{M}} > \omega_{\text{Dirac}}$. In Fig. 5-4 we plot these four numerical parameters as a function of the geometric parameters r_l, l and h. More specifically, we plot $\omega_{\mathbf{M}} - \omega_{\text{Dirac}}$ and v_{s} only as function of r_l and l, since we found that these quantities are largely insensitive to h. For the same reason, we plot $|E_0|^2$ and ω_{Dirac} only as a function of r_l and h, but not l.

Fig. 5-4(a) shows that $\omega_{\mathbf{M}} - \omega_{\text{Dirac}}$ initially increases with l, before decreasing in magnitude. Intuitively, once the holes reach the edges of the unit cell increasing l does not help any more. Instead, pushing the holes further out merges them together, reducing the volume of air holes. The figure also shows that $\omega_{\mathbf{M}} - \omega_{\text{Dirac}}$ can be increased by increasing the hole radius. Similarly, Fig. 5-4(b) shows that the slope of the Dirac cone v_{s} increases both with l (until the holes reach the edge of the unit cell) and the hole radius.

Fig. 5-4(c) shows that the electric filed intensity is largely insensitive to the hole radius, but varies inversely with h. This latter result makes intuitive sense – increasing the thickness of the slab expands the mode volume and, therefore, decreases the field concentration at the location of the emitters. Finally, Fig. 5-4(d) shows that ω_{Dirac} is inversely proportional to h and increases with hole radius. These results are simple consequences of the fact that increasing the relative volume of the dielectric inside the unit cell increases the effective refractive index of the medium and thus rescales all relevant length scales of the system, including the effective wavelength.

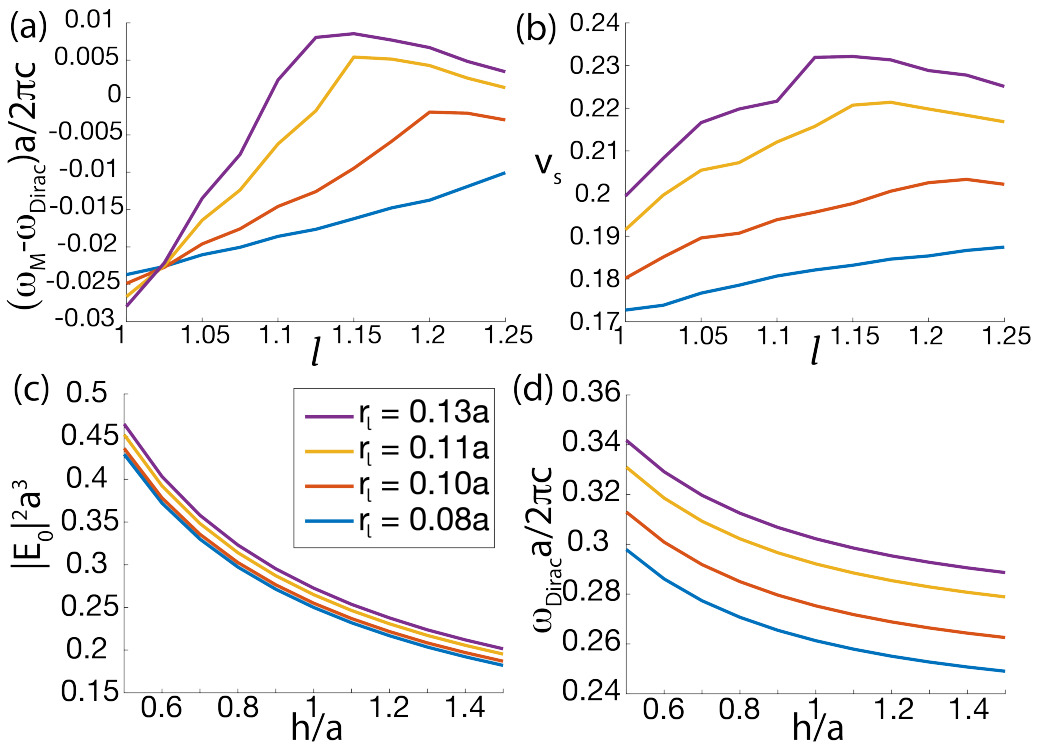

Figure 5-4: (a) The detuning $\omega_{\mathbf{M}} - \omega_{\text{Dirac}}$ as a function of r_l and l, the radius and radial displacement of the central holes. Slab height is $h = 1.13a$. (b) The slope constant v_s as a function of r_l and l for $h = 1.13a$. (c) The electric field strength $|E_0|^2$ as a function of r_l and the slab thickness h for $l = 0.4a$. (d) The frequency of the Dirac point ω_{Dirac} as a function of r_l and h for $l = 0.4a$. The inset of (c) provides the color-coded legend for the curves with different hole radii.

5.4 Calculation of the Green's function

In quantum optics, single atom decay rates and cooperative effects such as the dipole-dipole interaction and cooperative decay of atoms can be fully determined from the dyadic Green's function of the problem when the Born-Markov approximation holds [84, 172, 193, 195, 196]. In particular, the overall spontaneous decay rate of an atom can be expressed as

$$\Gamma = \frac{2d^2\omega_A^2}{\hbar\varepsilon_0 c^2}\text{Im}\{G_{\alpha\alpha}(\mathbf{0})\}, \tag{5.8}$$

where d is the transition dipole moment of the atom, ε_0 is the electric permittivity in vacuum, $\alpha = x, y, z$ and the Green's function is evaluated at the location of the

emitter ($\mathbf{r} = \mathbf{0}$). Similarly, the dipole-dipole interaction and cooperative decay rate between two atoms at a distance $\mathbf{r}$ apart are given by

$$\delta\omega_{\text{coop}}(\mathbf{r}) = \frac{d^2\omega_A^2}{\hbar\varepsilon_0 c^2}\text{Re}\{G_{\alpha\beta}(\mathbf{r})\}, \tag{5.9}$$

and

$$\Gamma_{\text{coop}}(\mathbf{r}) = \frac{2d^2\omega_A^2}{\hbar\varepsilon_0 c^2}\text{Im}\{G_{\alpha\beta}(\mathbf{r})\}, \tag{5.10}$$

respectively, where the first atom is assumed to be in its α-polarized excited state and the second atom is in its β-polarized state ($\alpha, \beta = x, y, z$). Note that the single-excitation atomic dynamics can be fully determined in terms of Γ, $\delta\omega_{\text{coop}}$ and Γ_{coop}, when the Born-Markov approximation is valid (see Ref. [193] for discussion of the case when these approximations break down). In this section we will derive an analytic approximation for the dyadic Green's function.

Before proceeding, we note that since the z-component of the TE-like modes of the slab is zero at the location of the emitters (see Section 5.2), the $|\pi\rangle$ states of the emitter do not couple to the the guided modes and thus

$$G_{zz} = G_{xz} = G_{zx} = G_{yz} = G_{zy} = 0. \tag{5.11}$$

Therefore, we will focus our attention on the x- and y-polarized states of the emitters and derive the Green's function for these states.

We start by expessing the momentum-space Green's function as a summation over the electric field eigenfunctions of the geometry (see Chapter 2)

$$g_{\alpha\beta}(\mathbf{p}) = \mathcal{A}c^2 \sum_n \frac{E^{(n)*}_{\mathbf{p},\alpha}(\mathbf{r}_1)\, E^{(n)}_{\mathbf{p},\beta}(\mathbf{r}_2)}{\omega_A^2 - \left(\omega^{(n)}_{\mathbf{p}}\right)^2}, \tag{5.12}$$

where $\mathcal{A} = \sqrt{3}/2a^2$ is the area of the hexagonal unit cell, $E^{(n)}_{\mathbf{p},\alpha}(\mathbf{r})$ denotes the α component ($\alpha = x, y$) of the electric field of the photonic crystal mode in the n^{th} band for quasi-momentum $\mathbf{p}$ at location $\mathbf{r}$, $\omega^{(n)}_{\mathbf{p}}$ is the corresponding frequency of

the mode and the summation runs over all bands. In the expression above $\mathbf{r}_1$ is the position of the emitter and $\mathbf{r}_2$ is the position where the Green's function is evaluated (e.g. the location of the second atom).

In order to find the Green's function in real space, it is necessary to integrate Eq. (5.12) across the entire irreducible Brillouin zone

$$G_{\alpha\beta}(\mathbf{r}_2) = \int_{\mathrm{BZ}} \frac{d^2\mathbf{p}}{(2\pi)^2} g_{\alpha\beta}(\mathbf{p}). \tag{5.13}$$

To perform this integral, we need to make a number of approximations.

First, note that given to the periodicity of the photonic crystal, the electric field eigenmodes can be expressed in the following Bloch form

$$E^{(n)}_{\mathbf{p},\alpha}(\mathbf{r}) = \frac{u^{(n)}_{\mathbf{p},\alpha}(\mathbf{r})}{\sqrt{a^3}} e^{\mathrm{i}\mathbf{p}\cdot\mathbf{r}}, \tag{5.14}$$

where $\mathbf{u}^{(n)}_{\mathbf{p}}(\mathbf{r}+\mathbf{R}) = \mathbf{u}^{(n)}_{\mathbf{p}}(\mathbf{r})$ is a periodic and dimensionless function and $\mathbf{R} = n\,\mathbf{a}_+ + m\,\mathbf{a}_-$ is any valid lattice vector of the triangular lattice, where $n, m \in \mathbb{Z}$ and $\mathbf{a}_\pm$ are defined in Eq. (5.1). The eigenmodes are normalized such that

$$\int_{\mathcal{V}} d^3\mathbf{r}\; \varepsilon(\mathbf{r})\, \mathbf{E}^{(n)}_{\mathbf{p}}(\mathbf{r}) \cdot \mathbf{E}^{(n)*}_{\mathbf{p}'}(\mathbf{r}) = \delta_{\mathbf{p}\mathbf{p}'}, \tag{5.15}$$

where $\varepsilon(\mathbf{r}+\mathbf{R}) = \varepsilon(\mathbf{r})$ describes the periodic dielectric permittivity of the photonic crystal in real space and the integral is performed over the quantization volume $\mathcal{V}$ [97, 196]. We also assume that $\mathbf{r}_2 = \mathbf{r}_1 + \mathbf{R}$, which allows us to write

$$E^{(n)*}_{\mathbf{p},\alpha}(\mathbf{r}_1)\, E^{(n)}_{\mathbf{p},\beta}(\mathbf{r}_2) = \frac{u^{(n)*}_{\mathbf{p},\alpha}(\mathbf{r}_1)\, u^{(n)}_{\mathbf{p},\beta}(\mathbf{r}_1)}{a^3} e^{i\mathbf{p}\cdot\mathbf{r}_{12}}, \tag{5.16}$$

where we have defined $\mathbf{r}_{12} = \mathbf{r}_1 - \mathbf{r}_2$. In addition, recall our assumption that $\omega_{\mathrm{Dirac}} - \omega_A \ll \omega_A$, which ensures that only the bands of the two inequivalent Dirac cones at $\mathbf{K}$ and $\mathbf{K}'$ contribute to the integral. Therefore, we can make the approximation

$$\omega_A^2 - (\omega^{(n)}_{\mathbf{p}})^2 \approx 2\omega_A(\omega_A - \omega^{(n)}_{\mathbf{p}}). \tag{5.17}$$

Finally, we assume that $\mathbf{r}_1$ (and hence $\mathbf{r}_2$) is positioned at the center of the unit cell, where Eqs. (5.3)-(5.7) are valid.

With these assumptions, the integral Eq. (5.13) can be evaluated in a closed form (see Appendix D) and we obtain

$$\begin{aligned}
G_{xx}(r,\phi) &= \sin\phi\, P^{-}(\mathbf{r}) H_1^{(2)}(r/\xi) \\
&\quad -iP^{+}(\mathbf{r}) H_0^{(2)}(r/\xi), && (5.18)\\
G_{yy}(r,\phi) &= -\sin\phi\, P^{-}(\mathbf{r}) H_1^{(2)}(r/\xi) \\
&\quad -iP^{+}(\mathbf{r}) H_0^{(2)}(r/\xi), && (5.19)\\
G_{xy}(r,\phi) &= \cos\phi\, P^{-}(\mathbf{r}) H_1^{(2)}(r/\xi), && (5.20)\\
G_{yx}(r,\phi) &= G_{xy}(r,\phi), && (5.21)
\end{aligned}$$

where $\mathbf{r} = r(\cos\phi, \sin\phi)$, $H_m^{(2)}$ denotes the Hankel function of the second kind of order m, $\xi = v_\mathrm{s}/\delta_A$ and $\delta_A = \omega_\mathrm{Dirac} - \omega_A$. The prefactors are given by

$$P^{\pm}(\mathbf{r}) = \frac{\mathcal{A}c^2|E_0|^2\delta_A}{8\omega_A v_\mathrm{s}^2}\left(e^{i\mathbf{p}_\mathbf{K}\cdot\mathbf{r}} \pm e^{i\mathbf{p}_{\mathbf{K}'}\cdot\mathbf{r}}\right). \tag{5.22}$$

Note that this Green's function expression is only valid when the position of the source ($\mathbf{r}_1$) is at the center of the unit cell of the photonic crystal and the Green's function is sampled at a position that is a lattice vector away ($\mathbf{r}_1 = \mathbf{r}_2 + \mathbf{R}$).

It is instructive to reexpress the Green's function in a circularly polarized basis using $|\sigma_\pm\rangle = \mp(|x\rangle \pm i|y\rangle)/\sqrt{2}$, which yields

$$\begin{aligned}
G_{\sigma_+\sigma_+}(\mathbf{r}) &= -P^{+}(\mathbf{r}) H_0^{(2)}(r/\xi), && (5.23)\\
G_{\sigma_-\sigma_-}(\mathbf{r}) &= -P^{+}(\mathbf{r}) H_0^{(2)}(r/\xi), && (5.24)\\
G_{\sigma_+\sigma_-}(\mathbf{r}) &= e^{i\phi} P^{-}(\mathbf{r}) H_1^{(2)}(r/\xi), && (5.25)\\
G_{\sigma_-\sigma_+}(\mathbf{r}) &= -e^{-i\phi} P^{-}(\mathbf{r}) H_1^{(2)}(r/\xi). && (5.26)
\end{aligned}$$

Note the presence of the *winding phases* $e^{\pm i\phi}$ in the off-diagonal terms [39, 40, 131]. These phases are of particular importance, as they give rise to chiral interactions and

topological behavior when emitters interact through the photonic Dirac cone. The topological properties of a two-dimensional lattice of emitters embedded in a photonic crystal are discussed in more detail in Chapter 6.

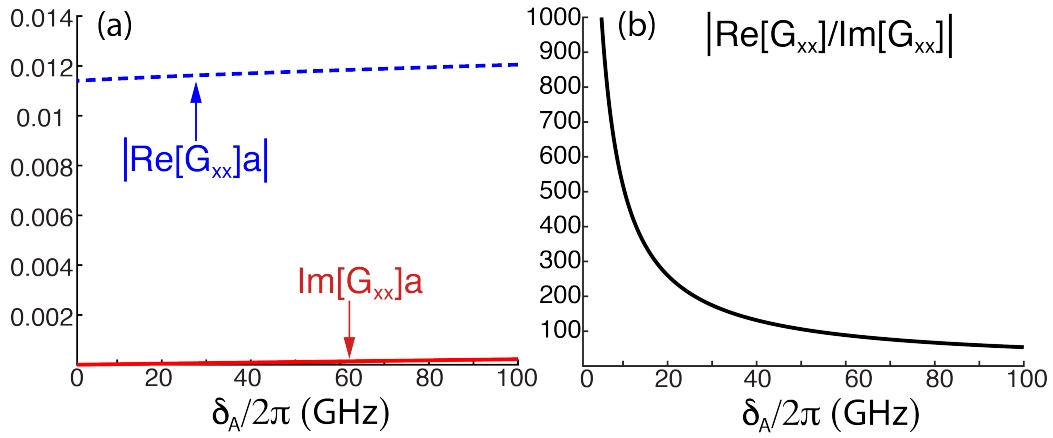

Figure 5-5: (a) Real and imaginary parts of the Green's function as a function of the detuning, δ_A, corresponding to the coherent and dissipative parts of the dipolar interaction, respectively. The dissipative part goes to zero at the Dirac point. (b) Ratio of the coherent and dissipative interactions as a function of the detuning, δ_A. The Green's function is evaluated 5 lattice sites away from the dipole source along the axis aligned with the $\mathbf{a}_+$ lattice vector. The transition wavelength of the atoms is assumed to be $\lambda = 738$nm and the Green's function parameters are $|E_0|^2/a^3 = 0.75$ and $v_s = 0.3c$.

5.5 Analysis of the dipolar interaction

In this section we analyze the dipolar interaction mediated by the photonic Dirac cone between atoms.

Recently, the dipolar interaction mediated by a photonic Dirac cone between atoms was studied in Ref. [193] using a tight-binding model. It was shown that the emerging atomic interactions are purely coherent, with negligible dissipative terms, and have a long range without exponential attenuation. This stands in sharp contrast with previous results in structured reservoirs, where dissipative terms could only be suppressed at the cost of making the interaction decay exponentially with distance [81, 93, 172]. As an application of our formalism, we now study the emergence of long-range coherent interactions, when all polarization effects are included, and then

provide expressions for the asymptotic behavior of the dipolar interaction as a function of distance.

Fig. 5-5(a) shows the real and imaginary parts of the Green's function (Eqs. (5.18)–(5.21)), corresponding to the coherent dipole-dipole interaction (Eq. (5.9)) and dissipative cooperative decay (Eq. (5.10)), as a function of the detuning δ_A. The two interacting atoms are assumed to be x-polarized and 5 lattice sites away. The dissipative part of the interaction goes to zero as the atomic frequencies become resonant with the Dirac point, whereas the coherent part remains finite. Fig. 5-5(b) shows the ratio of the coherent and dissipative parts of the interaction as a function of δ_A. Close to the Dirac point, the dipole-dipole interaction can be several orders of magnitude larger than the cooperative decay. Thus the interaction between atoms is almost completely coherent. Note that as $\delta_A \to 0$, the Born-Markov approximation eventually breaks down and the simple description of the dipolar interaction via the dyadic Green's function becomes invalid (see Ref. [193] and Chapter 6).

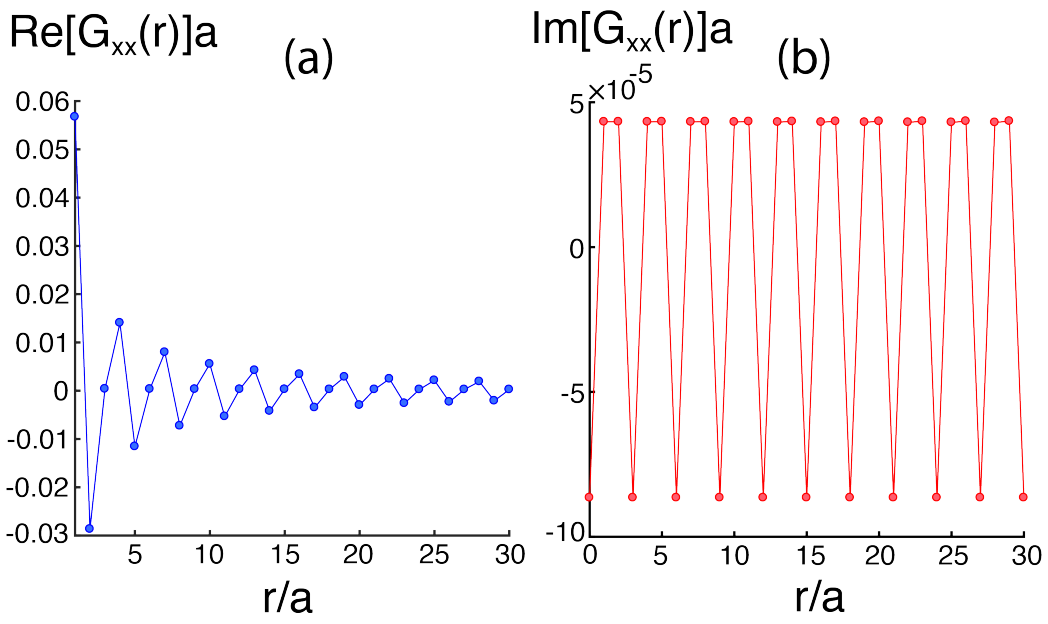

Figure 5-6: (a) Dipole-dipole interaction (Re$[G_{xx}(r)]$) and (b) cooperative decay (Im$[G_{xx}(r)]$) as a function of distance between two x-polarized atoms. The transition wavelength of the atoms is assumed to be $\lambda = 738$nm, the detuning is $\delta_A = 19.5$GHz, and the Green's function parameters used are $|E_0|^2/a^3 = 0.75$ and $v_s = 0.3c$.

In Fig. **??** we plot, as a function of distance, the real and imaginary parts of the

Green's function, which correspond to the dipole-dipole interaction and cooperative decay between two x-polarized atoms, respectively (see Eqs. (**??**)-(**??**)). The dipole-dipole interaction initially decreases rapidly away from the source, before transitioning to a slowly decaying oscillatory regime. Note that in Fig. **??**(b), the imaginary part of the Green's function is non-zero at the source, which corresponds to the decay rate of the x-polarized excited state into the modes of the slab (see Eq. (**??**)).

We obtain the asymptotic analytic behavior of the interaction, by re-expressing the Hankel functions of the Green's function in terms of Bessel functions as

$$H_m^{(2)}(x) = J_m(x) - iY_m(x), \tag{5.27}$$

and observing that for $x \gg 1$ to leading order we get

$$J_m(x) \sim \frac{1}{\sqrt{x}} \quad \text{and} \quad Y_m(x) \sim \frac{1}{\sqrt{x}}. \tag{5.28}$$

Thus, both the diagonal and off-diagonal terms of the Green's function fall off as $\sim 1/\sqrt{r}$ with distance. For completeness, we also note that when $x \ll 1$, we obtain $J_m(x) \sim 1$, $Y_0(x) \sim \ln(x)$ and $Y_1(x) \sim 1/x$.

These results confirm that the photonic Dirac cone mediates long-range coherent interactions between emitters without exponential attenuation. Such long-range coherent interactions are of significant importance in quantum information processing, as they can be utilized to entangle [81, 193, 196] and perform deterministic phase gates between distant atomic qubits [84]. Long-range coherent interactions are also advantageous for engineering nearly flat bands in topological quantum optical systems, which have important applications in exploring exotic many-body phases (see Chapter 6).

5.6 Conclusion

In conclusion, we have developed an analytic formalism to describe dipole radiation near a realistic two-dimensional photonic crystal slab with a photonic Dirac cone. We

derived a closed-form dyadic Green's function and showed that it mediates interactions that feature winding phases, which are key ingredients for engineering topology in photonic systems. As an example, we studied the long-range coherent interactions mediated by the Dirac cone between emitters, which have important applications in quantum information processing. We believe that these results will enable further, rigorous studies of the behavior of atomic emitters interacting via photonic Dirac cones.

Chapter 6

Topological Quantum Optics in Two-dimensional Photonic Crystals

6.1 Introduction

Since their discovery in electronic systems [12, 15, 157], topological phenomena have been explored in a variety of systems, including microwave [22–27], photonic [28–31], acoustic [32–34], mechanical [35–37], and cold atom environments [18, 21]. While such systems can exhibit reflection-free excitation transport on system edges, even in the presence of imperfections, they are generally robust only with respect to certain types of disorder [7, 33, 197]. This is in contrast to electronic systems with time-reversal symmetry breaking that are robust to arbitrary perturbations [158, 159]. In addition, the linear acoustic, microwave or photonic systems generally lack the interactions between constituent particles required to obtain exotic states of matter such as the fractional quantum Hall effect [198]. Recently, there has been significant interest in combining photonic systems with non-linear quantum emitters to realize robust topological phenomena at optical frequencies [114, 131, 199] and to study strongly-correlated states of light and matter [93, 172, 200–203]. While the coupling of a single quantum emitter to a topological photonic interface was recently demonstrated [186], development of a truly robust, many-body platform for topological quantum optics remains an outstanding challenge. Furthermore, strongly correlated systems

must be based on topological bands with negligible dispersion relative to the energy scale of the interactions, which typically requires careful fine-tuning of the system parameters that is difficult to realize in practice [39, 160, 204–207]. Realization of robust topological systems in the optical domain is especially interesting in light of potential applications to quantum networking [208].

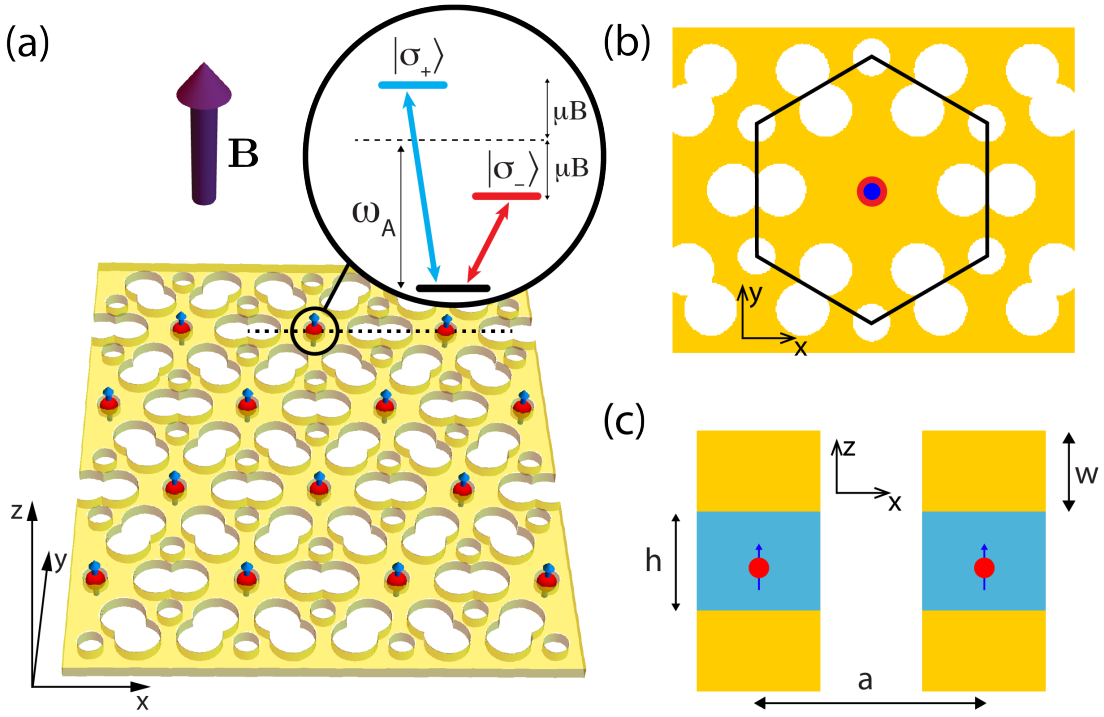

Figure 6-1: (a) Schematic depiction of the photonic crystal slab with air holes and the embedded triangular emitter array. Emitter spacing is $a = 240$nm, transition wavelength is $\lambda = 738$nm. Out-of-plane B-field splits the $|\sigma_+\rangle$ and $|\sigma_-\rangle$ atomic transitions. (b) Unit cell of the photonic crystal (black lines). The emitter is embedded at the center. The diameters of small and large holes are $d_\mathrm{s} = 40$nm and $d_\mathrm{l} = 56$nm, respectively. The large holes are centered $R = 96$nm away from the emitter. (c) Cross section of the photonic structure along the dotted line indicated in (a). The SiVs are embedded in a diamond ($n_\mathrm{d} = 2.4$) layer of thickness $h = 120$nm, which is surrounded on both sides by GaP ($n_\mathrm{GaP} = 3.25$) layers of thickness $w = 75$nm.

In this Chapter, we propose a novel, experimentally realistic nanophotonic platform integrated with quantum emitters, which gives rise to topological states at optical frequencies. In particular, we consider a two-dimensional atomic emitter array integrated with a two dimensional photonic crystal slab, where the emitter spacing is comparable to the wavelength. We show that in the presence of an out-of-plane mag-

netic field, the hybridization of the atomic levels and the photonic modes of the slab lead to energy bands with non-trivial Chern numbers and large band gaps. One of the bands is almost completely flat, making it a strong candidate for the realization of fractional Chern insulators. We demonstrate that topological edge states form on the system boundary that are robust to imperfections in the lattice and inhomogeneous broadening of the emitters.

6.2 Physical system

Fig. 6-1(a) provides a schematic depiction of the physical system. A triangular lattice of quantum emitters with spacing $a = \lambda/3$ is embedded in a two-dimensional photonic crystal (PhC) slab of air holes. Each atomic emitter has two optical transitions with wavelength λ between the ground state $|g\rangle$ and the two excited states $|\sigma_+\rangle$ and $|\sigma_-\rangle$ and is surrounded by a cavity-like hole structure. The emitters interact primarily via the guided modes of the slab. A uniform out-of-plane magnetic field Zeeman-splits the excited states of each emitter. The resulting hybridized polaritonic bands feature non-trivial Chern numbers and one of the topological bands is almost completely flat (Fig. 6-2(b)). In addition, a large energy gap is formed between the bands, which is two orders of magnitude larger than the gap in free space for comparable emitter spacings [114, 199]. Inside the gap topological edge states appear, which are protected by the large gap from scattering into extended bulk states or the guided modes of the slab and have a large group velocity. Thus these modes carry energy around the system boundary rapidly with minimal losses even in the presence of lattice imperfections and inhomogeneous emitter broadening. Note that this topological quantum optical system is significantly more accessible experimentally than topological atomic lattices in free space, which require deeply subwavelength interatomic spacing [114, 131, 199].

For concreteness, we now focus on the hybrid PhC structure illustrated in Fig. 6-1. The hexagonal unit cell of the PhC slab made of gallium phosphate (GaP) with air holes is shown in Fig. 6-1(b). Each atomic emitter is placed at the geometric center of

the unit cell, forming a periodic triangular lattice. In addition, the emitters are placed in the middle of the slab (in the $z = 0$ mirror plane) to ensure that they only couple to TE-like guided modes [41]. Such an arrangement can be achieved for different kinds of quantum emitters by introducing slight modifications to the PhC structure. One option is to create quantum dots directly into the dielectric slab [124, 186, 209–212]. Another option is to create an additional hole at the center of the cell and trap a neutral atom in the $z = 0$ plane using a combination of far-off resonance optical trapping, vacuum forces and side illumination [172] (see also Refs. [213–218]). Alternatively, atom-like color defects in diamond such as Silicon Vacancy (SiV) color centers can be integrated with the photonic structure [120, 219, 220], by using a thin diamond layer sandwiched between two layers of GaP as shown in Fig. 6-1(c).

The TE-like guided bands of the slab near the emitter frequency are shown in Fig. 6-2(a) (see Appendix E.1 for details of the calculation). The colors of the bands indicate the normalized field strength $|\mathbf{E}_{\mathbf{k}}(\mathbf{r}_A)|^2 a^3$ at the location of the emitter inside the unit cell, where $\mathbf{E}_{\mathbf{k}}(\mathbf{r})$ denotes the classical field solutions of Maxwell's equations for Bloch quasi-momentum $\mathbf{k}$ [41, 97, 196]. This photonic structure was specifically designed to ensure that there are no other guided modes within a few THz energy range just below the tip of the Dirac cone. Such a photonic spectrum is a general feature of PhC slabs with the cavity-like hole structure shown in Fig. 6-1(b) and can be achieved for a wide range of geometric and material parameters (see Chapter 5). The thickness of the layers and the size and spacing of the holes of the diamond-GaP structure are chosen such that the tip of the Dirac cone ω_{Dirac} is tuned within a few hundred GHz of $\omega_A = 2\pi c/\lambda$, the transition frequency of the SiV emitters ($\lambda = 738$nm). Thus the emitters interact primarily through the guided modes of the Dirac cone.

6.3 Hamiltonian

The dynamics of the embedded emitters (no-jump evolution in the master equation) in the presence of a magnetic field can be described by the following non-Hermitian

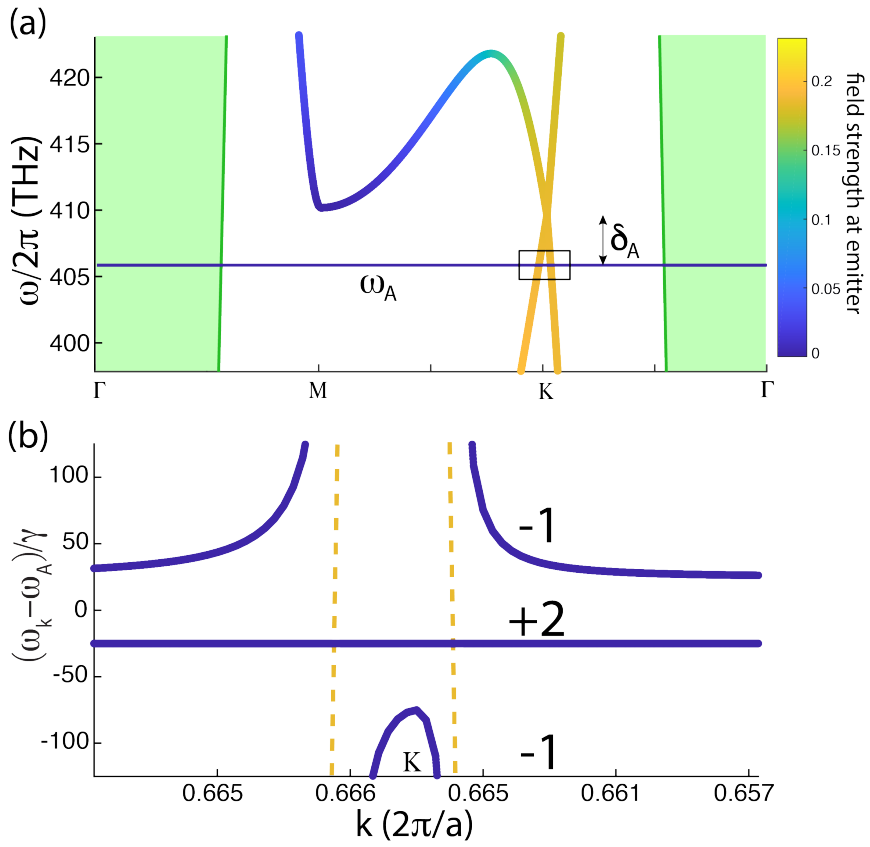

Figure 6-2: (a) TE-like photonic band structure of the slab in the vicinity of the SiV transition frequency ω_A. The light cone region is shaded green. The tip of the Dirac cone is detuned by $\delta_A = 3.74$THz from ω_A. Band colors reflect the normalized field strength $|\mathbf{E}_\mathbf{k}(\mathbf{r}_A)|^2 a^3$ at the location of the emitters. (b) Hybrid atomic-photonic bands in the presence of an out-of-plane B-field ($\mu B = 25\gamma$) in the immediate vicinity of the **K** point (see black box in (a)) for a detuning of $\delta_A = 0.321$THz. Yellow dashed lines indicate the bare photonic bands. One atomic band does not interact with the slab modes and remains flat. The other atomic band interacts with the photonic modes and avoided crossings arise. Chern numbers of the bands are indicated by black numbers.

Hamiltonian [109–112, 114, 199]

$$H = \hbar \sum_{i=1}^{N} \sum_{\alpha=\sigma_+,\sigma_-} \left(\omega_A + \mathrm{sgn}(\alpha_i)\mu B - \mathrm{i}\frac{\Gamma}{2}\right) |\alpha_i\rangle\langle\alpha_i| + \frac{3\pi\gamma\hbar c}{\omega_A n_\mathrm{d}} \sum_{i\neq j} \sum_{\alpha,\beta=\sigma_+,\sigma_-} G_{\alpha\beta}(\mathbf{r}_i - \mathbf{r}_j)|\alpha_i\rangle\langle\beta_j|, \tag{6.1}$$

where N is the number of atoms, we define $\mathrm{sgn}(\sigma_\pm) = \pm$, μB is the Zeeman-shift of the emitters with magnetic moment μ due to the magnetic field $\mathbf{B} = B\hat{z}$, γ is the emission rate of SiVs in bulk diamond, c is the speed of light and n_d is the refractive index of diamond. The dipolar spin-spin interaction of emitters is described by the dyadic Green's function $G_{\alpha\beta}(\mathbf{r})$ and $\mathbf{r}_i$ denotes the position of the i^{th} atom. The irreversible decay rate of individual emitters inside the slab is given by $\Gamma = \Gamma_{\mathrm{PC}} + \Gamma_0$, where Γ_{PC} and Γ_0 account for the coupling of the emitters to the guided slab modes and free-space modes, respectively. In general, $\Gamma_0 \ll \gamma$ due to total internal reflection at the surfaces of the patterned slab [124]. Thus, for now we neglect coupling to free-space modes. (The effect of coupling to free-space photons is discussed in detail in Appendix E.4)

6.4 Green's function of the photonic crystal

The dipolar coupling mediated by the photonic Dirac cone is described by the following Green's function (see Chapter 5)

$$\mathbf{G}(\mathbf{r}) = \begin{bmatrix} -P^+(\mathbf{r})H_0^{(2)}(r/\xi) & e^{\mathrm{i}\phi}P^-(\mathbf{r})H_1^{(2)}(r/\xi) \\ -e^{-\mathrm{i}\phi}P^-(\mathbf{r})H_1^{(2)}(r/\xi) & -P^+(\mathbf{r})H_0^{(2)}(r/\xi) \end{bmatrix}, \tag{6.2}$$

where $\mathbf{r} = r(\cos\phi, \sin\phi)$ is the position vector, the diagonal (off-diagonal) terms of $\mathbf{G}$ account for the coupling between atomic transitions of the same (opposite) circular polarization, $H_m^{(2)}$ denotes the Hankel function of the second kind of order m and $\xi = v_\mathrm{s}/\delta_A$ gives the length scale of the interaction as a function of the linear dispersion of the slab modes at the Dirac cone v_s and the atomic detuning from the tip of the Dirac cone $\delta_A = \omega_{\mathrm{Dirac}} - \omega_A$. The prefactors are given by

$$P^\pm(\mathbf{r}) = \mathrm{i}\frac{\mathcal{A}c^2|E_0|^2\delta_A}{8\omega_A v_\mathrm{s}^2}\left(e^{\mathrm{i}\mathbf{p_K}\cdot\mathbf{r}} \pm e^{\mathrm{i}\mathbf{p_{K'}}\cdot\mathbf{r}}\right), \tag{6.3}$$

where $\mathcal{A} = \sqrt{3}/2a^2$ is the area of the hexagonal unit cell, $|E_0|^2 = |\mathbf{E_k}(\mathbf{r}_A)|^2$ is the electric field intensity in the vicinity of the Dirac cone, which is approximately **k**-

independent, and $\mathbf{p_K}$ and $\mathbf{p_{K'}}$ are the quasi-momenta associated with the two inequivalent $\mathbf{K}$ points in the Brillouin zone. The parameters v_s and E_0 are obtained numerically (see Chapter 5). This analytic Green's function quantitatively captures the slab-mediated dipolar interaction, when δ_A is small. Note the presence of the winding phases $e^{\pm \mathrm{i}\phi}$ [39, 40, 131] in the off-diagonal terms of $\mathbf{G}$, which give rise to the topological properties of the system. These winding phases arise from the propagation-direction-dependent polarization structure of the photonic modes of the Dirac cone (see Chapter 5).

6.5 Photonic band structure

The single excitation eigenmodes of Eq. (6.1) are Bloch modes of the form

$$|\psi_\mathbf{k}\rangle = \sum_n e^{\mathrm{i}\mathbf{k}\cdot\mathbf{R}_n}\Big[c_{+,\mathbf{k}}|\sigma_{+,n}\rangle + c_{-,\mathbf{k}}|\sigma_{-,n}\rangle\Big], \tag{6.4}$$

where the summation runs over all lattice vectors $\{\mathbf{R}_n\}$ and $\mathbf{k}$ is the Bloch quasi-momentum. For each $\mathbf{k}$, there are two eigenvalues $\omega_\mathbf{k}$ that can be numerically calculated from the photonic band structure shown in Fig. 6-2(a) (see Appendix E.1). Fig. 6-2(b) shows the hybridized atomic-photonic bands in the immediate vicinity of the $\mathbf{K}$ symmetry point in the presence of an out-of-plane magnetic field. The bare photonic bands of the Dirac cone are also shown schematically as yellow dashed lines for reference. One of the atomic bands does not interact with the guided slab modes due to polarization mismatch, forming a flat band in the middle. The other atomic band hybridizes with the guided modes, forming avoided crossings that split the band into two disjoint parts. Two equal band gaps form just above and below the middle band and the three bands have Chern numbers -1, +2 and -1, respectively.

The size of the band gap Δ between topological bands is of particular importance, since the topological protection of the system (e.g. the robustness of edge states to defects) increases with gap size. Since the gap arises from the Zeeman-splitting of the atomic levels [199], the gap size is a linear function of the applied magnetic field

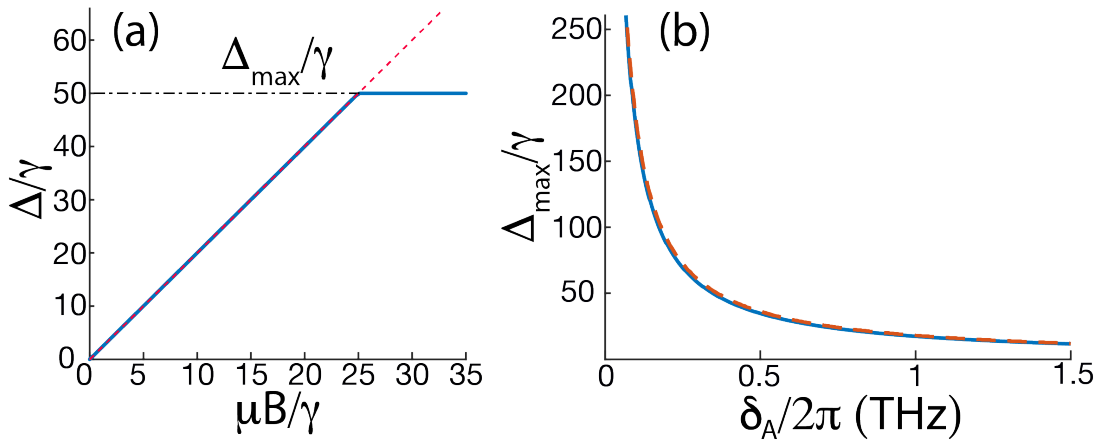

Figure 6-3: (a) Gap size scales linearly with B-field ($\Delta = 2\mu B$) until a plateau is reached at $\Delta_{\max}$ (blue line). (b) Maximum gap size $\Delta_{\max}$ as a function of the detuning $\delta_A = \omega_{\text{Dirac}} - \omega_A$ (blue line). The dashed red line is a $\sim 1/\delta_A$ fit.

(Fig. 6-3(a)), until a plateau is reached at $\Delta_{\max}$ when the middle band completely flattens. The maximum achievable gap size $\Delta_{\max}$ is plotted in Fig. 6-3(b) as a function of δ_A. As the tip of the photonic Dirac cone is tuned closer to the atomic frequency, the energy gap increases as $\sim 1/\delta_A$. Ultimately, the gap size is limited by the fact that our quantum optical model (which relies on the accuracy of the Markov approximation near the Dirac cone [193]) is only valid as long as the emitter-field correlation time τ_c is much shorter than the typical timescale on which the atomic system evolves τ_A. Here, the correlation time is set by the time it takes for a photon to leave the emitter array of size L (i.e. $\tau_c \sim L/v_s$), while the relevant time scale for the system evolution is set by the band gap ($\tau_A \sim \Delta^{-1}$) (Appendix E.2). As δ_A is reduced, the density of photonic states at the Dirac cone decreases linearly. Thus, the number of emitters in the array has to be increased as $\sim 1/\delta_A$ to maintain the density of states and the characteristic behavior of the system. Once the system size L becomes comparable to $v_s\,\Delta^{-1}$, the model breaks down. Assuming $\gamma/2\pi = 300$MHz for the bulk emission rate for SiVs [221], we find that this occurs around $\Delta \sim 250\gamma$ (Appendix E.2). Note that the accessible gap sizes in this system are two orders of magnitude larger than those that can be obtained in free space for similar emitter spacings [114, 199].

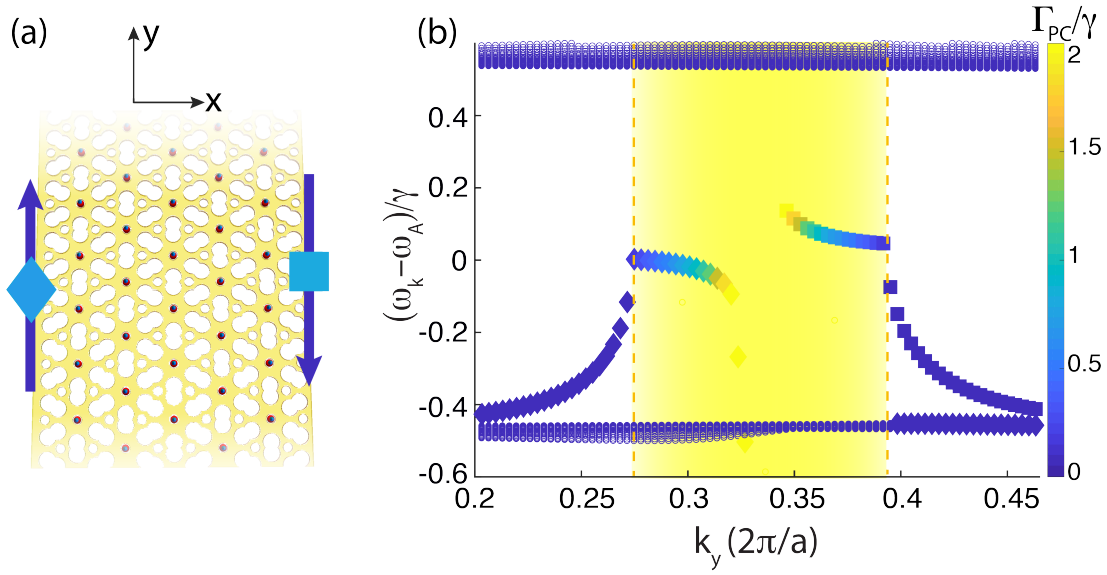

Figure 6-4: (a) An infinite stripe of emitters embedded in an extended photonic crystal slab. (b) Edge states inside the band gap near the **K** point. Unidirectional edge states on the left (right) boundary are indicated by diamonds (squares). The bulk modes are marked by dots, forming the two nearly flat bands near the top and bottom. Yellow shading and yellow dashed lines mark the region where bands can decay into resonant slab modes. Color coding shows the decay rate $\Gamma_{\rm PC}$. Relevant parameters are δ_A=18.73THz, $v_s = 0.25c$, $|E_0|^2 = 0.1855/a^3$, $\Delta = \gamma$ and $\mu B = 0.5\gamma$. Results were obtained for a stripe with 41 atoms in the transverse direction. States that have 5 times more overall amplitude on the five leftmost emitter columns than on the five rightmost columns, are classified as edge states.

6.6 Topological edge states

We next explore the topological edge states of the system. We consider a stripe of emitters, embedded in an extended PhC, that is infinite along the y-axis, but finite along the x-axis as shown in Fig. E-6(a). Fig. E-6(b) shows the unidirectional edge states inside the gap near the **K** point[1]. These states are confined to the system boundaries and carry energy only in a single direction, reflecting the broken time-reversal symmetry and the topological protection of the system [22–24, 114, 158, 159, 199]. Edge states on the left side of the stripe are marked with triangles, whereas edge states on the right side are marked with squares. The quasi-momentum region where the guided modes of the Dirac cone are resonant with the emitters is shaded

[1]Note that all edge state calculations are performed for a small gap size (i.e. large δ_A) to ensure sufficient density of states even for limited lattice sizes.

yellow and its boundaries are marked by yellow dashed lines (see yellow dashed lines in Fig. 6-2(b) for reference). In this region the emitters can directly couple to guided slab modes with decay rate Γ_{PC}, the magnitude of which is indicated in the figure by the color code. Modes that fall outside the yellow region cannot couple to slab modes due to the momentum mismatch, making these modes long-lived. Note that a different edge termination with slightly different edge state properties is obtained when the triangular lattice is rotated $\pi/6$ relative to the one shown in Fig. E-6(a) (see Appendix E.3 for more details).

Next, we study the time evolution of edge states in real space. Fig. 6-5(a) shows a defect-free triangular lattice of emitters with a hexagonal shape. The emitters are embedded in an extended PhC, whose spatial dimensions are much larger than those of the atomic lattice, such that Eq. (6.2) remains valid and can be directly substituted into Eq. (6.1) to obtain the Hamiltonian. We assume that one emitter on the edge is addressed by a weak laser with frequency ω_L that is resonant with the edge states in the lower half of the gap. The laser couples to the σ_+ and σ_- transitions with equal strength Ω, such that $\Omega \ll \Delta$. We calculate the time evolution of the wavefunction of the initial state by numerically exponentiating Eq. (6.1) [114]. The evolved state of the system is shown in Fig. 6-5(a), where the color of each site reflects the excitation probability of the emitter. The edge states excited by the laser carry energy only in the clock-wise direction, reflecting the broken time-reversal symmetry of the system. Coupling to bulk modes is strongly suppressed. Furthermore, the excitation routes around the lattice corners without reflection or significant loss into the guided modes of the slab.

The hallmark of topological edge states is their robustness to significant imperfections in the system. Fig. 6-5(b) shows a lattice, where a random 10% of the emitters is missing. Furthermore, we assume that the inhomogeneities in the nanophotonic environment (e.g. fabrication imperfections) give rise to the inhomogeneous broadening of emitters. Therefore, we sample the emitter frequencies from a Gaussian distribution, whose width is 10% of the gap. Fig. 6-5(b) shows a snapshot of the time-evolved state of the system. Despite the presence of the lattice defects and the inhomogeneity

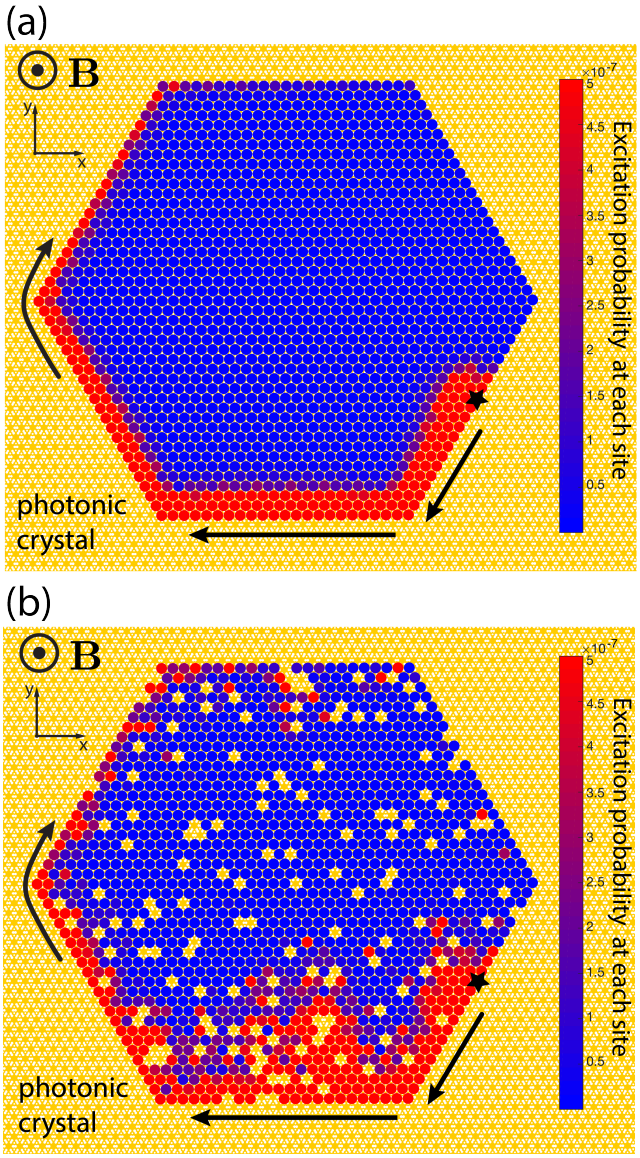

Figure 6-5: (a) Time-evolved state ($t = 161.5\gamma^{-1}$) of a hexagonal-shaped triangular lattice of emitters ($N = 1519$) embedded in an extended photonic crystal slab. An emitter at the edge (black star) is addressed by a laser (inset). The edge state propagates on the boundaries without reflection or significant decay into slab modes. The color code shows the excitation probability at each emitter. (b) Time-evolved state ($t = 297.5\gamma^{-1}$) state of the system ($N = 1380$) in the presence of imperfect lattice filling (90%) and inhomogeneous broadening, where the emitter frequencies are sampled from $P(\omega) = 1/\sqrt{2\pi\sigma^2}\exp(-(\omega-\omega_A)^2/(2\sigma^2))$, where $\sigma = 0.1\Delta$. Other relevant parameters are $\delta_A/2\pi = 18.73$THz, $v_s = 0.25c$, $|E_0|^2 = 0.1855/a^3$, $\Delta = \gamma$, $\mu B = 0.5\gamma$, $\Omega = 0.0059\gamma$ and $\omega_L = \omega_A - 0.37\gamma$. The laser drive is switched on adiabatically with the profile $\Omega(t) = \Omega\exp(-[t-t_0]^2/[2\Sigma^2])$, where $t_0 = 127.5\gamma^{-1}$ and $\Sigma = 23.3\gamma^{-1}$.

of emitters, the edge state propagates along the system edges, routing around all defects, including the cluster of missing emitters near the bottom edge. These results demonstrate the topological robustness of the edge states and the system as a whole.

6.7 Flat band and interactions

The flat middle band in Fig. 6-2(b) is another key feature of our topological system. The flatness of the band and the non-trivial Chern number are, in general, the two key ingredients for fractionalized topological phases in lattice models [39, 160, 175, 204–207, 222, 223]. Usually, such flat bands require careful tuning of the long-range hopping parameters. Here, away from the **K** point the band remains flat due to the fact that the guided photonic bands are far-detuned and coupling to them is weak (Fig. 6-2(a)). Near the **K** point, flatness arises from the combined effects of the uniform magnetic field and the fact that the middle band does not couple to the PhC bands due to polarization mismatch. The inherent non-linearity of the constituent emitters gives rise to a hard-core constraint for the bosonic excitations of the system, which provides a point-like interaction for the excitations. Such short-range interactions are ideal for the realization of interacting many-body topological phases [224]. Within such a system we expect non-trivial competition between states with strongly correlated topological phases and those that behave analogously to electronic charge density waves. This competition arises from the fact that the atoms interact primarily through the Dirac cone and, therefore, the Berry curvature is concentrated in the vicinity of the **K** points. Thus only states near the **K** points are expected to yield exotic topological many-body phases, whereas the rest of the band will likely contribute to states that resemble an ordered quantum fluid. Controlling the distribution of the Berry curvature in the flat band (e.g. using established techniques from cold atom experiments [225]) can be explored for engineering experimentally observable fractional topological phases.

While practical realization of the proposed systems constitutes a non-trivial challenge, most of the key ingredients have already been demonstrated recently. For

example, a hybrid system based on SiV color defects in diamond can be created by first fabricating a thin diamond slab [219, 226], SiVs can be implanted using focused ion beam implantation [227], while GaP can be positioned both sides of the slab [228] with the air-hole structure created by etching through the GaP and diamond layers. Alternatively, a PhC hole structure made entirely of diamond can potentially be used (see Appendix E.1 for more details).

6.8 Conclusion

In summary, we have demonstrated that two-dimensional quantum emitter arrays embedded in photonic crystals constitute a topological quantum optical system. The atomic bands have non-trivial Chern numbers in the presence of an out-of-plane magnetic field and the dispersion of one of the bands is significantly quenched. Long-lived topological edge states appear on the system boundaries, which are robust to imperfect lattice filling as well as to inhomogeneous broadening of the emitters. We believe that the experimental accessibility of this platform will open up exciting opportunities for exploring novel topological states of light and matter, including quantum optical analogues of fractional Chern insulators.

Chapter 7

Outlook

A natural extension of the work discussed in this thesis would be the study of topological quantum optics with multiple excitations and interactions. Interacting topological many-body physics gives rise to a wealth of remarkable phenomena, including the Fractional Quantum Hall effect [12] and anyonic excitations [4]. As noted in Chapter 1, anyonic excitations with non-Abelian statistics are key ingredients of theoretical proposals for topological quantum computing and could enable the implementation of large, fault-tolerant quantum computers.

However, finding and exploring non-Abelian anyons in Fractional Quantum Hall systems is a significant challenge in itself. Numerically studying such interacting systems is hard due to the limited system sizes that can be simulated using state-of-the-art computational resources [4]. At the same time, experimentally observing and characterizing quasi-particles with possibly non-Abelian statistics, such as those at $\nu = 5/2$ filling, is difficult in conventional solid-state systems due to the stringent requirements for high sample purity and low temperatures [229]. Therefore, it would be desirable to find alternative physical systems where the Fractional Quantum Hall effect can be studied with less demanding experimental requirements.

Given the experimental accessibility and wide tunability of parameters in quantum optical systems, finding analogues of the Fractional Quantum Hall effect in such systems would be of significant value. The presence of the flat band with a non-trivial Chern number in the photonic crystal system described in Chapter 6 makes

such a system a promising candidate for the exploration of quantum optical analogues of the Fractional Quantum Hall effect.

As discussed in Section 6.7, finding non-trivial topological many-body states requires a flat band with a reasonably uniform distribution of the Berry curvature across the Brillouin zone. In the system discussed in Chapter 6, the Berry curvature is tightly concentrated near the **K** symmetry points. Therefore, smearing out the Berry curvature across the Brillouin zone is of key importance for observing non-trivial interacting topological states. Conventional techniques that could achieve this include the shaking of the lattice, and applying electric or magnetic field gradients across the lattice to break translational invariance.

Appendix A

Appendices for Chapter 2

A.1 Derivation of a closed-form expression for the dipole-dipole interaction

In this section we show that the single-source Green function derived by Leonhardt [48, 53] for the 2D fish eye lens can be written as a sum over the eigenmodes of the lens (Eq. (2.7)). This result enables us to connect the Green's function to the expressions obtained for the atomic properties from the master equation treatment.

A.1.1 Green's function of the 2D fish eye

The single-source Green's function of Maxwell's 2D fish eye (of radius R_0, thickness b and refractive index profile $n(r) = \frac{2n_0}{1+(r/R_0)^2}$) is a solution of the following equation

$$\left(\partial_\alpha\partial_\nu - \delta_{\alpha\nu}\partial_\eta\partial_\eta\right) G_{\nu\beta}(\mathbf{r},\mathbf{r}',\omega_0) - \varepsilon(\mathbf{r})\,\frac{\omega_0^2}{c^2} G_{\alpha\beta}(\mathbf{r},\mathbf{r}',\omega_0) = \delta_{\alpha\beta}\delta(\mathbf{r}-\mathbf{r}'), \qquad \text{(A.1)}$$

where $\alpha,\beta,\mu,\nu = x,y,z$ and summation is implied over repeated indices and $\varepsilon(\mathbf{r}) = n(\mathbf{r})^2 = \left[2n_0/(1+(r/R_0)^2)\right]^2$ is the position-dependent electric permittivity. When b is chosen such that $\omega_0 \ll \pi c/b$, only the lowest TEM polarized mode of the fish eye can be excited and the electric field is invariant along the z-axis ($\partial_z\mathbf{E}(\mathbf{r}) = 0$). The explicit expression for the zz-components of the Green's function (Eq. (2.16)) is then

given by

$$G_{zz}(\mathbf{r}_1, \mathbf{r}_2, \omega) = F(\alpha_1, \alpha_2) - F(\alpha_1, 1/\alpha_2^*), \tag{A.2}$$

where

$$F(\alpha_1, \alpha_2) = -\frac{P_\nu(\xi(\alpha_1, \alpha_2))}{4b \sin(\pi\nu)}, \tag{A.3}$$

where P_ν is the Legendre function of (non-integer) oder ν,

$$\nu = \frac{1}{2}\left[\sqrt{4\frac{\omega^2}{c^2}R_0^2 n_0^2 + 1} - 1\right] \notin \mathbb{Z} \qquad \text{and} \qquad \xi(\alpha_1, \alpha_2) = \frac{|\zeta(\alpha_1, \alpha_2)|^2 - 1}{|\zeta(\alpha_1, \alpha_2)|^2 + 1}, \tag{A.4}$$

where

$$\zeta(\alpha_1, \alpha_2) = \frac{\alpha_1 - \alpha_2}{\alpha_1 \alpha_2^* + 1}, \qquad \text{and} \quad \alpha_j = \underbrace{\frac{r_j}{R_0}}_{\rho_j} e^{i\phi_j} \quad (j = 1, 2). \tag{A.5}$$

A.1.2 Virtual coordiantes

The stereographic transformation [49]

$$r_j \quad \mapsto \quad \frac{r_j^2 - R_0^2}{r_j^2 + R_0^2} = \frac{\rho_j^2 - 1}{\rho_j^2 + 1} \quad =: \quad \cos\theta_j, \tag{A.6}$$

can be used to map any point (r, ϕ) on the real plane to a point (θ, ϕ) on the surface of a virtual sphere (where ϕ is the same value in both coordinate systems). Using this transformation, we can simplify the definition of the Green's function

$$\begin{aligned}
\zeta(\alpha_1, \alpha_2) &= \frac{(\rho_1 \cos\phi_1 - \rho_2 \cos\phi_2) + i(\rho_1 \sin\phi_1 - \rho_2 \sin\phi_2)}{\rho_1\rho_2 \cos(\phi_1 - \phi_2) + 1 + i\rho_1\rho_2 \sin(\phi_1 - \phi_2)} \\
|\zeta(\alpha_1, \alpha_2)|^2 &= \frac{\rho_1^2 + \rho_2^2 - 2\rho_1\rho_2 \cos(\phi_1 - \phi_2)}{(\rho_1\rho_2)^1 + 1 + 2\rho_1\rho_2 \cos(\phi_1 - \phi_2)} \\
\xi(\alpha_1, \alpha_2) &= \frac{\rho_1^2 + \rho_2^2 - (\rho_1\rho_2)^2 - 1 - 4\rho_1\rho_2 \cos(\phi_1 - \phi_2)}{\rho_1^2 + \rho_2^2 + (\rho_1\rho_2)^2 + 1} = \\
&= -\left[\left(\frac{\rho_1^2 - 1}{\rho_1^2 + 1}\right)\left(\frac{\rho_2^2 - 1}{\rho_2^2 + 1}\right) + \left(\frac{2\rho_1}{\rho_1^2 + 1}\right)\left(\frac{2\rho_2}{\rho_2^2 + 1}\right)\cos(\phi_1 - \phi_2)\right] = \\
&= -\big[\cos\theta_1 \cos\theta_2 + \sin\theta_1 \sin\theta_2 \cos(\phi_1 - \phi_2)\big] = -\cos\theta_{12},
\end{aligned}$$

where θ_{12} is the spherical distance beetween two points, (θ_1, ϕ_1) and (θ_2, ϕ_2), on the surface of a unit sphere, since

$$\begin{aligned}\cos\theta_{12} = \mathbf{x}_1\mathbf{x}_2 &= \begin{bmatrix}\sin\theta_1\cos\phi_1\\ \sin\theta_1\sin\phi_1\\ \cos\theta_1\end{bmatrix}\cdot\begin{bmatrix}\sin\theta_2\cos\phi_2\\ \sin\theta_2\sin\phi_2\\ \cos\theta_2\end{bmatrix}\\ &= \cos\theta_1\cos\theta_2 + \sin\theta_1\sin\theta_2\cos(\phi_1-\phi_2). \qquad \text{(A.7)}\end{aligned}$$

Similarly,

$$\begin{aligned}\zeta(\alpha_1, 1/\alpha_2^*) &= \frac{(\rho_1\cos\phi_1 - \frac{1}{\rho_2}\cos\phi_2) + i(\rho_1\sin\phi_1 - \frac{1}{\rho_2}\sin\phi_2)}{\frac{\rho_1}{\rho_2}\cos(\phi_1-\phi_2) + 1 + i\frac{\rho_1}{\rho_2}\sin(\phi_1-\phi_2)},\\ |\zeta(\alpha_1, 1/\alpha_2^*)|^2 &= \frac{\rho_1^2 + \frac{1}{\rho_2^2} - 2\frac{\rho_1}{\rho_2}\cos(\phi_1-\phi_2)}{(\frac{\rho_1}{\rho_2})^1 + 1 + 2\frac{\rho_1}{\rho_2}\cos(\phi_1-\phi_2)},\\ \xi(\alpha_1, 1/\alpha_2^*) &= \frac{\rho_1^2 + \left(\frac{1}{\rho_2}\right)^2 - (\frac{\rho_1}{\rho_2})^2 - 1 - 4\frac{\rho_1}{\rho_2}\cos(\phi_1-\phi_2)}{\rho_1^2 + \left(\frac{1}{\rho_2}\right)^2 + (\frac{\rho_1}{\rho_2})^2 + 1} =\\ &= -\left[\left(\frac{\rho_1^2-1}{\rho_1^2+1}\right)\left(\frac{1-\rho_2^2}{\rho_2^2+1}\right) + \left(\frac{2\rho_1}{\rho_1^2+1}\right)\left(\frac{2\rho_2}{\rho_2^2+1}\right)\cos(\phi_1-\phi_2)\right] =\\ &= -\big[\cos\theta_1\cos(\pi-\theta_2) + \sin\theta_1\sin(\pi-\theta_2)\cos(\phi_1-\phi_2)\big] = -\cos\theta'_{12},\end{aligned}$$

where, now, θ'_{12} is the spherical distance between the points (θ_1, ϕ_1) and $(\pi-\theta_2, \phi_2)$.

Now, we can write the Green's function as

$$G_{zz}(\mathbf{r}_1, \mathbf{r}_2, \omega) = -\frac{P_\nu(-\cos\theta_{12}) - P_\nu(-\cos\theta'_{12})}{4b\sin(\pi\nu)}. \qquad \text{(A.8)}$$

A.1.3 Expansion in Spherical harmonics

Expansion with respect to l

The full set of Legendre polynomials, P_l, form a complete, orthogonal basis on the space of smooth $[-1, 1] \to \mathbb{R}$ functions. This allows us to expand the Legendre

function P_ν in terms of the Legendre polynomials P_l

$$P_\nu(x) = \sum_{l=0}^{\infty} c_l P_l(x), \qquad \text{where} \qquad c_l = \frac{2l+1}{2} \int_{-1}^{+1} dx\, P_l(x) P_\nu(x). \tag{A.9}$$

According to Abramowitz & Stegun, Section 8.14 [230]

$$\int_{-1}^{+1} dx\, P_\eta(x) P_\nu(x) = \frac{2}{\pi^2} \frac{2\sin(\pi\eta)\sin(\pi\nu)[\psi(\eta+1) - \psi(\nu+1)] + \pi\sin(\pi\nu - \pi\eta)}{(\nu-\eta)(\nu+\eta+1)},$$

where ψ is the digamma function and which expression, in case of $\eta = l \in \mathbb{N}$, simplifies to

$$\int_{-1}^{+1} dx\, P_l(x) P_\nu(x) = \frac{2}{\pi} \frac{(-1)^l \sin(\pi\nu)}{\nu(\nu+1) - l(l+1)}, \qquad \text{if} \quad l \in \mathbb{N}. \tag{A.10}$$

This means that

$$P_\nu(x) = \frac{\sin(\pi\nu)}{\pi} \sum_{l=0}^{\infty} (-1)^l \frac{2l+1}{\nu(\nu+1) - l(l+1)} P_l(x), \tag{A.11}$$

and we can write the Green's function as

$$G_{zz}(\mathbf{r}_1, \mathbf{r}_2, \omega) = -\frac{1}{4\pi b} \sum_{l=0}^{\infty} (-1)^l \frac{2l+1}{\nu(\nu+1) - l(l+1)} \big[P_l(-\cos\theta_{12}) - P_l(-\cos\theta'_{12})\big]. \tag{A.12}$$

Expansion with respect to m

According to the addition theorem of spherical harmonics,

$$P_l(\mathbf{x}_1 \cdot \mathbf{x}_2) = P_l(\cos\theta_{12}) = \frac{4\pi}{2l+1} \sum_{m=-l}^{+l} Y_l^{m*}(\theta_1, \phi_1) Y_l^m(\theta_2, \phi_2), \tag{A.13}$$

where the spherical harmonics are defined by

$$Y_l^m(\theta, \phi) = \sqrt{\frac{2l+1}{4\pi} \frac{(l-m)!}{(l+m)!}} P_l^m(\cos\theta) e^{im\phi}, \tag{A.14}$$

where P_l^m are the associated Legendre polynomials.

By using this theorem, and the property that $P_l(-x) = (-1)^l P_l(x)$, we can write

$$\begin{aligned}
P(-\cos\theta_{12}) &= (-1)^l \frac{4\pi}{2l+1} \sum_{m=-l}^{+l} Y_l^{m*}(\theta_1,\phi_1) Y_l^m(\theta_2,\phi_2), \\
P(-\cos\theta'_{12}) &= (-1)^l \frac{4\pi}{2l+1} \sum_{m=-l}^{+l} Y_l^{m*}(\theta_1,\phi_1) \underbrace{Y_l^m(\pi-\theta_2,\phi_2)}_{(-1)^{l-m}Y_l^m(\theta_2,\phi_2)}, \\
P(-\cos\theta_{12}) - P(-\cos\theta'_{12}) &= (-1)^l \frac{4\pi}{2l+1} \sum_{m=-l}^{+l} \Big[1-(-1)^{l-m}\Big] Y_l^{m*}(\theta_1,\phi_1) Y_l^m(\theta_2,\phi_2).
\end{aligned}$$

The expression inside the square brackets is zero if l and m have the same parity, and 2, if they have different parity. The set of m values for which the corresponding term is non-zero is $M_l = \{-(l-1), -(l-3), \ldots, (l-3), (l-1)\}$. Using this notation, we can write the Green's function as

$$G_{zz}(\mathbf{r}_1, \mathbf{r}_2, \omega) = -\frac{2}{b} \sum_{l=0}^{\infty} \sum_{m \in M_l} \frac{Y_l^{m*}(\theta_1,\phi_1) Y_l^m(\theta_2,\phi_2)}{\nu(\nu+1) - l(l+1)} \tag{A.15}$$

A.1.4 Expansion in cavity modes

Recall from Eq. (2.7) that the TEM eigenmodes of Maxwell's fish eye with radius R_0 and width b are

$$\begin{aligned}
f_{l,m}(\mathbf{r}) &= \sqrt{\frac{2}{bR_0^2 n_0^2}} \sqrt{\frac{2l+1}{4\pi} \frac{(l-m)!}{(l+m)!}} P_l^m\left(\frac{r^2-R_0^2}{r^2+R_0^2}\right) e^{im\phi} \\
&= \sqrt{\frac{2}{bR_0^2 n_0^2}} (-1)^m Y_l^m(\theta,\phi),
\end{aligned} \tag{A.16}$$

where r and ϕ are polar coordinates of $\mathbf{r}$ and $\cos\theta = \frac{r^2-R_0^2}{r^2+R_0^2}$. They satisfy the orthonormality condition,

$$\delta_{l,l'}\delta_{m,m'} = \int_0^{R_0} dr\, r \int_0^{2\pi} d\phi \int_0^b dz\, n^2(r) f_{l,m}^*(r,\phi) f_{l',m'}(r,\phi). \tag{A.17}$$

The corresponding (partially degenerate) eigenfrequencies are

$$\omega_{l,m} = \omega_l = \frac{c}{R_0 n_0}\sqrt{l(l+1)} =: ck_l. \tag{A.18}$$

Now, we can write the Green's function in Eq. (A.15) as

$$\begin{aligned} G_{zz}(\mathbf{r}_1, \mathbf{r}_2, \omega/c) &= -R_0^2 n_0^2 \sum_{l=0}^{\infty} \sum_{m\in M_l} \frac{f^*_{l,m}(\mathbf{r}_1) f_{l,m}(\mathbf{r}_2)}{\nu(\nu+1) - l(l+1)} \\ &= -\sum_{l=1}^{\infty} \sum_{m\in M_l} \frac{f^*_{l,m}(\mathbf{r}_1) f_{l,m}(\mathbf{r}_2)}{(\omega/c)^2 - k_l^2}, \end{aligned} \tag{A.19}$$

where we used the connection between ω_l and l, and ω and ν. Using Eq. (2.9), we can then write the dipole-dipole interaction within the fish eye in the following form

$$\delta\omega(\mathbf{r}_1, \mathbf{r}_2) = \frac{d_z^2\omega_0^2}{\hbar\varepsilon_0 c^2}\mathrm{Re}\{G_{zz}(\mathbf{r}_1, \mathbf{r}_2, \omega_0)\} = \frac{d_z^2\omega_0^2}{\hbar\varepsilon_0 c^2}\sum_{l=1}^{\infty}\sum_{m\in M_l}\frac{f^*_{l,m}(\mathbf{r}_1) f_{l,m}(\mathbf{r}_2)}{k_l^2 - (\omega_0/c)^2}. \tag{A.20}$$

We note that this decomposition of the Green's function in terms of the eigenmodes of the fish eye is a particular example of Fredholm's theorem [231].

A.1.5 Comparison with master equation results

Recall that the dipole-dipole interaction obtained from the master equation (see Eq. (2.15)) has the form

$$\delta\omega(\mathbf{r}_1, \mathbf{r}_2) = \frac{d_z^2}{\hbar\varepsilon_0}\sum_{l,m}\frac{\omega_l^2}{\omega_l^2 - \omega_0^2} f^*_{l,m}(\mathbf{r}_1) f_{l,m}(\mathbf{r}_2). \tag{A.21}$$

Making use of the transformation

$$\frac{\omega_l^2}{\omega_l^2 - \omega_0^2} = \left[1 + \frac{\omega_0^2}{\omega_l^2 - \omega_0^2}\right], \tag{A.22}$$

and the dipole-dipole interaction becomes

$$\delta\omega(\mathbf{r}_1,\mathbf{r}_2)=\frac{d_z^2}{\hbar\varepsilon_0}\left[\sum_{l,m}f_{l,m}(\mathbf{r}_1)f_{l,m}(\mathbf{r}_2)+\omega_0^2\sum_{l,m}\frac{f^*_{l,m}(\mathbf{r}_1)f_{l,m}(\mathbf{r}_2)}{\omega_l^2-\omega_0^2}\right]. \tag{A.23}$$

Since the modes $f_{l,m}$ form a complete basis, i.e.

$$\sum_{l,m}f^*_{l,m}(\mathbf{r}_1)f_{l,m}(\mathbf{r}_2)=\delta^{(3)}(\mathbf{r}_1-\mathbf{r}_2), \tag{A.24}$$

the first term inside the square brackets does not contribute if $\mathbf{r}_1\neq\mathbf{r}_2$, thus

$$\delta\omega(\mathbf{r}_1,\mathbf{r}_2)=\frac{d^2}{\hbar\varepsilon_0}\frac{\omega_0^2}{c^2}\sum_{l,m}\frac{f^*_{l,m}(\mathbf{r}_1)f_{l,m}(\mathbf{r}_2)}{k_l^2-(\omega_0/c)^2},\qquad\text{if}\quad\mathbf{r}_1\neq\mathbf{r}_2, \tag{A.25}$$

which is identical to Eq. (A.20). This shows that the right-hand side of Eq. (2.15) can indeed be replaced by Eq. (2.9) and Eq. (2.16).

More generally, using Eq. (A.22) and Eq. (A.24) we can express Eq. (A.19) in the form

$$\frac{d^2}{\hbar\varepsilon_0}\frac{\omega_0^2}{c^2}G_{zz}(\mathbf{r}_1,\mathbf{r}_2,\omega_0)=\frac{d^2}{2\hbar\varepsilon_0}\sum_{l,m}\omega_l f^*_{l,m}(\mathbf{r}_1)f_{l,m}(\mathbf{r}_2)\left(\frac{1}{\omega_0+\omega_l}-\frac{1}{\omega_0-\omega_l}\right), \tag{A.26}$$

from which it is straighforward to show that

$$\begin{aligned}\frac{d^2}{\hbar\varepsilon_0}\frac{(\omega_0+i\kappa)^2}{c^2}G_{zz}(\mathbf{r}_1,\mathbf{r}_2,\omega_0+i\kappa)=\frac{d^2}{2\hbar\varepsilon_0}\sum_{l,m}\omega_l\, f^*_{l,m}(\mathbf{r}_1)f_{l,m}(\mathbf{r}_2)\Bigg\{&\frac{(\omega_l+\omega_0)}{\kappa^2+(\omega_l+\omega_0)^2}\\&+\frac{(\omega_l-\omega_0)}{\kappa^2+(\omega_l-\omega_0)^2}-i\left(\frac{\kappa}{\kappa^2+(\omega_l+\omega_0)^2}-\frac{\kappa}{\kappa^2+(\omega_l-\omega_0)^2}\right)\Bigg\},\end{aligned} \tag{A.27}$$

which allows us to express the decay rates Eq. (2.24) and the dipole-dipole interaction (Eq. (2.25)) in the following closed form

$$\Gamma(\mathbf{r}_i,\mathbf{r}_j)=\frac{2d_z^2}{\hbar\varepsilon_0c^2}\mathrm{Im}\{(\omega_0+i\kappa)^2G_{zz}(\mathbf{r}_i,\mathbf{r}_j,\omega_0+i\kappa)\}. \tag{A.28}$$

and

$$\delta\omega(\mathbf{r}_i,\mathbf{r}_j)=\frac{d_z^2}{\hbar\varepsilon_0 c^2}\mathrm{Re}\{(\omega+i\kappa)^2 G_{zz}(\mathbf{r}_i,\mathbf{r}_j,\omega_0+i\kappa)\}. \tag{A.29}$$

We note that $G_{zz}(\mathbf{r}_i,\mathbf{r}_j,\omega_0+i\kappa)$ is the solution of the following equation

$$\begin{aligned}(\partial_\alpha\partial_\nu-\delta_{\alpha\nu}\partial_\eta\partial_\eta)\,G_{\nu\beta}(\mathbf{r},\mathbf{r}',\omega_0+i\kappa)&\\ -\frac{n(\mathbf{r})^2\,(\omega_0+i\kappa)^2}{c^2}G_{\alpha\beta}(\mathbf{r},\mathbf{r}',\omega_0+i\kappa)&=\delta_{\alpha\beta}\delta(\mathbf{r}-\mathbf{r}'),\end{aligned} \tag{A.30}$$

which can be thought of as the dyadic equation for the fish eye lens with the complex refractive index $\tilde{n}(\mathbf{r})=n(\mathbf{r})(1+i\kappa/\omega_0)$, since

$$n(\mathbf{r})^2(\omega_0+i\kappa)^2=n(\mathbf{r})^2(1+i\kappa/\omega_0)^2\omega_0^2=\tilde{n}(\mathbf{r})^2\omega_0^2. \tag{A.31}$$

Noting that for $\kappa\ll\omega_0$ the following approximations hold

$$\begin{aligned}\Gamma(\mathbf{r}_i,\mathbf{r}_j)&\approx\frac{2d_z^2\omega_0^2}{\hbar\varepsilon_0 c^2}\mathrm{Im}\{G_{zz}(\mathbf{r}_i,\mathbf{r}_j,\omega_0+i\kappa)\}\\ \delta\omega(\mathbf{r}_i,\mathbf{r}_j)&\approx\frac{d_z^2\omega_0^2}{\hbar\varepsilon_0 c^2}\mathrm{Re}\{G_{zz}(\mathbf{r}_i,\mathbf{r}_j,\omega_0+i\kappa)\},\end{aligned} \tag{A.32}$$

we find that photon loss from the modes of the fish eye of the form of Eq. (2.21) can simply be modeled with the complex refractive index profile $\tilde{n}(\mathbf{r})$.

A.2 Numerical Solution of the Schrödinger Equation

In this Appendix we describe an efficient way to numerically solve the Schrödinger Equation while including the two atoms and the modes of the fish eye in the dynamics.

A.2.1 Hamiltonian

Electric dipole interaction of a single atom

Recall that the electric dipole coupling of a single atom, placed at $\mathbf{r}_i$, to the electromagnetic field modes of the fish eye is given by

$$V = -\mathbf{d}_i \cdot \mathbf{E}(\mathbf{r}_i), \quad \text{where} \quad \mathbf{d}_i = d_z \hat{z}\big(\sigma_i^\dagger + \sigma_i\big), \qquad \text{where} \quad \sigma_i = |g_i\rangle\langle e_i|, \tag{A.33}$$

where d_z is the magnitude of the transition dipole moment between the two states of the atom $|e_i\rangle$ and $|g_i\rangle$, whose energy difference is $\hbar\omega_0$. Substituting Eq. (2.3) into Eq. (A.33) and neglecting the counter-rotating terms in V, we arrive at

$$V_{RWA} = \sum_{l,m} id\sqrt{\frac{\hbar\omega_l}{bR_0^2\varepsilon_0}}\big[a_{l,m}\sigma^\dagger Y_{l,m}(\theta,\phi) - a_{l,m}^\dagger \sigma Y_{l,m}(\theta,\phi)\big], \tag{A.34}$$

where $n_0 = 1$ was assumed.

Two atoms

Assuming that there are two identical atoms positioned at $\mathbf{r}_1$ and at $\mathbf{r}_2$, the interaction term takes the form $V_{RWA}(\mathbf{r}_1) + V_{RWA}(\mathbf{r}_2)$. The total Hamiltonian then becomes

$$\begin{aligned} H &= \hbar\omega_0\sigma_1^\dagger\sigma_1 + \hbar\omega_0\sigma_2^\dagger\sigma_2 + \sum_{l,m}\hbar\omega_l a_{l,m}^\dagger a_{l,m} \\ &+ \sum_l \hbar g_l\left[\sigma_1^\dagger\sum_m a_{l,m}Y_{l,m}(\theta_1,\phi_1) + \sigma_2^\dagger\sum_m a_{l,m}Y_{l,m}(\theta_2,\phi_2)\right] + \text{h.c.}, \end{aligned} \tag{A.35}$$

where $g_l = \frac{id_z}{\sqrt{\hbar b R_0^2\varepsilon_0}}\sqrt{\omega_l}$.

The diagonal terms $\hbar\omega_0\left(\sigma_1^\dagger\sigma_1 + \sigma_2^\dagger\sigma_2 + \sum_{l,m} a_{l,m}^\dagger a_{l,m}\right)$, simply give a constant energy shift to all eigenvectors in the subspace of interest and can, therefore, be sub-

tracted from the Hamiltonian. The modified Hamiltonian then takes the form

$$\begin{aligned} H/\hbar &= \sum_l \delta_l \sum_m a^\dagger_{l,m} a_{l,m} \\ &+ \sum_l g_l \left[\sigma_1^\dagger \sum_m a_{l,m} Y_{l,m}(\theta_1, \phi_1) + \sigma_2^\dagger \sum_m a_{l,m} Y_{l,m}(\theta_2, \phi_2) \right] + \text{h.c.}, \end{aligned} \tag{A.36}$$

where $\delta_l = \omega_l - \omega_0$.

Opposite positions

If the two atoms are placed at opposite positions ($\theta = \theta_1 = \theta_2$ and $\phi = \phi_1 = -\phi_2$), then we can write the interaction part of H as

$$V/\hbar = \sum_l g_l \sum_m \left[\sigma_1^\dagger a_{l,m} y_{l,m} + \sigma_2^\dagger a_{l,m} (-1)^m y_{l,m} + \text{h.c.} \right], \tag{A.37}$$

where $y_{l,m} = Y_{l,m}(\theta, \phi)$. Here we used that $Y_{l,m}(\theta, -\phi) = (-1)^m Y_{l,m}(\theta, \phi)$. Since the summation of m goes over $m = -l+1, -l+3, \ldots l-3, l-1$, m and l always have opposite parity, and we can pull out $(-1)^m = (-1)^{l+1}$ from the summation, giving

$$V/\hbar = \sum_l g_l \left[\sigma_1^\dagger + (-1)^{l+1} \sigma_2^\dagger \right] \sum_m a_{l,m} y_{l,m} + \text{h.c.} \tag{A.38}$$

We define an incomplete set of new modes,

$$A_l = \frac{\sum_m a_{l,m} y_{l,m}}{N_l}, \qquad N_l^2 = \sum_m |y_{l,m}|^2, \quad [A_l, A_l^\dagger] = 1. \tag{A.39}$$

The normalization factor can be calculated as follows.

$$\sum_{m \in M} |Y_{l,m}(\theta, \phi)|^2 = \sum_{m=-l}^{+l} \frac{1 - (-1)^{l-m}}{2} |Y_{l,m}(\theta, \phi)|^2, \tag{A.40}$$

$$M = \{-l+1, -l+3, \ldots l-3, l-1\}. \tag{A.41}$$

Recall the sum rule:

$$\sum_{m=-l}^{+l} Y^*_{l,m}(\theta_1,\phi_1)Y_{l,m}(\theta_2,\phi_2) = \frac{2l+1}{4\pi}P_l(\cos\theta_{12}), \tag{A.42}$$

where θ_{12} is the angle between point 1 and 2 on the unit sphere, and P_l is the lth Legendre polynomial. We use Eq. (A.42) to evaluate the two series:

$$\begin{aligned}
\sum_{m=-l}^{+l} |Y_{l,m}(\theta,\phi)|^2 &= \frac{2l+1}{4\pi}P_l(1) = \frac{2l+1}{4\pi}, &\text{(A.43)}\\
\sum_{m=-l}^{+l} (-1)^{l-m}|Y_{l,m}(\theta,\phi)|^2 &= \sum_{m=-l}^{+l} Y^*_{l,m}(\pi-\theta,\phi)Y_{l,m}(\theta,\phi)\\
&= \frac{2l+1}{4\pi}P_l\big(\cos(\pi-2\theta)\big), &\text{(A.44)}
\end{aligned}$$

where we used that $(-1)^{l-m}Y_{l,m}(\theta,\phi) = Y_{l,m}(\pi-\theta,\phi)$ and that the angle between point (θ,ϕ) and point $(\pi-\theta,\phi)$ is $\theta_{12} = \pi - 2\theta$.

Using these new A_l modes, the interaction can be written as

$$V/\hbar = \sum_l g_l N_l \left[\sigma_1^\dagger + (-1)^{l+1}\sigma_2^\dagger\right] A_l + \text{h.c.} \tag{A.45}$$

Modes A_l with different l parity couple to different combination of the two atoms. Let us define

$$\sigma_o = \frac{\sigma_1+\sigma_2}{\sqrt{2}}, \qquad \sigma_e = \frac{\sigma_1-\sigma_2}{\sqrt{2}}, \tag{A.46}$$

and write

$$V/\hbar = \sum_{l\in\text{odd}} G_l(A_l\sigma_o^\dagger + A_l^\dagger\sigma_o) + \sum_{l\in\text{even}} G_l(A_l\sigma_e^\dagger + A_l^\dagger\sigma_e), \tag{A.47}$$

where

$$G_l = \sqrt{2}g_l N_l = \sqrt{\frac{d_z^2 c}{\hbar b R_0^3 \varepsilon_0}}\sqrt{\frac{(2l+1)\sqrt{l(l+1)}}{4\pi}\big[1 - P_l(\cos(\pi-2\theta))\big]}. \tag{A.48}$$

A.2.2 Numerical analysis

Hilbert space

We are interested in the dynamics of a single excitation, i.e. we truncate the Hilbert space to

$$\mathcal{H} = \mathrm{Span}\Big\{ \underbrace{|e\rangle|g\rangle|\mathrm{vac}\rangle}_{|a\rangle},\ \underbrace{|g\rangle|e\rangle|\mathrm{vac}\rangle}_{|b\rangle},\ \{\underbrace{|g\rangle|g\rangle A_l^\dagger|\mathrm{vac}\rangle}_{|l\rangle}\ :\ l = 1, 2, \ldots l_{\max}\}\Big\}, \tag{A.49}$$

and separate it into two subspaces

$$\mathcal{H}_o = \mathrm{Span}\Big\{ \underbrace{\sigma_o^\dagger|g\rangle|g\rangle|\mathrm{vac}\rangle}_{|o\rangle},\ \{\underbrace{A_l^\dagger|g\rangle|g\rangle|\mathrm{vac}\rangle}_{|l\rangle}\ :\ l = 1, 3, 5, \ldots\}\Big\} \tag{A.50}$$

$$\mathcal{H}_e = \mathrm{Span}\Big\{ \underbrace{\sigma_e^\dagger|g\rangle|g\rangle|\mathrm{vac}\rangle}_{|e\rangle},\ \{\underbrace{A_l^\dagger|g\rangle|g\rangle|\mathrm{vac}\rangle}_{|l\rangle}\ :\ l = 2, 4, 6, \ldots\}\Big\}, \tag{A.51}$$

each of which is governed by its own Hamiltonian block.

Hamiltonian

The following H_o, H_e act as two independent blocks on $\mathcal{H}_o$ and $\mathcal{H}_e$.

$$\begin{aligned} H_o &= \sum_{l\in\mathrm{odd}} \Big[\delta_l A_l^\dagger A_l + G_l(A_l\sigma_o^\dagger + A_l^\dagger\sigma_o)\Big] \\ &= \sum_{l\in\mathrm{odd}} \big[\delta_l|l\rangle\langle l| + G_l(|o\rangle\langle l| + |l\rangle\langle o|)\big] \qquad \text{(A.52)} \\ H_e &= \sum_{l\in\mathrm{even}} \Big[\delta_l A_l^\dagger A_l + G_l(A_l\sigma_e^\dagger + A_l^\dagger\sigma_e)\Big] \\ &= \sum_{l\in\mathrm{even}} \big[\delta_l|l\rangle\langle l| + G_l(|e\rangle\langle l| + |l\rangle\langle e|)\big], \qquad \text{(A.53)} \end{aligned}$$

where

$$\delta_l = \frac{c}{R_0}\left[\sqrt{l(l+1)} - \sqrt{l_0(l_0+1)}\right], \tag{A.54}$$

where l_0 stands for the atomic frequency, i.e. $\omega_0 = \frac{c}{R_0}\sqrt{l_0(l_0+1)}$ and

$$G_l = \sqrt{\frac{d_z^2 c}{\hbar b R_0^3 \varepsilon_0}}\sqrt{\frac{(2l+1)\sqrt{l(l+1)}}{4\pi}\big[1 - P_l(\cos(\pi - 2\theta))\big]}. \quad \text{(A.55)}$$

Results: Time series

We start the system from $|\psi(0)\rangle = |e\rangle|g\rangle|\text{vac}\rangle = |a\rangle = \frac{|o\rangle+|e\rangle}{\sqrt{2}}$, evolve it with $U(t) = \exp[-iHt/\hbar]$, to get

$$\begin{aligned} |\psi(t)\rangle &= \frac{1}{\sqrt{2}}\big[e^{-iH_o t/\hbar}|o\rangle + e^{-iH_e t/\hbar}|e\rangle\big] \\ &= \frac{1}{\sqrt{2}}\big[\sum_j \langle\phi_{o,j}|o\rangle e^{-i\Omega_{o,j}t}|\phi_{o,j}\rangle + \sum_k \langle\phi_{e,k}|e\rangle e^{-i\Omega_{e,k}t}|\phi_{e,k}\rangle\big], \end{aligned} \quad \text{(A.56)}$$

where $\Omega_{o,j}$, $|\phi_{o,j}\rangle$ and $\Omega_{e,k}$, $|\phi_{e,k}\rangle$ are eigenvalues and eigenstates of $H_o/\hbar$ and $H_e/\hbar$, respectively.

Finally, we note that the numerical results shown in Fig. 2-5 are independent of the atomic parameters and the thickness of the lens as only ratios of the dipole-dipole interaction, spontaneous decay and cooperative decay are considered (each of which is proportional to the square of the prefactor $\sqrt{d_z^2 c/\hbar b R_0^3 \epsilon_0}$).

Appendix B

Appendices for Chapter 3

B.1 Green's function expressions

In free space the permittivity is $\varepsilon = 1$ and Eq. (3.14) can be solved using Fourier techniques to obtain the following momentum-space representation of the dyadic Green's function [151]

$$G_{0,\alpha\beta}(\mathbf{r}) = \int \frac{d^3\mathbf{p}}{(2\pi)^3} e^{i\mathbf{p}\cdot\mathbf{r}} \frac{1}{k^2} \frac{k^2\delta_{\alpha\beta} - p_\alpha p_\beta}{k^2 - p^2}, \tag{B.1}$$

where $\mathbf{p} = p_x\hat{x} + p_y\hat{y} + p_z\hat{z}$, $p = |\mathbf{p}|$ and $k = \omega/c$. Eq. (3.14) also has a closed-form solution in position space [151] given by

$$G_{0,\alpha\beta}(\mathbf{r}) = -\left(\frac{1}{k^2}\partial_\alpha\partial_\beta + \delta_{\alpha\beta}\right)\frac{e^{ikr}}{4\pi r}. \tag{B.2}$$

After evaluating the derivatives [232, 233], we obtain the following Green's function components [104, 149]

$$\begin{aligned} G_{0,\alpha\beta}(\mathbf{r}) = -\frac{e^{ikr}}{4\pi r}\Bigg[&\left(1 + \frac{i}{kr} - \frac{1}{(kr)^2}\right)\delta_{\alpha\beta} \\ &+\left(-1 - \frac{3i}{kr} + \frac{3}{(kr)^2}\right)\frac{x_\alpha x_\beta}{r^2}\Bigg] + \frac{\delta_{\alpha\beta}\delta^{(3)}(\mathbf{r})}{3k^2}. \end{aligned} \tag{B.3}$$

B.2 Green's function regularization

We regularize the Green's function by inserting a Gaussian momentum cut-off of the form [109]

$$\tilde{\mathcal{R}}(a_{\rm ho}, \mathbf{p}) = e^{-a_{\rm ho}^2 p^2/2} \tag{B.4}$$

into the Fourier integral of the Green's function (Eq. B.1), which yields

$$G^*_{0,\alpha\beta}(\mathbf{r}) = \int \frac{d^3\mathbf{p}}{(2\pi)^3} e^{i\mathbf{p}\cdot\mathbf{r}} \frac{k^2\delta_{\alpha\beta} - p_\alpha p_\beta}{k^2(k^2-p^2)} e^{-a_{\rm ho}^2 p^2/2}. \tag{B.5}$$

The momentum cut-off removes the high-frequency contributions that are associated with momenta $p \gg 1/a_{\rm ho}$. Eq. (B.5) is a convolution between the Green's function and the momentum cut-off and, therefore, by the convolution theorem we obtain

$$G^*_{0,\alpha\beta}(\mathbf{r}) = \int d^3\mathbf{q}\; G_{0,\alpha\beta}(\mathbf{r}-\mathbf{q})\mathcal{R}(a_{\rm ho}, \mathbf{q}), \tag{B.6}$$

where $\mathcal{R}(a_{\rm ho}, \mathbf{q})$ is the Fourier transform of the momentum cut-off function $\tilde{\mathcal{R}}(a_{\rm ho}, \mathbf{p})$ given by

$$\begin{aligned} \mathcal{R}(a_{\rm ho}, \mathbf{q}) &= \int \frac{d^3\mathbf{p}}{(2\pi)^3} e^{i\mathbf{p}\cdot\mathbf{q}} e^{-a_{\rm ho}^2 p^2/2} \\ &= \frac{1}{(\sqrt{2\pi}a_{\rm ho})^3} e^{-q^2/2a_{\rm ho}^2} \\ &= |\psi_0(\mathbf{q})|^2, \end{aligned} \tag{B.7}$$

where $\psi_0(\mathbf{q})$ is the ground state wavefunction of a quantum harmonic oscillator of frequency $\omega_{\rm ho} = \hbar/(2ma_{\rm ho}^2)$. Eq. (B.6) thus represents the averaging over the ground state fluctuations of a harmonically trapped atom, where $a_{\rm ho}$ is the amplitude of the ground state fluctuations [109]. Substituting Eq. (3.15) into Eq. (B.6), setting $\mathbf{r} = \mathbf{0}$ and evaluating the integral gives Eq. (3.23).

In order to find the fluctuation-averaged Weyl decomposition of the free-space Green's function in the plane of the atoms ($z = 0$), we need to evaluate the following

expression

$$g^*_{\alpha\beta}(\mathbf{p}_{x\text{-}y};0) = \int \frac{dp_z}{2\pi} \frac{k^2\delta_{\alpha\beta} - p_\alpha p_\beta}{k^2(k^2 - p^2 + i\epsilon)} e^{-a_{\rm ho}^2 p^2/2}, \tag{B.8}$$

where, as part of the Sommerfeld prescription to make the Green's function causal, we have included an infinitesimal imaginary number with $\epsilon > 0$ in the denominator to move the poles off from the real axis [151]. The six independent components are given by

$$\begin{aligned}
g^*_{xx} &= (k^2 - p_x^2)\mathcal{I}_0, \\
g^*_{yy} &= (k^2 - p_y^2)\mathcal{I}_0, \\
g^*_{zz} &= (k^2\mathcal{I}_0 - \mathcal{I}_2), \\
g^*_{xy} &= g^*_{yx} = -p_x p_y \mathcal{I}_0 \\
g^*_{xz} &= g^*_{zx} = -p_x \mathcal{I}_1, \\
g^*_{yz} &= g^*_{zy} = -p_y \mathcal{I}_1
\end{aligned} \tag{B.9}$$

where the integrals are given by

$$\mathcal{I}_0 = \mathcal{C} \int dp_z \frac{e^{-a_{\rm ho}^2 p_z^2/2}}{(k^2 - p_x^2 - p_y^2) + i\epsilon - p_z^2}, \tag{B.10}$$

$$\mathcal{I}_1 = \mathcal{C} \int dp_z \frac{p_z e^{-a_{\rm ho}^2 p_z^2/2}}{(k^2 - p_x^2 - p_y^2) + i\epsilon - p_z^2}, \tag{B.11}$$

and

$$\mathcal{I}_2 = \mathcal{C} \int dp_z \frac{p_z^2 e^{-a_{\rm ho}^2 p_z^2/2}}{(k^2 - p_x^2 - p_y^2) + i\epsilon - p_z^2}, \tag{B.12}$$

where

$$\mathcal{C}(p_x, p_y) = \frac{1}{2\pi k^2} e^{-a_{\rm ho}^2 (p_x^2 + p_y^2)/2}. \tag{B.13}$$

Using the closed-form solutions for these integrals (see e.g. [230]), we obtain Eqs. (3.25) and (3.26).

B.3 Cut-off independence of Green's regularization

As described in Ref. [109], in order to demonstrate that Eq. (3.29) is independent of $a_{\rm ho}$, we need to differentiate Eq. (3.29) with respect to $a_{\rm ho}^2$ and show that the value of the resulting derivative goes to zero as the $a_{\rm ho} \to 0$ limit is taken. To simplify the calculations, we use the form of the Green's function as given in Eq. (B.2) and the following observation [104, 151]

$$\frac{e^{ikr}}{4\pi r} = -\int \frac{d^3\mathbf{p}}{(2\pi)^3} \frac{e^{i\mathbf{p}\cdot\mathbf{r}}}{k^2 - p^2}. \tag{B.14}$$

We substitute into Eq. (3.29) the following expression

$$G^*_{0,\alpha\beta}(\omega, \mathbf{r}) = \left[\delta_{\alpha\beta} + \frac{\partial_{r_\alpha}\partial_{r_\beta}}{k^2}\right] \int \frac{d^3\mathbf{p}}{(2\pi)^3} \frac{e^{i\mathbf{p}\cdot\mathbf{r}}}{k^2 - p^2} e^{-a_{\rm ho}^2 p^2/2}. \tag{B.15}$$

After taking the derivative with respect to $a_{\rm ho}^2$ and performing the resulting Gaussian integral, we obtain

$$\begin{aligned} &\lim_{a_{\rm ho}\to 0} \partial_{a_{\rm ho}^2} \left[e^{k^2 a_{\rm ho}^2} \sum_{\mathbf{R}\neq 0} e^{i\mathbf{k}_B\cdot\mathbf{R}} G^*_{\alpha\beta}(\mathbf{R}) \right] \\ &\qquad = \lim_{a_{\rm ho}\to 0} \sum_{\mathbf{R}\neq 0} e^{i\mathbf{k}_B\cdot\mathbf{R}} \left(\delta_{\alpha\beta} + \frac{\partial_{r_\alpha}\partial_{r_\beta}}{k^2}\right) \frac{e^{a_{\rm ho}^2 k^2}}{2} \left(\frac{2\pi}{a_{\rm ho}^2}\right)^{3/2} e^{-\frac{R^2}{4a_{\rm ho}^2}} = 0, \end{aligned} \tag{B.16}$$

where the last equality follows from the observation that $\exp(-R^2/4a_{\rm ho}^2) \to 0$ as $a_{\rm ho} \to 0$ for $R \neq 0$.

B.4 Green's function near a flat surface

The Weyl decomposition of the Green's function in the presence of flat surface has previously been derived by a number of authors [104, 123, 234, 235]. Assuming the interface is located at $z = -h$, for $z > -h$ the Weyl decomposition is given by

$$g_{\alpha\beta}(\mathbf{p}_{x\text{-}y}; z) = g_{0,\alpha\beta}(\mathbf{p}_{x\text{-}y}; z) + g^{(1)}_{{\rm sc},\alpha\beta}(\mathbf{p}_{x\text{-}y}; z), \tag{B.17}$$

where $g_{0,\alpha\beta}(\mathbf{p}_{x\text{-}y}; z)$ is the Green's function in free space discussed previously and the term accounting for the scattering from the surface is given by

$$g^{(1)}_{\mathrm{sc},\alpha\beta}(\mathbf{p}_{x\text{-}y}; z) = \frac{-ie^{ik_d(2h+z)}}{2k_d}\left[r_S\hat{\mathbf{S}}_\alpha\hat{\mathbf{S}}_\beta + r_P\hat{\mathbf{P}}^-_\alpha\hat{\mathbf{P}}^+_\beta\right], \tag{B.18}$$

where the Fresnel coefficients are given by

$$r_S = \frac{k_d - k_m}{k_d + k_m} \quad \text{and} \quad r_P = \frac{\varepsilon_m k_d - \varepsilon_d k_m}{\varepsilon_m k_d + \varepsilon_d k_m}, \tag{B.19}$$

with

$$k_d = \left(\varepsilon_d k^2 - p_x^2 - p_y^2\right)^{1/2} \geq 0 \tag{B.20}$$

and

$$k_m = \left(\varepsilon_m k^2 - p_x^2 - p_y^2\right)^{1/2} \geq 0, \tag{B.21}$$

where $k = \omega/c$. The unit vectors for the S- and P-polarizations are given by:

$$\hat{\mathbf{S}} = \frac{1}{p}(p_y\hat{x} - p_x\hat{y}), \tag{B.22}$$

$$\hat{\mathbf{P}}^\pm = \frac{1}{k\sqrt{\varepsilon_d}}\left(\sqrt{p_x^2 + p_y^2}\hat{z} \mp k_d\frac{p_x\hat{x} + p_y\hat{y}}{\sqrt{p_x^2 + p_y^2}}\right). \tag{B.23}$$

Using these expressions, we obtain the following matrix expressions

$$\hat{\mathbf{S}}\hat{\mathbf{S}} = \begin{bmatrix} \frac{p_y^2}{p_x^2+p_y^2} & -\frac{p_x p_y}{p_x^2+p_y^2} & 0 \\ -\frac{p_x p_y}{p_x^2+p_y^2} & \frac{p_x^2}{p_x^2+p_y^2} & 0 \\ 0 & 0 & 0 \end{bmatrix}, \tag{B.24}$$

and

$$\hat{\mathbf{P}}^{-}\hat{\mathbf{P}}^{+} = \begin{bmatrix} -\frac{k_d^2}{\varepsilon_d k^2}\frac{p_x^2}{p_x^2+p_y^2} & -\frac{k_d^2}{\varepsilon_d k^2}\frac{p_x p_y}{p_x^2+p_y^2} & -\frac{k_d}{\varepsilon_d k^2}p_x \\ -\frac{k_d^2}{\varepsilon_d k^2}\frac{p_x p_y}{p_x^2+p_y^2} & -\frac{k_d^2}{\varepsilon_d k^2}\frac{p_y^2}{p_x^2+p_y^2} & -\frac{k_d}{\varepsilon_d k^2}p_y \\ \frac{k_d}{\varepsilon_d k^2}p_x & \frac{k_d}{\varepsilon_d k^2}p_y & \frac{p_x^2+p_y^2}{\varepsilon_d k^2} \end{bmatrix}. \tag{B.25}$$

Therefore, the full matrix expression in Cartesian coordinates for the scattered part of the Green's function is given by

$$\mathbf{g}_{\mathrm{sc}}(\mathbf{p}_{x\text{-}y}; z) = -\frac{i}{2k_d} e^{ik_d(2d+z)}\mathbf{W},$$

where the matrix $\mathbf{W}$ is given by

$$\mathbf{W} = \begin{bmatrix} \frac{p_y^2}{p_x^2+p_y^2}\, r_S - \frac{k_d^2}{\varepsilon_d k^2}\frac{p_x^2}{p_x^2+p_y^2}\, r_P & -\frac{p_x p_y}{p_x^2+p_y^2}\, r_S - \frac{k_d^2}{\varepsilon_d k^2}\frac{p_x p_y}{p_x^2+p_y^2}\, r_P & -\frac{k_d}{\varepsilon_d k^2}p_x\, r_P \\ -\frac{p_x p_y}{p_x^2+p_y^2}\, r_S - \frac{k_d^2}{\varepsilon_d k^2}\frac{p_x p_y}{p_x^2+p_y^2}\, r_P & \frac{p_x^2}{p_x^2+p_y^2}\, r_S - \frac{k_d^2}{\varepsilon_d k^2}\frac{p_y^2}{p_x^2+p_y^2}\, r_P & -\frac{k_d}{\varepsilon_d k^2}p_y\, r_P \\ \frac{k_d}{\varepsilon_d k^2}p_x\, r_P & \frac{k_d}{\varepsilon_d k^2}p_y\, r_P & \frac{p_x^2+p_y^2}{\varepsilon_d k^2}\, r_P \end{bmatrix}. \tag{B.26}$$

For completeness, we note that for $z < -h$ the Weyl decomposition takes the form

$$g_{\alpha\beta}(\mathbf{p}_{x\text{-}y}; z) = g^{(2)}_{\mathrm{sc},\alpha\beta}(\mathbf{p}_{x\text{-}y}; z), \tag{B.27}$$

where $g^{(2)}_{\mathrm{sc},\alpha\beta}$ is given by [104, 123, 234, 235]

$$g_{\mathrm{sc},\alpha\beta}(\mathbf{p}_{x\text{-}y}; z) = \frac{ie^{i(k_d h - k_m(h+z))}}{2k_d}\left[t_S\hat{\mathbf{S}}_\alpha\hat{\mathbf{S}}_\beta + t_P\hat{\mathbf{P}}^m_\alpha\hat{\mathbf{P}}^+_\beta\right], \tag{B.28}$$

where the Fresnel coefficients are given by

$$t_S = \frac{2k_d}{k_d + k_m} \quad \text{and} \quad t_P = \frac{2k_d\sqrt{\varepsilon_d\varepsilon_m}}{\varepsilon_m k_d + \varepsilon_d k_m}, \tag{B.29}$$

and

$$\hat{\mathbf{P}}^m = \frac{1}{k\sqrt{\varepsilon_m}}\left(\left(p_x^2 + p_y^2\right)\hat{z} - k_m \frac{p_x\hat{x} + p_y\hat{y}}{\sqrt{p_x^2 + p_y^2}}\right). \tag{B.30}$$

Furthermore, we note that our method can be extended to describe atoms in the presence of multiple interfaces in a straightforward manner, since the Green's function in *momentum space* can be written down in a closed form in the presence of arbitrarily layered planar media. In particular, the above expressions for the Green's function depend on the particular planar geometry only through the Fresnel coefficients. In order to treat a more complicated planar geometry, we simply need to substitute the relevant Fresnel coefficients into Eq. (B.18) (see Ref. [123] for more details).

In order to perform the summation in momentum space, it is also necessary to find an expression for $G_{\mathrm{sc},\alpha\beta}(\mathbf{0})$, which can be expressed in terms of the following integral

$$G_{\mathrm{sc},\alpha\beta}(\mathbf{0}) = \int \frac{dp_x\, dp_y}{(2\pi)^2} g_{\mathrm{sc},\alpha\beta}(\mathbf{p}_{x\text{-}y}; 0). \tag{B.31}$$

After performing the angular integral in the p_x-p_y plane, only the diagonal terms survive and we are left with the components

$$G_{\mathrm{sc,xx}}(\mathbf{0}) = -\frac{i}{8\pi}k\left[\mathcal{I}_{xx,s} - \frac{1}{\varepsilon_d}\mathcal{I}_{xx,p}\right] \tag{B.32}$$

and

$$G_{\mathrm{sc,yy}}(\mathbf{0}) = G_{\mathrm{sc,xx}}(\mathbf{0}), \tag{B.33}$$

and

$$G_{\mathrm{sc,zz}}(\mathbf{0}) = -\frac{i}{4\pi}\frac{1}{\varepsilon_d}k\,\mathcal{I}_{zz,p}, \tag{B.34}$$

where the dimensionless contour integrals are given by

$$\mathcal{I}_{xx,s} = \int_0^\infty dx \frac{x}{\Lambda_d} \frac{\Lambda_d - \Lambda_m}{\Lambda_d + \Lambda_m} e^{i\Lambda_d 2kd}, \tag{B.35}$$

and

$$\mathcal{I}_{xx,p} = \int_0^\infty dx \; x \, \Lambda_d \frac{\varepsilon_m \Lambda_d - \varepsilon_d \Lambda_m}{\varepsilon_m \Lambda_d + \varepsilon_d \Lambda_m} e^{i\Lambda_d 2kd}, \tag{B.36}$$

and

$$\mathcal{I}_{zz,p} = \int_0^\infty dx \frac{x^3}{\Lambda_d} \frac{\varepsilon_m \Lambda_d - \varepsilon_d \Lambda_m}{\varepsilon_m \Lambda_d + \varepsilon_d \Lambda_m} e^{i\Lambda_d 2kd}. \tag{B.37}$$

The x-dependent functions Λ_d and Λ_m are given by

$$\Lambda_d(x) = \sqrt{\varepsilon_d - x^2}, \tag{B.38}$$

and

$$\Lambda_m(x) = \sqrt{\varepsilon_m - x^2}, \tag{B.39}$$

where the square root with $\mathrm{Re}(\Lambda_d) \geq 0$, $\mathrm{Im}(\Lambda_d) \geq 0$ and $\mathrm{Im}(\Lambda_m) \geq 0$, $\mathrm{Re}(\Lambda_m) \geq 0$ is taken to preserve causality. Note that these integral have previously been obtained in the context of studying qubit relaxation rates near metallic surfaces [236–238].

Appendix C

Appendices for Chapter 4

This Appendix is organized as follows. In Sections C.1 and C.2, we discuss the theory behind our calculations for the atomic lattice. In Section C.3, we discuss energy bands inside the light cone. In Section C.4, we discuss edge modes on the zig-zag boundary. In Section C.5, we discuss the influence of lattice size on the decay rate of edge modes. In Section C.6, we discuss the polarization independence of unidirectional emission. In Section C.7, we discuss atom-photon bound modes in the bulk of the lattice. Finally, in Section C.8, we discuss the effects of atomic fluctuations on the spectrum.

C.1 Dyadic Green's function in free space

The dyadic Green's function $G_{\alpha\beta}(\mathbf{r})$ in Eq. (4.1) is the solution of the dyadic equation [104]

$$\frac{\omega^2}{c^2}G_{\nu\beta}(\mathbf{r}) - \left(\partial_\alpha\partial_\nu - \delta_{\alpha\nu}\partial_\eta\partial_\eta\right)G_{\alpha\beta}(\mathbf{r}) = \delta_{\nu\beta}\delta(\mathbf{r}). \tag{C.1}$$

The Cartesian components of the Green's function are given by [104, 149]

$$\begin{aligned} G_{\alpha\beta}(\mathbf{r}) = -\frac{e^{ikr}}{4\pi r}\Bigg[&\left(1+\frac{i}{kr}-\frac{1}{(kr)^2}\right)\delta_{\alpha\beta} \\ &+\left(-1-\frac{3i}{kr}+\frac{3}{(kr)^2}\right)\frac{x_\alpha x_\beta}{r^2}\Bigg] + \frac{\delta_{\alpha\beta}\delta^{(3)}(\mathbf{r})}{3k^2}, \end{aligned} \tag{C.2}$$

where $k = \omega/c$ and $\alpha, \beta = x, y, z$ and $r = \sqrt{x^2 + y^2 + z^2}$.

C.2 Band structure calculation

The modes of the periodic lattice with Bloch quasi-momentum $\mathbf{k}_B$ can be obtained by substituting Eq. (4.1) and Eq. (4.2) into $H|\psi\rangle = \hbar E_{\mathbf{k}_B}|\psi\rangle$. After transforming to a Cartesian basis using the relation $|\sigma_\pm\rangle = \mp(|x\rangle \pm i|y\rangle)/\sqrt{2}$, finding the Bloch eigenmodes reduces to the diagonalization of the following 4×4 complex matrix

$$\begin{aligned} \mathbf{M}_{\alpha\mu,\beta\nu} &= (\omega_A - i\Gamma_0/2)\,\delta_{\alpha\beta}\delta_{1\mu}\delta_{1\nu} + \xi_{\alpha\mu,\beta\nu} \\ &+ (\omega_A - i\Gamma_0/2)\,\delta_{\alpha\beta}\delta_{2\mu}\delta_{2\nu} + \chi_{\alpha\mu,\beta\nu}, \end{aligned} \tag{C.3}$$

where

$$\xi_{\alpha\mu,\beta\nu} = -i\mu B(\delta_{\alpha x}\delta_{\beta y} - \delta_{\alpha y}\delta_{\beta x})(\delta_{1\mu}\delta_{1\nu} + \delta_{2\mu}\delta_{2\nu}), \tag{C.4}$$

gives the Zeeman splitting of the atoms and the terms accounting for the atom-atom interactions are given by

$$\begin{aligned} \chi_{\alpha\mu,\beta\nu} = \frac{3\pi\Gamma_0 c}{\omega_A} \Bigg[& \sum_{\mathbf{R}\neq 0} e^{i\mathbf{k}_B\cdot\mathbf{R}} G_{\alpha\beta}(\mathbf{R})\delta_{1\mu}\delta_{1\nu} \\ & + \sum_{\mathbf{R}} e^{i\mathbf{k}_B\cdot\mathbf{R}} G_{\alpha\beta}(\mathbf{R}+\mathbf{b})\delta_{1\mu}\delta_{2\nu} \\ & + \sum_{\mathbf{R}\neq 0} e^{i\mathbf{k}_B\cdot\mathbf{R}} G_{\alpha\beta}(\mathbf{R})\delta_{2\mu}\delta_{2\nu} \\ & + \sum_{\mathbf{R}} e^{i\mathbf{k}_B\cdot\mathbf{R}} G_{\alpha\beta}(\mathbf{R}-\mathbf{b})\delta_{2\mu}\delta_{1\nu} \Bigg], \end{aligned} \tag{C.5}$$

where $\mathbf{b}$ is the basis vector pointing from one site to the other within the unit cell of the non-Bravais honeycomb lattice which has two sites, $\alpha, \beta = x, y$ label the polarization components and $\mu, \nu = 1, 2$ are the sublattice indices. Diagonalizing $\mathbf{M}_{\alpha\mu,\beta\nu}$ gives four eigenvalues of the form $E_{\mathbf{k}_B} = \omega_{\mathbf{k}_B} - i\gamma_{\mathbf{k}_B}$ for each $\mathbf{k}_B$ within the Brillouin zone, where the real and imaginary parts of the eigenvalues correspond to the energies and

decay rates of the modes respectively.

To ensure rapid convergence, it is convenient to perform the summation in momentum space. We use Poisson's summation formula [109, 114, 129] to obtain

$$\begin{aligned}\sum_{\mathbf{R}\neq 0} e^{i\mathbf{k}_B\cdot\mathbf{R}} G_{\alpha\beta}(\mathbf{R}) &= \sum_{\mathbf{R}} e^{i\mathbf{k}_B\cdot\mathbf{R}_n} G_{\alpha\beta}(\mathbf{R}) - G_{\alpha\beta}(\mathbf{0}) \\ &= \frac{1}{\mathcal{A}}\sum_{\mathbf{G}} g_{\alpha\beta}(\mathbf{G}-\mathbf{k}_B;0) - G_{\alpha\beta}(\mathbf{0}),\end{aligned} \tag{C.6}$$

and

$$\sum_{\mathbf{R}} e^{i\mathbf{k}_\mathrm{B}\cdot\mathbf{R}} G_{\alpha\beta}(\mathbf{R}\pm\mathbf{b}) = \frac{1}{\mathcal{A}}\sum_{\mathbf{G}} g_{\alpha\beta}(\mathbf{G}-\mathbf{k}_\mathrm{B};0) e^{\pm i\mathbf{b}\cdot(\mathbf{G}-\mathbf{k}_\mathrm{B})}, \tag{C.7}$$

where $\mathcal{A}$ is the area of the periodic unit cell and the summation is performed over the reciprocal lattice vectors $\{\mathbf{G}\}$ in the 2D plane, which obey $\mathbf{R}\cdot\mathbf{G} = 2\pi m$ for integer m and $g_{\alpha\beta}(\mathbf{q};z)$ stands for the Weyl decomposition of the Green's function in terms of 2D plane waves at position z along the z-axis. In the plane of the atoms ($z=0$) it is given by [114, 151]

$$g_{\alpha,\beta}(\mathbf{q};0) = \int \frac{dq_z}{2\pi}\frac{1}{k^2}\frac{k^2\delta_{\alpha\beta}-q_\alpha q_\beta}{k^2-q^2-q_z^2+i\epsilon}, \tag{C.8}$$

where $\mathbf{q} = q_x\hat{x}+q_y\hat{y}$ and $q=|\mathbf{q}|$ and we restrict ourselves to $\alpha,\beta = x,y$.

The terms on the right-hand side of (C.6) are divergent, but after regularizing both terms, their difference becomes finite. Regularization is performed by inserting a Gaussian momentum cut-off $e^{-a_{\mathrm{ho}}^2(q_x^2+q_y^2+q_z^2)/2}$ into the Fourier decomposition of each term [109, 114, 129]. Upon substitution, the regularized Weyl decomposition becomes

$$g^*_{\alpha,\beta}(\mathbf{q};0) = \int \frac{dq_z}{2\pi}\frac{1}{k^2}\frac{k^2\delta_{\alpha\beta}-q_\alpha q_\beta}{k^2-q^2-q_z^2+i\epsilon} e^{-a_{\mathrm{ho}}^2(q^2+q_z^2)/2}. \tag{C.9}$$

This integral can be evaluated in a closed form [114] and the resulting components

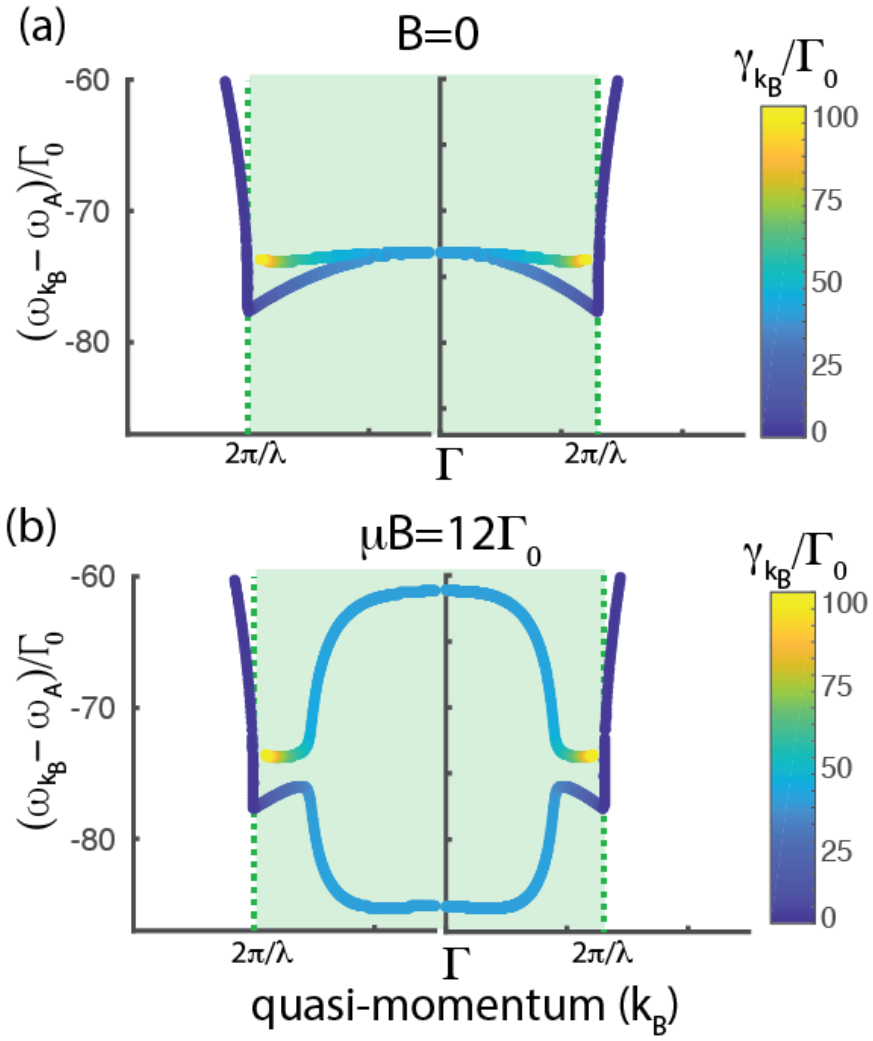

Figure C-1: Close-up view of the lower part ($\omega_{\mathbf{k}_B} < \omega_A$) of the light cone region in Fig. 4-1. (a) When $B = 0$ the two bands touch at the $\mathbf{\Gamma}$ point, where a quadratic degeneracy is formed. The decay rate of the upper band diverges as it approaches the edges of the light cone, whereas the lower band is continuous across the edges of the light cone. (b) When a magnetic field is switched on the degeneracy is lifted.

are given by

$$\begin{aligned} g^*_{xx}(\mathbf{q};0) &= (k^2 - q_x^2)\mathcal{I}(\mathbf{q}), \\ g^*_{yy}(\mathbf{q};0) &= (k^2 - q_y^2)\mathcal{I}(\mathbf{q}), \\ g^*_{xy}(\mathbf{q};0) &= g^*_{yx}(\mathbf{q};0) = -q_x q_y \mathcal{I}(\mathbf{q}), \end{aligned} \tag{C.10}$$

where we have defined

$$\mathcal{I}(\mathbf{q}) = \chi(\mathbf{q})\frac{\pi}{\Lambda(\mathbf{q})}[-i + \mathrm{erfi}(a_{\mathrm{ho}}\Lambda(\mathbf{q})/\sqrt{2})] \tag{C.11}$$

with

$$\chi(\mathbf{q}) = \frac{1}{2\pi k^2} e^{-a_{\mathrm{ho}}^2(q_x^2+q_y^2+\Lambda(\mathbf{q})^2)/2} \tag{C.12}$$

and

$$\Lambda(\mathbf{q}) = (k^2 - q_x^2 - q_y^2)^{1/2}, \tag{C.13}$$

where $\mathrm{Im}(\Lambda) \geq 0$ and $\mathrm{Re}(\Lambda) \geq 0$ is assumed and $\mathrm{erfi}(x)$ stands for the imaginary error function. The regularized Green's function at the source takes the form [109]

$$G^*_{\alpha\beta}(\mathbf{0}) = \frac{k}{6\pi}\left[\left(\frac{\mathrm{erfi}(ka_{\mathrm{ho}}/\sqrt{2}) - i}{e^{(ka_{\mathrm{ho}})^2/2}}\right) - \frac{(-1/2) + (ka_{\mathrm{ho}})^2}{(\pi/2)^{1/2}(ka_{\mathrm{ho}})^3}\right]\delta_{\alpha\beta}. \tag{C.14}$$

It can be shown using the methods developed in [109] that

$$\exp(k^2 a_{\mathrm{ho}}^2/2)[1/\mathcal{A}\sum_{\mathbf{G}} g^*_{\alpha\beta}(\mathbf{G} - \mathbf{k}_B;0) - G^*_{\alpha\beta}(\mathbf{0})] \tag{C.15}$$

approaches the value of the left-hand side of Eq. (C.6) as the limit $a_{\mathrm{ho}} \to 0$ is taken [114]. Therefore, choosing a small a_{ho} such that $a_{\mathrm{ho}} \ll \lambda$ we obtain

$$\sum_{\mathbf{R}\neq 0} e^{i\mathbf{k}_B\cdot\mathbf{R}} G_{\alpha\beta}(\mathbf{R}) \approx \frac{e^{k^2 a_{\mathrm{ho}}^2/2}}{\mathcal{A}} \sum_{\mathbf{G}} g^*_{\alpha\beta}(\mathbf{G} - \mathbf{k}_B;0) - G^*_{\alpha\beta}(\mathbf{0}), \tag{C.16}$$

where $g^*_{\alpha\beta}$ is given by Eq. (C.10) and $G^*_{\alpha\beta}$ is given by Eq. (C.14). The summation over $\mathbf{G}$ converges rapidly.

C.3 Energy bands within the light cone

Fig. C-1 shows a close-up view of the lower part ($\omega_{\mathbf{k}_B} < \omega_A$) of the light cone region of Fig. 4-1. For $B = 0$, the two bands are close to each other in energy and touch at the $\mathbf{\Gamma}$ point in a quadratic degeneracy. The quadratic degeneracy arises due to the inversion symmetry of the reciprocal lattice with respect to the $\mathbf{\Gamma}$ point [162]. Switching on a magnetic field raises the degeneracy and the bands exchange one unit of Berry flux ($\Delta C_\pm = \pm 1$). The modes in the lower band are predominantly polarized in the longitudinal direction, whereas the modes in the upper band have transversal polarization. Therefore, the lower band couples weakly to the transversely polarized free-space modes and remains continuous as it crosses the edges of the light cone. In contrast, the upper band couples strongly to free-space modes and the decay rate of the modes diverges as the edges of the light cone are approached, effectively 'dissolving' the band due to broadening. In particular, for the upper band $\gamma \sim 1/\sqrt{1-(k_B/k_L)^2}$, where k_B is the magnitude of the in-plane Bloch vector and $k_L = 2\pi/\lambda$ [110]. Physically, the divergence arises due to the fact that a free-space photon traveling exactly in-plane would interact with an infinite number of atoms and, therefore, a transversely polarized extended lattice mode with $k_B = 2\pi/\lambda$ would decay immediately through its overlap with free-space modes of the same momentum [11].

C.4 4. Edge modes on the zig-zag boundary

In addition to the bearded and armchair modes, a honeycomb lattice can also be terminated by a zig-zag boundary. Fig. C-2 shows the spectrum of the edge modes on such a boundary. Edge modes in the bottom half of the band gap have quasi-

[11] We thank D. S. Wild for pointing this out

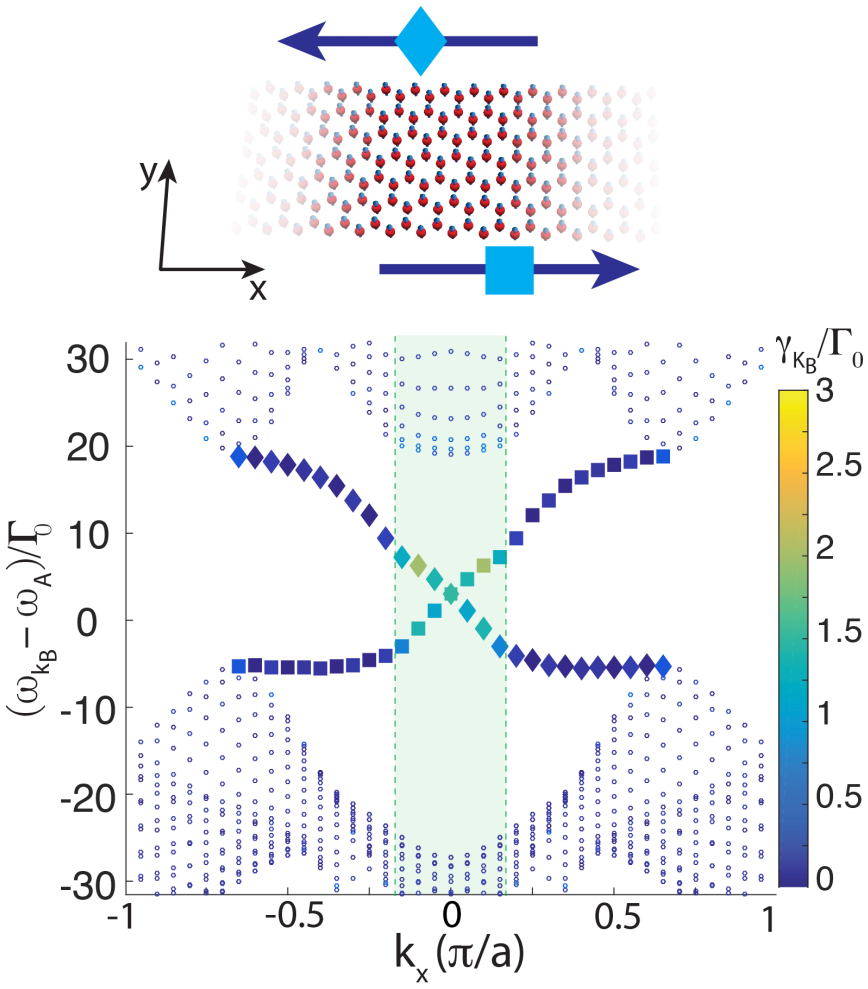

Figure C-2: Edge modes on the zig-zag boundary of a honeycomb lattice. Edge modes in the bottom half of the band gap have quasi-momenta $k_B < \omega_{\mathbf{k}_B}/c$ and are short-lived. Modes in the top half of the gap have quasi-momenta $k_B > \omega_{\mathbf{k}_B}/c$ and are long-lived. Relevant parameters are $\lambda = 790$nm, $\Gamma_0 = 2\pi \times 6$MHz, $a = 0.05\lambda$ and $\mu B = 12\Gamma_0$ and the spectrum was obtained from a lattice with 40x41 atoms with periodic boundary conditions along the first dimension. States for which the ratio of the total amplitude on the top (bottom) four atom rows to the bottom (top) four rows is greater than 15 are classified as edge states.

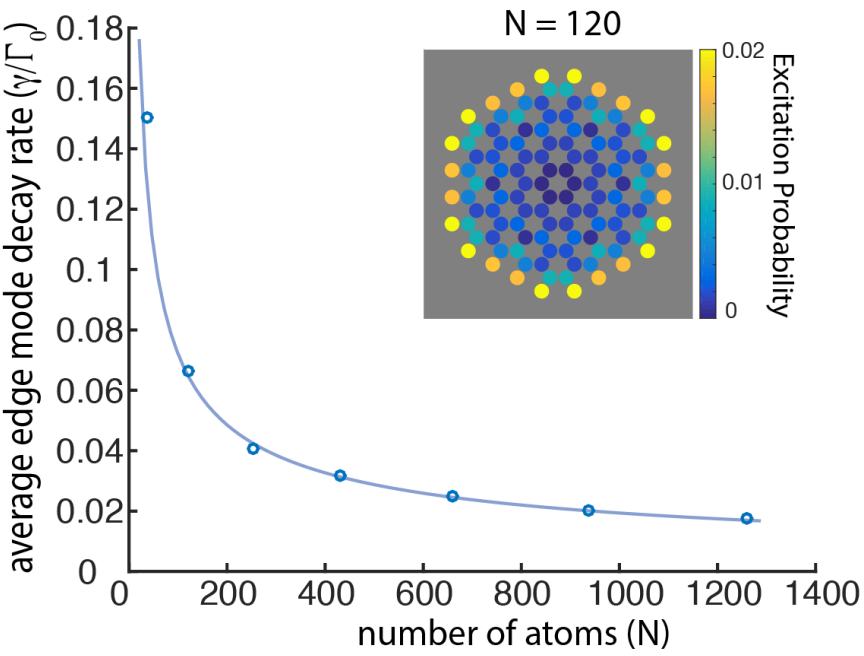

Figure C-3: Scaling of the decay rate of the edge modes on the bearded boundary as a function of the total number of atoms in the hexagonal-shaped atom lattice. The decay rate scales approximately as $\sim 1/\sqrt{N}$. The numerical fit to the data points $\sim 1/N^{0.57}$ is shown as a solid line. To obtain each point in the plot, a hexagonal-shaped lattice of N atoms with bearded boundaries was considered with $a = \lambda/20$ and $\mu B = 12\Gamma_0$. The average decay rate was obtained by averaging the decay rates of all edge states inside the band gap. The inset shows the probability amplitudes of a bearded edge state on a lattice of $N = 120$ atoms.

momenta $k_B < \omega_{\mathbf{k}_B}/c$ and are short-lived, whereas modes in the top half of the gap have quasi-momenta $k_B > \omega_{\mathbf{k}_B}/c$ and are long-lived. By tuning the frequency of a laser to be resonant with the modes in the top half of the gap, we can predominantly excite the long-lived edge modes of the zig-zag edge.

C.5 Influence of system size on decay rate of edge modes

For an infinite lattice, modes with quasi-momenta $k_B > \omega_{\mathbf{k}_B}/c$ are decoupled from free-space modes and, therefore, do not decay. In contrast, for finite lattices even such modes have a finite lifetime. Fig. C-3 shows the decay rate of the bearded edge

modes with $k_B > \omega_{\mathbf{k}_B}/c$ as the total number of atoms in the lattice is varied. The interatomic spacing is assumed to be fixed at $a = \lambda/20$. The decay rate of the modes scales approximately as $\sim 1/\sqrt{N}$, where N is the total number of atoms in the 2D lattice. This scaling is consistent with the observation that, since edge modes are confined to the boundaries, they explore only the 1D perimeter of the lattice, which scales with $\sim \sqrt{N}$.

Note that changing the size of the lattice has little effect on the decay rate of short-lived edge modes with quasi-momenta $k_{\mathrm{B}} < \omega_{\mathbf{k}_B}/c$. These modes couple directly to free-space modes and thus their loss via out-of-plane emission dominates, making finite-size effects negligible in comparison.

C.6 Polarization independence of unidirectional emission

In Fig. 4-4 a single atom on the lattice boundary is driven by a laser. When the transitions to the $|\sigma_+\rangle$ and $|\sigma_-\rangle$ states are driven with equal coupling strengths Ω, approximately 96% of the excitation emitted by the driven atom is coupled in the edge modes carrying energy in the forward direction. If only one of the transitions to the $|\sigma_-\rangle$ or $|\sigma_+\rangle$ states is driven, the efficiency of coupling into the unidirectional edge modes changes to approximately 90% and 97%, respectively.

Note that the fact that unidirectional emission does not depend on which transition of the atom is driven demonstrates that the unidirectionality arises from topology and not from polarization selection as, for example, in Ref. [239].

C.7 Bulk excitations within the band gap

In Chapter 4 we discussed the system dynamics when edge states are excited through an individual atom that is located near the boundary of the lattice. Here we focus on the time evolution of the system when an atom in the bulk is excited with a laser, whose frequency ω_{L} falls inside the band gap. The driving laser is adiabati-

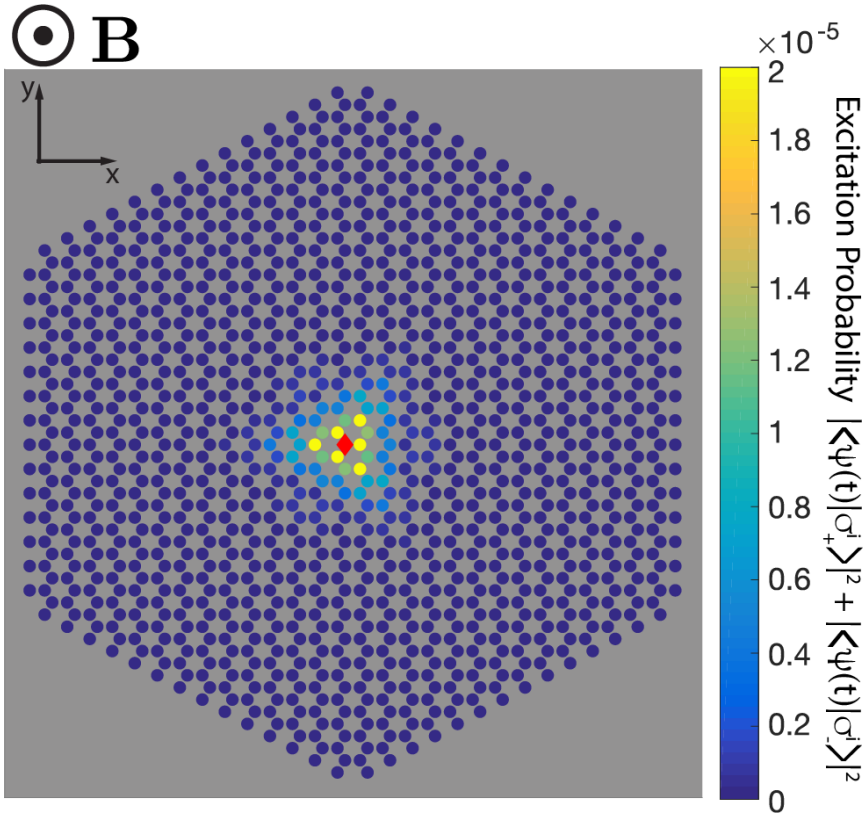

Figure C-4: A sub-radiant atom-photon bound state forms when an atom in the bulk of the lattice (marked with a red diamond) is driven by a laser with its frequency inside the band gap. The decay rate of the bound state is sensitive to the polarization of the driving laser. Relevant parameters are $N = 1260$, $\lambda = 790\text{nm}$, $\Gamma_0 = 2\pi \times 6\text{MHz}$, $a = 0.05\lambda$ and $\mu B = 12\Gamma_0$. The strength of the drive is $\Omega = 1\Gamma_0$ and the frequency of the laser is tuned such that $\omega_L = \omega_A + 10\Gamma_0$. The driving laser is adiabatically switched on with a sigmoid profile $\Omega(t) = \Omega\left[1 + \exp\left(-\left(t - 3\Gamma_0^{-1}\right)/0.3\Gamma_0^{-1}\right)\right]^{-1}$. The figure shows a snapshot at $t = 10\Gamma_0^{-1}$.

cally switched using a sigmoid profile to avoid exciting non-resonant modes and it continuously excites the atom.

Since inside the band gap there are no extended bulk modes, the atom cannot resonantly couple to any of the extended lattice modes. Instead, the atom weakly dresses the far-detuned modes. Consequently, the atom exchanges energy only with atoms in its immediate neighborhood and a spatially confined atom-photon bound state is formed as shown in Fig. C-4. This is analogous to the atom-photon bound states that are predicted to exist in photonic crystals with band gaps [93, 240].

Here a sigmoid profile is preferred to a Gaussian one, since the higher order derivatives of the sigmoid function vary slower as the function approaches its maximum value than the corresponding derivatives of a Gaussian profile. Thus the sigmoid profile performs better than a Gaussian in not exciting far detuned extended bulk modes, making the weak, off-resonant dressing of bulk modes observable.

Since the majority of the extended bulk modes above and below the band gap are long-lived, the bound state itself is sub-radiant with a decay rate that depends on the polarization of the exciting laser. In particular, since the band gap arises from the Zeeman-splitting of the $|\sigma_+\rangle$ and $|\sigma_-\rangle$ levels, the bulk modes above and below the band gap couple more strongly to light polarized along $\hat{\sigma}_+$ and $\hat{\sigma}_-$ respectively. Since the modes close to the center of the Brillouin zone and immediately above the gap are short-lived, a laser with polarization $\hat{\sigma}_+$ excites a shorter lived bound state with $\gamma = \Gamma_0/4.7$, whereas a laser with polarization $\hat{\sigma}_-$ yields $\gamma = \Gamma_0/7.7$. For an $\hat{x}$ polarized laser we obtain $\gamma = \Gamma_0/5.7$.

C.8 Effect of fluctuating atomic positions

The Hamiltonian in Eq. (4.1) assumes that the position of the atoms is fixed at the sites of the lattice. In practice, even when the atoms are tightly trapped and are occupying their motional ground state, their position will fluctuate around the lattice sites. These quantum fluctuations are uncorrelated between different sites. To quantify how the quantum fluctuations in atomic positions affect our results,

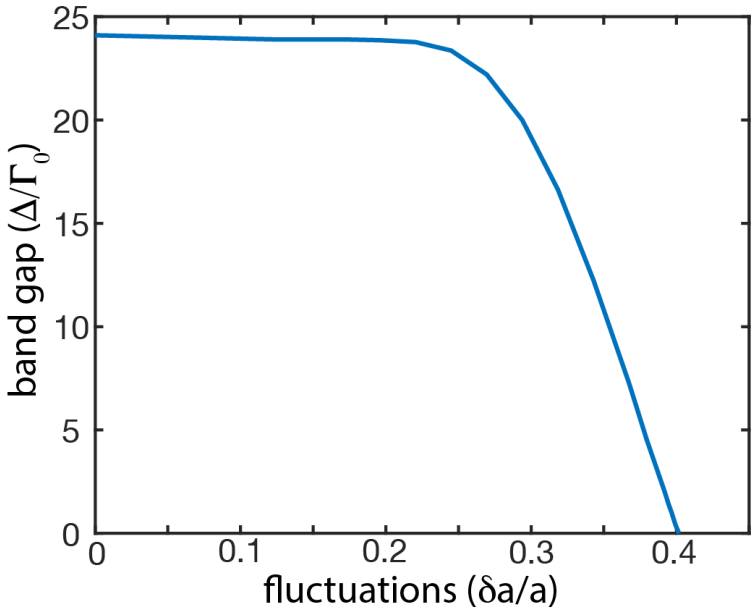

Figure C-5: Maximum gap size $\Delta_{\max}$ as the atomic positions fluctuate with amplitude δa around the lattice sites with fixed interatomic spacing $a = 0.05\lambda$ and $\mu B = 12\Gamma_0$. When the amplitude of the fluctuations is less than 25% of the interatomic spacing a, the band structure is not significantly affected.

we assume a harmonic trapping potential of frequency ω_{ho}, with the corresponding spatial extent of the ground state oscillations on the order of $\delta a = \sqrt{\hbar/(2m\omega_{\text{ho}})}$. We then average the dyadic Green's function in the Hamiltonian with respect to the ground state fluctuations [109, 114]. Fig. C-5 shows how the size of the band gap between the topological bands changes as the magnitude of δa is varied as a fraction of the interatomic spacing a. Larger fluctuations smear out the well-defined phase between different atoms and eventually the gap closes. However, when the extent of the fluctuations is less than 25% of the interatomic spacing, the size of the gap (and the band structure as a whole) is not significantly affected. This shows that our results are robust against moderate fluctuations in atomic positions around the lattice sites.

Appendix D

Appendices for Chapter 5

In this Appendix, we describe the analytic calculations behind obtaining the Green's function of Eqs. (5.18)-(5.22).

Given the approximations described in Section 5.4, we can rewrite Eq. (5.13) as

$$G_{\alpha\beta}(\mathbf{r}_2) \approx \frac{\mathcal{A}c^2}{8\pi^2\omega_A a^3}\Bigg(I^{(+)}_{\mathbf{K},\alpha\beta} + I^{(-)}_{\mathbf{K},\alpha\beta} + I^{(+)}_{\mathbf{K}',\alpha\beta} + I^{(-)}_{\mathbf{K}',\alpha\beta}\Bigg), \tag{D.1}$$

where the four terms in the brackets correspond to the contributions from the upper and lower bands of the Dirac cones at the $\mathbf{K}$ and $\mathbf{K}'$ points. The integrals at the $\mathbf{K}$ point are given by

$$I^{(\pm)}_{\mathbf{K},\alpha\beta} = \int d^2\mathbf{p} \frac{u^{(\mathbf{K},\pm)*}_{\mathbf{p},\alpha}(\mathbf{r}_1)\, u^{(\mathbf{K},\pm)}_{\mathbf{p},\beta}(\mathbf{r}_1)}{\omega_A - \omega^{(\mathbf{K},\pm)}_{\mathbf{p}}} e^{i\mathbf{p}\cdot\mathbf{r}_{12}}, \tag{D.2}$$

and an analogous expressions holds at the $\mathbf{K}'$ point. The evaluation of these integrals follows closely the methods outlined in Ref. [172].

First, we substitute Eq. (5.2) into the denominator, and after changing changing variables to $\mathbf{k} = \mathbf{p} - \mathbf{p}_{\mathbf{K}}$, we obtain

$$I^{(\pm)}_{\mathbf{K},\alpha\beta} = e^{i\mathbf{p}_{\mathbf{K}}\cdot\mathbf{r}_{12}} \int d^2\mathbf{k} \frac{u^{(\pm)*}_{\mathbf{p}_{\mathbf{K}}+\mathbf{k},\alpha}\, u^{(\pm)}_{\mathbf{p}_{\mathbf{K}}+\mathbf{k},\beta}}{\omega_A - \omega_{\text{Dirac}} \mp v_{\text{s}}|\mathbf{k}|} e^{i\mathbf{k}\cdot\mathbf{r}_{12}}, \tag{D.3}$$

where for notational convenience we have made the positional argument of $u^{(\pm)*}_{\mathbf{p_K}+\mathbf{k},\alpha}(\mathbf{r}_1)$ implicit.

We proceed by parameterizing the position vector $\mathbf{r}_{12}$ and momentum vector $\mathbf{k}$ as follows

$$\mathbf{r}_{12} = r(\cos\phi, \sin\phi), \tag{D.4}$$

$$\mathbf{k} = k(\cos\Phi_{\mathbf{K}}, \sin\Phi_{\mathbf{K}}), \tag{D.5}$$

where ϕ is measured from the x-axis and $\Phi_{\mathbf{K}}$ is given by Eq. (5.4). Using these parameterizations, we obtain

$$\mathbf{k}\cdot\mathbf{r}_{12} = k\, r\cos(\phi - \Phi_{\mathbf{K}}), \tag{D.6}$$

and substituting this expression into Eq. (D.3) yields

$$I^{(\pm)}_{\mathbf{K},\alpha\beta} = e^{i\mathbf{p_K}\cdot\mathbf{r}_{12}}\int d^2\mathbf{k}\frac{u^{(\pm)*}_{\mathbf{p_K}+\mathbf{k},\alpha}\, u^{(\pm)}_{\mathbf{p_K}+\mathbf{k},\beta} e^{ikr\cos(\phi-\Phi_{\mathbf{K}})}}{\omega_A - \omega_{\text{Dirac}} \mp v_{\text{s}}|\mathbf{k}|}. \tag{D.7}$$

First, we evaluate this expression for the top band when $\alpha\beta = xx$. Substituting Eq. (5.3) and Eq. (5.14) into Eq. (D.7), we obtain

$$I^{(+)}_{\mathbf{K},xx} \;=\; a^3|E_0|^2 e^{i\mathbf{p_K}\cdot\mathbf{r}_{12}}\int_0^{k_c} kdk\frac{\Lambda(\phi,kr)}{-\delta_A - v_{\text{s}}k}, \tag{D.8}$$

where we take the limit of the integral to be $k_c = |\mathbf{p_K}|$ for simplicity. We have also used the notation $\delta_A = \omega_{\text{Dirac}} - \omega_A$ and $|\mathbf{k}| = k$, and defined the expression

$$\Lambda(\phi,kr) = \int_0^{2\pi} d\Phi_{\mathbf{K}}\ \sin^2\left(\frac{\Phi_{\mathbf{K}}}{2} - \frac{\pi}{4}\right) e^{ik\,r\cos(\phi-\Phi_{\mathbf{k}})}, \tag{D.9}$$

which, after changing variables to $\phi - \Phi_{\mathbf{K}} = \theta$, evaluates to

$$\Lambda(\phi,kr) = \pi J_0(kr) - i\pi\sin\phi\ J_1(kr). \tag{D.10}$$

Next, we substitute this expression into Eq. (D.8) and change variables to $q = v_s k/\delta_A$. We also extend the limit of integration with respect to q to infinity based on the observation that $v_s k_c/\delta_A \gg 1$ when δ_A is small. Performing the resulting integral yields

$$I^{(+)}_{\mathbf{K},xx} = -\frac{a^3|E_0|^2\delta_A\pi}{2v_s^2} e^{i\mathbf{p_K}\cdot\mathbf{r}_{12}} \Bigg(\frac{2}{r/\xi} + \pi Y_0(r/\xi) \\ -\pi H_0(r/\xi) + i\pi \sin\phi \big[Y_1(r/\xi) + H_{-1}(r/\xi) \big] \Bigg), \tag{D.11}$$

where $Y_m(r)$ and $H_m(r)$ are Bessel and Struve functions of order m, respectively, and we have defined $\xi = v_s/\delta_A$, which sets the length scale of the interaction mediated by the Green's function.

For the bottom band, we need to evaluate the integral

$$I^{(-)}_{\mathbf{K},xx} = a^3|E_0|^2 e^{i\mathbf{p_K}\cdot\mathbf{r}_{12}} \int_0^{k_c} k dk \frac{\Lambda'(\phi, kr)}{-\delta_A + v_s k}, \tag{D.12}$$

where

$$\begin{aligned} \Lambda'(\phi, kr) &= \int_0^{2\pi} d\Phi_{\mathbf{K}} \ \sin^2\left(\frac{\Phi_{\mathbf{K}}}{2} + \frac{\pi}{4}\right) e^{ik\,r\cos(\phi - \Phi_{\mathbf{k}})}, \\ &= \pi J_0(kr) + i\pi \sin\phi \ J_1(kr). \end{aligned} \tag{D.13}$$

This integral is singular, since the denominator can be zero. To make the integral well-defined, we introduce a small imaginary component $+i\varepsilon$, where $\varepsilon > 0$, into the denominator to move the pole off the real axis. This corresponds to only considering the outgoing waves that arise from the point source, making the Green's function causal [151]. Then, after changing variables and extending the limit of integration as for the top band, we use the following identity

$$\frac{1}{x \pm i\varepsilon} = \mathrm{P}\left[\frac{1}{x}\right] \mp i\pi\delta(x), \tag{D.14}$$

to obtain

$$\begin{aligned} I^{(-)}_{\mathbf{K},xx} &= -\frac{a^3|E_0|^2\delta_A\pi}{2v_{\rm s}^2}e^{i\mathbf{p}_\mathbf{K}\cdot\mathbf{r}_{12}}\Bigg(-\frac{2}{r/\xi}+\pi Y_0(r/\xi) \\ &+ \pi H_0(r/\xi)+i\pi\sin\phi\big[Y_1(r/\xi)-H_{-1}(r/\xi)\big], \\ &+ 2i\big[\pi J_0(r/\xi)+i\pi\sin\phi\ J_1(r/\xi)\big]\Bigg). \end{aligned} \tag{D.15}$$

Finally, adding up the contributions from the top and bottom bands, we obtain

$$\begin{aligned} I^{(+)}_{\mathbf{K},xx}+I^{(-)}_{\mathbf{K},xx} = \frac{a^3|E_0|^2\delta_A\pi^2}{v_{\rm s}^2}e^{i\mathbf{p}_\mathbf{K}\cdot\mathbf{r}_{12}}\Bigg(&-iH_0^{(2)}(r/\xi) \\ &+\sin\phi H_1^{(2)}(r/\xi)\Bigg), \end{aligned} \tag{D.16}$$

where we have used the the definition for the Henkel function of the second kind of order m in terms of Bessel functions (Eq. (5.27)).

The integrals near the $\mathbf{K}'$ point can be evaluated using analogous calculations. The only difference is that we need to use $\mathbf{p}_{\mathbf{K}'}$ instead of $\mathbf{p}_\mathbf{K}$ and the electric field modes are different. The results are identical to those in Eq. (D.16) with the replacements $\mathbf{p}_\mathbf{K}\to\mathbf{p}_{\mathbf{K}'}$ and $\sin\phi\to-\sin\phi$ yielding

$$\begin{aligned} I^{(+)}_{\mathbf{K}',xx}+I^{(-)}_{\mathbf{K}',xx} = \frac{a^3|E_0|^2\delta_A\pi^2}{v_{\rm s}^2}e^{i\mathbf{p}'_\mathbf{K}\cdot\mathbf{r}_{12}}\Bigg(&-iH_0^{(2)}(r/\xi) \\ &-\sin\phi H_1^{(2)}(r/\xi)\Bigg). \end{aligned} \tag{D.17}$$

Substituting all four terms into Eq. (5.13), we obtain

$$\begin{aligned} G_{xx}(r,\phi) &= \sin\phi\,P^-(\mathbf{r})H_1^{(2)}(r/\xi) \\ &\quad -iP^+(\mathbf{r})H_0^{(2)}(r/\xi), \end{aligned} \tag{D.18}$$

where

$$P^{\pm}(\mathbf{r}) = \frac{\mathcal{A}c^2|E_0|^2\delta_a}{8\omega_A v_{\rm s}^2}\left(e^{i\mathbf{p_K}\cdot\mathbf{r}} \pm e^{i\mathbf{p_{K'}}\cdot\mathbf{r}}\right). \tag{D.19}$$

The Green's function for the cases when $\alpha\beta = yy$, $\alpha\beta = xy$ and $\alpha\beta = yx$ can be calculated analogously. In particular, the final result for G_{yy} can be obtained by making the substitution $\sin\phi \to -\sin\phi$ in Eq. (D.18) to get

$$\begin{aligned} G_{yy}(r,\phi) &= -\sin\phi\, P^-(\mathbf{r}) H_1^{(2)}(r/\xi) \\ &\quad -iP^+(\mathbf{r}) H_0^{(2)}(r/\xi). \end{aligned} \tag{D.20}$$

The expression for G_{xy} is given by

$$G_{xy}(r,\phi) = \cos\phi\, P^-(\mathbf{r}) H_1^{(2)}(r/\xi), \tag{D.21}$$

and we note that

$$G_{yx}(r,\phi) = G_{xy}(r,\phi). \tag{D.22}$$

These results are summarized in Eqs. (5.18)-(5.22).

Appendix E

Appendices for Chapter 6

This Appendix is organized as follows. In Section E.1, we discuss the calculations for obtaining the atomic band structure. In Section E.2, we discuss the validity of our model and the limits on the maximum achievable gap size in our system. In Section E.3, we describe the calculations behind obtaining the edge states in our system. Finally, in Section E.4, we analyze the edge states in the presence of free space decay.

E.1 Calculation of the atomic band structure

In this section, we calculate the Bloch modes of the hybrid emitter-photonic crystal system. For simplicity, we focus on the atomic interactions mediated by the photonic crystal modes and neglect coupling to free-space photons. This is motivated by previous studies of a triangular lattice of emitters in free space [114]. The cooperative effects mediated by free-space photons reported in Ref. [114] are, in general, an order magnitude smaller than those mediated by the photonic crystal modes described here.

E.1.1 Analytic calculations

The Bloch eigenmodes of our system with quasi-momentum $\mathbf{k}$ can be obtained by substituting Eqs. (6.1) and (6.4) into $H|\psi_{\mathbf{k}}\rangle = \hbar\omega_{\mathbf{k}}|\psi_{\mathbf{k}}\rangle$. After transforming to a

Cartesian basis using the relation $|\sigma_\pm\rangle = \mp(|x\rangle \pm i|y\rangle)/\sqrt{2}$, the Bloch modes are obtained by diagonalizing the following 2x2 matrix

$$\begin{aligned} M_{\alpha\beta}(\mathbf{k}) &= \left(\tilde{\omega}_A - \mathrm{i}\frac{\Gamma_{\mathrm{PC}}}{2}\right)\delta_{\alpha\beta} + \xi_{\alpha,\beta} \\ &+ \frac{3\pi\gamma c}{\omega_A n_{\mathrm{d}}} \sum_{\mathbf{R}\neq 0} e^{\mathrm{i}\mathbf{k}\cdot\mathbf{R}} G_{\alpha\beta}(\mathbf{R}), \end{aligned} \tag{E.1}$$

where $\alpha, \beta = x, y$ label the polarization components and $\tilde{\omega}_A$ denotes the 'dressed' atomic transition frequency in the photonic crystal. The summation is implied over the set of triangular lattice vectors $\{\mathbf{R} = n_1\mathbf{R}_1 + n_2\mathbf{R}_2\}$, where $n_1, n_2 = 0, \pm 1, \pm 2, \ldots$ and

$$\mathbf{R}_1 = a\left(\frac{\sqrt{3}}{2}, \frac{1}{2}\right) \quad \text{and} \quad \mathbf{R}_2 = a\left(\frac{\sqrt{3}}{2}, -\frac{1}{2}\right). \tag{E.2}$$

The Zeeman splitting of the atomic levels is given by

$$\xi_{\alpha,\beta} = -\mathrm{i}\mu B(\delta_{\alpha x}\delta_{\beta y} - \delta_{\alpha y}\delta_{\beta x}). \tag{E.3}$$

To simplify Eq. (E.1), we write the atomic transition frequency as

$$\tilde{\omega}_A = \omega_A + \delta\omega_{\mathrm{PC}}, \tag{E.4}$$

where ω_A is the 'bare' atomic transition in bulk diamond and $\delta\omega_{\mathrm{PC}}$ is the energy shift of the individual atoms due to the presence of the photonic crystal environment. We make use of the fact that

$$\frac{3\pi\gamma\hbar c}{\omega_A n_{\mathrm{d}}} G_{\alpha\beta}(\mathbf{0}) = \delta\omega_{\mathrm{PC}} - \mathrm{i}\frac{\Gamma_{\mathrm{PC}}}{2} \tag{E.5}$$

to rewrite Eq. (E.1) as

$$M_{\alpha\beta}(\mathbf{k}) = \omega_A\ \delta_{\alpha\beta} + \xi_{\alpha,\beta} + \frac{3\pi\gamma c}{\omega_A n_{\mathrm{d}}} \sum_{\mathbf{R}} e^{\mathrm{i}\mathbf{k}\cdot\mathbf{R}} G_{\alpha\beta}(\mathbf{R}). \tag{E.6}$$

Generally, it is difficult to find an exact expression for the Green's function in real space, even numerically. Therefore, it is convenient to transform the summation over real-space lattice vectors $\{\mathbf{R}\}$ to a summation over momentum-space reciprocal lattice vectors $\{\mathbf{G} = n_1\mathbf{G}_1 + n_2\mathbf{G}_2\}$, where

$$\mathbf{G}_1 = \frac{2\pi}{a}\left(\frac{1}{\sqrt{3}}, 1\right) \quad \text{and} \quad \frac{2\pi}{a}\left(\frac{1}{\sqrt{3}}, -1\right). \tag{E.7}$$

The momentum-space summation can be performed over the Fourier-transform of the Green's function in momentum space.

In particular, we substitute into Eq. (E.6) the following expression

$$G_{\alpha\beta}(\mathbf{r}) = \int_{BZ} \frac{d^2\mathbf{p}}{(2\pi)^2} g_{\alpha\beta}(\mathbf{p}) e^{\mathrm{i}\mathbf{p}\cdot\mathbf{r}}, \tag{E.8}$$

where the integral is performed over the irreducible Brillouin zone of the photonic crystal and $g_{\alpha\beta}(\mathbf{p})$ stands for the Green's function in momentum space. Next, we make use of the following form of Poisson's identity

$$\sum_{\mathbf{R}} e^{\mathrm{i}(\mathbf{k}+\mathbf{p})\cdot\mathbf{R}} = \frac{1}{\mathcal{A}} \sum_{\mathbf{G}} (2\pi)^2 \delta^{(2)}(\mathbf{p} + \mathbf{k} - \mathbf{G}) \tag{E.9}$$

to transform the summation to momentum space, where $\mathcal{A}$ is the area of the hexagonal unit cell in real space. We perform the integral to obtain

$$\begin{aligned} &\frac{1}{\mathcal{A}} \sum_{\mathbf{G}} \int_{BZ} d^2\mathbf{p}\; g_{\alpha\beta}(\mathbf{p}) \delta^{(2)}(\mathbf{p} - (\mathbf{G} - \mathbf{k})) \\ &\quad = \frac{1}{\mathcal{A}} g_{\alpha\beta}(-\mathbf{k}) = \frac{1}{\mathcal{A}} g_{\alpha\beta}(\mathbf{k}), \end{aligned} \tag{E.10}$$

where the first equality follows from the fact that only the Dirac delta with $\mathbf{G} = 0$ contributes to the integral (since the integral is restricted to the irreducible Brillouin zone), and the second equality follows from time-reversal symmetry of the photonic

crystal spectrum [14]. Using this expression, we can rewrite Eq. (E.6) as

$$M_{\alpha\beta}(\mathbf{k}) = \omega_A\, \delta_{\alpha\beta} + \xi_{\alpha,\beta} + \frac{3\pi\gamma c}{\omega_A n_{\mathrm{d}}} \frac{1}{\mathcal{A}} g_{\alpha\beta}(\mathbf{k}). \tag{E.11}$$

Finally, we expess the momentum-space Green's function in terms of its eigenvalue expansion [196] as

$$g_{\alpha\beta}(\mathbf{k}) = \mathcal{A}c^2 \sum_n \frac{E^{(n)*}_{\mathbf{k},\alpha}(\mathbf{r}_A)\, E^{(n)}_{\mathbf{k},\beta}(\mathbf{r}_A)}{\omega_A^2 - \left(\omega^{(n)}_{\mathbf{k}}\right)^2}, \tag{E.12}$$

where $E^{(n)}_{\mathbf{k},\alpha}(\mathbf{r})$ denotes the α component ($\alpha = x, y$) of the electric field of the photonic crystal mode in the n^{th} band at quasi-momentum $\mathbf{k}$, while $\omega^{(n)}_{\mathbf{k}}$ is the corresponding frequency of the mode.

Even though $E^{(n)}_{\mathbf{k},\alpha}(\mathbf{r})$ gives the electric field distribution inside the entire real-space unit cell, we only sample the field at the position of the emitter ($\mathbf{r} = \mathbf{r}_A$), which we choose to be at the geometric center of the hexagonal cell and $z = 0$ to ensure that the emitter only couples to TE-like modes [41].

Due to the underlying periodicity of the photonic crystal lattice, the electric field mode can be expressed in a canonical Bloch form as

$$E^{(n)}_{\mathbf{k},\alpha}(\mathbf{r}) = \frac{u^{(n)}_{\mathbf{k},\alpha}(\mathbf{r})}{\sqrt{a^3}} e^{\mathrm{i}\mathbf{k}\cdot\mathbf{r}}, \tag{E.13}$$

where $a = |\mathbf{R}|$ is the periodicity of the lattice and $\mathbf{u}^{(n)}_{\mathbf{k}}(\mathbf{r} + \mathbf{R}) = \mathbf{u}^{(n)}_{\mathbf{k}}(\mathbf{r})$ is a dimensionless periodic vector function that is normalized to ensure that

$$\int_{\mathcal{V}} d^3\mathbf{r}\; \varepsilon(\mathbf{r})\, \mathbf{E}^{(n)}_{\mathbf{k}}(\mathbf{r}) \cdot \mathbf{E}^{(n)*}_{\mathbf{k}'}(\mathbf{r}) = \delta_{\mathbf{k}\mathbf{k}'}, \tag{E.14}$$

where $\varepsilon(\mathbf{r} + \mathbf{R}) = \varepsilon(\mathbf{r})$ is the periodic dielectric permittivity function describing the photonic crystal in real space and the integral is performed over the quantization volume [97, 196].

E.1.2 Numerical calculations using MPB

We use the open-source MIT Photonic Bands 1.4.2 (MPB) numerical software package [194] to directly obtain the expressions for $\omega_{\mathbf{k}}^{(n)}$ and the normalized $u_{\mathbf{k},\alpha}^{(n)}(\mathbf{r}_A)$ [1]. MPB is an iterative eigensolver that uses a planewave basis to iteratively improve approximations to the eigenstates and eigenvalues of Maxwell's equations. MPB approximates the solution using a planewave cutoff, which corresponds to the spatial discretization of the unit cell. In our simulations, we take a supercell of height 4a and run the calculations with a supercell discretization resolution of $256 \times 256 \times 64$.

In particular, we perform the numerical calculations by defining a rhombic 2D supercell that contains a 3×3 triangular array of holes with hole spacing $d = a/3$. We remove the central hole and push the surrounding 6 holes radially outward (Fig. E-1), such that the center of these 6 holes is a distance $1.2d$ away from the center. The radii of these 6 holes is increased to $r_{\mathrm{l}} = 0.35d$. We leave the other two holes in place, which have a radius of $r_{\mathrm{s}} = 0.25d$. The slab is composed of three different layers. In the middle, we define a diamond ($\varepsilon_{\mathrm{d}} = 5.76$) layer of thickness $0.5a$, which is sandwiched between two GaP ($\varepsilon_{\mathrm{GaP}} = 10.5625$) layers of thickness $0.315a$. In the resulting band structure, the tip of the Dirac cone is at $\omega a/(2\pi c) = 0.32545$. The eigenenergies $\omega_{\mathbf{k}}^{(n)}$ and the corresponding field intensities $|u_{\mathbf{k},\alpha}^{(n)}(\mathbf{r}_A)|^2$ of the TE-like modes at the location of the emitters ($\mathbf{r}_A = \mathbf{0}$) are plotted in Fig. 6-2(a). After substituting $\omega_{\mathbf{k}}^{(n)}$ and $u_{\mathbf{k},\alpha}^{(n)}(\mathbf{r}_A)$ into Eq. (E.13) and Eq. (E.11), we diagonalize the 2×2 matrix in Eq. (E.12) and we obtain two eigenvalues $\omega_{\mathbf{k}}^{(m)}$ ($m = 1, 2$) for each $\mathbf{k}$. The results are plotted in Fig. 6-2(b) for a non-zero magnetic field.

E.1.3 All-diamond photonic crystal slab

Note that it is also possible to use an all-diamond photonic crystal with SiVs, which would significantly simply the fabrication process. An all-diamond structure with the cavity-like arrangement of air holes shown in Fig. E-1 would also have a stand-alone Dirac cone and give rise to dipolar interactions with winding phases (Chapter 5).

[1] S. G. Johnson, Official MPB Documentation (online), https://mpb.readthedocs.io/en/latest/Scheme_User_Interface/#field-normalization

However, given that diamond has a lower refractive index than GaP, tuning the photonic Dirac cone resonant with the SiVs would require a photonic structure with significantly larger lattice spacing a than for the hybrid structure. This reduces the size of the irreducible Brillouin zone in k-space to the extent that the entire Brillouin zone falls within the light cone region ($k < 2\pi/\lambda$). This, in turn, implies that all of the edge states of the system could couple to free-space photons (see Section E.4 for more details).

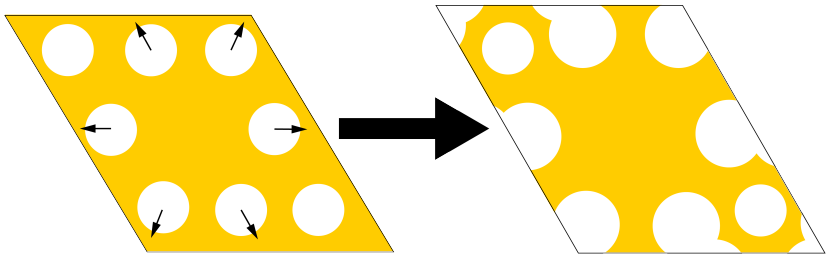

Figure E-1: Constructing the unit cell for the photonic crystal. We take a rhombic supercell with a 3×3 triangular array of holes with spacing d and radius $0.25d$. The central hole is removed and the surrounding 6 holes are pushed radially outward to a distance of $1.2d$, while also increasing their radii to $0.35d$. The spacing between units cells is $a = 3d$.

E.2 Model validity and maximum gap size

In Fig. 6-3(b) we found that the size of the gap is inversely proportional to δ_A, the detuning of the atomic frequency from the tip of the photonic Dirac cone. Eventually, as δ_A is decreased, our theory breaks down, limiting the maximum achievable gap size. In this section we discuss for what parameters this breakdown occurs.

The non-Hermitian Hamiltonian in Eq. (6.1) describes the evolution of the system in the absence of quantum jumps and is obtained from the canonical master equation for open quantum systems [114]. Since the derivation of the master equation assumes the validity of the Born-Markov approximation [38], our results are guaranteed to be valid only as long as these approximations hold. However, the Born-Markov approx-

imation is known to break down as the atomic emitters are tuned close to the Dirac vertex [193].

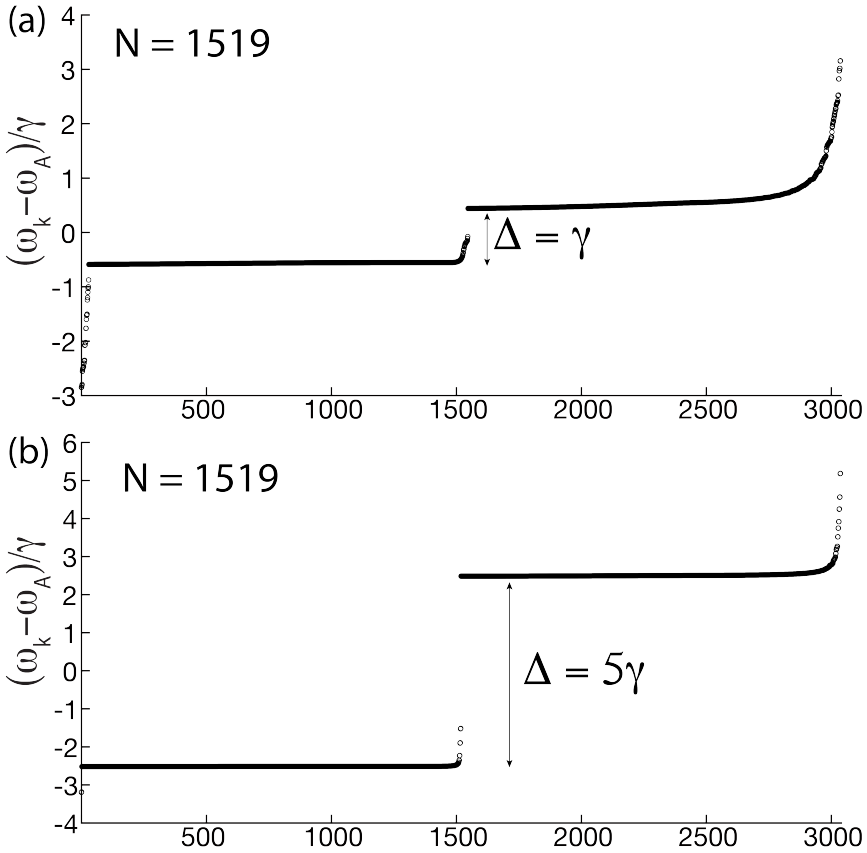

Figure E-2: (a) Spectrum for a hexagonal array of $N = 1519$ emitters with $\delta_A = 18.73$THz, $\Delta = \gamma$, $\mu B = 0.5\gamma$ and $a = \lambda/3$. Eigenstates are sorted in ascending order. The edge states form a dense set in the bottom half of the gap, leading to the dispersive time-evolution of the edge states shown in Fig. 6-5(a). (b) Spectrum for a hexagonal array of $N = 1519$ emitters with $\delta_A = 3.78$THz, $\Delta = 5\gamma$, $\mu B = 2.5\gamma$ and $a = \lambda/3$. The edge states are sparse in the bottom half of the gap due to the reduced density of states for the resonant photonic slab modes. Excitation of the edge states leads to the characteristic few-mode dynamics depicted in Fig. E-3. For both (a) and (b), the emitters are assumed to be embedded in the same photonic crystal as in Fig. 6-1, with $v_s = 0.25c$ and $|E_0|^2 = 0.1855/a^3$.

The Born approximation assumes that the state of the environment (i.e. the collection of photonic crystal modes) is not significantly affected by its interaction with the emitters. This assumption is guarenteed to hold as long as the photonic crystal is much larger than the emitter array.

The Markov approximation assumes that the correlation time τ_c between the

environment and the emitters is much smaller than the typical time scale for the evolution of the system τ_A, (i.e. $\tau_c \ll \tau_A$). Here, the correlation time τ_c of the environment corresponds to the time it takes for a photon to leave the emitter array, since for $t < \tau_c$ the photon can still be reabsorbed by another emitter. Denoting the characteristic size of the emitter array with L, we find that $\tau_c \sim L/v_\mathrm{s}$, where v_s is the group velocity of the guided modes of the photonic crystal slab.

Our focus here is the excitation and time evolution of edge states, for which the relevant time scale is $\tau_\mathrm{s} \sim \Delta^{-1}$, where Δ is the energy gap (recall that the group velocity of the edge states is proportional to Δ). Thus the Markov approximation requires that

$$\Delta \ll v_\mathrm{s}/L. \tag{E.15}$$

Note that the system size L and the gap size Δ cannot be varied independently. The gap size scales as $\Delta \sim 1/\delta_A$, and as δ_A is reduced, the density of photonic states (DOS) through which the emitters interact decreases as DOS $\sim \delta_A \sim 1/\Delta$. To illustrate how the DOS of the photonic slab modes influences the edges states of our system, in Fig. E-2(a) and (b) we plot the spectrum for $N = 1519$ emitters for $\Delta = \gamma$ ($\delta_A = 18.73$THz) and $\Delta = 5\gamma$ ($\delta_A = 3.78$THz), respectively. All eigenstates are ordered in ascending order. The energy gap is indicated in both spectra with a double arrow. All eigenstates inside the gap are edge modes. The parameters in Fig. E-2(a) correspond to those used for the time-domain simulation in Fig. 6-5. Note that the edge states are densely packed in the lower half of the gap. This leads to dispersive edge state propagation on the system boundaries (see Fig. 6-5 for reference). In contrast, Fig. E-2(b) shows the spectrum when δ_A is reduced by a factor a 5, leading to a 5 times larger band gap, but also to 5 times fewer edge states in the gap. Fig. E-3 shows a snapshot from the time-dynamics when these edge states are excited. Given that only a few modes are excited, no dispersive propagation is observed. Instead, patches of delocalized excitations are formed that appear and disappear as the system evolves in time. This interference effect is the expected behavior for the time evolution

of a limited set of modes that have similar energies.

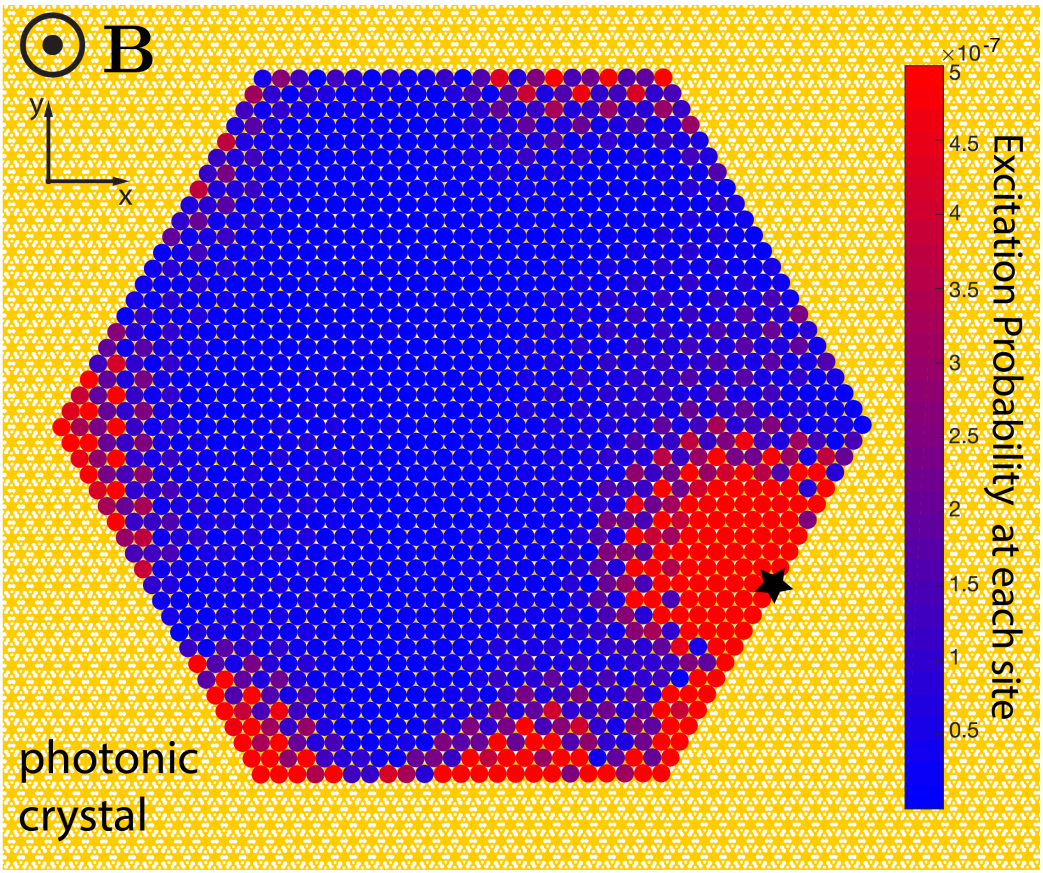

Figure E-3: (a) Time-evolved state ($t = 306\gamma^{-1}$) of a hexagonal-shaped triangular lattice of emitters ($N = 1519$), showing the non-dispersive edge state dynamics when the density of photonic states mediating emitter interactions is small. A single emitter at the edge (black star) is addressed by a laser of stength Ω and frequency ω_L. Relevant parameters are $\delta_A/2\pi = 3.78$THz, $v_s = 0.25c$, $|E_0|^2 = 0.1855/a^3$, $\Delta = 5\gamma$, $\mu B = 2.5\gamma$, $\Omega = 0.0295\gamma$ and $\omega_L = \omega_A - 1.85\gamma$. The laser drive is switched on adiabatically with the profile $\Omega(t) = \Omega \exp(-[t - t_0]^2/[2\Sigma^2])$, where $t_0 = 127.5\gamma^{-1}$ and $\Sigma = 23.3\gamma^{-1}$.

In order to keep the number of edge states inside the gap constant while Δ is increased, the number of emitters has to be increased as $N \sim \Delta$. In general, the required number of emitters for dispersive edge state propagation scales approximately as $N \approx \Lambda n$, where we introduced n to parameterize the size of the gap as $\Delta = n\gamma$ and $\Lambda \approx 1600$ is a phenomenological constant that we deduce from Fig. E-2(a), where $N \approx 1600\Delta/\gamma$. Since the size of the emitter array scales as $L \sim \sqrt{N}a$, we can rewrite

Eq. (E.15) as

$$n\gamma \ll v_{\mathrm{s}}/(\sqrt{\Lambda n}a), \tag{E.16}$$

which, after rearrangement, yields

$$n \ll \left(\frac{v_{\mathrm{s}}}{a\gamma\sqrt{\Lambda}}\right)^{2/3}. \tag{E.17}$$

Substituting $v_{\mathrm{s}} = 0.25c$, $\gamma/2\pi = 300\mathrm{THz}$, $a = \lambda/3$, $\lambda = 738\mathrm{nm}$ and $\Lambda \approx 1600$, we find that in our system the Markov approximation holds as long as the gap size satisfies

$$\Delta \ll 250\gamma. \tag{E.18}$$

E.3 Calculation of edge states

In this section we describe how to numerically calculate the edge states of the system and analyze them in detail.

We consider stripes of atoms that are infinite along one direction and finite in the other as shown schematically in Fig. E-4. The periodic unit cells of the stripes are identified with black rectangles. The unit cells for both orientations are also shown with $m = 17$ atoms. The set of unit cells form a periodic 1D lattice. For the stripe along the x axis the 1D lattice vector is $\mathbf{R}_x = a\hat{x}$, whereas for the the y axis it is $\mathbf{R}_y = \sqrt{3}a\hat{y}$. Here, we describe the calculation of the edge states for the stripe oriented along the y axis. The calculation for the other stripe orientation proceeds analogously.

For the stripe oriented along the y axis, the Bloch ansatz takes the following form

$$|\psi_{k_y}\rangle = \sum_{l=0,\pm1,\ldots} \sum_{b=1}^{m} e^{\mathrm{i}k_y l R_y} \left(c_+^b |\sigma_{+,l}^b\rangle + c_-^b |\sigma_{-,l}^b\rangle\right), \tag{E.19}$$

where the summation over l is implied over all unit cells, which are placed $|\mathbf{R}_y| = R_y = \sqrt{3}a$ apart along the y axis, k_y is the Bloch quasi-momentum and b labels each of the

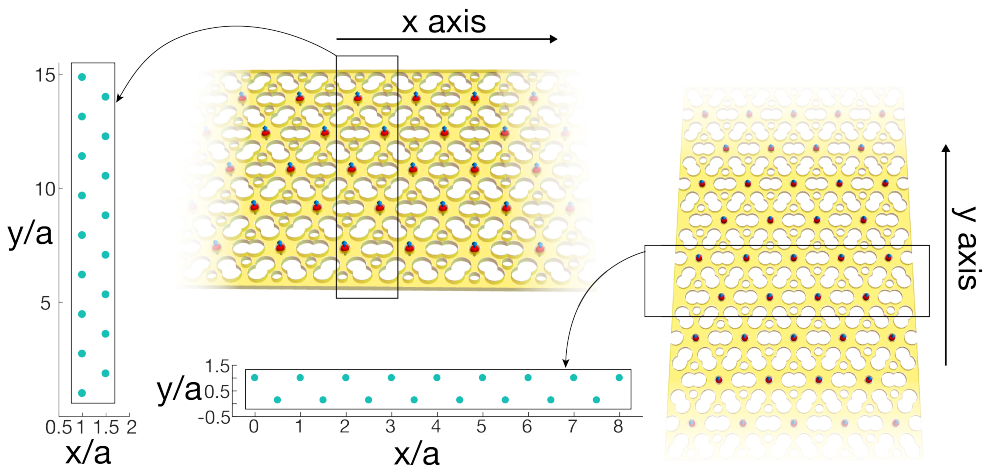

Figure E-4: Unit cells for stripes of emitters with two different orientations relative to the triangular lattice. The set of unit cells form 1D lattices with lattice spacing $R_x = a$ along the x axis and $R_y = \sqrt{3}a$ along the y axis.

m emitters inside the unit cell. Acting on Eq. (E.19) with the Hamiltonian (Eq. 6.1), neglecting the term responsible for coupling to free-space photons and making use of Eq. (E.5), we find that the eigenvalues of the stripe can be obtained by diagonalizing the following $(2 \times m) \times (2 \times m)$ Hamiltonian

$$\begin{aligned} M_{\alpha\mu,\beta\nu}(k_y) &= \sum_{b=1}^{m} \omega_A \delta_{\alpha\beta}\delta_{b\mu}\delta_{b\nu} \\ &\quad + \frac{3\pi\gamma c}{\omega_A n_\mathrm{d}} \sum_{b=1}^{m}\sum_{b'=1}^{m} \Lambda_{\alpha b,\beta b'}\delta_{b\mu}\delta_{b'\nu}, \end{aligned} \tag{E.20}$$

where we have defined

$$\Lambda_{\alpha b,\beta b'}(k_y) = \sum_{l} e^{\mathrm{i}k_y l R_y} G_{\alpha\beta}(l R_y \hat{y} + \mathbf{r}_b - \mathbf{r}_{b'}), \tag{E.21}$$

where $\mathbf{r}_b = x_b\hat{x} + y_b\hat{y}$ and $\mathbf{r}_{b'} = x_{b'}\hat{x} + y_{b'}\hat{y}$ denote emitter coordinates within a single cell.

Similar to the 2D band structure calculation (see Section E.1), it is convenient to transform the real-space summation that runs over l to a summation in momentum space. In order to perform this transformation over the lattice sites along the y-axis, we need to find an expression for the Green's function that depends on p_y and x.

Thus, we need to Fourier transform the Green's function along the y-axis only. We express the Green's function as

$$G_{\alpha\beta}(x,y) = \int \frac{dp_y}{2\pi} g_{\alpha\beta}(p_y;x) e^{\mathrm{i}p_y y}, \tag{E.22}$$

where

$$g_{\alpha\beta}(p_y;x) = \int \frac{dp_x}{2\pi} g_{\alpha\beta}(p_x,p_y) e^{\mathrm{i}p_x x}. \tag{E.23}$$

In addition, we also make use of Poisson's summation formula in the following form

$$\sum_l e^{\mathrm{i}p_y R_y l} = \frac{1}{R_y} \sum_{G_y} 2\pi\delta(p_y - G_y), \tag{E.24}$$

where $\{G_y\}$ is the set of reciprocal lattice vectors along the k_y axis. Using these expressions, we obtain

$$\begin{aligned} \Lambda_{\alpha b,\beta b'} &= \frac{1}{R_y} \sum_{G_y} g_{\alpha\beta}(G_y - k_y; x_b - x_{b'}) e^{\mathrm{i}(G_y - k_y)(y_b - y_{b'})} \\ &= \frac{1}{R_y} g_{\alpha\beta}(k_y; x_b - x_{b'}) e^{-\mathrm{i}k_y(y_b - y_{b'})}, \end{aligned} \tag{E.25}$$

where the second equality follows from the fact that only the irreducible Brillouin zone, where $G_y = 0$, contributes to the summation and from the observation that $g(-k_y;x) = g(k_y;x)$ due to the time-reversal symmetry of the photonic crystal spectrum.

To proceed, we need to numerically evaluate Eq. (E.23). Substituting Eq. (E.12) into Eq. (E.23), we obtain

$$g_{\alpha\beta}(p_y;x) = \mathcal{A}c^2 \int \frac{dp_x}{2\pi} \sum_n \frac{E^{(n)*}_{\mathbf{p},\alpha}(\mathbf{r}_A)\, E^{(n)}_{\mathbf{p},\beta}(\mathbf{r}_A)}{\omega_A^2 - \left(\omega^{(n)}_{\mathbf{p}}\right)^2} e^{\mathrm{i}p_x x},$$

where $\mathbf{p} = (p_x, p_y)$ and the summation runs over all bands. The sum is dominated

by the two bands that constitute the Dirac cone (which we label (+) and (−)), and there are two inequivalent Dirac cones at the $\mathbf{K}$ and $\mathbf{K}'$ points. Therefore, to a good approximation, we can rewrite the above expression as

$$\begin{aligned} g_{\alpha\beta}(p_y;x) &= g_{\alpha\beta}^{(\mathbf{K},+)}(p_y;x) + g_{\alpha\beta}^{(\mathbf{K},-)}(p_y;x) \\ &+ g_{\alpha\beta}^{(\mathbf{K}',+)}(p_y;x) + g_{\alpha\beta}^{(\mathbf{K}',-)}(p_y;x), \end{aligned} \tag{E.26}$$

where we have defined

$$g_{\alpha\beta}^{(\mathbf{K},\pm)}(p_y;x) = \mathcal{A}c^2 \int \frac{dp_x}{2\pi} \frac{E_{\mathbf{p},\alpha}^{(\mathbf{K},\pm)*}(\mathbf{r}_A)\, E_{\mathbf{p},\beta}^{(\mathbf{K},\pm)}(\mathbf{r}_A)}{\omega_A^2 - \left(\omega_{\mathbf{p}}^{(\mathbf{K},\pm)}\right)^2} e^{\mathrm{i}p_x x},$$

and

$$g_{\alpha\beta}^{(\mathbf{K}',\pm)}(p_y;x) = \mathcal{A}c^2 \int \frac{dp_x}{2\pi} \frac{E_{\mathbf{p},\alpha}^{(\mathbf{K}',\pm)*}(\mathbf{r}_A)\, E_{\mathbf{p},\beta}^{(\mathbf{K}',\pm)}(\mathbf{r}_A)}{\omega_A^2 - \left(\omega_{\mathbf{p}}^{(\mathbf{K}',\pm)}\right)^2} e^{\mathrm{i}p_x x}.$$

To proceed, we need to utilize the analytic approximations developed in Chapter 5 for the band dispersion and electric field near the $\mathbf{K}$ and $\mathbf{K}'$ points. The band dispersion near the $\mathbf{K}$ point is well approximated by

$$\omega_{\mathbf{p}}^{(\mathbf{K},\pm)} = \omega_{\mathrm{Dirac}} \pm v_{\mathrm{s}} \sqrt{(p_x - p_{\mathbf{K},x})^2 + (p_y - p_{K,y})^2},$$

where $\mathbf{p}_{\mathbf{K}} = (p_{\mathbf{K},x}, p_{\mathbf{K},y})$ is the quasi-momentum associated with the $\mathbf{K}$ point inside the irreducible Brillouin zone. Similarly, near the $\mathbf{K}'$ point we have

$$\omega_{\mathbf{p}}^{(\mathbf{K}',\pm)} = \omega_{\mathrm{Dirac}} \pm v_{\mathrm{s}} \sqrt{(p_x - p_{\mathbf{K}',x})^2 + (p_y - p_{\mathbf{K}',y})^2},$$

where $\mathbf{p}_{\mathbf{K}'} = (p_{\mathbf{K}',x}, p_{\mathbf{K}',y})$. The electric field of the guided modes near the $\mathbf{K}$ point is well-approximated by

$$\mathbf{E}_{\mathbf{p}}^{(\mathbf{K},\pm)}(\mathbf{r}_A) = E_0 \left[\sin\left(\frac{\Phi_{\mathbf{K}}}{2} \mp \frac{\pi}{4}\right) \hat{x} \pm \sin\left(\frac{\Phi_{\mathbf{K}}}{2} \pm \frac{\pi}{4}\right) \hat{y} \right],$$

where

$$\Phi_{\mathbf{K}}(p_x, p_y) = \arctan\left(\frac{p_y - p_{\mathbf{K},y}}{p_x - p_{\mathbf{K},x}}\right),$$

whereas the electric field of the modes near the $\mathbf{K}'$ point is given by

$$\mathbf{E}_{\mathbf{p}}^{(\mathbf{K}',\pm)}(\mathbf{r}_A) = E_0\left[\sin\left(\frac{\Phi_{\mathbf{K}'}}{2} \pm \frac{\pi}{4}\right)\hat{x} \mp \sin\left(\frac{\Phi_{\mathbf{K}'}}{2} \mp \frac{\pi}{4}\right)\hat{y}\right],$$

where

$$\Phi_{\mathbf{K}'}(p_x, p_y) = \arctan\left(\frac{p_y - p_{\mathbf{K}',y}}{p_x - p_{\mathbf{K}',x}}\right).$$

The numerical evaluation of $g_{\alpha\beta}^{(\mathbf{K},\pm)}$ and $g_{\alpha\beta}^{(\mathbf{K}',\pm)}$ is somewhat subtle, as the integrands contain poles, branch cuts and branch points. Thus, special care has to be taken to define the appropriate integration contour. Here we describe how to evaluate $g_{\alpha\beta}^{(\mathbf{K},\pm)}$ (i.e. the contributions from the $\mathbf{K}$ point). Evaluating $g_{\alpha\beta}^{(\mathbf{K}',\pm)}$ proceeds analogously.

First, note that the integral $g_{\alpha\beta}^{(\mathbf{K},-)}(p_y; x)$ has a pole when $\omega_A = \omega_{\mathbf{p}}^{(\mathbf{K},-)}$, i.e. when the atomic frequency is resonant with the photonic modes of the lower half of the Dirac cone. While these resonant states occupy a circle in the $p_x - p_y$ space, since we are integrating along the p_x axis, there are at most two such singular points along the integration path. These two points are located at

$$p_x^{\pm} = p_{\mathbf{K},x} \pm \sqrt{\frac{1}{v_{\mathrm{s}}^2}(\omega_{\mathrm{Dirac}} - \omega_A)^2 - (p_{\mathbf{K},y} - p_y)^2},$$

whenever the expression under the square root sign is positive (otherwise there are no poles). These poles in the integrand can be avoided by using an 'ϵ-prescription'. In particular, we introduce a small imaginary term $+\mathrm{i}\epsilon$ with $\epsilon > 0$ into the denominator of the integrand to obtain

$$g_{\alpha\beta}^{(\mathbf{K},-)}(p_y; x) = \mathcal{A}c^2 \int \frac{dp_x}{2\pi} \frac{E_{\mathbf{p},\alpha}^{(\mathbf{K},\pm)*}(\mathbf{r}_A)\, E_{\mathbf{p},\beta}^{(\mathbf{K},\pm)}(\mathbf{r}_A)}{\omega_A^2 - \left(\omega_{\mathbf{p}}^{(\mathbf{K},\pm)}\right)^2 + \mathrm{i}\epsilon} e^{\mathrm{i}p_x x}.$$

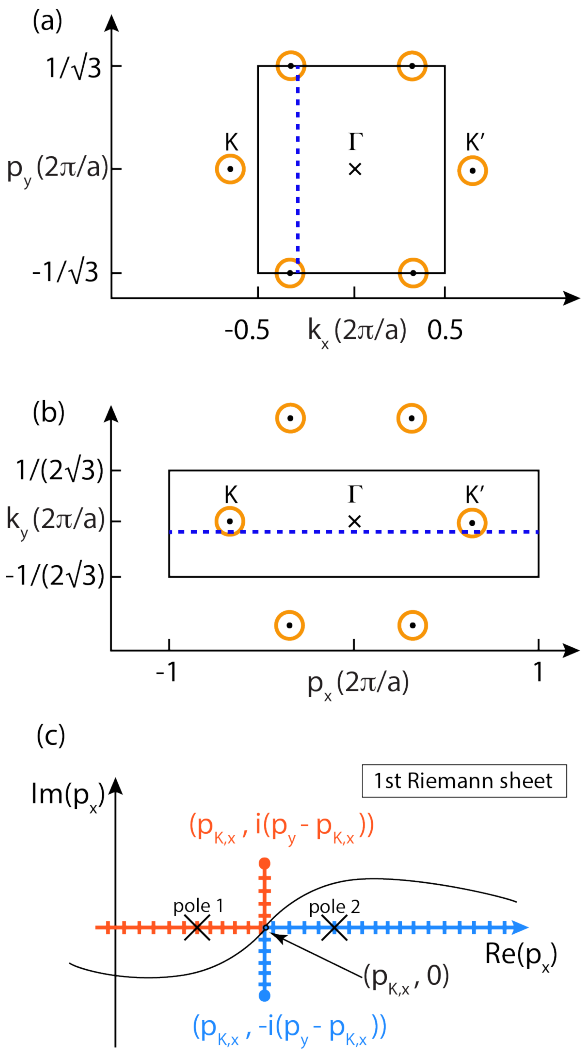

Figure E-5: (a) Integration inside the 2D Brillouin zone to obtain edge states along the k_x axis. Black dots mark the $\mathbf{K}$ and $\mathbf{K}'$ points, whereas orange circles indicate the set of modes in the photonic Dirac cone that are resonant with the emitters. The eigenmodes can be obtained for any Bloch vector $k_x \in [-\pi/a, \pi/a]$, by integrating the interval between $-2\pi/(\sqrt{3}a) \leq p_y \leq 2\pi/(\sqrt{3}a)$. Blue dotted line shows an example of such an integration path. (b) Integration inside the 2D Brillouin zone to obtain edge states along the k_y axis. The eigenmodes can be obtained for any Bloch vector $k_y \in [-\pi/(\sqrt{3}a), \pi/(\sqrt{3}a)]$, by integrating the interval between $-2\pi/a \leq p_y \leq 2\pi/a$. (c) Integration contour near the $\mathbf{K}$ point for the blue dotted line shown in (b). Poles are indicated by black crosses, the branch cuts and branch points the arise from the square root function are shown in red and blue.

This prescription makes the integral well-defined and corresponds to the *causal* Green's function, which represents the outgoing radiation from a point source [151]. The relevant integration path (that is equivalent to the ϵ-prescription via a contour defor-

mation) is indicated in Fig. E-5(c). Note that for $g_{\alpha\beta}^{(\mathbf{K},+)}(p_y;x)$ the integrand has no poles. However, we may use the same ϵ-prescription prescription for simplicity.

Furthermore, it is also necessary to choose the appropriate branch when taking the square root $\sqrt{(p_x-p_{\mathbf{K},x})^2+(p_y-p_{\mathbf{K},y})^2}$ to find $\omega_{\mathbf{p}}^{(\mathbf{K},\pm)}$. The square root function (with a quadratic function as its argument) introduces *two* branch cuts that emanate from two branch points at $\pm\mathrm{i}(p_y-p_{\mathbf{K},y})$, as shown in see Fig. E-5(c). Causality of the Green's function requires that we follow the ϵ-prescription path on the first Riemann sheet [151]. Doing so corresponds to enforcing

$$\mathrm{Re}(\sqrt{(p_x-p_{\mathbf{K},x})^2+(p_y-p_{\mathbf{K},y})^2})\geq 0$$

and

$$\mathrm{Im}(\sqrt{(p_x-p_{\mathbf{K},x})^2+(p_y-p_{\mathbf{K},y})^2})\geq 0.$$

Note that the two branch cuts come infinitesimally close at $(\mathrm{Re}(p_x),\mathrm{Im}(p_x))=(p_{\mathbf{K},x},0)$, which makes this point ill-defined. Therefore, it is essential to break the integration contour into separate paths, such that the first path ends at $(p_{\mathbf{K},x},0)$, whereas the second one starts from there.

In addition, we also need to ensure that the appropriate branches are chosen when evaluating the inverse tangent function to obtain $\Phi_{\mathbf{K}}$. In particular, we need to ensure that $\Phi_{\mathbf{K}}\in[-\pi,\pi]$.

With these prescriptions, the integral $g_{\alpha\beta}^{(\mathbf{K},\pm)}(p_y;x)$ can be numerically evaluated (see Fig. E-5(b) for the relevant integration limits). Analogous prescriptions apply to $g_{\alpha\beta}^{(\mathbf{K}',\pm)}(p_y;x)$. Then, substituting Eq. (E.26) into Eq. (E.25), we can diagonalize the matrix $M_{\alpha\beta}(k_y)$ in Eq. (E.20) for any $k_y\in[-2\pi/(2\sqrt{3}a),2\pi/(2\sqrt{3}a)]$ inside the 1D irreducible Brillouin zone, yielding $2m$ eigenvalues for each k_y.

Finally, we note that the calculation for the other stripe orientation can be performed analogously, where the only difference is that the integration is performed along the p_y axis with different limits and the $\mathbf{K}$ and $\mathbf{K}'$ points are located at the edges of the integration interval (see Fig. E-5(a)).

E.4 Analysis of edge states in the presence of free-space decay

In Chapter 6, we analyzed the topological edges states when emission to free space modes is neglected. Here, we discuss the effect of free-space emission on the decay rate of edge states.

Before proceeding, we note that standard high-performance calculations for the eigenmodes of photonic crystals, which are based on the plane-wave expansion method to numerically solve Maxwell's equations [194], do not accurately account for the coupling of non-guided modes to free-space photons within the light cone. While there exist techniques for numerically obtaining the out-of-plane decay rate of such modes based on finite-difference time-domain calculations [241], doing such calculations at a massive scale would require prohibitively large amounts of computational resources. Therefore, here we utilize prior results from Refs. [114, 199] on the decay rates of edge states, arising from cooperative atomic behavior, to analyze the edge states of our system in the presence of free-space decay. In particular, we will make use of the observation that edge modes inside the free-space light cone can decay out of plane at a decay rate comparable to the individual free-space linewidth of the atoms Γ_0, whereas modes outside the light cone cannot couple to free-space photons due to momentum mismatch [114, 199].

The edge states for the two different stripe orientations are illustrated in detail in Fig. E-6, where a small detuning of $\delta_A = 0.321$THz was used to analyze the edge states for a large gap of $\Delta = 50\gamma$. The properties of the edge states for the two different stripe orientations can be understood by considering the 2D Brillouin zone in momentum space and its projection onto the k_x and k_y axes as shown in Fig. E-6(a), (b) and (c) (note that we would obtain one of these two types of edge terminations when projecting along any of the 5 other edges or vertices of the 2D Brillouin zone). The light cone region with $|\mathbf{k}| < 2\pi/\lambda$ is shown in green and the modes of the photonic Dirac cone that are resonant with ω_A are marked with yellow circles. Edge states arise only near the Dirac cones (which are the sources of topology in our system). While

the projection of the light cone covers the entire 1D Brillouin zone on the k_y axis, it only covers the central part on the k_x axis. Furthermore, while the two inequivalent Dirac cones project to the center of the Brillouin zone on the k_y axis, on the k_x axis they project outside the light cone.

Fig. E-6(d) shows the localization of a typical edge states near the boundary. Fig. E-6(e) shows the edge states on the k_x-axis. Edge states on the top boundary of the strip are colored purple, whereas edge states on the bottom boundary are colored blue. The part of the Brillouin zone that falls inside the light cone ($k_x < 2\pi/\lambda$) is shaded green. Modes that fall outside the light cone ($k_x > 2\pi/\lambda$) cannot couple to free-space modes due to the momentum mismatch (note that $\langle k_x|k_x'\rangle = \delta_{k_x,k_x'}$ in the momentum basis), making these modes long-lived [114, 199]. In contrast, modes inside the light cone can couple to free-space photons and, therefore, their decay rate is on the order of Γ_0 [114, 199]. The edge states have non-negligible dispersion only in the immediate vicinity of the $\mathbf{K}$ and $\mathbf{K}'$ points. Fig. E-6(f) provides a zoomed-in view of the edge modes near the $\mathbf{K}'$ point. Inside the yellow region, atomic bands overlap with guided modes of the Dirac cone with the same energy and momentum, and coupling to these modes effectively dissolves the atomic bands (their broadening exceeds the gap size). Fig. E-6(f) also shows that the edge states traverse the lower half of the gap outside the light cone and only cross into the yellow region near the center of the gap. Therefore, the edge states in the lower half of the gap are long-lived [199].

Figs. E-6(g) and (h) show the edge states on the k_y axis. The edge states have non-negligible dispersion only near the $\mathbf{K}$ and $\mathbf{K}'$ points, which are both projected to the center of the Brillouin zone for this geometry. Thus all edge modes fall inside the light cone and have an out-of-plane decay rate of approximately Γ_0.

Crucially, for these parameters the edge states traverse an energy interval of $\delta\omega = 25\gamma$ over a momentum interval of $\delta k \approx 0.002(2\pi/a)$, leading to a large group velocity of $v_g \approx \delta\omega/\delta k \approx 2000a/\gamma^{-1}$. Therefore, making the conservative assumption that $\Gamma_0 \approx \gamma$, an excitation would hop 2000 sites before decaying into far-field photons even if carried by edge modes that can decay to free-space photons.

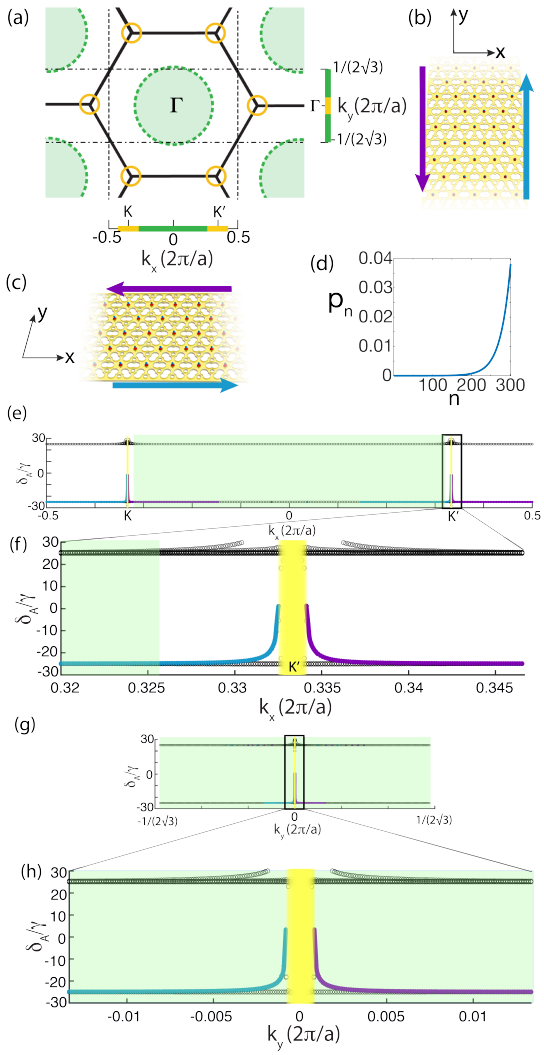

Figure E-6: (a) Projection of the 2D Brillouin zone onto the k_x and k_y axes. The light cone region ($|\mathbf{k}| < 2\pi/\lambda$) is shaded green, while guided slab modes resonant with ω_A are marked with yellow circles. The projection of the light cone spans the entire Brillouin zone on the k_y-axis, while covering only the central portion on the k_x axis. (b) & (c) Schematic illustration of infinite stripes of atoms along the y and x axes, respectively. (d) Typical edge state probability amplitude distribution for a stripe with 300 atoms in the transverse direction, showing localization at one edge. (e) Edge states inside the 1D Brillouin zone on the k_x axis. Edge states traverse the gap very close to the $\mathbf{K}$ and $\mathbf{K}'$ points. The lossy region falling inside the light cone is shaded green. (f) Zoomed-in view of the edge states near the $\mathbf{K}'$ point. Edge states on the top (bottom) boundaries are colored purple (blue). Yellow shading indicates region where bands rapidly decay into guided slab modes (the broadening of the modes exceeds the gap size). (d)-(f) Results for a strip along the y axis. The entire Brillouin zone falls insider the light cone making all edge states lossy.

In general, as δ_A is decreased to increase the gap size Δ, the group velocity of the edge states increases as $\sim 1/\delta_A^2$. To understand this scaling, note that $v_g \approx \delta\omega/\delta k$, where $\delta\omega$ and δk are the energy and momentum intervals traversed by the edge states inside the Brillouin zone. Since $\delta\omega \sim \Delta \sim 1/\delta_A$ and $\delta k \sim \delta_A/v_\mathrm{s}$ (from $\omega_\mathbf{p} = \omega_\mathrm{Dirac} \pm v_\mathrm{s}|\mathbf{k}|$), we obtain $v_g \sim 1/\delta_A^2$.

These considerations show that in order to obtain long-lived topological edge states in our system, the lattice edges should be terminated as shown in Fig. E-6(c). For such an edge termination, long-lived edge states can be excited, where losses arise only from finite-size effects, such as corners, and imperfections in the periodic lattice [199]. The key strategy for ensuring that excitations propagate a significant distance, even in the presence of corners and defects, is to maximize the group velocity of the edge states by increasing the gap size. Thus, lossy regions, where decay occurs on a $t \sim \Gamma_0^{-1}$ time scale, will be traversed quickly by the excitation, leading to negligible emission [199].

Recall, however, that obtaining a large energy gap requires δ_A to be small, which leads to a small density of states. Thus, a large system is needed to ensure that there are a sufficient number of edge modes in the gap to enable the dispersive propagation of the excitations on the boundaries. Given the limits on system sizes that can be readily simulated with state-of-the-art computational resources, in Chapter 6 (Figs. E-6 and 6-5) we focused on systems with a large detuning and small band gap, and ignored emission into free-space modes. However, as the preceding analysis shows (see also Ref. [199]), the inclusion of emission into free space does not significantly change the results as long as $\Delta \gg \Gamma_0$.

Bibliography

[1] N. Gisin and R. Thew, "Quantum communication," Nature Photonics **1**, 165–171 (2007).

[2] P. W. Shor and P. W., "Polynomial-Time Algorithms for Prime Factorization and Discrete Logarithms on a Quantum Computer," SIAM Journal on Computing **26**, 1484–1509 (1997).

[3] I. Georgescu, S. Ashhab, and F. Nori, "Quantum simulation," Reviews of Modern Physics **86**, 153–185 (2014).

[4] C. Nayak, S. H. Simon, A. Stern, M. Freedman, and S. Das Sarma, "Non-Abelian anyons and topological quantum computation," Reviews of Modern Physics **80**, 1083–1159 (2008).

[5] M. Z. Hasan and C. L. Kane, "*Colloquium*: Topological insulators," Reviews of Modern Physics **82**, 3045–3067 (2010).

[6] H. J. Kimble, "The quantum internet," Nature **453**, 1023–1030 (2008).

[7] L. Lu, J. D. Joannopoulos, and M. Soljačić, "Topological photonics," Nature Photonics **8**, 821–829 (2014).

[8] M. Soljačić and J. D. Joannopoulos, "Enhancement of nonlinear effects using photonic crystals," Nature Materials **3**, 211–219 (2004).

[9] H. Walther, B. T. H. Varcoe, B.-G. Englert, and T. Becker, "Cavity quantum electrodynamics," Reports on Progress in Physics **69**, 1325–1382 (2006).

[10] M. H. Freedman, A. Kitaev, M. J. Larsen, and Z. Wang, "Topological quantum computation," Bulletin of the American Mathematical Society **40**, 31–39 (2002).

[11] F. Wilczek, "Quantum Mechanics of Fractional-Spin Particles," Physical Review Letters **49**, 957–959 (1982).

[12] D. C. Tsui, H. L. Stormer, and A. C. Gossard, "Two-Dimensional Magnetotransport in the Extreme Quantum Limit," Physical Review Letters **48**, 1559–1562 (1982).

[13] X. G. Wen, "Non-Abelian statistics in the fractional quantum Hall states," Physical Review Letters **66**, 802–805 (1991).

[14] B. A. Bernevig and T. L. Hughes, *Topological Insulators and Topological Superconductors* (Princeton University Press., 2013).

[15] K. V. Klitzing, G. Dorda, and M. Pepper, "New Method for High-Accuracy Determination of the Fine-Structure Constant Based on Quantized Hall Resistance," Physical Review Letters **45**, 494–497 (1980).

[16] D. Tong, "Lectures on the Quantum Hall Effect," (2016), arXiv:1606.06687 .

[17] F. D. M. Haldane, "Model for a Quantum Hall Effect without Landau Levels: Condensed-Matter Realization of the "Parity Anomaly"," Physical Review Letters **61**, 2015–2018 (1988).

[18] J. Dalibard, F. Gerbier, G. Juzeliūnas, and P. Öhberg, "Colloquium: Artificial gauge potentials for neutral atoms," Reviews of Modern Physics **83**, 1523–1543 (2011).

[19] H. Miyake, G. A. Siviloglou, C. J. Kennedy, W. C. Burton, and W. Ketterle, "Realizing the Harper Hamiltonian with Laser-Assisted Tunneling in Optical Lattices," Physical Review Letters **111**, 185302 (2013).

[20] C. J. Kennedy, W. C. Burton, W. C. Chung, and W. Ketterle, "Observation of Bose–Einstein condensation in a strong synthetic magnetic field," Nature Physics **11**, 859–864 (2015).

[21] A. Eckardt, "Colloquium: Atomic quantum gases in periodically driven optical lattices," Reviews of Modern Physics **89**, 011004 (2017).

[22] F. D. M. Haldane and S. Raghu, "Possible Realization of Directional Optical Waveguides in Photonic Crystals with Broken Time-Reversal Symmetry," Physical Review Letters **100**, 013904 (2008).

[23] S. Raghu and F. D. M. Haldane, "Analogs of quantum-Hall-effect edge states in photonic crystals," Physical Review A **78**, 033834 (2008).

[24] Z. Wang, Y. D. Chong, J. D. Joannopoulos, and M. Soljačić, "Reflection-Free One-Way Edge Modes in a Gyromagnetic Photonic Crystal," Physical Review Letters **100**, 013905 (2008).

[25] K. Liu, L. Shen, and S. He, "One-way edge mode in a gyromagnetic photonic crystal slab," Optics Letters **37**, 4110 (2012).

[26] Z. Wang, Y. Chong, J. D. Joannopoulos, and M. Soljačić, "Observation of unidirectional backscattering-immune topological electromagnetic states," Nature **461**, 772–775 (2009).

[27] Z. Yu, G. Veronis, Z. Wang, and S. Fan, "One-Way Electromagnetic Waveguide Formed at the Interface between a Plasmonic Metal under a Static Magnetic Field and a Photonic Crystal," Physical Review Letters **100**, 023902 (2008).

[28] M. C. Rechtsman, J. M. Zeuner, Y. Plotnik, Y. Lumer, D. Podolsky, F. Dreisow, S. Nolte, M. Segev, and A. Szameit, "Photonic Floquet topological insulators," Nature **496**, 196–200 (2013).

[29] M. Hafezi, E. A. Demler, M. D. Lukin, and J. M. Taylor, "Robust optical delay lines with topological protection," Nature Physics **7**, 907–912 (2011).

[30] M. Hafezi, S. Mittal, J. Fan, A. Migdall, and J. M. Taylor, "Imaging topological edge states in silicon photonics," Nature Photonics **7**, 1001–1005 (2013).

[31] K. Fang, Z. Yu, and S. Fan, "Realizing effective magnetic field for photons by controlling the phase of dynamic modulation," Nature Photonics **6**, 782–787 (2012).

[32] A. B. Khanikaev, R. Fleury, S. H. Mousavi, and A. Alù, "Topologically robust sound propagation in an angular-momentum-biased graphene-like resonator lattice," Nature Communications **6**, 8260 (2015).

[33] Z. Yang, F. Gao, X. Shi, X. Lin, Z. Gao, Y. Chong, and B. Zhang, "Topological Acoustics," Physical Review Letters **114**, 114301 (2015).

[34] J. Lu, C. Qiu, L. Ye, X. Fan, M. Ke, F. Zhang, and Z. Liu, "Observation of topological valley transport of sound in sonic crystals," Nature Physics **13**, 369–374 (2017).

[35] R. Susstrunk and S. D. Huber, "Observation of phononic helical edge states in a mechanical topological insulator," Science **349**, 47–50 (2015).

[36] S. H. Mousavi, A. B. Khanikaev, and Z. Wang, "Topologically protected elastic waves in phononic metamaterials," Nature Communications **6**, 8682 (2015).

[37] L. M. Nash, D. Kleckner, A. Read, V. Vitelli, A. M. Turner, and W. T. M. Irvine, "Topological mechanics of gyroscopic metamaterials." Proceedings of the National Academy of Sciences of the United States of America **112**, 14495–500 (2015).

[38] M. Gross and S. Haroche, "Superradiance: An essay on the theory of collective spontaneous emission," Physics Reports **93**, 301–396 (1982).

[39] D. Peter, N. Y. Yao, N. Lang, S. D. Huber, M. D. Lukin, and H. P. Büchler, "Topological bands with a Chern number C = 2 by dipolar exchange interactions," Physical Review A **91**, 053617 (2015).

[40] T. Karzig, C.-E. Bardyn, N. H. Lindner, and G. Refael, "Topological Polaritons," Physical Review X **5**, 031001 (2015).

[41] J. D. Joannopoulos, S. G. Johnson, J. N. Winn, and R. D. Meade, *Photonic Crystals: Molding the Flow of Light (Second Edition).* (Princeton University Press, 2008).

[42] J. C. Maxwell, "Problems," Cambridge and Dublin Mathematical Journal **8** (1854).

[43] C. T. Tai, "Maxwell Fish-eye treated by Maxwell Equations," Nature **182** (1958).

[44] H. Rosu and M. Reyes, "Electromagnetic modes of Maxwell fisheye lens," Il Nuovo Cimento D **16**, 517–522 (1994).

[45] A. Greenwood and Jian-Ming Jin, "A field picture of wave propagation in inhomogeneous dielectric lenses," IEEE Antennas and Propagation Magazine **41**, 9–18 (1999).

[46] A. J. Makowski and K. J. Górska, "Quantization of the Maxwell fish-eye problem and the quantum-classical correspondence," Physical Review A **79**, 052116 (2009).

[47] H. C. Rosu, M. Reyes, K. B. Wolf, and O. Obregon, "Supersymmetric features of the maxwell fish-eye lens," in *Proc. SPIE 2730, Second Iberoamerican Meeting on Optics, 436 (February 5, 1996)*, edited by D. Malacara-Hernandez, S. E. Acosta-Ortiz, R. Rodriguez-Vera, Z. Malacara, and A. A. Morales (1996) pp. 436–439.

[48] U. Leonhardt, "Perfect imaging without negative refraction," New Journal of Physics **11**, 093040 (2009).

[49] U. Leonhardt and T. Philbin, *Geometry and light: the science of invisibility* (Dover Publications, 2010).

[50] Y. G. Ma, S. Sahebdivan, C. K. Ong, T. Tyc, and U. Leonhardt, "Evidence for subwavelength imaging with positive refraction," New Journal of Physics **13**, 033016 (2011).

[51] M. Born and E. Wolf, *Principles of optics: electromagnetic theory of propagation, interference and diffraction of light* (Cambridge University Press, 1999).

[52] U. Leonhardt and T. G. Philbin, "Reply to 'Comment on 'Perfect imaging with positive refraction in three dimensions' '," Physical Review A **82**, 057802 (2010).

[53] U. Leonhardt, "Reply to comment on 'Perfect imaging without negative refraction?'," New Journal of Physics **12**, 058002 (2010).

[54] U. Leonhardt, "Reply to comment on 'Perfect imaging without negative refraction'," New Journal of Physics **13**, 028002 (2011).

[55] T. Tyc and X. Zhang, "Forum Optics: Perfect lenses in focus," Nature **480**, 42–43 (2011).

[56] R. J. Blaikie, "Comment on 'Perfect imaging without negative refraction'," New Journal of Physics **12**, 058001 (2010).

[57] R. Merlin, "Comment on "Perfect imaging with positive refraction in three dimensions"," Physical Review A **82**, 057801 (2010).

[58] R. J. Blaikie, "Perfect imaging without refraction?" New Journal of Physics **13**, 125006 (2011).

[59] P. Kinsler, "Active drains and causality," Physical Review A **82**, 055804 (2010).

[60] J. C. González, P. Benítez, and J. C. Miñano, "Perfect drain for the Maxwell fish eye lens," New Journal of Physics **13**, 023038 (2011).

[61] O. Quevedo-Teruel, R. C. Mitchell-Thomas, and Y. Hao, "Frequency dependence and passive drains in fish-eye lenses," Physical Review A **86**, 053817 (2012).

[62] J. C. González, D. Grabovičkić, P. Benítez, and J. C. Miñano, "Circuital model for the spherical geodesic waveguide perfect drain," New Journal of Physics **14**, 083033 (2012).

[63] L. Xu and H. Chen, "Coherent perfect absorber makes a perfect drain for Maxwell's fish-eye lens," EPL (Europhysics Letters) **100**, 34001 (2012).

[64] Y. Ma, T. Wu, and C. K. Ong, "Subwavelength drains designed for mirror-closed dielectric lenses," Journal of Optics **15**, 125705 (2013).

[65] F. Sun and S. He, "Can Maxwell's fish eye lens really give perfect imaging?" Progress In Electromagnetics Research **108**, 307–322 (2010).

[66] F. Sun, X. C. Ge, and S. He, "Can Maxwell's fish eye lens really give perfect imaging? Part II. The case with passive drains," Progress In Electromagnetics Research **110**, 313–328 (2010).

[67] P. Kinsler and A. Favaro, "Comment on 'Reply to comment on "Perfect imaging without negative refraction"'," New Journal of Physics **13**, 028001 (2011).

[68] U. Leonhardt and S. Sahebdivan, "Perfect imaging: they do not do it with mirrors," Journal of Optics **13**, 024016 (2011).

[69] L. A. Pazynin and G. O. Kryvchikova, "Focusing properties of Maxwell's fish eye medium," Progress In Electromagnetics Research **131**, 425–440 (2012).

[70] J. Liu, R. Mendis, and D. M. Mittleman, "A Maxwell's fish eye lens for the terahertz region," Applied Physics Letters **103**, 031104 (2013).

[71] T. Tyc and A. Danner, "Resolution of Maxwell's fisheye with an optimal active drain," New Journal of Physics **16**, 063001 (2014).

[72] M. A. Alonso, "Is the Maxwell–Shafer fish eye lens able to form super-resolved images?" New Journal of Physics **17**, 073013 (2015).

[73] S. A. R. Horsley, R. N. Foster, T. Tyc, and T. G. Philbin, "Active absorption of electromagnetic pulses in a cavity," New Journal of Physics **17**, 053050 (2015).

[74] S. He, F. Sun, S. Guo, S. Zhong, L. Lan, W. Jiang, Y. Ma, and T. Wu, "Can Maxwell's fish eye lens really give perfect imaging? Part III. A careful reconsideration of the "Evidence for subwavelength imaging with positive refraction"," Progress In Electromagnetics Research **152**, 1–15 (2015).

[75] G. Rosenblatt and M. Orenstein, "Power drainage and energy dissipation in lossy but perfect lenses," Physical Review A **95**, 053857 (2017).

[76] J. C. Miñano, R. Marqués, J. C. González, P. Benítez, V. Delgado, D. Grabovickic, and M. Freire, "Super-resolution for a point source better than $\lambda/500$ using positive refraction," New Journal of Physics **13**, 125009 (2011).

[77] J. C. Miñano, J. Sánchez-Dehesa, J. C. González, P. Benítez, D. Grabovičkić, J. Carbonell, and H. Ahmadpanahi, "Experimental evidence of super-resolution better than $\lambda/105$ with positive refraction," New Journal of Physics **16**, 033015 (2014).

[78] U. Leonhardt, S. Sahebdivan, A. Kogan, and T. Tyc, "A simple model explaining super-resolution in absolute optical instruments," New Journal of Physics **17**, 053007 (2015).

[79] U. Leonhardt and S. Sahebdivan, "Theory of Maxwell's fish eye with mutually interacting sources and drains," Physical Review A **92**, 053848 (2015).

[80] R. Gomez-Medina, P. San Jose, A. Garcia-Martin, M. Lester, M. Nieto-Vesperinas, and J. J. Saenz, "Resonant Radiation Pressure on Neutral Particles in a Waveguide," Physical Review Letters **86**, 4275–4277 (2001).

[81] E. Shahmoon and G. Kurizki, "Nonradiative interaction and entanglement between distant atoms," Physical Review A **87**, 033831 (2013).

[82] D. E. Chang, A. S. Sørensen, P. R. Hemmer, and M. D. Lukin, "Quantum Optics with Surface Plasmons," Physical Review Letters **97**, 053002 (2006).

[83] A. Gonzalez-Tudela, D. Martin-Cano, E. Moreno, L. Martin-Moreno, C. Tejedor, and F. J. Garcia-Vidal, "Entanglement of Two Qubits Mediated by One-Dimensional Plasmonic Waveguides," Physical Review Letters **106**, 020501 (2011).

[84] D. Dzsotjan, A. S. Sørensen, and M. Fleischhauer, "Quantum emitters coupled to surface plasmons of a nanowire: A Green's function approach," Physical Review B **82**, 075427 (2010).

[85] K. Lalumiere, B. C. Sanders, A. F. van Loo, A. Fedorov, A. Wallraff, and A. Blais, "Input-output theory for waveguide QED with an ensemble of inhomogeneous atoms," Physical Review A **88**, 043806 (2013).

[86] A. F. van Loo, A. Fedorov, K. Lalumière, B. C. Sanders, A. Blais, and A. Wallraff, "Photon-Mediated Interactions Between Distant Artificial Atoms," Science **342** (2013).

[87] K. Inomata, K. Koshino, Z. Lin, W. Oliver, J. Tsai, Y. Nakamura, and T. Yamamoto, "Microwave Down-Conversion with an Impedance-Matched Λ System in Driven Circuit QED," Physical Review Letters **113**, 063604 (2014).

[88] P. Domokos, P. Horak, and H. Ritsch, "Quantum description of light-pulse scattering on a single atom in waveguides," Physical Review A **65**, 033832 (2002).

[89] P. Horak, P. Domokos, and H. Ritsch, "Giant Lamb shift of atoms near lossy multimode optical micro-waveguides," Europhysics Letters (EPL) **61**, 459–465 (2003).

[90] V. V. Klimov and M. Ducloy, "Spontaneous emission rate of an excited atom placed near a nanofiber," Physical Review A **69**, 013812 (2004).

[91] F. Le Kien, V. I. Balykin, and K. Hakuta, "Scattering of an evanescent light field by a single cesium atom near a nanofiber," Physical Review A **73**, 013819 (2006).

[92] D. E. Chang, L. Jiang, A. V. Gorshkov, and H. J. Kimble, "Cavity QED with atomic mirrors," New Journal of Physics **14**, 063003 (2012).

[93] J. S. Douglas, H. Habibian, C.-L. Hung, A. V. Gorshkov, H. J. Kimble, and D. E. Chang, "Quantum many-body models with cold atoms coupled to photonic crystals," Nature Photonics **9**, 326–331 (2015).

[94] B. J. Justice, J. J. Mock, L. Guo, A. Degiron, D. Schurig, and D. R. Smith, "Spatial mapping of the internal and external electromagnetic fields of negative index metamaterials," Optics Express **14**, 8694 (2006).

[95] Y. Liu, T. Zentgraf, G. Bartal, and X. Zhang, "Transformational Plasmon Optics," Nano Letters **10**, 1991–1997 (2010).

[96] T. Zentgraf, Y. Liu, M. H. Mikkelsen, J. Valentine, and X. Zhang, "Plasmonic Luneburg and Eaton lenses," Nature Nanotechnology **6**, 151–155 (2011).

[97] R. J. Glauber and M. Lewenstein, "Quantum optics of dielectric media," Physical Review A **43**, 467–491 (1991).

[98] P. W. Milonni and P. L. Knight, "Retardation in the resonant interaction of two identical atoms," Physical Review A **10**, 1096–1108 (1974).

[99] T. Pellizzari, S. A. Gardiner, J. I. Cirac, and P. Zoller, "Decoherence, Continuous Observation, and Quantum Computing: A Cavity QED Model," Physical Review Letters **75**, 3788–3791 (1995).

[100] J. I. Cirac, P. Zoller, H. J. Kimble, and H. Mabuchi, "Quantum State Transfer and Entanglement Distribution among Distant Nodes in a Quantum Network," Physical Review Letters **78**, 3221–3224 (1997).

[101] D. E. Chang, A. S. Sørensen, E. A. Demler, and M. D. Lukin, "A single-photon transistor using nanoscale surface plasmons," Nature Physics **3**, 807–812 (2007).

[102] A. Fuhrmanek, R. Bourgain, Y. R. P. Sortais, and A. Browaeys, "Free-Space Lossless State Detection of a Single Trapped Atom," Physical Review Letters **106**, 133003 (2011).

[103] M. J. Gibbons, C. D. Hamley, C.-Y. Shih, and M. S. Chapman, "Nondestructive Fluorescent State Detection of Single Neutral Atom Qubits," Physical Review Letters **106**, 133002 (2011).

[104] H. T. Dung, L. Knöll, and D.-G. Welsch, "Three-dimensional quantization of the electromagnetic field in dispersive and absorbing inhomogeneous dielectrics," Physical Review A **57**, 3931–3942 (1998).

[105] H. T. Dung, L. Knöll, and D.-G. Welsch, "Resonant dipole-dipole interaction in the presence of dispersing and absorbing surroundings," Physical Review A **66**, 063810 (2002).

[106] S. Scheel and S. Y. Buhmann, "Acta Physica Slovaca," Acta Physica Slovaca **58**, 675–809 (2008).

[107] S. Y. Buhmann, *Dispersion Forces I. Springer Tracts in Modern Physics, vol 247* (Springer, Berlin, Heidelberg, 2012).

[108] A. Erdélyi, ed., *Higher Transcendental Functions,*, Vol. 1 (McGraw-Hill, New York-London, 1953).

[109] M. Antezza and Y. Castin, "Spectrum of Light in a Quantum Fluctuating Periodic Structure," Physical Review Letters **103**, 123903 (2009).

[110] E. Shahmoon, D. S. Wild, M. D. Lukin, and S. F. Yelin, "Cooperative Resonances in Light Scattering from Two-Dimensional Atomic Arrays," Physical Review Letters **118**, 113601 (2017).

[111] T. Bienaimé, N. Piovella, and R. Kaiser, "Controlled Dicke Subradiance from a Large Cloud of Two-Level Systems," Physical Review Letters **108**, 123602 (2012).

[112] W. Guerin, M. O. Araújo, and R. Kaiser, "Subradiance in a Large Cloud of Cold Atoms," Physical Review Letters **116**, 083601 (2016).

[113] J. Perczel, J. Borregaard, D. E. Chang, H. Pichler, S. F. Yelin, P. Zoller, and M. D. Lukin, "Topological Quantum Optics in Two-Dimensional Atomic Arrays," Physical Review Letters **119**, 023603 (2017).

[114] J. Perczel, J. Borregaard, D. E. Chang, H. Pichler, S. F. Yelin, P. Zoller, and M. D. Lukin, "Photonic band structure of two-dimensional atomic lattices," Physical Review A **96**, 063801 (2017).

[115] G. K. Brennen, I. H. Deutsch, and P. S. Jessen, "Entangling dipole-dipole interactions for quantum logic with neutral atoms," Physical Review A **61**, 062309 (2000).

[116] F. Dolde, I. Jakobi, B. Naydenov, N. Zhao, S. Pezzagna, C. Trautmann, J. Meijer, P. Neumann, F. Jelezko, and J. Wrachtrup, "Room-temperature entanglement between single defect spins in diamond," Nature Physics **9**, 139–143 (2013).

[117] A. Sipahigil, K. Jahnke, L. Rogers, T. Teraji, J. Isoya, A. Zibrov, F. Jelezko, and M. Lukin, "Indistinguishable Photons from Separated Silicon-Vacancy Centers in Diamond," Physical Review Letters **113**, 113602 (2014).

[118] S. Kolkowitz, A. Safira, A. A. High, R. C. Devlin, S. Choi, Q. P. Unterreithmeier, D. Patterson, A. S. Zibrov, V. E. Manucharyan, H. Park, and M. D. Lukin, "Probing Johnson noise and ballistic transport in normal metals with a single-spin qubit," Science **347**, 1129–1132 (2015).

[119] T. Iwasaki, F. Ishibashi, Y. Miyamoto, Y. Doi, S. Kobayashi, T. Miyazaki, K. Tahara, K. D. Jahnke, L. J. Rogers, B. Naydenov, F. Jelezko, S. Yamasaki, S. Nagamachi, T. Inubushi, N. Mizuochi, and M. Hatano, "Germanium-Vacancy Single Color Centers in Diamond," Scientific Reports **5**, 12882 (2015).

[120] A. Sipahigil, R. E. Evans, D. D. Sukachev, M. J. Burek, J. Borregaard, M. K. Bhaskar, C. T. Nguyen, J. L. Pacheco, H. A. Atikian, C. Meuwly, R. M. Camacho, F. Jelezko, E. Bielejec, H. Park, M. Lončar, and M. D. Lukin, "An integrated diamond nanophotonics platform for quantum-optical networks," Science **354**, 847–850 (2016).

[121] A. A. High, R. C. Devlin, A. Dibos, M. Polking, D. S. Wild, J. Perczel, N. P. de Leon, M. D. Lukin, and H. Park, "Visible-frequency hyperbolic metasurface," Nature **522**, 192–196 (2015).

[122] G. C. des Francs, J. Barthes, A. Bouhelier, J. C. Weeber, A. Dereux, A. Cuche, and C. Girard, "Plasmonic Purcell factor and coupling efficiency to surface plasmons. Implications for addressing and controlling optical nanosources," Journal of Optics **18**, 094005 (2016).

[123] J. E. Sipe, "New Green-function formalism for surface optics," Journal of the Optical Society of America B **4**, 481 (1987).

[124] M. Arcari, I. Sollner, A. Javadi, S. Lindskov Hansen, S. Mahmoodian, J. Liu, H. Thyrrestrup, E. Lee, J. Song, S. Stobbe, and P. Lodahl, "Near-Unity Coupling Efficiency of a Quantum Emitter to a Photonic Crystal Waveguide," Physical Review Letters **113**, 093603 (2014).

[125] I. H. Deutsch, R. J. C. Spreeuw, S. L. Rolston, and W. D. Phillips, "Photonic band gaps in optical lattices," Physical Review A **52**, 1394–1410 (1995).

[126] D. van Coevorden, R. Sprik, A. Tip, and A. Lagendijk, "Photonic Band Structure of Atomic Lattices," Physical Review Letters **77**, 2412–2415 (1996).

[127] P. de Vries, D. van Coevorden, and A. Lagendijk, "Point scatterers for classical waves," Reviews of Modern Physics **70**, 447–466 (1998).

[128] J. A. Klugkist, M. Mostovoy, and J. Knoester, "Mode Softening, Ferroelectric Transition, and Tunable Photonic Band Structures in a Point-Dipole Crystal," Physical Review Letters **96**, 163903 (2006).

[129] M. Antezza and Y. Castin, "Fano-Hopfield model and photonic band gaps for an arbitrary atomic lattice," Physical Review A **80**, 013816 (2009).

[130] M. Antezza and Y. Castin, "Photonic band gap in an imperfect atomic diamond lattice: Penetration depth and effects of finite size and vacancies," Physical Review A **88**, 033844 (2013).

[131] R. J. Bettles, J. Minář, C. S. Adams, I. Lesanovsky, and B. Olmos, "Topological properties of a dense atomic lattice gas," Physical Review A **96**, 041603 (2017).

[132] R. J. Bettles, S. A. Gardiner, and C. S. Adams, "Enhanced Optical Cross Section via Collective Coupling of Atomic Dipoles in a 2D Array," Physical Review Letters **116**, 103602 (2016).

[133] S. V. Syzranov, M. L. Wall, B. Zhu, V. Gurarie, and A. M. Rey, "Emergent Weyl excitations in systems of polar particles," Nature Communications **7**, 13543 (2016).

[134] A. Asenjo-Garcia, M. Moreno-Cardoner, A. Albrecht, H. J. Kimble, and D. E. Chang, "Exponential Improvement in Photon Storage Fidelities Using Subradiance and "Selective Radiance" in Atomic Arrays," Physical Review X **7**, 031024 (2017).

[135] G. Facchinetti, S. D. Jenkins, and J. Ruostekoski, "Storing Light with Subradiant Correlations in Arrays of Atoms," Physical Review Letters **117**, 243601 (2016).

[136] R. Collin, "Hertzian dipole radating over a lossy earth or sea: some early and late 20th-century controversies," IEEE Antennas and Propagation Magazine **46**, 64–79 (2004).

[137] T. W. Ebbesen, H. J. Lezec, H. F. Ghaemi, T. Thio, and P. A. Wolff, "Extraordinary optical transmission through sub-wavelength hole arrays," Nature **391**, 667–669 (1998).

[138] F. J. García de Abajo, "Colloquium: Light scattering by particle and hole arrays," Reviews of Modern Physics **79**, 1267–1290 (2007).

[139] A. Y. Nikitin, F. J. García-Vidal, and L. Martín-Moreno, "Surface Electromagnetic Field Radiated by a Subwavelength Hole in a Metal Film," Physical Review Letters **105**, 073902 (2010).

[140] A. V. Kildishev, A. Boltasseva, and V. M. Shalaev, "Planar Photonics with Metasurfaces," Science **339** (2013).

[141] M. S. Tame, K. R. Mcenery, Ş. K. Özdemir, J. Lee, S. A. Maier, and M. S. Kim, "Quantum plasmonics," Nature Physics **9**, 329–340 (2013).

[142] A. Delga, J. Feist, J. Bravo-Abad, and F. Garcia-Vidal, "Quantum Emitters Near a Metal Nanoparticle: Strong Coupling and Quenching," Physical Review Letters **112**, 253601 (2014).

[143] H. Pichler, T. Ramos, A. J. Daley, and P. Zoller, "Quantum optics of chiral spin networks," Physical Review A **91**, 042116 (2015).

[144] C. W. Gardiner and P. Zoller, *Quantum noise: a handbook of Markovian and non-Markovian quantum stochastic methods with applications to quantum optics* (Springer, 2010).

[145] J. Dalibard, Y. Castin, and K. Mølmer, "Wave-function approach to dissipative processes in quantum optics," Physical Review Letters **68**, 580–583 (1992).

[146] H. Carmichael, *An open systems approach to quantum optics: lectures presented at the Université libre de Bruxelles, October 28 to November 4, 1991* (Springer-Verlag, 1993).

[147] K. Mølmer, Y. Castin, and J. Dalibard, "Monte Carlo wave-function method in quantum optics," Journal of the Optical Society of America B **10**, 524 (1993).

[148] C. Bena and G. Montambaux, "Remarks on the tight-binding model of graphene," New Journal of Physics **11**, 095003 (2009).

[149] O. Morice, Y. Castin, and J. Dalibard, "Refractive index of a dilute Bose gas," Physical Review A **51**, 3896–3901 (1995).

[150] N. W. Ashcroft and N. D. Mermin, *Solid state physics* (Holt, Rinehart and Winston, 1976).

[151] W. C. Chew, *Wave and fields in inhomogeneous media* (IEEE, 1999).

[152] T. Fukui, Y. Hatsugai, and H. Suzuki, "Chern Numbers in Discretized Brillouin Zone: Efficient Method of Computing (Spin) Hall Conductances," Journal of the Physical Society of Japan **74**, 1674–1677 (2005).

[153] I. Bloch, "Ultracold quantum gases in optical lattices," Nature Physics **1**, 23–30 (2005).

[154] P. Lalanne and J. P. Hugonin, "Interaction between optical nano-objects at metallo-dielectric interfaces," Nature Physics **2**, 551–556 (2006).

[155] H. Liu and P. Lalanne, "Microscopic theory of the extraordinary optical transmission," Nature **452**, 728–731 (2008).

[156] P. Lalanne, "A microscopic view of the electromagnetic properties of sub-$\lambda\lambda$ metallic surfaces," Surface Science Reports **64**, 453–469 (2009).

[157] M. Konig, S. Wiedmann, C. Brune, A. Roth, H. Buhmann, L. W. Molenkamp, X.-L. Qi, and S.-C. Zhang, "Quantum Spin Hall Insulator State in HgTe Quantum Wells," Science **318**, 766–770 (2007).

[158] B. I. Halperin, "Quantized Hall conductance, current-carrying edge states, and the existence of extended states in a two-dimensional disordered potential," Physical Review B **25**, 2185–2190 (1982).

[159] R. B. Laughlin, "Quantized Hall conductivity in two dimensions," Physical Review B **23**, 5632–5633 (1981).

[160] N. Y. Yao, C. R. Laumann, A. V. Gorshkov, S. D. Bennett, E. Demler, P. Zoller, and M. D. Lukin, "Topological Flat Bands from Dipolar Spin Systems," Physical Review Letters **109**, 266804 (2012).

[161] F. Wu, T. Lovorn, and A. MacDonald, "Topological Exciton Bands in Moiré Heterojunctions," Physical Review Letters **118**, 147401 (2017).

[162] Y. D. Chong, X.-G. Wen, and M. Soljačić, "Effective theory of quadratic degeneracies," Physical Review B **77**, 235125 (2008).

[163] Y. Plotnik, M. C. Rechtsman, D. Song, M. Heinrich, J. M. Zeuner, S. Nolte, Y. Lumer, N. Malkova, J. Xu, A. Szameit, Z. Chen, and M. Segev, "Observation of unconventional edge states in 'photonic graphene'," Nature Materials **13**, 57–62 (2013).

[164] B. Dayan, a. S. Parkins, T. Aoki, E. P. Ostby, K. J. Vahala, and H. J. Kimble, "A Photon Turnstile Dynamically Regulated by One Atom," Science **319**, 1062–1065 (2008).

[165] W. Chen, K. M. Beck, R. Bucker, M. Gullans, M. D. Lukin, H. Tanji-Suzuki, and V. Vuletic, "All-Optical Switch and Transistor Gated by One Stored Photon," Science **341**, 768–770 (2013).

[166] L. Neumeier, M. Leib, and M. J. Hartmann, "Single-Photon Transistor in Circuit Quantum Electrodynamics," Physical Review Letters **111**, 063601 (2013).

[167] I. Shomroni, S. Rosenblum, Y. Lovsky, O. Bechler, G. Guendelman, and B. Dayan, "All-optical routing of single photons by a one-atom switch controlled by a single photon," Science **345** (2014).

[168] B. Olmos, D. Yu, Y. Singh, F. Schreck, K. Bongs, and I. Lesanovsky, "Long-Range Interacting Many-Body Systems with Alkaline-Earth-Metal Atoms," Physical Review Letters **110**, 143602 (2013).

[169] S. Stellmer, F. Schreck, and T. C. Killian, "Degenerate quantum gases of strontium," in *Annual Review of Cold Atoms and Molecules* (World Scientific Publishing Co., 2014) pp. 1–80.

[170] T. Akatsuka, M. Takamoto, and H. Katori, "Optical lattice clocks with non-interacting bosons and fermions," Nature Physics **4**, 954–959 (2008).

[171] W. S. Bakr, A. Peng, M. E. Tai, R. Ma, J. Simon, J. I. Gillen, S. Folling, L. Pollet, and M. Greiner, "Probing the Superfluid-to-Mott Insulator Transition at the Single-Atom Level," Science **329**, 547–550 (2010).

[172] A. González-Tudela, C.-L. Hung, D. E. Chang, J. I. Cirac, and H. J. Kimble, "Subwavelength vacuum lattices and atom–atom interactions in two-dimensional photonic crystals," Nature Photonics **9**, 320–325 (2015).

[173] W. Yi, A. J. Daley, G. Pupillo, and P. Zoller, "State-dependent, addressable subwavelength lattices with cold atoms," New Journal of Physics **10**, 073015 (2008).

[174] S. Nascimbene, N. Goldman, N. R. Cooper, and J. Dalibard, "Dynamic Optical Lattices of Subwavelength Spacing for Ultracold Atoms," Physical Review Letters **115**, 140401 (2015).

[175] Y.-F. Wang, H. Yao, C.-D. Gong, and D. N. Sheng, "Fractional quantum Hall effect in topological flat bands with Chern number two," Physical Review B **86**, 201101 (2012).

[176] C. Robert, D. Lagarde, F. Cadiz, G. Wang, B. Lassagne, T. Amand, A. Balocchi, P. Renucci, S. Tongay, B. Urbaszek, and X. Marie, "Exciton radiative lifetime in transition metal dichalcogenide monolayers," Physical Review B **93**, 205423 (2016).

[177] H. Li, A. W. Contryman, X. Qian, S. M. Ardakani, Y. Gong, X. Wang, J. M. Weisse, C. H. Lee, J. Zhao, P. M. Ajayan, J. Li, H. C. Manoharan, and X. Zheng, "Optoelectronic crystal of artificial atoms in strain-textured molybdenum disulphide," Nature Communications **6**, 7381 (2015).

[178] C. Palacios-Berraquero, D. M. Kara, A. R. P. Montblanch, M. Barbone, P. Latawiec, D. Yoon, A. K. Ott, M. Loncar, A. C. Ferrari, and M. Atature, "Large-scale quantum-emitter arrays in atomically thin semiconductors," Nature Communications **8**, 15093 (2017).

[179] Y. Lin, X. Ling, L. Yu, S. Huang, A. L. Hsu, Y.-H. Lee, J. Kong, M. S. Dresselhaus, and T. Palacios, "Dielectric Screening of Excitons and Trions in Single-Layer MoS_2," Nano Letters **14**, 5569–5576 (2014).

[180] Y. Zhou, G. Scuri, D. S. Wild, A. A. High, A. Dibos, L. A. Jauregui, C. Shu, K. de Greve, K. Pistunova, A. Joe, T. Taniguchi, K. Watanabe, P. Kim, M. D. Lukin, and H. Park, "Probing dark excitons in atomically thin semiconductors via near-field coupling to surface plasmon polaritons," Nature Nanotechnology **12**, 856–860 (2017).

[181] P. Back, M. Sidler, O. Cotlet, A. Srivastava, N. Takemura, M. Kroner, and A. Imamoglu, "Giant paramagnetism induced valley polarization of electrons in charge-tunable monolayer MoSe2," Physical Review Letters **118**, 237404 (2017).

[182] B. Hunt, J. D. Sanchez-Yamagishi, A. F. Young, M. Yankowitz, B. J. LeRoy, K. Watanabe, T. Taniguchi, P. Moon, M. Koshino, P. Jarillo-Herrero, and R. C. Ashoori, "Massive Dirac Fermions and Hofstadter Butterfly in a van der Waals Heterostructure," Science **340** (2013).

[183] K. S. Novoselov, A. K. Geim, S. V. Morozov, D. Jiang, Y. Zhang, S. V. Dubonos, I. V. Grigorieva, and A. A. Firsov, "Electric field effect in atomically thin carbon films." Science (New York, N.Y.) **306**, 666–9 (2004).

[184] A. H. C. Neto, F. Guinea, N. M. R. Peres, K. S. Novoselov, and A. K. Geim, "The electronic properties of graphene," Reviews of Modern Physics **81**, 109 (2009).

[185] S. Barik, H. Miyake, W. DeGottardi, E. Waks, and M. Hafezi, "Two-dimensionally confined topological edge states in photonic crystals," New Journal of Physics **18**, 113013 (2016).

[186] S. Barik, A. Karasahin, C. Flower, T. Cai, H. Miyake, W. DeGottardi, M. Hafezi, and E. Waks, "A topological quantum optics interface." Science (New York, N.Y.) **359**, 666–668 (2018).

[187] R. A. Sepkhanov, Y. B. Bazaliy, and C. W. J. Beenakker, "Extremal transmission at the Dirac point of a photonic band structure," Physical Review A **75**, 063813 (2007).

[188] S. R. Zandbergen and M. J. A. de Dood, "Experimental Observation of Strong Edge Effects on the Pseudodiffusive Transport of Light in Photonic Graphene," Physical Review Letters **104**, 043903 (2010).

[189] O. Bahat-Treidel, O. Peleg, M. Grobman, N. Shapira, M. Segev, and T. Pereg-Barnea, "Klein Tunneling in Deformed Honeycomb Lattices," Physical Review Letters **104**, 063901 (2010).

[190] X. Zhang, "Observing *Zitterbewegung* for Photons near the Dirac Point of a Two-Dimensional Photonic Crystal," Physical Review Letters **100**, 113903 (2008).

[191] J. Bravo-Abad, J. D. Joannopoulos, and M. Soljačić, "Enabling single-mode behavior over large areas with photonic Dirac cones." Proceedings of the National Academy of Sciences of the United States of America **109**, 9761–5 (2012).

[192] K. Xie, H. Jiang, A. D. Boardman, Y. Liu, Z. Wu, M. Xie, P. Jiang, Q. Xu, M. Yu, and L. E. Davis, "Trapped photons at a Dirac point: a new horizon for photonic crystals," Laser & Photonics Reviews **8**, 583–589 (2014).

[193] A. González-Tudela and J. I. Cirac, "Exotic quantum dynamics and purely long-range coherent interactions in Dirac conelike baths," Physical Review A **97**, 043831 (2018).

[194] S. Johnson and J. Joannopoulos, "Block-iterative frequency-domain methods for Maxwell's equations in a planewave basis," Optics Express **8**, 173 (2001).

[195] D. Dzsotjan, J. Kästel, and M. Fleischhauer, "Dipole-dipole shift of quantum emitters coupled to surface plasmons of a nanowire," Physical Review B **84**, 075419 (2011).

[196] J. Perczel, P. Kómár, and M. D. Lukin, "Quantum optics in Maxwell's fish eye lens with single atoms and photons," Physical Review A **98**, 033803 (2018).

[197] S. D. Huber, "Topological mechanics," Nature Physics **12**, 621–623 (2016).

[198] R. B. Laughlin, "Anomalous Quantum Hall Effect: An Incompressible Quantum Fluid with Fractionally Charged Excitations," Physical Review Letters **50**, 1395–1398 (1983).

[199] J. Perczel, J. Borregaard, D. Chang, H. Pichler, S. Yelin, P. Zoller, and M. Lukin, "Topological Quantum Optics in Two-Dimensional Atomic Arrays," Physical Review Letters **119**, 023603 (2017).

[200] I. Carusotto and C. Ciuti, "Quantum fluids of light," Reviews of Modern Physics **85**, 299–366 (2013).

[201] P. Lodahl, S. Mahmoodian, S. Stobbe, A. Rauschenbeutel, P. Schneeweiss, J. Volz, H. Pichler, and P. Zoller, "Chiral quantum optics," Nature **541**, 473–480 (2017).

[202] D. G. Angelakis, *Quantum Science and Technology*, edited by D. G. Angelakis, Quantum Science and Technology (Springer International Publishing, Cham, 2017) p. 214.

[203] J. I. Cirac and H. J. Kimble, "Quantum optics, what next?" Nature Photonics **11**, 18–20 (2017).

[204] T. Neupert, L. Santos, C. Chamon, and C. Mudry, "Fractional Quantum Hall States at Zero Magnetic Field," Physical Review Letters **106**, 236804 (2011).

[205] E. Tang, J.-W. Mei, and X.-G. Wen, "High-Temperature Fractional Quantum Hall States," Physical Review Letters **106**, 236802 (2011).

[206] K. Sun, Z. Gu, H. Katsura, and S. Das Sarma, "Nearly Flatbands with Nontrivial Topology," Physical Review Letters **106**, 236803 (2011).

[207] N. Y. Yao, A. V. Gorshkov, C. R. Laumann, A. M. Läuchli, J. Ye, and M. D. Lukin, "Realizing Fractional Chern Insulators in Dipolar Spin Systems," Physical Review Letters **110**, 185302 (2013).

[208] N. Sangouard, C. Simon, H. de Riedmatten, and N. Gisin, "Quantum repeaters based on atomic ensembles and linear optics," Reviews of Modern Physics **83**, 33–80 (2011).

[209] A. Javadi, I. Söllner, M. Arcari, S. L. Hansen, L. Midolo, S. Mahmoodian, G. Kiršanskė, T. Pregnolato, E. H. Lee, J. D. Song, S. Stobbe, and P. Lodahl, "Single-photon non-linear optics with a quantum dot in a waveguide," Nature Communications **6**, 8655 (2015).

[210] S. Sun, H. Kim, G. S. Solomon, and E. Waks, "A quantum phase switch between a single solid-state spin and a photon," Nature Nanotechnology **11**, 539–544 (2016).

[211] P. Lodahl, S. Mahmoodian, and S. Stobbe, "Interfacing single photons and single quantum dots with photonic nanostructures," Reviews of Modern Physics **87**, 347–400 (2015).

[212] I. Söllner, S. Mahmoodian, S. L. Hansen, L. Midolo, A. Javadi, G. Kiršanskė, T. Pregnolato, H. El-Ella, E. H. Lee, J. D. Song, S. Stobbe, and P. Lodahl, "Deterministic photon–emitter coupling in chiral photonic circuits," Nature Nanotechnology **10**, 775–778 (2015).

[213] J. D. Thompson, T. G. Tiecke, N. P. de Leon, J. Feist, A. V. Akimov, M. Gullans, A. S. Zibrov, V. Vuletić, and M. D. Lukin, "Coupling a Single Trapped Atom to a Nanoscale Optical Cavity," Science **340** (2013).

[214] T. G. Tiecke, J. D. Thompson, N. P. de Leon, L. R. Liu, V. Vuletić, and M. D. Lukin, "Nanophotonic quantum phase switch with a single atom," , 8–11 (2014).

[215] J. D. Hood, A. Goban, A. Asenjo-Garcia, M. Lu, S.-P. Yu, D. E. Chang, and H. J. Kimble, "Atom-atom interactions around the band edge of a photonic crystal waveguide." Proceedings of the National Academy of Sciences of the United States of America **113**, 10507–12 (2016).

[216] A. Goban, C.-L. Hung, J. D. Hood, S.-P. Yu, J. A. Muniz, O. Painter, and H. J. Kimble, "Superradiance for Atoms Trapped along a Photonic Crystal Waveguide," Physical Review Letters **115**, 063601 (2015).

[217] A. Goban, C.-L. Hung, S.-P. Yu, J. Hood, J. Muniz, J. Lee, M. Martin, A. McClung, K. Choi, D. Chang, O. Painter, and H. Kimble, "Atom–light interactions in photonic crystals," Nature Communications **5**, 3808 (2014).

[218] S.-P. Yu, J. D. Hood, J. A. Muniz, M. J. Martin, R. Norte, C.-L. Hung, S. M. Meenehan, J. D. Cohen, O. Painter, and H. J. Kimble, "Nanowire photonic crystal waveguides for single-atom trapping and strong light-matter interactions," Applied Physics Letters **104**, 111103 (2014).

[219] A. Faraon, C. Santori, Z. Huang, V. M. Acosta, and R. G. Beausoleil, "Coupling of Nitrogen-Vacancy Centers to Photonic Crystal Cavities in Monocrystalline Diamond," Physical Review Letters **109**, 033604 (2012).

[220] J. Riedrich-Möller, C. Arend, C. Pauly, F. Mücklich, M. Fischer, S. Gsell, M. Schreck, and C. Becher, "Deterministic Coupling of a Single Silicon-Vacancy Color Center to a Photonic Crystal Cavity in Diamond," Nano Letters **14**, 5281–5287 (2014).

[221] R. E. Evans, A. Sipahigil, D. D. Sukachev, A. S. Zibrov, and M. D. Lukin, "Narrow-Linewidth Homogeneous Optical Emitters in Diamond Nanostructures via Silicon Ion Implantation," Physical Review Applied **5**, 044010 (2016).

[222] S. Yang, Z.-C. Gu, K. Sun, and S. Das Sarma, "Topological flat band models with arbitrary Chern numbers," Physical Review B **86**, 241112 (2012).

[223] M. Trescher and E. J. Bergholtz, "Flat bands with higher Chern number in pyrochlore slabs," Physical Review B **86**, 241111 (2012).

[224] Z.-X. Gong, M. F. Maghrebi, A. Hu, M. L. Wall, M. Foss-Feig, and A. V. Gorshkov, "Topological phases with long-range interactions," Physical Review B **93**, 041102 (2016).

[225] Y.-C. He, F. Grusdt, A. Kaufman, M. Greiner, and A. Vishwanath, "Realizing and adiabatically preparing bosonic integer and fractional quantum Hall states in optical lattices," Physical Review B **96**, 201103 (2017).

[226] N. H. Wan, S. Mouradian, and D. Englund, "Two-dimensional photonic crystal slab nanocavities on bulk single-crystal diamond," Applied Physics Letters **112**, 141102 (2018).

[227] J. L. Pacheco, M. Singh, D. L. Perry, J. R. Wendt, G. Ten Eyck, R. P. Manginell, T. Pluym, D. R. Luhman, M. P. Lilly, M. S. Carroll, and E. Bielejec, "Ion implantation for deterministic single atom devices," Review of Scientific Instruments **88**, 123301 (2017).

[228] A. Aparna, V. Brahmajirao, and T. Karthikeyan, "Review on Synthesis and Characterization of Gallium Phosphide," Procedia Materials Science **6**, 1650–1657 (2014).

[229] X. Lin, R. Du, and X. Xie, "Recent experimental progress of fractional quantum Hall effect: 5/2 filling state and graphene," National Science Review **1**, 564–579 (2014).

[230] M. Abramowitz and I. A. Stegun, *Handbook of mathematical functions: with formulas, graphs, and mathematical tables* (Dover Publications, 1970).

[231] I. Fredholm, "Sur une classe d'équations fonctionnelles," Acta Mathematica **27**, 365–390 (1903).

[232] C. P. Frahm, "Some novel delta-function identities," American Journal of Physics **51**, 826–829 (1983).

[233] J. Franklin, "Comment on "Some novel delta-function identities" by Charles P. Frahm [Am. J. Phys. 51, 826–829 (1983)]," American Journal of Physics **78**, 1225–1226 (2010).

[234] M. S. Tomaš, "Green function for multilayers: Light scattering in planar cavities," Physical Review A **51**, 2545–2559 (1995).

[235] A. Archambault, T. V. Teperik, F. Marquier, and J. J. Greffet, "Surface plasmon Fourier optics," Physical Review B **79**, 195414 (2009).

[236] C. Henkel, S. Pötting, and M. Wilkens, "Loss and heating of particles in small and noisy traps," Applied Physics B **69**, 379–387 (1999).

[237] L. S. Langsjoen, A. Poudel, M. G. Vavilov, and R. Joynt, "Qubit relaxation from evanescent-wave Johnson noise," Physical Review A **86**, 010301 (2012).

[238] L. S. Langsjoen, A. Poudel, M. G. Vavilov, and R. Joynt, "Electromagnetic fluctuations near thin metallic films," Physical Review B **89**, 115401 (2014).

[239] R. Mitsch, C. Sayrin, B. Albrecht, P. Schneeweiss, and A. Rauschenbeutel, "Quantum state-controlled directional spontaneous emission of photons into a nanophotonic waveguide," Nature Communications **5**, 5713 (2014).

[240] S. John and J. Wang, "Quantum electrodynamics near a photonic band gap: Photon bound states and dressed atoms," Physical Review Letters **64**, 2418–2421 (1990).

[241] S. Fan and J. D. Joannopoulos, "Analysis of guided resonances in photonic crystal slabs," Physical Review B **65**, 235112 (2002).